

DESIGN, SYNTHESIS, AND BIOLOGICAL ACTIVITY OF
RHODIUM METALLOINSERTORS

Thesis by
Alexis C. Komor

In Partial Fulfillment of the Requirements
for the Degree of
Doctor of Philosophy in Chemistry

California Institute of Technology

Pasadena, CA

2014

(Defended May 23, 2014)

© 2014

Alexis C. Komor

All Rights Reserved

Acknowledgements

There are many people that I would like to thank, some that helped me throughout graduate school directly via their mentorship or help with experiments, and some that helped me indirectly through their love and support. I would first and foremost like to thank my advisor, Professor Jacqueline Barton. Your enthusiasm and optimism are incredibly motivating and allowed me to keep going even at the worst of times. Thank you for being a wonderful role model and showing me that women in science can both be successful and have a family.

To my committee chair, Professor Harry Gray, thank you for your unwavering support throughout the years. It was an incredibly rewarding and humbling experience to TA for you these past three years; I know I am a better mentor because of it. Words truly cannot express what you've taught me or how much I appreciate you. My committee members, Professors Doug Rees and Jonas Peters, have been so incredibly supportive and willing to talk about science with me regardless of their busy schedules. My committee is made up of some of the smartest people alive, yet an outsider would never guess it from the down-to-earth way they interact with me on a daily basis. Thank you all for giving me the opportunity to discuss my ideas with you. It has most assuredly made me a better scientist.

I would also like to thank Professor John Bercaw and Dr. Jay Winkler for the opportunity to teach with them. Between you two and Harry, I have been taught to teach and mentor by the best. I will remember these experiences every time I mentor a student, thank you so much for sharing your knowledge with me.

To Maureen Renta, thank you for not only being the glue that keeps our lab together but also for being a friend. I don't think I could have made it through my candidacy, committee meetings, and proposals defense without you to distract me while I waited in the hot seat for my committee to discuss my future. Thank you.

To Agnes Tong, thank you for making every single administrative problem go away without me ever having to do anything. You are amazing at your job and an even more amazing friend. Thank you for being there for me.

I would like to thank Nathan Dalleska for the countless hours he spent fixing the ICP-MS whenever it broke, and never ever losing his temper at me for asking him multiple times a day if the instrument was fixed. Thank you to Scott Virgil for helping me separate my enantiomers and providing me with more information that I could ever know what to do with while doing so. Thank you to Mike Takase for solving all my crystal structures, without which Chapter 5 could not have happened. Thank you to Dave VanderVelde for being so incredibly willing to help with NMR experiments. To Shelley Diamond, you are such an absolute delight to work with, I hope that one day I will know 1/10 of the stuff that you know.

I would like to thank Julie Bailis for her hard work in trying to bring these compounds to clinical trials. Thank you for believing in our work, for all your help with cell culture techniques, and for performing all the experiments that we don't have the instrumentation to do!

To the men and women of the Barton lab, thank you for making my work environment supportive and enjoyable. You guys made coming into lab something that I look forward to. I would especially like to thank Hang Song for teaching me how to do

all the *in vitro* work and showing me the ropes when I first joined the lab. I would also like to personally thank Russ Ernst for not only teaching me how to do biology, but for being a great friend. The Barton lab just hasn't been the same since you graduated. Thank you to Curtis Schneider and Alyson Weidmann, who I have had the privilege of directly working with. It is always nice to have someone to share your frustration with when you screw up an experiment, so thank you for being there for me. Thanks to Aaron Sattler who, even though he was only in the lab for about 4 months, really got Chapter 5 going. I want to thank Tim Mui for being my first friend at Caltech and being a fabulous roommate. You really set the bar high for Andrew. I would also like to thank Ariel Furst for being a great friend and for always lending me an ear when I need to vent.

Thank you to Maraia Ener and Bryan Hunter; despite the craziness of Chem 153 I think we actually taught the students a thing or two about Inorganic Chemistry. I enjoyed every second of teaching with you guys.

To my fellow '09 matriculators, thank you for your friendship and in many cases help with science. I know I would have gone crazy without you guys there to hang out with. Special thanks to Jeff Holder, JJ Kang, JeanLuc Chaubard, and Anna and Seth Arnold. Myles thank you for keeping the atmosphere in the apartment light and for bringing Hank and Lupe into my life.

Thanks to my non-Caltech friends, Sarah, Edlyn, Audra, Heather, Kate, and Danielle; I definitely would have gone insane long ago without you to yank me back to the real world.

To my family, you mean the world to me. Mom, thank you for teaching me the importance of education. Dad, thank you for always being my biggest fan. Russ, thank

you for doing everything three years ahead of me so I always know what to expect. Thank you to the Wangs for being my second family.

Andrew, I could not have done any of this without you. You have helped me with science, listened to me practice every single talk I have ever given, and calmed me down every time I have been nervous about anything. You take care of me every day of my life and most of the time put my needs before your own. You have always known what to do about every problem I have ever had. You are the most wonderful person in the world and I am so happy to be spending the rest of my life with you. Thank you.

Abstract

Deficiencies in the mismatch repair (MMR) pathway are associated with several types of cancers, as well as resistance to commonly used chemotherapeutics. Rhodium metalloinsertors have been found to bind DNA mismatches with high affinity and specificity *in vitro*, and also exhibit cell-selective cytotoxicity, targeting MMR-deficient cells over MMR-proficient cells.

Here we examine the biological fate of rhodium metalloinsertors bearing dipyridylamine ancillary ligands. These complexes are shown to exhibit accelerated cellular uptake which permits the observation of various cellular responses, including disruption of the cell cycle and induction of necrosis, which occur preferentially in the MMR-deficient cell line. These cellular responses provide insight into the mechanisms underlying the selective activity of this novel class of targeted anti-cancer agents.

In addition, ten distinct metalloinsertors with varying lipophilicities are synthesized and their mismatch binding affinities and biological activities studied. While they are found to have similar binding affinities, their cell-selective antiproliferative and cytotoxic activities vary significantly. Inductively coupled plasma mass spectrometry (ICP-MS) experiments show that all of these metalloinsertors localize in the nucleus at sufficient concentrations for binding to DNA mismatches. Furthermore, metalloinsertors with high rhodium localization in the mitochondria show toxicity that is not selective for MMR-deficient cells. This work supports the notion that specific targeting of the metalloinsertors to nuclear DNA gives rise to their cytotoxic and antiproliferative activities that are selective for cells deficient in MMR.

To explore further the basis of the unique selectivity of the metalloinsertors in targeting MMR-deficient cells, experiments were conducted using engineered NCI-H23 lung adenocarcinoma cells that contain a doxycycline-inducible shRNA which suppresses the expression of the MMR gene MLH1. Here we use this new cell line to further validate rhodium metalloinsertors as compounds capable of differentially inhibiting the proliferation of MMR-deficient cancer cells over isogenic MMR-proficient cells. General DNA damaging agents, such as cisplatin and etoposide, in contrast, are less effective in the induced cell line defective in MMR.

Finally, we describe a new subclass of metalloinsertors with enhanced potency and selectivity, in which the complexes show Rh-O coordination. In particular, it has been found that both Δ and Λ enantiomers of $[\text{Rh}(\text{chrysi})(\text{phen})(\text{DPE})]^{2+}$ bind to DNA with similar affinities, suggesting a possible different binding conformation than previous metalloinsertors. Remarkably, all members of this new family of compounds have significantly increased potency in a range of cellular assays; indeed, all are more potent than the FDA-approved anticancer drugs cisplatin and MNNG. Moreover, these activities are coupled with high levels of selectivity for MMR-deficient cells.

Table of Contents

Chapter 1: Introduction.	1
1.1 Metal-Based Chemotherapeutics.	1
1.2 DNA as a Target.	4
1.2.1 Covalent Interactions.	4
1.2.2 Intercalation.	6
1.2.3 Insertion.	11
1.3 Biological Activities of Metal Complexes.	13
1.3.1 Polypyridyl Complexes.	15
1.3.2 Ruthenium Arene Complexes.	19
1.3.3 Rhodium Metalloinsertors.	19
1.4 Cellular Uptake of Metal Complexes.	23
1.4.1 Methods to Monitor Cellular Uptake.	23
1.4.2 Relationships Between Drug Uptake and Activity.	24
1.4.3 Mechanisms of Uptake.	28
1.5 Subcellular localization of the Metal Complex.	38
1.5.1 Methods to monitor Localization.	38
1.5.2 Peptide Conjugation.	41
1.6 Targeted Therapeutics.	46
1.6.1 Proteins as Targets.	46
1.6.2 Organelles as Targets.	50
1.6.3 DNA Lesions as Targets.	50
1.7 Conclusion.	51

1.8	References.	53
-----	------------------	----

Chapter 2: Selective Cytotoxicity of Rhodium Metalloinsertors in Mismatch Repair-Deficient Cells.62

2.1	Introduction.	62
2.2	Experimental Protocols.	66
2.2.1	Materials.	66
2.2.2	Synthesis of Metal Complexes.	66
2.2.2.1	[Rh(NH ₃) ₆][OTf] ₃	66
2.2.2.2	[Rh(NH ₃) ₄ (chrysi)]Cl ₃	67
2.2.2.3	N-methyl-N-(pyridin-2-yl)pyridin-2-amine (MeDPA) . . .	68
2.2.2.4	[Rh(XDPA) ₂ (chrysi)]Cl ₃ (X=H, Me)	68
2.2.3	Cell Culture.	69
2.2.3.1	ICP-MS Assay for Cellular Rhodium Levels.	69
2.2.3.2	Cellular Proliferation ELISA.	70
2.2.3.3	MTT Cytotoxicity Assay.	70
2.2.4	Cell Cycle Distribution Flow Cytometry Assay.	71
2.2.5	Cell Death Mode Flow Cytometry Assay.	71
2.3	Results.	72
2.3.1	ICP-MS of whole cell lysates.	72
2.3.2	MTT cytotoxicity assay.	72
2.3.3	Cell cycle distribution.	75
2.3.4	Mode of cell death.	77
2.3.5	Caspase inhibition.	79

2.3.6	PARP inhibition.	81
2.4	Discussion.	81
2.4.1	Uptake.	81
2.4.2	Cytotoxicity.	83
2.4.3	Cell Cycle Distribution.	85
2.4.4	Necrotic Mode of Cell Death.	86
2.4.5	General Implications.	88
2.5	Conclusions.	89
2.6	References.	91

Chapter 3: Cell-Selective Biological Activity of Rhodium

Metalloinsertors Correlates with Subcellular Localization.96

3.1	Introduction.	96
3.2	Experimental Protocols.	98
3.2.1	Materials.	98
3.2.2	Oligonucleotide Synthesis.	98
3.2.3	Synthesis and Characterization of Metal Complexes.	99
3.2.3.1	[Rh(chrysi)(phen)(NH ₃) ₂]Cl ₃	99
3.2.3.2	1,1-di(pyridin-2-yl)ethanol (DPE)	100
3.2.3.3	N-alkyl-N-(pyridin-2-yl)pyridin-2-amine (alkyl = methyl or propyl; MeDPA, PrDPA)	100
3.2.3.4	[Rh(NH ₃) ₄ (phzi)]Cl ₃	101
3.2.3.5	[Rh(chrysi)(phen)(L)]Cl ₃ (L= HDPA, MeDPA, PrDPA)	102

3.2.3.6	[Rh(chrysi)(phen)(DPE)]Cl ₂	103
3.2.4	Photocleavage Competition Titrations.	103
3.2.4.1	Binding Constant Determination.	104
3.2.5	Cell Culture.	107
3.2.5.1	Cellular Proliferation ELISA.	107
3.2.5.2	MTT Cytotoxicity Assay.	107
3.2.6	Nuclear Isolation Protocol.	108
3.2.7	Mitochondrial Isolation Protocol.	108
3.2.8	ICP-MS Assay for Whole-Cell Rhodium Levels.	109
3.2.9	ICP-MS Assay for Nuclear Rhodium Levels.	109
3.2.10	ICP-MS Assay for Mitochondrial Rhodium Levels.	110
3.3	Results.	111
3.3.1	Binding Affinities for Metal Complexes at Single Base Mismatches. . .	111
3.3.2	Quantitation of Inhibition of Cellular Proliferation using an Enzyme-Linked Immunosorbent Assay (ELISA)	111
3.3.3	MTT Cytotoxicity Assay.	117
3.3.4	ICP-MS Assay for Whole-Cell Rhodium Levels.	119
3.3.5	ICP-MS Assay for Nuclear Rhodium Levels.	122
3.3.6	ICP-MS Assay for Mitochondrial Rhodium Levels.	124
3.4	Discussion.	125
3.4.1	Variations in Complexes Synthesized.	125
3.4.2	Metalloinsertor Uptake and Nuclear Accumulation.	127
3.4.3	Mitochondrial Accumulation of Rhodium Metalloinsertors.	130

3.4.4	General Implications for Design.	132
3.5	Conclusion.	132
3.6	References.	135

Chapter 4: An Inducible, Isogenic Cancer Cell Further Validates Rhodium Metalloinsertors as Selective Chemotherapeutic Agents. . . . 138

4.1	Introduction.	138
4.2	Experimental Protocols.	140
4.2.1	Antibodies and Western Blots.	140
4.2.2	Cell Viability Assays.	141
4.2.3	Statistical Analysis.	141
4.2.4	Synthesis of Chemical Compounds.	142
4.3	Results.	142
4.3.1	Inhibition of MLH1 by shRNA Reduces MLH1 Protein Levels.	142
4.3.2	MLH1-Deficient NCI-H23 Subclones Exhibit Increased Resistance to Chemotherapeutic Drugs.	144
4.3.3	MLH1-deficient NCI-H23 Subclones Display Increased Sensitivity to Rhodium Metalloinsertor Compounds.	148
4.4	Discussion.	154
4.4.1	Generation of Isogenic Cell Lines.	154
4.4.2	Implications for Chemotherapy.	157
4.5	Conclusion.	159
4.6	References.	161

Chapter 5: An Unusual Ligand Coordination Gives Rise to a New Family of Rhodium Metalloinsertors with Improved Selectivity and Potency.....164

5.1	Introduction.....	164
5.2	Experimental Protocols.....	168
5.2.1	Materials.....	168
5.2.2	Oligonucleotide Synthesis.....	168
5.2.3	Synthesis and Characterization of Ligands and Metal Complexes.....	169
5.2.3.1	1-R-1-(pyrid-2-yl) ethanol (R = phenyl, methyl, hexyl; PPE, PPO, PyOctanol).....	169
5.2.3.2	[Rh(chrysi)(phen)(L)]Cl ₂ (L = PPE, PPO, PyOctanol) ..	170
5.2.3.3	Enantiomeric Separation.....	172
5.2.4	X-Ray Structure Determination.....	172
5.2.4.1	[Rh(HDPA) ₂ (chrysi)]Cl ₂	172
5.2.4.2	[Rh(chrysi)(phen)(DPE)]Cl ₂	173
5.2.4.3	[Rh(chrysi)(phen)(PPE)]Cl ₂	174
5.2.4.4	[Rh(chrysi)(phen)(PPO)]Cl ₂	176
5.2.5	Metalloinsertor pH Titrations.....	176
5.2.6	Photocleavage Competition Titrations.....	177
5.2.6.1	Binding Constant Determination.....	178
5.2.7	Covalent DNA binding assay.....	178
5.2.8	Circular Dichroism Study of Δ/Λ-[Rh(chrysi)(phen)(DPE)] ²⁺ Bound to Mismatched DNA.....	181

5.2.9	Cell Culture.	181
5.2.9.1	Cellular Proliferation ELISA.	182
5.2.9.2	MTT Cytotoxicity Assay.	182
5.2.9.3	Cell Death Mode Flow Cytometry Assay.	183
5.2.10	ICP-MS Assay for Whole-Cell Rhodium Levels.	183
5.3	Results.	184
5.3.1	Synthesis and Characterization of Compounds.	184
5.3.2	Binding Affinities for Metal Complexes at Single Base Mismatches. . .	191
5.3.3	Covalent DNA Binding.	193
5.3.4	Quantitation of Inhibition of Cellular Proliferation using an Enzyme-Linked Immunosorbent Assay (ELISA)	196
5.3.5	MTT Cytotoxicity Assay.	198
5.3.6	ICP-MS Assay for Whole-Cell Rhodium Levels.	200
5.3.7	Mode of cell death.	203
5.4	Discussion.	205
5.4.1	<i>In Vitro</i> Characterization.	205
5.4.2	<i>In Cellulo</i> Characterization.	209
5.5	Conclusion.	212
5.6	References.	213
	Chapter 6: Conclusion.	216
	Appendix: Crystallographic Data.	218
A.1	[Rh(HDPA) ₂ (chrysi)]Cl ₂	218

A.2	[Rh(chrysi)(phen)(DPE)]Cl ₂	230
A.3	[Rh(chrysi)(phen)(PPE)]Cl ₂	244
A.4	[Rh(chrysi)(phen)(PPO)]Cl ₂	257

List of Figures and Tables

Figure 1.1 Chemical structures of classical platinum-based chemotherapeutics.	2
Figure 1.2 Crystal structure at 2.6-Å resolution of the intrastrand crosslink between cisplatin and the N7 atoms of adjacent guanines.	5
Figure 1.3 The 1.2-Å resolution crystal structure of the sequence-specific rhodium intercalator, Δ - α -[Rh[(R,R)-Me ₂ trien]phi] ³⁺ , bound to a duplex octamer.	8
Figure 1.4 The 0.92-Å resolution structure of two Δ -[Ru(bpy) ₂ (dppz)] ²⁺ complexes intercalated from the minor groove into a duplex 12-mer containing two AA mismatched sites.	10
Figure 1.5 The 1.1-Å resolution structure of Δ -[Rh(bpy) ₂ (chrysi)] ³⁺ bound to an AC mismatch.	12
Figure 1.6 Chemical structures of four ruthenium polypyridyl complexes studied by Novakova and coworkers.	14
Figure 1.7 Four Ru(II) polypyridyl complexes studied by Tan and coworkers.	16
Figure 1.8 Chemical structures of various compounds studied by the Sheldrick laboratory.	18
Figure 1.9 Compounds studied by the Sadler laboratory.	20
Figure 1.10 Chemical structures (top) and biological activities (bottom) of the rhodium metalloinsertor [Rh(bpy) ₂ (chrysi)] ³⁺ (left), and the DNA alkylating agent MNNG (right) studied in the Barton laboratory.	22
Figure 1.11 Chemical structures of Rh(III) polypyridyl complexes synthesized and studied to monitor uptake.	25
Figure 1.12 Chemical structures of three isomeric terphenyl Ru(II) piano-stool complexes studied by Bugarcic and coworkers.	27

Figure 1.13 Chemical structures (top) of a series of luminescent rhenium(I) polypyridyl complexes by Louie and coworkers.	29
Figure 1.14 Schematic diagram of the different possible routes of entry into the cell taken by small complexes.	31
Figure 1.15 $[\text{Ru}(\text{DIP})_2(\text{dppz})]^{2+}$, a luminescent polypyridyl ruthenium complex that enters HeLa cells via passive diffusion.	35
Figure 1.16 $[\text{Ru}_2(\text{phen})_4((\text{bpy}')_2(\text{CH}_2)_{16}))]^{4+}$, a compound shown to enter L1210 murine leukemia cells via an energy-dependent mechanism as well as passive diffusion.	37
Figure 1.17 The peptide conjugate studied by Kirin and coworkers.	42
Figure 1.18 The rhodium metalloinsertor-peptide conjugate synthesized in order to accelerate uptake.	44
Figure 1.19 Chemical structures (top) and confocal microscopy images (bottom) of the two metal-peptide fluorophore conjugates examined in our laboratory.	45
Figure 1.20 Chemical structures of targeted chemotherapeutics.	47
Figure 1.21 Design of Octasporine complexes as inhibitors of protein kinases.	49
Figure 2.1 Chemical structures of rhodium metalloinsertors $[\text{Rh}(\text{HDPA})_2\text{chrysi}]^{3+}$ and $[\text{Rh}(\text{MeDPA})_2\text{chrysi}]^{3+}$	63
Figure 2.2 ICP-MS assay for rhodium accumulation.	73
Figure 2.3 Selective toxicity of $[\text{Rh}(\text{HDPA})_2\text{chrysi}]^{3+}$ and $[\text{Rh}(\text{MeDPA})_2\text{chrysi}]^{3+}$ in MMR-deficient cells.	74
Figure 2.4 Cell cycle distribution assay.	76
Figure 2.5 Flow cytometry assay of cell death.	78
Figure 2.6 Caspase inhibition assay.	80

Figure 2.7 PARP inhibition assay.	82
Figure 2.8 Model for the cellular response to rhodium metalloinsertors.	90
Figure 3.1 Binding affinities determined through DNA photocleavage.	105
Figure 3.2 Representative sigmoidal curve for binding affinity determination.	106
Figure 3.3 Chemical structures, binding affinities for CC mismatches, and approximated nuclear concentration of all compounds studied.	112
Figure 3.4 Inhibitory effects of (from top to bottom) $[\text{Rh}(\text{NH}_3)_4(\text{phzi})]^{3+}$, $[\text{Rh}(\text{chrysi})(\text{phen})(\text{DPE})]^{2+}$, $[\text{Rh}(\text{DPAE})_2(\text{chrysi})]^{3+}$, $[\text{Rh}(\text{HDPA})_2(\text{chrysi})]^{3+}$, and $[\text{Rh}(\text{chrysi})(\text{phen})(\text{HDPA})]^{3+}$ as a function of incubation time on cellular proliferation.	114
Figure 3.5 Inhibitory effects of (from top to bottom) $[\text{Rh}(\text{bpy})_2(\text{chrysi})]^{3+}$, $[\text{Rh}(\text{chrysi})(\text{phen})(\text{MeDPA})]^{3+}$, $[\text{Rh}(\text{chrysi})(\text{phen})(\text{PrDPA})]^{3+}$, $[\text{Rh}(\text{PrDPA})_2(\text{chrysi})]^{3+}$, and $[\text{Rh}(\text{PrDPA})_2(\text{chrysi})]^{3+}$ as a function of incubation time on cellular proliferation.	115
Figure 3.6 Inhibitory effects of rhodium metalloinsertors as a function of metalloinsertor identity.	116
Figure 3.7 Differential cytotoxicities of rhodium metalloinsertors.	118
Figure 3.8 ICP-MS assay for whole-cell rhodium accumulation.	120
Figure 3.9 ICP-MS assay for nuclear and mitochondrial rhodium accumulation.	123
Figure 3.10 Model for the requirements for MMR-deficient cell-selectivity by rhodium metalloinsertors.	133
Figure 4.1 MLH1 shRNA expression is inducible.	143

Figure 4.2 NCI-H23 subclones that were uninduced or induced for MLH1 shRNA were treated with etoposide.	145
Figure 4.3 NCI-H23 subclones that were uninduced or induced for MLH1 shRNA were treated with temozolomide.	146
Figure 4.4 MLH1-deficient NCI-H23 subclones display increased resistance to DNA-damaging drugs.	147
Figure 4.5 Independent MLH1 shRNA constructs confer differential sensitivity to compounds.	149
Figure 4.6 MLH1-deficient NCI-H23 cells display increased cell sensitivity to rhodium metalloinsertor compounds.	151
Figure 4.7 MLH1-deficient NCI-H23 cells display increased cell sensitivity only to rhodium metalloinsertors that exhibit DNA mismatch binding.	152
Figure 4.8 Independent MLH1 shRNA constructs confer differential sensitivity to rhodium metalloinsertors.	153
Figure 4.9 Treatment of NCI-H23 subclones with rhodium metalloinsertor compounds does not alter MSI status.	155
Figure 5.1 Chemical structures and binding affinities for CC mismatches of all compounds studied.	165
Figure 5.2 X-ray crystal structure of [Rh(chrysi)(phen)(DPE)]Cl ₂	166
Figure 5.3 X-ray crystal structure of [Rh(HDPA) ₂ (chrysi)]Cl ₂	167
Figure 5.4 Binding affinities determined through DNA photocleavage.	179
Figure 5.5 Representative sigmoidal curve for binding affinity determination.	180
Figure 5.6 X-ray crystal structure of [Rh(chrysi)(phen)(PPE)]Cl ₂	185

Figure 5.7 X-ray crystal structure of $[\text{Rh}(\text{chrysi})(\text{phen})(\text{PPO})]\text{Cl}_2$.	186
Figure 5.8 pH titration of $[\text{Rh}(\text{HDPA})_2(\text{chrysi})]^{3+}$.	187
Figure 5.9 pH titration of $[\text{Rh}(\text{chrysi})(\text{phen})(\text{DPE})]^{2+}$.	189
Figure 5.10 Absorption spectra of $[\text{Rh}(\text{chrysi})(\text{phen})(\text{DPE})]^{2+}$ and $[\text{Rh}(\text{HDPA})_2(\text{chrysi})]^{3+}$ bound to mismatched DNA.	190
Figure 5.11 Circular dichroism (CD) spectra of Δ - and Λ - $[\text{Rh}(\text{chrysi})(\text{phen})(\text{DPE})]^{2+}$ in water.	192
Figure 5.12 Circular dichroism (CD) spectra of Δ - and Λ - $[\text{Rh}(\text{chrysi})(\text{phen})(\text{DPE})]^{2+}$ bound to mismatched DNA.	194
Figure 5.13 Assessment of the ability of $[\text{Rh}(\text{chrysi})(\text{phen})(\text{PPE})]^{2+}$ to bind covalently to mismatched DNA.	195
Figure 5.14 Inhibitory effects of <i>rac</i> - $[\text{Rh}(\text{chrysi})(\text{phen})(\text{DPE})]^{2+}$, <i>rac</i> - $[\text{Rh}(\text{chrysi})(\text{phen})(\text{PPE})]^{2+}$, <i>rac</i> - $[\text{Rh}(\text{chrysi})(\text{phen})(\text{PPO})]^{2+}$, $[\text{Rh}(\text{HDPA})_2(\text{chrysi})]^{3+}$, MNNG, and cisplatin.	197
Figure 5.15 Differential cytotoxicities of <i>rac</i> - $[\text{Rh}(\text{chrysi})(\text{phen})(\text{DPE})]^{2+}$, <i>rac</i> - $[\text{Rh}(\text{chrysi})(\text{phen})(\text{PPE})]^{2+}$, <i>rac</i> - $[\text{Rh}(\text{chrysi})(\text{phen})(\text{PPO})]^{2+}$, and <i>rac</i> - $[\text{Rh}(\text{chrysi})(\text{phen})(\text{PyOctanol})]^{2+}$.	199
Figure 5.16 Differential cytotoxicities of Δ - and Λ - $[\text{Rh}(\text{chrysi})(\text{phen})(\text{DPE})]^{2+}$.	201
Figure 5.17 ICP-MS assay for whole-cell rhodium accumulation.	202
Figure 5.18 Flow cytometry assay of cell death.	204
Figure 5.19 Modeling of new family of compounds bound to mismatched DNA.	208
Table 3.1 Qualitative nuclear and mitochondrial uptake properties, as well as the presence or absence of cell-selective biological activity for all ten metalloinsertors.	128

Table A.1 Crystal data and structure refinement for [Rh(HDPA) ₂ (chrysi)]Cl ₂	218
Table A.2 Atomic coordinates (x 10 ⁴) and equivalent isotropic displacement parameters (Å ² x 10 ³) for [Rh(HDPA) ₂ (chrysi)]Cl ₂	220
Table A.3 Selected bond lengths [Å] and angles [°] for [Rh(HDPA) ₂ (chrysi)]Cl ₂	222
Table A.4 Anisotropic displacement parameters (Å ² x 10 ³) for [Rh(HDPA) ₂ (chrysi)]Cl ₂	223
Table A.5 Hydrogen coordinates (x 10 ⁴) and isotropic displacement parameters (Å ² x 10 ³) for [Rh(HDPA) ₂ (chrysi)]Cl ₂	226
Table A.6 Hydrogen bonds for [Rh(HDPA) ₂ (chrysi)]Cl ₂ [Å and °].	228
Table A.7 Crystal data and structure refinement for [Rh(chrysi)(phen)(DPE)]Cl ₂	230
Table A.8 Atomic coordinates (x 10 ⁴) and equivalent isotropic displacement parameters (Å ² x 10 ³) for [Rh(chrysi)(phen)(DPE)]Cl ₂	232
Table A.9 Selected bond lengths [Å] and angles [°] for [Rh(chrysi)(phen)(DPE)]Cl ₂	235
Table A.10 Anisotropic displacement parameters (Å ² x 10 ³) for [Rh(chrysi)(phen)(DPE)]Cl ₂	236
Table A.11 Hydrogen coordinates (x 10 ⁴) and isotropic displacement parameters (Å ² x 10 ³) for [Rh(chrysi)(phen)(DPE)]Cl ₂	239
Table A.12 Hydrogen bonds for [Rh(chrysi)(phen)(DPE)]Cl ₂ [Å and °].	243
Table A.13 Crystal data and structure refinement for [Rh(chrysi)(phen)(PPE)]Cl ₂	244
Table A.14 Atomic coordinates (x 10 ⁴) and equivalent isotropic displacement parameters (Å ² x 10 ³) for [Rh(chrysi)(phen)(PPE)]Cl ₂	246
Table A.15 Selected bond lengths [Å] and angles [°] for [Rh(chrysi)(phen)(PPE)]Cl ₂	249

Table A.16 Anisotropic displacement parameters ($\text{\AA}^2 \times 10^3$) for [Rh(chrysi)(phen)(PPE)]Cl ₂	250
Table A.17 Hydrogen coordinates ($\times 10^4$) and isotropic displacement parameters ($\text{\AA}^2 \times 10^3$) for [Rh(chrysi)(phen)(PPE)]Cl ₂	253
Table A.18 Hydrogen bonds for [Rh(chrysi)(phen)(PPE)]Cl ₂ [\AA and $^\circ$].	256
Table A.19 Crystal data and structure refinement for [Rh(chrysi)(phen)(PPO)]Cl ₂	257
Table A.20 Atomic coordinates ($\times 10^4$) and equivalent isotropic displacement parameters ($\text{\AA}^2 \times 10^3$) for [Rh(chrysi)(phen)(PPO)]Cl ₂	259
Table A.21 Selected bond lengths [\AA] and angles [$^\circ$] for [Rh(chrysi)(phen)(PPO)]Cl ₂	261
Table A.22 Anisotropic displacement parameters ($\text{\AA}^2 \times 10^3$) for [Rh(chrysi)(phen)(PPO)]Cl ₂	262
Table A.23 Hydrogen coordinates ($\times 10^4$) and isotropic displacement parameters ($\text{\AA}^2 \times 10^3$) for [Rh(chrysi)(phen)(PPO)]Cl ₂	265
Table A.24 Hydrogen bonds for [Rh(chrysi)(phen)(PPO)]Cl ₂ [\AA and $^\circ$].	267

Chapter 1: Introduction^{*,†}

1.1 Metal-Based Chemotherapeutics

Since the successful application of cisplatin as an anticancer drug, the field of inorganic medicinal chemistry has undergone a revolution.¹⁻⁴ For many years, the field focused on the development of more potent analogues (second and third generation derivatives), leading to the FDA approval of two additional *cis*-platinum(II) complexes, carboplatin and oxaliplatin (**Figure 1.1**).⁵ Cisplatin and carboplatin, in particular, have been highly successful in the treatment of a variety of cancers, including testicular, ovarian, cervical, and non-small cell lung cancers.⁶ However, these treatments are often associated with severe side effects and a build-up of resistance. In addition, two ruthenium complexes are currently in clinical trials,^{7,8} and studies on the biological effects of potential metal-based therapeutics are being published at an increasing rate. Anticancer compounds have a myriad of targets (DNA, proteins, membranes, etc.), and in fact the true lesion responsible for the biological activity of a compound is difficult to determine.⁹ These issues have led researchers to focus more recently on the development of novel non-platinum chemotherapeutics.

The rich photophysical and photochemical properties of metal complexes, in addition to their basic coordination chemistry, make them ideal scaffolds for a wide variety of biological applications. Though the pharmaceutical industry in general has shied away from “heavy metal” pharmaceuticals, with the exception of cisplatin and its derivatives, there are in fact real opportunities in the development of transition metal

* Komor, A.C.; Barton, J. K. The Path for Metal Complexes to a DNA Target. *Chem. Commun.* **2013**, 49, 3617-3630 – Adapted by permission of The Royal Society of Chemistry.

† Adapted from Weidmann, A. G.; Komor, A. C.; Barton, J. K. Targeted Chemotherapy with Metal Complexes. *Comments in Inorg. Chem.* **2014**, DOI: 10.1080/02603594.2014.890099.

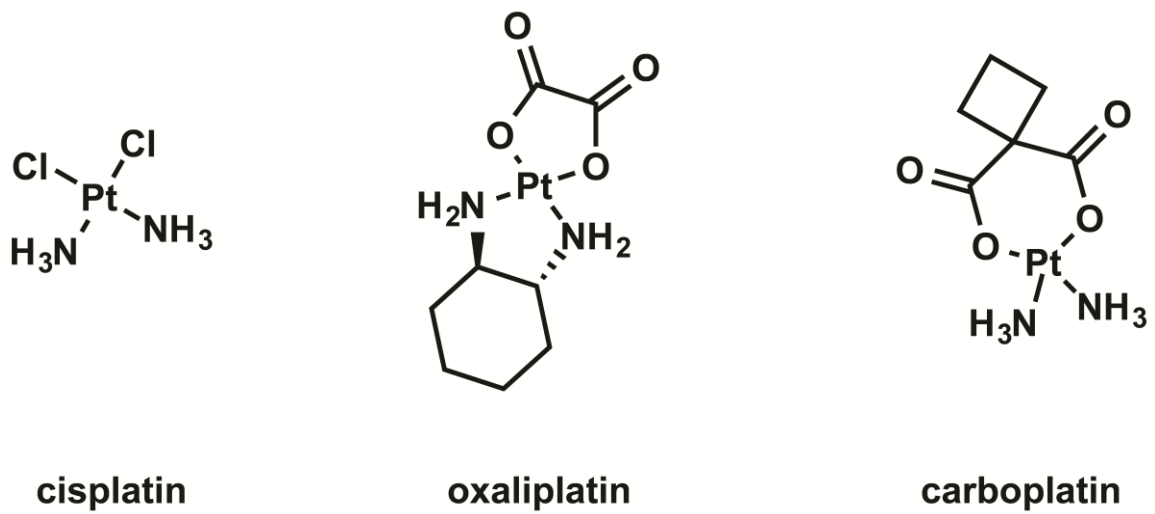


Figure 1.1 Chemical structures of classical platinum-based chemotherapeutics.

pharmaceuticals, given their high modularity, ease of synthesis in preparing molecules of complex shapes and symmetries, and the ability to monitor their fate within the cell using a variety of spectroscopies.

The focus of many laboratories has been on the preparation of more potent metal complexes that function like cisplatin in coordinating to DNA, but are more effective due to either more optimum uptake characteristics or the inability of lesions formed to be easily detected and repaired. Much time and attention have been spent in this arena. However, the goal has moved also to the design of complexes with a new strategy based upon selectivity, with the preparation of transition metal complexes that are more selective than cisplatin, owing to a design strategy where the complex interacts with a specific biological target found prominently in cancer cells.

Here I describe recent results on a variety of transition metal complexes targeted to DNA to illustrate many of the issues involved in new therapeutic design. This is followed by a short discussion on metal complexes as targeted chemotherapeutics; complexes that are tailored towards various biomolecules associated with cancer. I discuss studies of “classical” metal complex chemotherapeutics to explore their differences in structural interactions with DNA, their biological fates inside the cell, and the tools and techniques being used to probe the path taken by the small molecule in reaching its DNA target. Establishing cellular uptake and even the subcellular distributions of the metal complexes are critically important in understanding and optimizing their activity. While the subtle hydrolysis reactions associated with cisplatin uptake probably could not have been strategically designed, they are key to its mode of action.

1.2 DNA as a Target

DNA represents a fruitful target for metal complexes. DNA can function as a ligand either through interactions with the sugar-phosphate backbone or coordination to the bases. Moreover, non-covalent interactions with DNA lead to additional targets, and greater specificity, through an ensemble of interactions in the DNA grooves and base stack.

1.2.1 Covalent Interactions

It has been widely accepted since the 1970s that DNA is the biological target of cisplatin *in vivo*.^{10,11} However, the nature of the adduct formed between cisplatin and DNA was not determined until the 1980s. This interaction was proposed to be an intrastrand cross-link between the N7 atoms of adjacent guanines and cisplatin based on the results of numerous biochemical studies.^{12,13} This adduct was further characterized by gel electrophoresis, and it was found that the DNA duplex was bent by $\sim 40^\circ$.¹⁴ However, this adduct was not fully structurally characterized by x-ray crystallography until 1995, when the Lippard group published the 2.6-Å resolution crystal structure of cisplatin bound to a double-stranded DNA dodecamer (**Figure 1.2**).¹⁵

In this structure, the duplex is bent considerably toward the major groove but without disruption of the Watson-Crick hydrogen bonding. In fact, the duplex is distorted to such a degree that the duplex changes conformation from B-DNA to A-DNA throughout most of the duplex. Such a significant distortion of the DNA is likely readily recognized by a host of cellular proteins. How efficiently such lesions are recognized and repaired rather than initiating a protein response and signaling cascade is a question we still need to understand and which may make the difference between biological efficacy

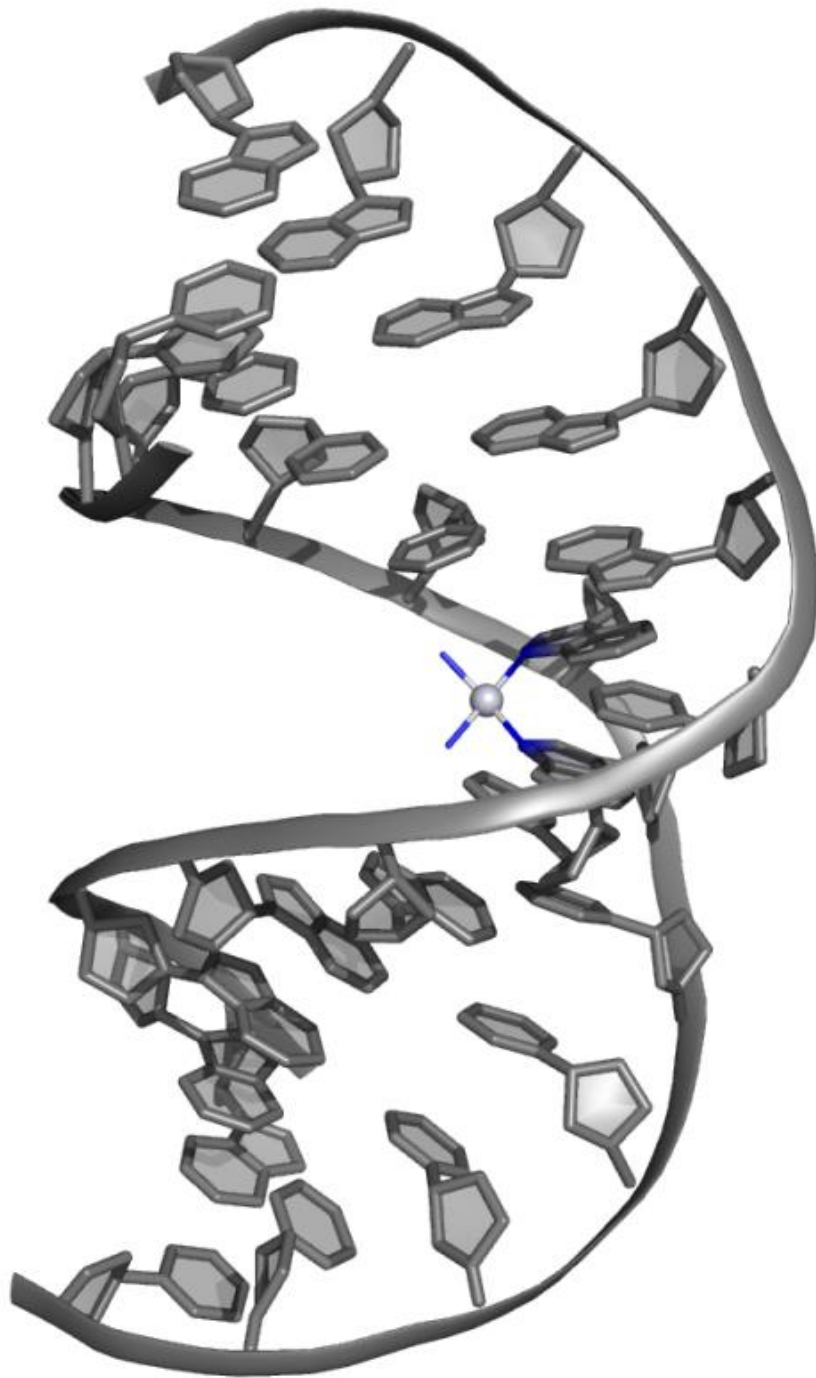


Figure 1.2 Crystal structure at 2.6-Å resolution of the intrastrand crosslink between cisplatin and the N7 atoms of adjacent guanines.¹⁵ The platinum center is shown as a light grey sphere, and its four nitrogen-based ligands are shown in blue. DNA is shown in grey. The dodecamer duplex is bent considerably towards the major groove, and the structure is no longer B-form DNA, but mostly A-form throughout the duplex.

and little reaction.¹⁶

1.2.2 Intercalation

Metallointercalation is a DNA binding mode that has been extensively studied. The term was coined by Lippard and coworkers in studies of square planar Pt complexes with DNA.¹⁷ As with organic intercalators, these planar complexes contain aromatic heterocyclic ligands that could stack among the DNA base pairs. However, the lack of site-specificity inherent in intercalation by a planar complex made detailed structural characterization difficult. The first structural characterization of metallointercalation was the 1.1-Å resolution crystal structure of the platinum complex $[\text{Pt}(\text{SEtOH})(\text{terpy})]^+$ intercalated into the dinucleotide dimer deoxy CpG.¹⁸ Although not able to establish long-range structural perturbations to DNA associated with intercalation, this structure did reveal that, associated with intercalation, the DNA unwinds to accommodate the metal complex between bases and the pucker of the sugar rings changes geometry. This alternate sugar puckering was suggested as the basis for the “neighbour exclusion principle” associated with DNA intercalation, where, at most, intercalators bind in every other interbase-pair site.

In succeeding years, the Barton laboratory focused on intercalation by octahedral complexes containing at least one aromatic heterocyclic ligand for stacking, or partial intercalation, in between base pairs. The symmetry and functionality associated with the non-intercalated ligands could then provide the basis for highly specific interactions with several bases along the groove of DNA, once oriented by stacking in the helix of the intercalated ligand. In particular, we found the enantioselective intercalative binding of right-handed Δ -complexes into right-handed B-DNA.¹⁹ One of the first structural

characterizations of metallointercalation into a long DNA duplex was thus provided from the 1.2-Å resolution crystal structure of the sequence-specific rhodium intercalator, Δ - α -[Rh[(R,R)-Me₂trien]phi]³⁺, bound to a duplex octamer (**Figure 1.3**).²⁰ The complex was designed to target the sequence 5'-TGCA-3' through a mix of hydrogen bonding and methyl-methyl interactions in the DNA major groove. The complex was also shown as a result of its sequence-specificity to inhibit the binding of sequence-specific DNA-binding proteins, a first step in specifically inhibiting gene expression.²¹

Critically, the structure obtained provided detailed information on how metallointercalation in general modifies the conformation of DNA. In this structure, intercalation occurs from the major groove, with the aromatic intercalating phi ligand π -stacking with the π -orbitals of the flanking base pairs, similar to the stacking of consecutive base pairs in duplex DNA. This structure also confirmed the conformational changes revealed by shorter intercalated oligonucleotides, such as doubling of the rise, buckling of the base pairs flanking the intercalation site, and a slight unwinding of the DNA localized at the site of intercalation. Interestingly, there were no long range effects on the DNA structure- no bending or kinking of the helix. Indeed, even the alternating sugar-pucker was not evident. The metallointercalator was simply like another base pair in the helical stack.

Structural characterization of intercalation from the minor groove was recently obtained from two independent crystal structures of dppz complexes of Ru(II) intercalated into duplex DNA. The first is the 0.92-Å resolution structure of two Δ -[Ru(bpy)₂(dppz)]²⁺ complexes intercalated from the minor groove into a duplex 12-mer containing two mismatched sites.²² There are also two ruthenium complexes bound to the

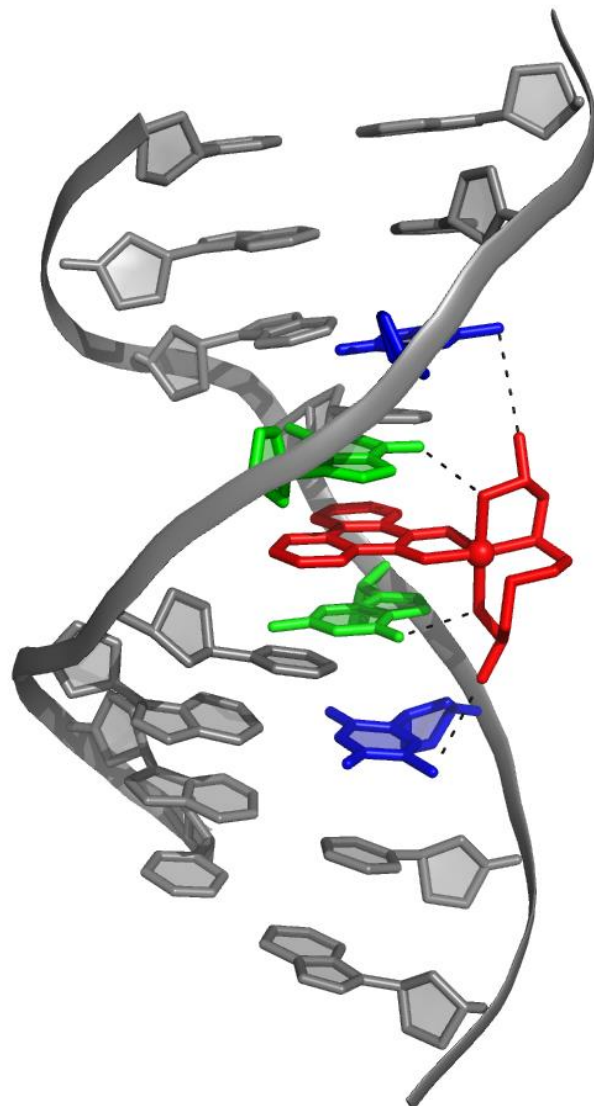


Figure 1.3 The 1.2-Å resolution crystal structure of the sequence-specific rhodium intercalator, $\Delta\text{-}\alpha\text{-}[\text{Rh}[(\text{R,R})\text{-Me}_2\text{trien}]\text{phi}]^{3+}$, bound to a duplex octamer.²⁰ The complex binds specifically to 5'-TGCA-3'. There are two Van der Waals Me-Me interactions between the metal complex ligand and T (T shown in blue, interaction shown with the black dotted line), and a hydrogen bond between the NH group on the metal complex ligand and the O6 of G (G shown in green, interaction shown with the black dotted line). This structure displays the doubling of the rise of the DNA, buckling of the adjacent base pairs, and a slight unwinding of the DNA upon intercalation.

mismatched sites via insertion (*vide infra*), as well as the extruded adenosines π -stack with the bpy ligands of the intercalated complexes, serving to stabilize the intercalated complex in the minor groove (**Figure 1.4**). Intercalation of this complex from the minor groove was in contrast to NMR^{23,24} and competitive fluorescence studies²⁵, both of which suggested that intercalation of the ruthenium complex occurred from the major groove. Crystal packing forces may play a role here in directing intercalation from the minor groove side; in any case, it is clear that the energetic differences between intercalation from the major groove versus minor groove must be small. Furthermore, this structure showed the doubling of the rise of the DNA at each intercalation site, and an unwinding of the base pairs to accommodate the complexes. Interestingly, while the rise is doubled at each intercalation site, the rise between the base pairs with no metal complex bound is reduced from the 3.3Å that is expected, consistent with π -stacking interactions between the extruded mismatches and the ancillary bpy ligands being the dominating interaction that may be directing intercalation from the minor groove.

The second set of structures show the binding of Λ -[Ru(phen)₂(dppz)]²⁺ to two different duplex 10-mers.²⁶ These structures reveal three different conformations of intercalation for the same complex. Namely, when intercalated at the TA/TA central step of the oligonucleotide d(CCGGTACCGG)₂, the complex is intercalated deeply, perpendicularly, and symmetrically into the base stack from the minor groove. However, when the complex intercalates at the terminal GG/CC step, the intercalation geometry is shallower and angled. Finally, this angled intercalation allows for the phenanthroline ligands to semi-intercalate into the neighboring duplex. This “semi-intercalation” was also seen in a structure of Λ -[Ru(TAP)₂(dppz)]²⁺ bound to a duplex 10-mer.²⁷

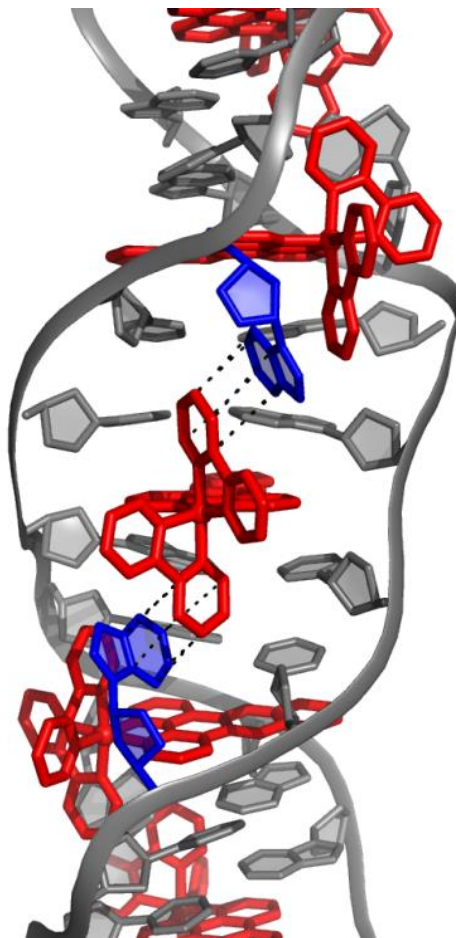


Figure 1.4 The 0.92-Å resolution structure of two Δ -[Ru(bpy)₂(dppz)]²⁺ complexes intercalated from the minor groove into a duplex 12-mer containing two AA mismatched sites.²² The mismatches are extruded from the base stack by two other Δ -[Ru(bpy)₂(dppz)]²⁺ complexes that are metalloinserted at these sites. The extruded bases (shown in blue) π -stack with the bpy rings of the intercalated metal complexes (interactions shown in black, metal complexes shown in red).

These various structural characterizations of metallointercalation highlight the versatility of this binding mode, and likely also the shallow energy profile among different intercalative binding modes. Likely the structural diversity reflects the sequence selectivity associated with the different complexes, where the non-intercalating interactions in the DNA groove lead to some structural variations. But none of these conformational changes yield dramatic changes in DNA structure, like the bend in DNA generated by a Pt crosslink. In the context of therapeutic design, the fact that metallointercalators cause no major structural distortions in DNA needs to be considered. Intercalators generally, especially those that have no sequence-specificity, have little therapeutic applicability. It may be because a strongly defined DNA lesion is not produced with intercalation that limits the biological consequences for metallointercalators.

1.2.3 Insertion

Rhodium metalloinsertors, as described in the Barton laboratory, bind to mismatches in DNA with high affinity and specificity.^{28,29} While it was known that these compounds could preferentially target thermodynamically destabilized mismatches in DNA over matched base pairs by a factor of over 1000,³⁰ for ten years there was no structural information on the interaction between these metal complexes and mismatched DNA. The 1.1-Å resolution crystal structure of $[\text{Rh}(\text{bpy})_2(\text{chrysi})]^{3+}$ bound to an AC mismatch revealed the binding mode to be metalloinsertion, where the chrysi ligand inserts into the base stack via the minor groove and ejects both mismatched bases (**Figure 1.5**).³¹

Metalloinsertion of this complex results in only small conformational changes in

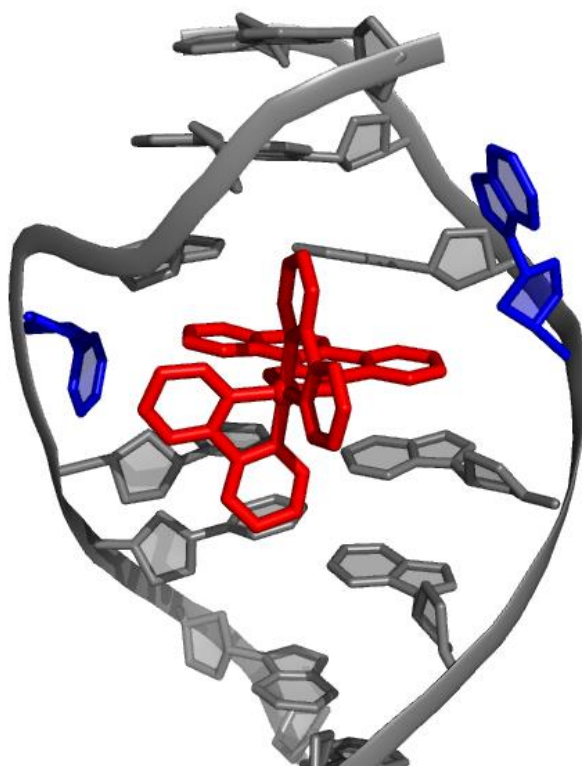


Figure 1.5 The 1.1-Å resolution structure of Δ -[Rh(bpy)₂(chrysi)]³⁺ bound to an AC mismatch.³¹ The rhodium complex, shown in red, inserts into the DNA from the minor groove and completely ejects the mismatched bases, shown in blue.

the duplex near the binding site, but a large perturbation is associated with the ejection of the mismatched bases into the DNA groove. The structure also explains the enantiospecificity of binding of $[\text{Rh}(\text{bpy})_2(\text{chrysi})]^{3+}$; the deep insertion of the complex within the minor groove with no increase in base pair rise results in a steric clash between the ancillary ligands and the sugar phosphate backbone if the left-handed isomer were to be bound. For intercalation, in contrast, where there is an increase in rise at the binding site, enantioselective intercalation requires a much bulkier ancillary ligand than bpy.³² As with the case of cisplatin, this structure may also suggest the basis for the biological activity of these complexes. Ejection of the mismatched bases results in a large lesion that could be easily recognized *in vivo*. This lesion likely is responsible for the selective cell death of MMR-deficient cells over MMR-proficient cells following rhodium treatment, as there are 1000 times as many mismatches in the MMR-deficient cells.

This binding conformation has been corroborated by additional crystal structures of this same compound bound to different mismatches.³³ Furthermore, the generality of metalloinsertion as a binding mode for different bulky metal complexes has been established by the crystal structure mentioned earlier, that of $\Delta\text{-}[\text{Ru}(\text{bpy})_2(\text{dppz})]^{2+}$ bound by insertion at two mismatched sites.²² Again, the information garnered from these structures is instrumental in unraveling the mechanism of action of these therapeutic agents, and thus in the development of future agents with improved biological activity.

1.3 Biological Activities of Metal Complexes

Undeniably, optimizing a compound as a therapeutic requires the complete assessment of its biological activity *in vitro*. Here I discuss the biological activity *in cellulo* of several classes of transition metal complexes that are thought to target DNA.

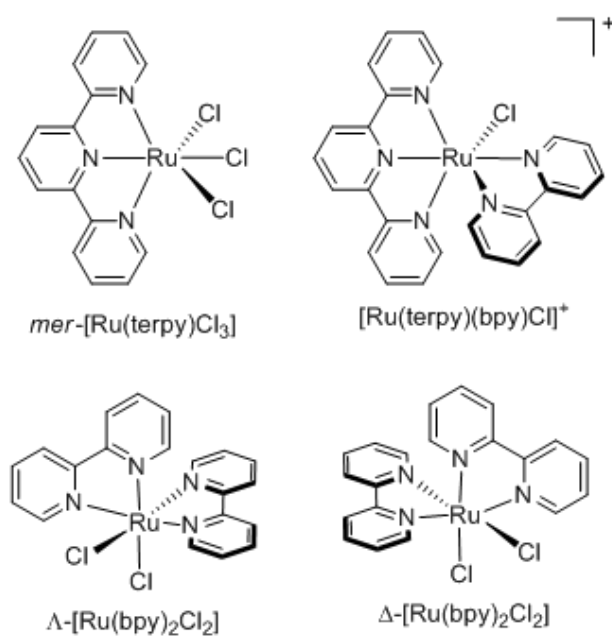


Figure 1.6 Chemical structures of four ruthenium polypyridyl complexes studied by Novakova and coworkers.³⁸ Out of all four complexes, only the $mer\text{-}[Ru(terpy)Cl_3]$ complex displays significant cytotoxicity in human and murine tumor cell lines.

As the activities of cisplatin and other platinum compounds have been extensively discussed elsewhere,^{16,34,35} non-platinum-based therapeutics are the focus here.

1.3.1 Polypyridyl Complexes

The biological activities of countless ruthenium polypyridyl complexes have been reported in the literature and have been the subject of many reviews.³⁶ Indeed, the exploration of biological activities of polypyridyl complexes began more than fifty years ago in classic studies by Dwyer and coworkers.³⁷ At that stage, no biological target was identified, but more recent studies on coordinatively saturated metal complexes suggest that DNA was likely the target for the full family of complexes examined earlier.

Many more studies have been conducted on ruthenium complexes that bind DNA covalently, by analogy to cisplatin, than those which are coordinatively saturated and inert to substitution, binding non-covalently. In one of the earliest studies, Novakova and coworkers studied four chloropolypyridyl ruthenium complexes (**Figure 1.6**) in murine and human tumor cell lines. Interestingly, only the complex with three leaving chloride ligands, *mer*-[Ru(terpy)Cl₃], displayed significant cytotoxicity. While the binding affinities of the different complexes could not explain this discrepancy, it was discovered that only the *mer*-[Ru(terpy)Cl₃] complex had the ability to form interstrand crosslinks in the DNA, thus harkening on the importance of specific lesions and structural distortion in determining biological activities, not simply avidity for binding DNA.³⁸

In a more recent study conducted by Tan and coworkers, several inert ruthenium polypyridyl complexes were studied, three ruthenium complexes containing a β -carboline ligand, along with the control compound [Ru(phen)₂(dppz)]²⁺ (**Figure 1.7**). They observed that upon substitution of the dppz ligand for the β -carboline ligand, the

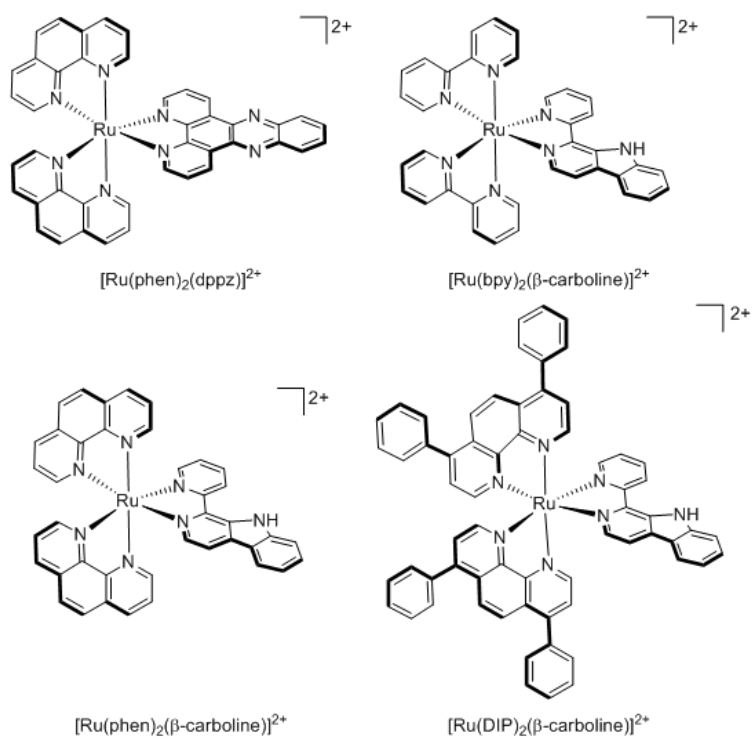


Figure 1.7 Four Ru(II) polypyridyl complexes studied by Tan and coworkers.³⁹ All three complexes with β -carboline as a ligand were cytotoxic towards HeLa cells, whereas the control $[\text{Ru}(\text{phen})_2(\text{dppz})]^{2+}$ complex was not.

complex now accumulates in the nucleus as well as the cytoplasm. Furthermore, the complexes with β -carboline ligands are significantly more cytotoxic towards HeLa cells, inducing apoptosis and autophagy, while $[\text{Ru}(\text{phen})_2(\text{dppz})]^{2+}$ does not. Since the cytotoxicities of the β -carboline complexes correlated well with their DNA binding affinities, they concluded that genomic DNA may be their primary target *in cellulo*.³⁹ The comparative results with these complexes, however, also suggest that the differential activities of the complexes may depend on more than just affinities. Both cellular uptake and localization may be issues. Moreover, the bulkiness and geometry of the coordinated carboline ligand may indicate that metalloinsertion plays some role in the binding interaction.

The Sheldrick laboratory has focused on studies of a variety of rhodium polypyridyl complexes that can bind both covalently and non-covalently with DNA.^{40,41} A series of polypyridyl rhodium complexes containing a facial tripodal (tpm), Cp*, or thioether ([9]aneS₃) ligand (**Figure 1.8**) were synthesized and their cytotoxicities towards the MCF-7 and HT-29 cell lines examined. They observed, in general, while keeping the facial ligand constant, an increase in potency with increasing surface area and hydrophobicity of the polypyridyl ligand. Furthermore, it was found that for the polypyridyl ligands phen, dpq, and dppz, the facial ligands had the effect of increasing the cytotoxicity in the order [Cp*] < [9]aneS₃ < tpm. This trend was found to be consistent not with binding affinity, but with the magnitude of rhodium uptake into the cells.⁴²⁻⁴⁴ Some of these complexes were furthermore found to selectively target lymphoma (BJAB) cells over healthy leukocytes.⁴⁵

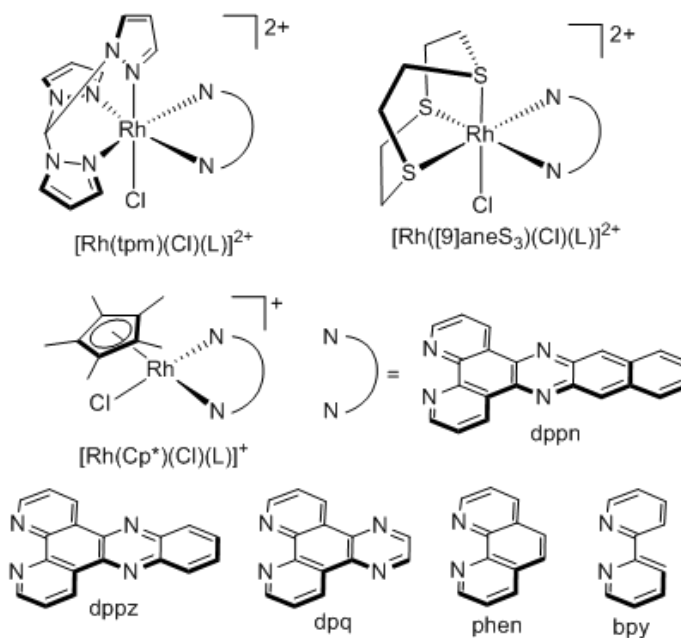


Figure 1.8 Chemical structures of various compounds studied by the Sheldrick laboratory.⁴²⁻⁴⁵ An extensive structure-activity study was undertaken on all complexes in the MCF-7 and HT-29 cell lines. Upon increasing the surface area of the “L” ligand, the cellular uptake of the drug increased, resulting in an increased potency of the drug.

1.3.2 Ruthenium Arene Complexes

There have been many studies exploring the cytotoxicities of “piano stool” complexes.⁴⁶ Compounds of the type $[(\eta^6\text{-arene})\text{Ru}(\text{L})(\text{X})]^+$ (where L is a bidentate ligand and X is a halide, **Figure 1.9**) have been shown to exhibit anticancer activity,⁴⁷ while their analogs with three monodentate ligands are completely inactive towards A2780 human ovarian cancer cells.⁴⁸ In particular, the results from a few studies by the Sadler laboratory revealed that while the identity of the halide and chelating ligand had minor effects on the biological activities of these complexes towards A2780 cells, the size of the arene ligand had a major effect. The potency of the drug followed the trend benzene < *p*-cymene < biphenyl < dihydroanthracene < tetrahydroanthracene, which suggests that increased cellular accumulation enhances their activity.^{48,49} It was also noted that the arene complexes of the form type $[(\eta^6\text{-arene})\text{Ru}(\text{en})(\text{Cl})]^+$ (en=ethylenediamine) did not display cross-resistance with cisplatin, suggesting an entirely different mechanism of action of these types of compounds.

Further studies confirmed that these complexes bind to DNA and induce structural distortions to the DNA that are distinct from those induced by cisplatin.⁵⁰ Specifically, they have been found to bind selectively to G bases in DNA oligonucleotides, regardless of the presence of other biologically relevant binding sites,⁵¹ along with partial intercalation of the arene ligand into the base stack.⁵²

1.3.3 Rhodium Metalloinsertors

The biological activities of rhodium metalloinsertors, showing a preferential activity in mismatch repair (MMR) –deficient cells, reflect well on the initial strategy used for their design, namely targeting DNA mismatches and therefore cells that have a

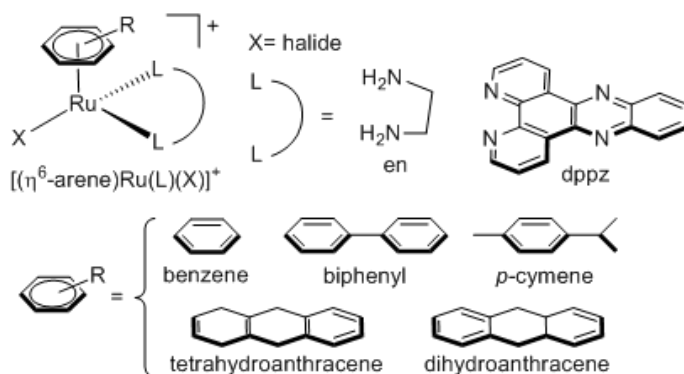


Figure 1.9 Compounds studied by the Sadler laboratory.⁴⁸⁻⁵² It was discovered that as the lipophilicity of the arene ligand increased, the potency of the drug towards A2780 cells increased. It was also found that complexes with L=en have a mechanism of action distinct from cisplatin.

higher frequency of DNA mismatches, the MMR-deficient cells. First studies were designed and carried out to establish *in vitro* that the complexes bind to DNA mismatches with high affinity and specificity.^{28,29} Several years later, their unique biological activity was characterized. Two metalloinsertors were found to preferentially inhibit growth in MMR-deficient cells over MMR-proficient cells (**Figure 1.10**).⁵³ Furthermore, while only the Δ -[Rh(bpy)₂(chrysi)]³⁺ enantiomer binds to mismatches *in vitro*, likewise only this enantiomer was found to possess this biological activity, implying that the biological activity of these complexes originates from binding to mismatches *in cellulo*. Further evidence to support this notion was achieved in a succeeding study in which the ability of several different metalloinsertors with varying ancillary ligands to preferentially target MMR-deficient cells was directly correlated with their mismatch binding affinities.⁵⁴ A subsequent study on the mechanism of activity of these metalloinsertors revealed that not only do they selectively inhibit growth of MMR-deficient cells, but after longer incubation times, they are also selectively cytotoxic, inducing necrosis in the MMR-deficient cells.⁵⁵ The ability of these complexes to target MMR-deficient cells over MMR-proficient cells with this selectivity is distinctive. Commonly used chemotherapeutics, alkylators, DNA damaging agents as well as cisplatin, all suffer from a selective toxicity instead with MMR-proficient cells, leading to a build-up in resistance to MMR-deficient cancers (**Figure 1.10**).⁵⁶ Moreover, it appears that the selective activity of metalloinsertors in MMR-deficient cells is not only unique but also general to the full family of metalloinsertors. The further development of this class of compounds, then, might help overcome one of the largest issues we have with current platinum-based therapeutics: acquired or inherent resistance.

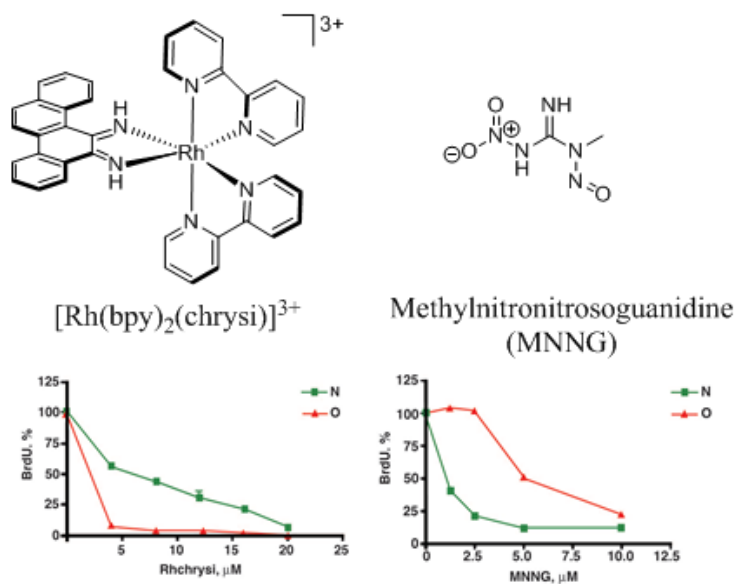


Figure 1.10 Chemical structures (top) and biological activities (bottom) of the rhodium metalloinsertor $[\text{Rh}(\text{bpy})_2(\text{chrysi})]^{3+}$ (left), and the DNA alkylating agent MNNG (right) studied in the Barton laboratory.⁵³ MMR-proficient (green) and MMR-deficient (red) cells were treated with varying concentrations of each compound, and the proliferation of growth was quantified *via* a BrdU incorporation assay. With the rhodium metalloinsertor, the MMR-deficient cells are preferentially targeted over MMR-proficient cells, whereas the DNA alkylating agent targets the MMR-proficient cells, a trend seen with many commonly used DNA-targeted therapeutics.

1.4 Cellular Uptake of Metal Complexes

Establishing biological activity of small molecules and complexes in the cellular milieu is clearly more complicated than establishing chemical targets and structures in a test tube. A key element underlying this complexity is whether and how the complex enters the cell. Does it ever make it to its test tube target?

1.4.1 Methods to Monitor Cellular Uptake

Because transition metals like Rh, Ru, and Pt are not inherently found in the cell, techniques that focus on detecting metals, such as atomic absorption spectroscopy (AAS) or inductively coupled plasma mass spectrometry (ICP-MS), are invaluable to monitor cellular uptake. The foundation of AAS is the aspect that metal ions absorb strongly at discrete, characteristic wavelengths. In this technique, the sample is suctioned into an atomizer, which reduces everything in the sample to its atomic states. The atoms are then irradiated, during which time they will absorb light of a certain energy which equals a specific electronic transition of a particular element. The remaining radiation then passes through a monochromator, which picks out the wavelength of light specific to the metal of interest, and sends it to the detector. Quantitative information is obtained by taking the ratio of the flux without a sample to the flux with the sample and converting to concentration using the Beer-Lambert Law.^{57,58}

ICP-MS is highly sensitive and is applicable to a wide range of metals. Furthermore, it is compatible with a wide range of sample matrices, including many biologically relevant ones. The sample is introduced into a spray chamber, where it is nebulized into an aerosol. These small droplets are then transferred to the inductively coupled plasma. The sample droplets are atomized and ionized by the plasma, leading to

atomic, singly charged ions which are subsequently transferred to the mass spectrometer, which is used to determine the concentration of the metals of interest.⁵⁹

Confocal fluorescence microscopy allows for the acquisition of high-resolution 3-D images with low background interference, and can be used to observe intracellular fluorescent compounds.⁶⁰ As such, confocal fluorescence microscopy has been utilized in countless studies to probe the cellular uptake of metal complexes, but only those that are luminescent.⁶¹ However, due to differences in the quantum yields among different luminescent compounds, this technique cannot be utilized to *quantify* the amount of drug localized inside the cell. Another technique that can be used to monitor uptake of luminescent molecules is flow cytometry. In this technique, cells are individually counted based on the amount of luminescence inside of them. A stream of cells is passed through a laser beam, and the instrument records their light scatter and luminescence. The readout is a histogram showing the number of cells versus luminescence intensity. Importantly, combining either of these techniques with ICP-MS or AAS can give much more information than either technique alone.

1.4.2 Relationships Between Drug Uptake and Activity

One major disadvantage to cisplatin treatment is acquired resistance.⁶² While there are several different explanations that can account for this resistance, one important mechanism of cisplatin resistance is decreased cellular accumulation of the drug.⁶³ Specifically, in an early study by Andrews and coworkers, AAS was used to quantify cisplatin accumulation into parent and cisplatin-resistant 2008 human ovarian carcinoma cells. The resistant cells, which exhibited a 3.3-fold resistance, displayed 50% less intracellular platinum than the parental cell line.⁶⁴ Since this study, there have been

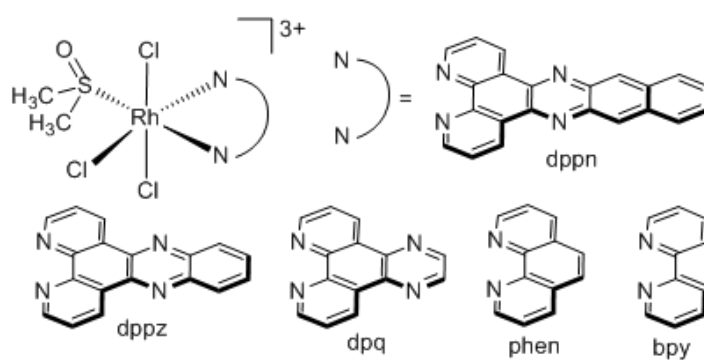


Figure 1.11 Chemical structures of Rh(III) polypyridyl complexes synthesized and studied to monitor uptake. As complexes increased in lipophilicity (bpy to phen to dpq to dppz to dppn derivatives), their cellular uptake into MCF-7 and HT-29 cells increased, resulting in increased potency.⁶⁵

numerous investigations on various different cell lines, many of which employed AAS or ICP-MS, to corroborate this observation.

In a study done by the Sheldrick laboratory, a series of rhodium(III) polypyridyl complexes (**Figure 1.11**) was synthesized and their cytotoxicities towards MCF-7 and HT-29 cancer cells determined. It was noted that as the lipophilicity of the polypyridyl ligand was increased, the cytotoxicity increased as well, and they therefore measured the cellular accumulation of each compound using AAS. As with the cisplatin example, the most potent complexes exhibited the greatest amount of cellular rhodium accumulation.⁶⁵

The relationship between intracellular drug concentration and efficacy is not always as straightforward as in the above studies, however. For example, in a study conducted by Bugarcic and coworkers, three isomeric terphenyl Ru(II) piano-stool complexes (**Figure 1.12**) were examined. Their cytotoxicities against two cisplatin-sensitive and two cisplatin-resistant cancer cell lines were determined, and their intracellular ruthenium concentrations were determined by AAS. Surprisingly, the extent of ruthenium uptake of the three complexes did not correlate at all with their different cytotoxicities. In fact, the most potent of the three complexes (the *p*-terp complex) displayed the least amount of ruthenium uptake into the cells. After numerous DNA binding studies, the authors attributed the enhanced cytotoxicity of this complex to its ability to not only covalently interact with DNA (as the other two isomers could) but also intercalate into DNA.⁶⁶ Perhaps the structural distortions generated in this bound lesion produced a great cellular response. In any case, this study nicely highlights the fact that in many cases more information than just intracellular drug concentration is necessary in order to explain biological activity.

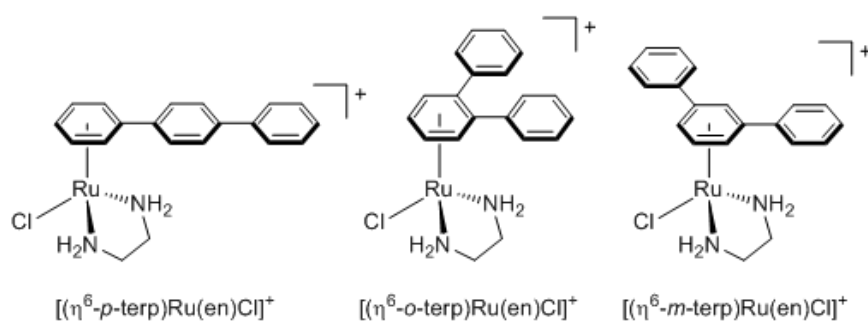


Figure 1.12 Chemical structures of three isomeric terphenyl Ru(II) piano-stool complexes studied by Bugarcic and coworkers.⁶⁶ Uptake of the complexes into two cisplatin-resistant and two cisplatin-sensitive cell lines was found not to correlate with their potencies.

One study that combines ICP-MS and fluorescence microscopy to study the relationship among structure, activity, and uptake was done by Louie and coworkers. In this work, a series of luminescent rhenium(I) polypyridyl was examined (**Figure 1.13**). Here there was a direct correlation found between intracellular rhenium concentrations, determined by ICP-MS, and cytotoxicities in HeLa cells. Due to the luminescent nature of the complexes, the authors were also able to monitor uptake in live cells via confocal microscopy, and even observe the localization of the complexes in the mitochondria of the cells.⁶⁷

1.4.3 Mechanisms of Uptake

While knowing the relationship between the amount of a therapeutic taken into a cell and the activity of the drug is important, understanding *how* the compound gains entry into the cell is likewise crucial for optimization of next-generation complexes. The mechanism of cellular uptake of a drug can direct its localization within the cell as well as the specificity of a given compound for one cell type versus others. The different routes of entry into the cell include passive diffusion, facilitated diffusion, active protein transport, and endocytosis (**Figure 1.14**). Passive diffusion is the movement of the molecule of interest across the cell's lipid bilayer, facilitated by the concentration gradient. Facilitated diffusion is the transport of the molecule of interest across the cell's lipid bilayer, facilitated by a membrane-bound transport protein such as a channel or a passive carrier. Active transport is very similar, but the proteins involved in this type of transport are membrane-bound ATPases, meaning that the process of moving a substance from the outside of the cell to the inside uses ATP. Endocytosis is a general term for the process by which the cell will "engulf" a molecule using a vesicle formed from the

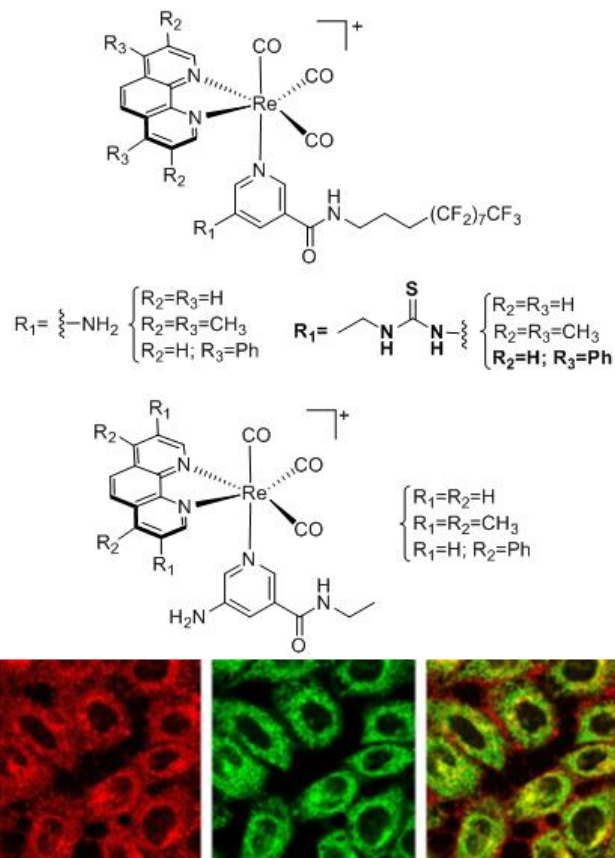


Figure 1.13 Chemical structures (top) of a series of luminescent rhenium(I) polypyridyl complexes by Louie and coworkers.⁶⁷ Using ICP-MS, the authors were able to correlate the cytotoxicities of these complexes in HeLa cells with intracellular rhenium concentrations. Using fluorescence microscopy (bottom), the authors were able to observe the localization of one such complex (structure shown in bold, fluorescence shown on bottom left in red) in HeLa cells. The authors then used MitoTracker (bottom middle in green) to show that the complex localizes mainly in the mitochondria (bottom right, yellow shows the overlap).

plasma membrane.⁶⁸ Endocytosis can be broken down into five different categories: macropinocytosis, clathrin-mediated endocytosis, caveolin-mediated endocytosis, clathrin- and caveolin-independent endocytosis, and phagocytosis. All forms of endocytosis involve the formation of a membrane compartment, and simply differ in the size and composition of the compartments involved. Phagocytosis involves the uptake of particles larger than 0.5 μm in diameter, and thus is not applicable to small transition metal complexes.⁶⁹ Macropinocytosis involves “ruffling” of the membrane to form large pockets greater than 1 μm in diameter, or endocytic vesicles, which are filled with both extracellular solvent and solute molecules. These vesicles are then broken down by endosomes or lysosomes. Clathrin-mediated endocytosis is mediated by “clathrin-coated pits”, which are about 100 nm in diameter, and have a crystalline coat made up of transmembrane receptors associated with the protein clathrin. These receptors bind their respective ligands (or a therapeutic agent that resembles their ligand) and then pinch off to form clathrin-coated vesicles (CCVs), which are internalized into the cell. In caveolin-mediated endocytosis, flask-shaped pits in the plasma membrane, about 60 to 80 nm in diameter, are shaped by caveolin, a protein that binds cholesterol. Finally, in clathrin and caveolin-independent endocytosis, small structures that are 40 to 50 nm in diameter act as “rafts”, freely diffusing along the cell surface. These rafts will then be captured and internalized within any endocytic vesicle.^{70,71}

However, just as membrane-bound proteins can facilitate the entry of a complex into the cell, certain proteins, called efflux transporters, can facilitate the extrusion of such compounds from the cell. In fact, multidrug efflux pumps, which can recognize multiple structurally dissimilar compounds, are often responsible for chemotherapeutic

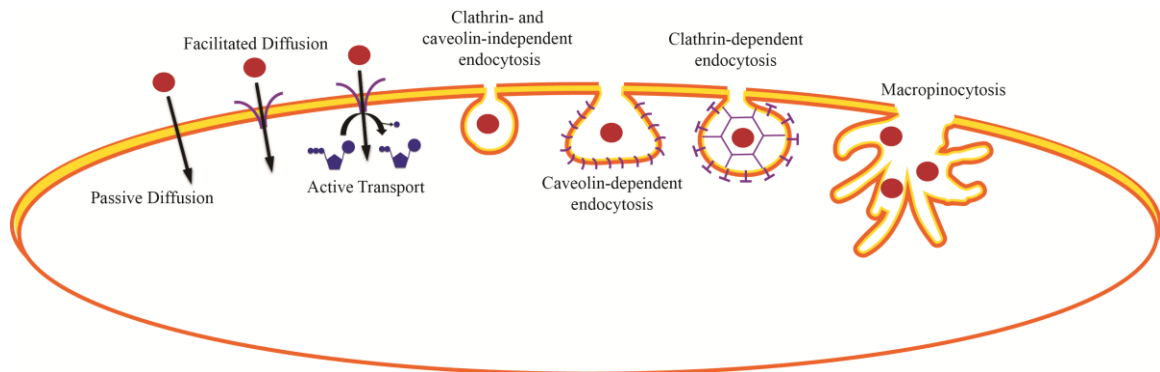


Figure 1.14 Schematic diagram of the different possible routes of entry into the cell taken by small complexes.

resistance.⁷² The most well-studied of such mammalian efflux transporters is the ATP-binding cassette (ABC) family. These efflux transporters use ATP hydrolysis to drive the extrusion of drugs from the cell, and can do so against significant concentration gradients.⁷³ The reason behind the broad substrate specificity of these efflux transporters is the presence of a large, flexible hydrophobic binding pocket which allows for substrate binding via hydrophobic and electrostatic interactions, rather than the specific hydrogen-bonding networks present in less promiscuous transport proteins.⁷⁴

A basic experiment in elucidating the mechanism of uptake is determining whether the mechanism of uptake is energy-dependent or –independent. Both passive and active diffusion are energy-independent, while active transport and endocytosis are energy-dependent. By incubating cells at a low temperature (4° C) or in the presence of metabolic inhibitors (2-deoxyglucose and oligomycin), processes that require energy will be blocked. If the drug of interest has decreased uptake under these conditions, the mechanism of uptake involves an energy-dependent process, while if uptake is unchanged the mechanism is an energy-independent process.^{75,76}

Passive diffusion has the broadest range in substrates out of all uptake mechanisms, and is therefore an attractive mode of uptake for therapeutics. Uptake mediated by passive diffusion is the most difficult to modulate, but it can be done. Uptake of positively charged molecules, such as many inorganic therapeutics, can be driven by the plasma membrane potential of the cell. In mammalian cells, the membrane potential is generated and maintained by a potassium concentration gradient. This potential can be reduced either by using media with a potassium concentration equal to the intracellular potassium concentration, or by adding gramicidin A to the media, a

polypeptide that will form transmembrane channels which allow unrestricted potassium traversal, thus destroying the concentration gradient. In contrast, the cell can be hyperpolarized by adding valinomycin to the media, a potassium-specific ionophore that will increase potassium transportation across the membrane.⁷⁷

Protein-mediated transport, facilitated diffusion, and active transport have the capability of being cell-type or tissue-type specific. This allows for the development of targeted drugs, thus attenuating dose-limiting side effects.⁷⁸ This type of uptake can be repressed by using known inhibitors of specific transport proteins. If uptake of the compound of interest is decreased in the presence of the inhibitor, then the respective transport protein most likely is involved in uptake. Likewise, many efflux transporters have known inhibitors; if uptake of a compound is *increased* in the presence of an inhibitor, then the compound is likely a substrate for the respective efflux protein.

As with protein-mediated transport, the different types of endocytosis can be mediated by using known inhibitors of the different processes. Ammonium chloride and chloroquine diphosphate are general endocytosis inhibitors.⁷⁹ Chlorpromazine hydrochloride, monodansylcadaverine (MDC), and phenylarsine oxide are inhibitors of clathrin-mediated endocytosis and macropinocytosis.⁸⁰ Filipin and nystatin selectively inhibit caveolin-mediated endocytosis via cholesterol sequestration.⁸¹ Amiloride, as well as 5-(N,N-dimethyl) amiloride (DMA) and 5-(N-ethyl-N-isopropyl) amiloride (EIPA) inhibit macropinocytosis and phagocytosis by obstructing Na^+/H^+ exchange.⁸²

Cisplatin is the prototypical medicinal inorganic drug. There have been many studies on the activity, uptake, and subcellular distribution of this molecule, and these serve as illustrations of how mechanism may be elucidated. For many years it was widely

accepted that cisplatin entered the cell via passive diffusion. In one such study on the mechanism of uptake of cisplatin, Binks and Dobrota measured the amount of uptake of cisplatin into rat small intestines using AAS. They found that uptake of the drug was linear with respect to time and not saturable up to a concentration of 1.0 mM. The authors also found no change in uptake of cisplatin when the experiments were repeated under metabolic inhibition, confirming that the mechanism of uptake is energy-independent and through passive diffusion.⁸³ More recently, however, it was found that several protein-mediated transport pathways can also be responsible for cisplatin uptake. The most important of these pathways are the organic cation transporters and the copper influx transporter CTR1.⁸⁴ To demonstrate the contribution of CTR1 to cisplatin uptake, Howell and coworkers measured cisplatin uptake in A2780 human ovarian cancer cells using ICP-MS. They increased expression of CTR1 20-fold and found that intracellular platinum levels increased by 55% after 24 hours of platinum incubation.⁸⁵

Many ruthenium complexes are easy to monitor in uptake studies owing to their strong luminescence. For example, the Barton lab has used flow cytometry to study the uptake of the luminescent lipophilic ruthenium complex $[\text{Ru}(\text{DIP})_2(\text{dppz})]^{2+}$ into HeLa cells (**Figure 1.15**). It was found that under metabolic inhibition, uptake of the ruthenium complex remained unchanged. Additionally, increasing the incubation temperature from 4° C to 37° C had no effect on uptake. These experiments showed that the mechanism of uptake was energy-independent. To rule out facilitated diffusion by organic cation transporters (OCTs), uptake of the ruthenium complex was also studied in the absence and presence of a variety of OCT inhibitors (tetra-*n*-alkylammonium salts, procainamide, and cimetidine), and was found to be unaffected by the presence of these compounds.

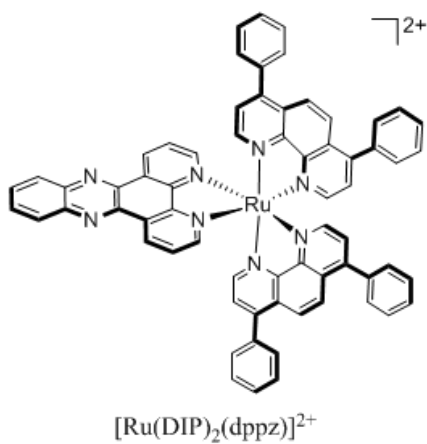


Figure 1.15 $[\text{Ru}(\text{DIP})_2(\text{dppz})]^{2+}$, a luminescent polypyridyl ruthenium complex that enters HeLa cells via passive diffusion.⁸⁶

Lastly, the effect of changes in the membrane potential on uptake of the ruthenium compound was studied. When incubated with 170 mM potassium (which reduces the membrane potential to zero), uptake decreased substantially. Furthermore, in the presence of valinomycin (which will increase the membrane potential), uptake of the compound increased substantially. Taken together, it was concluded that uptake of $[\text{Ru}(\text{DIP})_2(\text{dppz})]^{2+}$ was solely via passive diffusion.⁸⁶ It is interesting to consider this complex being taken up at all efficiently. The complex has a diameter of approximately 21 Å, not unlike many small proteins, yet it is efficiently taken up through the cell membrane to the cytoplasm and, to some extent, to the nucleus of the cell.

In one last study by Pisani and coworkers, the mechanism of cellular uptake of a dinuclear polypyridylruthenium(II) complex (**Figure 1.16**) into L1210 murine leukemia cells was determined through flow cytometry experiments. In this study, the authors found that varying the temperature of incubation from 4° C to 20° C to 37° C had an effect on uptake, with the 4° C sample having the least amount of intracellular ruthenium. Furthermore, when the cells were incubated with an increased amount of glucose, uptake of the ruthenium complex was significantly enhanced. Conversely, under metabolic inhibition, uptake marginally decreased. In order to rule out endocytosis, the authors measured ruthenium uptake in the presence of a variety of different endocytosis inhibitors (chloroquine diphosphate, filipin, dimethyl amiloride, ammonium chloride, and chlorpromazine hydrochloride), and found that uptake was either unchanged or *increased* in the presence of these inhibitors. Furthermore, when incubated with a variety of OCT inhibitors (tetra-*n*-alkylammonium salts or procainamide), uptake remained unchanged. The authors concluded that uptake was in large part due to passive diffusion, with a

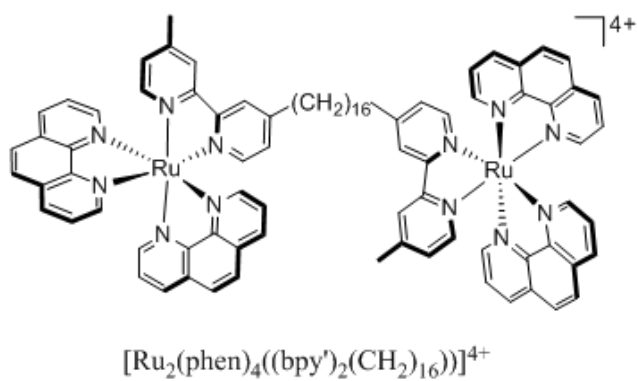


Figure 1.16 $[\text{Ru}_2(\text{phen})_4((\text{bpy}')_2(\text{CH}_2)_{16})]^{4+}$, a compound shown to enter L1210 murine leukemia cells via an energy-dependent mechanism as well as passive diffusion.⁸⁷

minor contribution from protein-mediated active transport.⁸⁷ It is important to consider that complexes so similar in chemical structure need not have similar mechanisms of uptake. Experiments need to be determined in each case to establish the uptake mechanism.

1.5 Subcellular localization of the Metal Complex

Once a therapeutic has entered the cell, there are a plethora of different organelles in which it can localize. Moreover, activities and targets depend on where within the cell the complex becomes localized. This localization can also determine unwanted toxicities associated with a given complex.

1.5.1 Methods to monitor Localization

The most commonly exploited technique for the subcellular mapping of inorganic therapeutics is fluorescence microscopy. However, this technique can only be used if the complex of interest is inherently luminescent. Cells can be treated with the luminescent drug of interest concomitantly with any of the various fluorescent organelle-specific probes. The extent of overlap between the drug and the probe will provide information on the localization of the drug. For example, Matson and coworkers synthesized a variety of dppz complexes of Ru derivatized with alkyl ether chains of various lengths and used confocal laser scanning microscopy to study their subcellular localization in CHO-K1 cells.⁸⁸ Using various RNA and membrane-specific dyes, they found, perhaps not surprisingly, that the least lipophilic compound localized in the nucleus, while the most lipophilic localized in membranes.

While fluorescence microscopy has the capability of providing a qualitative assessment of the localization of therapeutics in living cells, due to differences in the

quantum yields among different luminescent compounds, this technique cannot be utilized to quantify the amount of drug localized inside the cell. Furthermore, many metal-based luminescent compounds have been shown to exhibit different quantum yields depending on the environment surrounding the compound,⁸⁹ which further complicates the quantitation of the localization of luminescent metal complexes using this technique.

In a study by Groessl and co-workers, ICP-MS was used to track the uptake and subcellular localization of cisplatin as well as two ruthenium-based chemotherapeutics currently in clinical trials, NAMI-A and KP1019. Reduced mitochondrial accumulation of cisplatin was observed in cisplatin-resistant cells, while the ruthenium-based drugs were found to have different localization patterns than cisplatin, which did not change from one cell type to the other.⁹⁰

While AAS and ICP-MS can provide quantitative information on the subcellular localization of inorganic complexes, the process of sample preparation for these methods involves the destruction of the cells, and, therefore, no structural information is obtained. One method for the visualization of the subcellular localization of metal-based therapeutics while obtaining the structural integrity of the cell is electron microscopy. Electron microscopy has the advantage of providing spatial resolution that is almost three orders of magnitude better than conventional light microscopy, allowing for the resolution of structural details in the nanometer range.⁹¹ Furthermore, the electron-dense property of metal ions can be detected inside cells by electron microscopy due to mass contrast. In transmission electron microscopy (TEM), cells are fixed, dehydrated with organic solvent, embedded in resin, and then thinly sliced (50 to 400 nm thick). These

thin samples are then exposed to an electron beam, which will be either scattered by regions of high electron density (metal ions), or transmitted through low electron density regions of the sample to a detector, which then constructs a “contrast image” of the sample, where areas of high electron density have higher contrast. In a study by van Rijt and coworkers, the distribution of a osmium(II) arene complex in ovarian cancer cells was determined by TEM. It was observed that upon treatment of A2780 cells with 5 μ M osmium complex, increased contrast was observed in the mitochondria, nucleolus, and nuclear membrane. The morphological changes associated with apoptosis were able to be observed at the same time, illustrating the utility of electron microscopy.⁹²

Electron microscopy can in certain cases be combined with elemental mapping to obtain a technique called energy-filtered transmission electron microscopy (EFTEM). In this technique, as the electrons from the electron beam hit the sample, some will undergo an inelastic collision, losing an amount of energy that is equivalent to the core atomic level of the element that it just collided with. In this way, not only will an image be created with the resolution of electron microscopy, but also element distribution maps of the sample can be obtained.⁹³

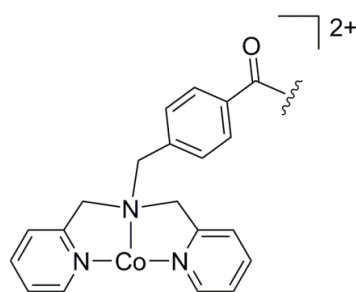
The last technique to consider here is nano-scale secondary ion mass spectrometry (NanoSIMS). In this technique, a high-energy primary ion beam bombards the surface of a sample, “sputtering” secondary ions, which are then detected and analyzed by a mass spectrometer.⁹⁴ In this way, NanoSIMS can provide spatial resolution up to 50 nm, as well as elemental and isotopic information of the sample. This technique is in its infancy and, as such, has not been widely utilized in the subcellular mapping of metal-based therapeutics. However, in one study by the Berners-Price lab, a complementary EFTEM

and NanoSIMS study was performed on an antitumor gold(I) phosphine complex.⁹⁵ In this study, human breast cancer cells (MDA) were treated with the gold complex and analyzed by both EFTEM and NanoSIMS for subcellular gold localization. Using EFTEM, the localization of gold could be observed, as well as the morphological changes accompanying gold treatment. NanoSIMS allowed for the mapping of $^{12}\text{C}^{14}\text{N}^-$ (to show cell morphology), $^{31}\text{P}^-$ (to show the location of nucleic acids), $^{197}\text{Au}^-$ (to show localization of the therapeutic), and $^{34}\text{S}^-$ (to show the localization of thiols). The gold signal clearly co-localized with the sulfur signal, thus supporting the idea that the mechanism of action of Au(I) compounds involves the inhibition of thiol-containing protein families.

1.5.2 Peptide Conjugation

DNA is the cellular target of many inorganic chemotherapeutic agents. As such, it is important for these complexes to localize mainly in the nucleus of cells. One strategy to alter the subcellular localization of a compound is through peptide conjugation. Nuclear localization sequences (NLS) are small peptides which, when appended to a protein, will in essence allow the protein to be imported into the nucleus by nuclear transport.⁹⁶ As an example, Kirin and coworkers utilized the NLS Pro-Lys-Lys-Lys-Arg-Lys-Val to enhance the uptake and nuclear localization of the cobalt complex shown in **Figure 1.17** into HT-29 cells. AAS experiments revealed that not only does the conjugate have enhanced uptake compared to the unconjugated cobalt complex, but also the intracellular cobalt concentration of the conjugate is higher than the extracellular cobalt concentration. Furthermore, the fraction of intracellular cobalt localized in the nucleus increased for the conjugates compared to the unconjugated cobalt complex.⁹⁷

However, in the design of peptide-therapeutic conjugates, care must be taken to



$\text{wavy line} = \text{OH, OMe, Ahx-Pro-Lys-Lys-Lys-Arg-Lys-Val-NH}_2$
 where Ahx = $\text{wavy line}-\text{HN}(\text{CH}_2)_6\text{O-wavy line}$

Figure 1.17 The peptide conjugate studied by Kirin and coworkers. Upon conjugation of the cobalt complex to the nuclear localization peptide, uptake of the complex into the nucleus of HT-29 cells increased significantly.⁹⁷

ensure that the conjugate itself still has the same biological target as the unconjugated molecule. For example, in an attempt to increase and accelerate the cellular uptake of rhodium metalloinsertors, the $[\text{Rh}(\text{phen})(\text{bpy}'\text{-Arg}_8)(\text{chrysi})]^{11+}$ complex shown in **Figure 1.18** was synthesized. Uptake studies conducted on the fluorescein-appended analogue confirmed fast (within 60 min) nuclear uptake into HeLa cells. However, DNA binding studies revealed that, with the octaarginine appendage, the nonspecific binding affinity of both complexes for mismatched and matched DNA increased, due to the substantial added positive charge of the peptide.⁹⁸ In fact, studies of cellular proliferation with the metalloinsertor-peptide conjugate confirmed that the complexes no longer showed the preferential inhibition of MMR-deficient cells, as expected if specific binding only to mismatched DNA was lost. One route to restore specificity would be to include a self-cleavable linker so that the conjugate would be removed once inside the nucleus. The work thus illustrates the utility but also subtle new issues that arise with peptide conjugates for therapeutic applications.

Many laboratories append fluorescent tags onto molecules of interest to follow their subcellular localization. The process of appending a fluorescent tag to the molecule of interest can, however, also alter the subcellular localization.⁹⁹ As an illustration, the localization properties of two $\text{Ru}(\text{dppz})$ -peptide conjugates, one with and one without a fluorescent tag (**Figure 1.19**) were explored. The conjugate with only the octaarginine peptide was localized throughout the cytoplasm in punctate distributions and was completely absent from the nucleus. On the other hand, the conjugate with both octaarginine and fluorescein exhibited nuclear staining when incubated under the same conditions as the previous conjugate. This study clearly shows the consequences of

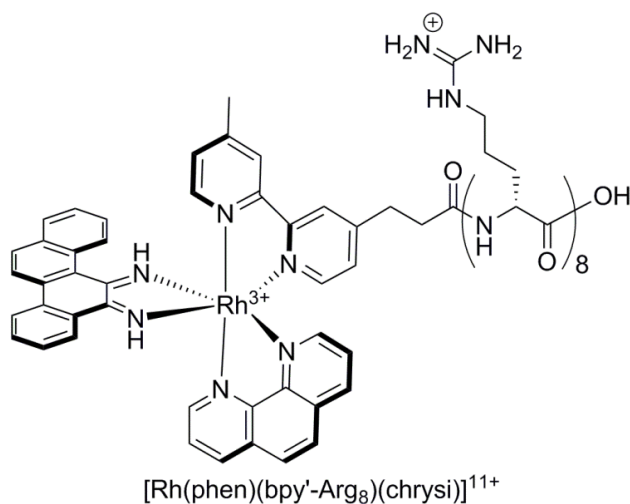


Figure 1.18 The rhodium metalloinsertor-peptide conjugate synthesized in order to accelerate uptake. While uptake is accelerated upon conjugation of the metalloinsertor to the octaarginine peptide, the presence of the octaarginine increases the nonspecific binding affinity of the complex for matched and mismatched DNA.

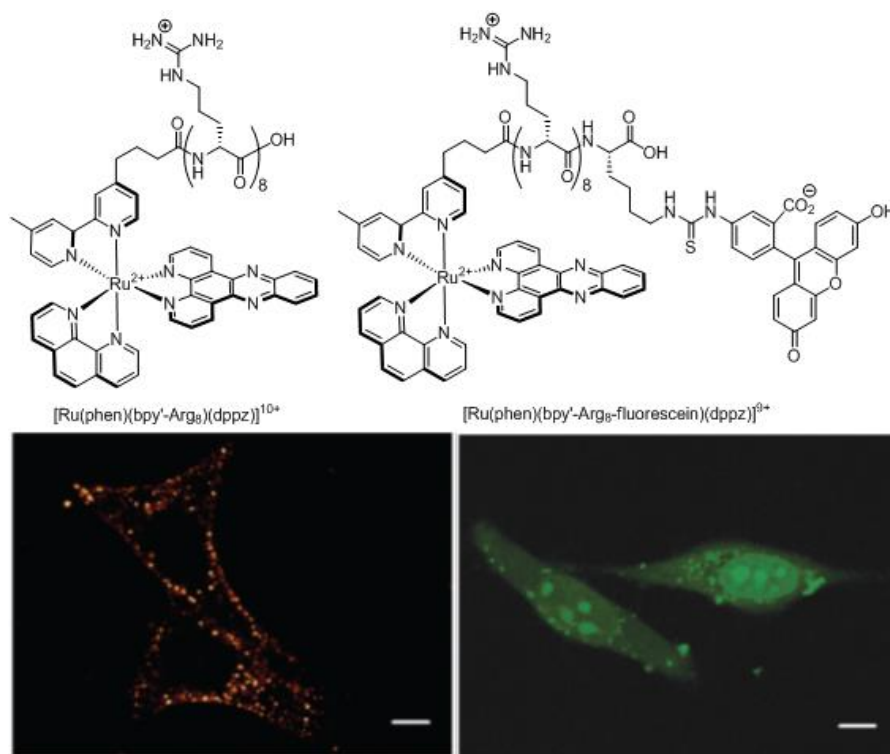


Figure 1.19 Chemical structures (top) and confocal microscopy images (bottom) of the two metal-peptide fluorophore conjugates examined in our laboratory. The octaarginine conjugate (left) displays only cytosolic localization, while the octaarginine fluorescein conjugate (right) exhibits nuclear localization.

appending fluorescent tags to non-fluorescent molecules in order to study their subcellular localizations.

1.6 Targeted Therapeutics

Cisplatin and its analogues were developed as “classical” chemotherapeutics. These types of drugs are meant to interfere with replication and/or the mitotic processes of tumor cells.¹⁰⁰ In this way, they achieve potency by damaging cancer cells *more* than healthy cells. While this approach has been fruitful, it has been known to cause a litany of side effects, such as nephrotoxicity, neurotoxicity, leukopenia, and thrombocytopenia, as well as nausea, vomiting, and hair loss.¹⁰¹ For these reasons, research efforts in recent years have shifted towards the development of targeted chemotherapy. In “targeted” therapy, a drug is developed to target a specific cellular signaling pathway on which cancer cells depend for growth, metastasis, or angiogenesis.¹⁰² These types of compounds aim to damage cancer cells *instead* of healthy cells. Targeted therapy focuses on the development of selective therapeutics, whereas classical therapy has focused on the development of increasingly cytotoxic compounds. The next generation of chemotherapeutics has focused on targeting biomolecules, including proteins, organelles, and specific DNA lesions (**Figure 1.20**).

1.6.1 Proteins as Targets

As an illustration, the high levels of mutagenesis in cancerous cells often lead to upregulation and overexpression of proteins, making them attractive candidates for targeting. Metal complexes, due to their modular nature and inherent chirality, are uniquely able to selectively target these chiral biomolecules. In particular, this approach has been applied toward the selective inhibition of kinase activity. Phosphorylation of

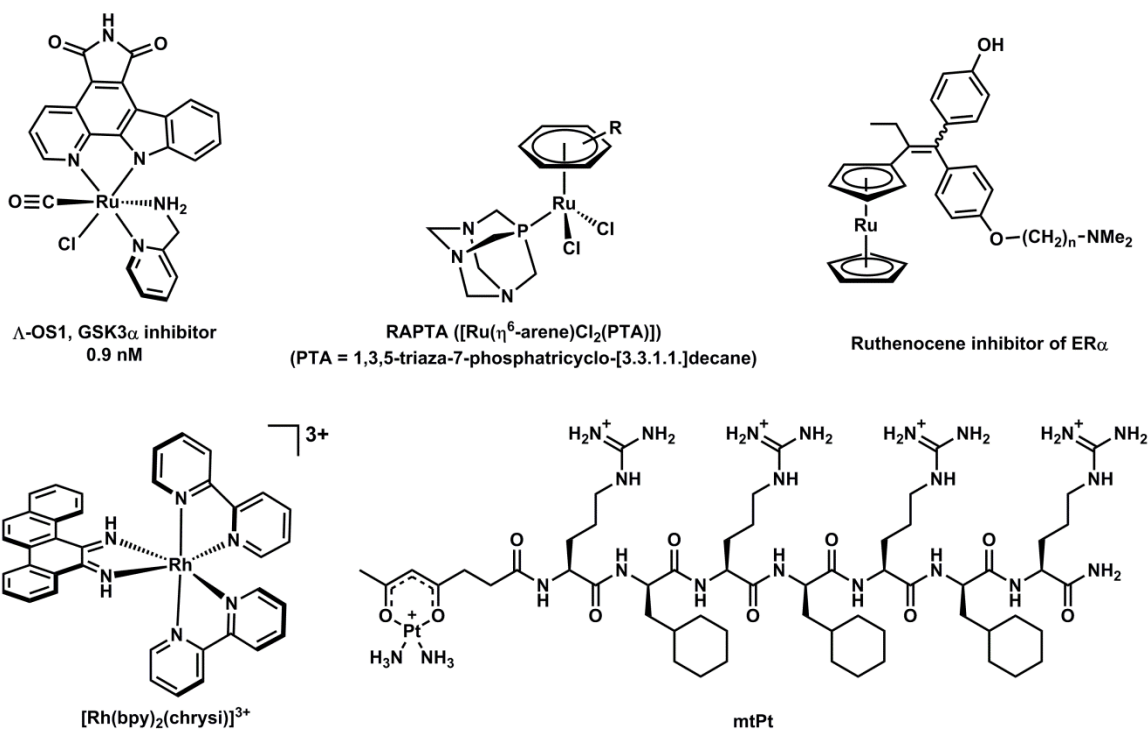


Figure 1.20 Chemical structures of targeted chemotherapeutics: (top, left to right) The octasporine complex OS1, a potent inhibitor of the protein kinase GSK3 α ; General architecture of RAPTA cathepsin B inhibitors; Ruthenocene analogues of tamoxifen for the selective targeting of ER α ; (bottom, left to right) The first generation rhodium metalloinsertor, [Rh(bpy)₂(chrysi)]³⁺, selectively binds to mismatched and abasic sites in duplex DNA; Structure of mtPt, a cisplatin analogue designed to localize to the mitochondria.

proteins by kinases is a highly important regulatory activity. However, over-phosphorylation of proteins is common in many types of cancer.¹⁰³ In a recent study by Meggers et al., inert metal complexes, inspired by the natural product staurosporine and termed octasporines, were designed as highly selective kinase inhibitors (**Figure 1.20**).^{104,105} Six complexes were synthesized, all containing a ruthenium or iridium center and a bidentate pyridocarbazole ligand designed to bind the hinge region of the ATP-binding pocket of the kinase. However, the remaining ligands on each complex were designed to make up a unique set of hydrogen-bonding interactions with the glycine-rich loop of the ATP-binding pockets of six distinct kinases (**Figure 1.21**).¹⁰⁴ *In vivo* studies have revealed the anti-angiogenic properties of one of these types of compounds in zebrafish embryos, exemplifying their potential.¹⁰⁵

Whereas the previous example utilized the structural complexity of inert metal complexes, the reactive nature of certain metal centers can also be exploited in targeted therapy. Proteases play a crucial role in tumorigenesis by suppressing cell-death pathways and promoting cell-survival pathways.¹⁰⁶ One such protease, cathepsin B, has been targeted by ruthenium arene RAPTA compounds (**Figure 1.20**).^{107,108} These compounds were found to inhibit cathepsin B protease activity and exhibited selective anti-metastatic activity *in vivo*.^{108,109}

Estrogen receptors such as estrogen receptor α (ER α), which is overexpressed in several types of breast cancer, have also been the subject of targeted therapy studies.¹¹⁰ Several organometallic analogues of tamoxifen, an antagonist of estrogen receptors, have been developed to selectively target ER α (**Figure 1.20**).^{111,112} These complexes have demonstrated cytotoxic activity selectively in ER α -positive breast cancer cell lines.¹¹¹

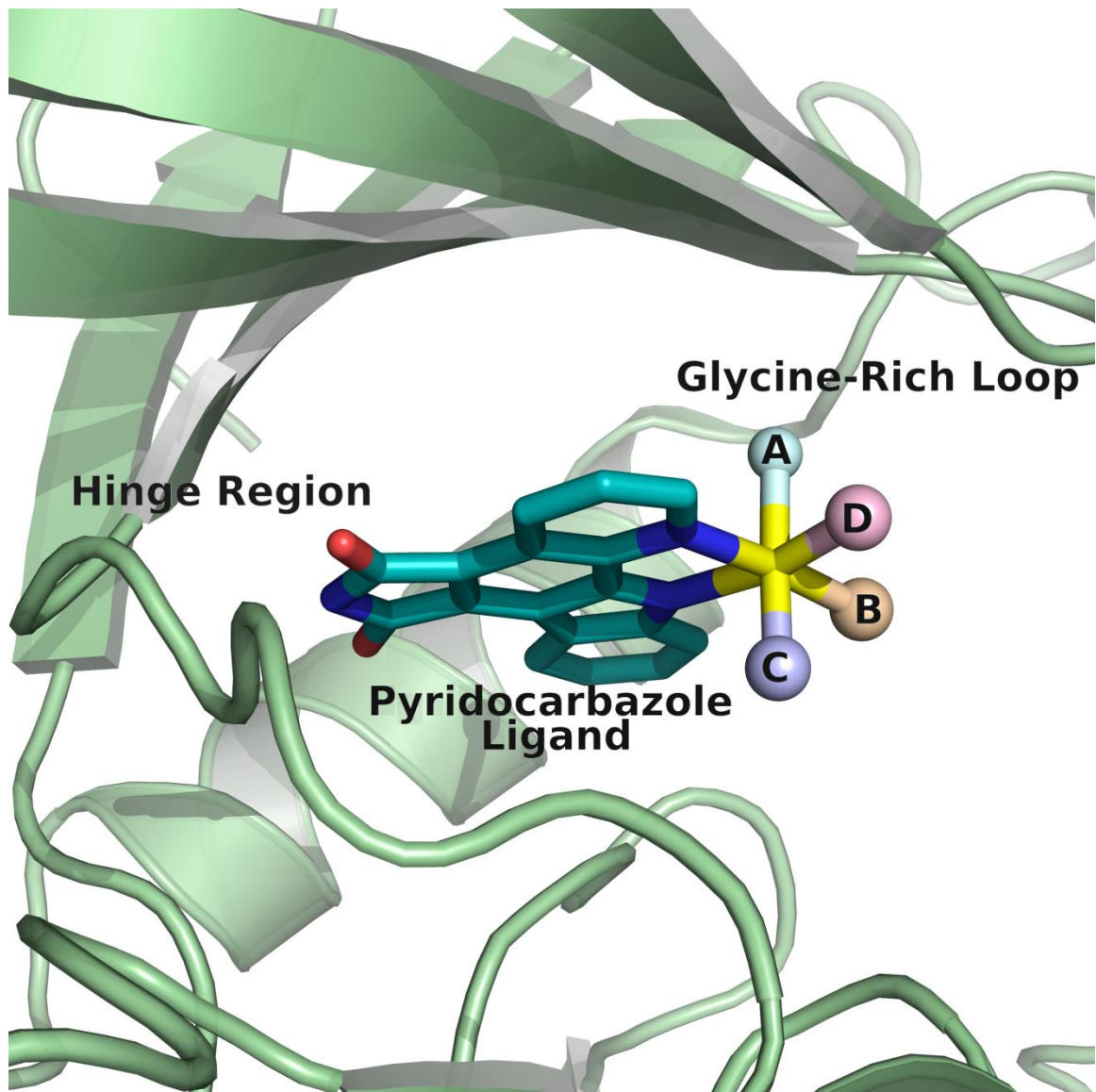


Figure 1.21 Design of Octasporine complexes as inhibitors of protein kinases (adapted from reference 104). The pyridocarbazole ligand, common to all complexes, binds to the hinge region (where the adenine portion of ATP binds) of the ATP-binding pocket. The remaining A, B, C, and D ligands make up a set of hydrogen-bonding interactions with the glycine-rich loop (where the ribose triphosphate portion of ATP binds) of the ATP binding pocket, each unique to a particular kinase.

1.6.2 Organelles as Targets

In addition to protein targeting, the mitochondria can also serve as a valuable target for drug design. Mitochondria produce reactive oxygen species as a byproduct of metabolism, and they also play a crucial role in the regulation of cell death pathways.¹¹³ Targeting mitochondria and mitochondrial DNA can induce apoptosis in tumorigenic cells, as was recently demonstrated by Lippard and Kelley.¹¹⁴ They constructed a *cis*-platinum(II) complex tethered to a mitochondrial penetrating peptide, which contained alternating cationic and lipophilic residues to enhance mitochondrial uptake (**Figure 1.20**). This complex was shown to localize almost exclusively to mitochondria in several cancer cell lines. Moreover, the complex was able to induce apoptosis in cisplatin-resistant ovarian cancer cells by damaging mitochondrial DNA.

1.6.3 DNA Lesions as Targets

The proposed mechanism of action of classical platinum-based chemotherapeutics is the formation of covalent DNA adducts, followed by cellular processing of these lesions.⁶ The synthesis of new-generation classical therapeutics with enhanced DNA-binding properties in order to increase cytotoxicity has been extensively explored. However, the design and synthesis of therapeutics that bind to specific DNA lesions that are more prevalent in cancer cells than normal cells may represent a targeted strategy for new chemotherapy. In particular, rhodium metalloinsertors (**Figure 1.20**) bind mismatches in duplex DNA *in vitro* with high specificity and affinity, preferentially targeting thermodynamically destabilized mismatches over matched base pairs by a factor of over 1000.^{29,30} The binding mode of these complexes to mismatched DNA is illustrated in **Figure 1.5**; the chrysi ligand inserts into the DNA from the minor groove

and ejects both mismatched bases in a binding mode termed metalloinsertion.^{31,33} Ejection of the mismatched bases results in a large lesion that is hypothesized to have the potential to be recognized *in vivo*.

Mismatches in genomic DNA arise naturally as a consequence of replication, but if left uncorrected can lead to mutations.^{115,116} The mismatch repair (MMR) pathway serves as a checkpoint to increase the fidelity of DNA replication ~1000 fold.¹¹⁷ Importantly, deficiencies in the mismatch repair machinery have been associated with several types of cancer, as well as increased resistance to classical chemotherapeutics such as cisplatin.¹¹⁸ Therefore, the development of a targeted therapy for MMR-deficient cancers would be invaluable in the clinic. Due to the unique DNA mismatch-binding properties of rhodium metalloinsertors, their biological properties in MMR-deficient cells were investigated. The compounds have been found to inhibit growth and selectively induce necrosis in MMR-deficient colorectal cancer cells over MMR-proficient cells.^{53,55} Clearly, the strategy of targeting a specific lesion in DNA is a promising alternative to the classical approach.

1.7 Conclusion

The development of new therapeutic agents with improved effectiveness is imperative, and metal complexes offer a wealth of possibilities. The thorough examination of current therapeutics is vital to this process. Structural characterization of the interaction between a given complex and its target can provide insight as to what changes can be made to the complex in order to strengthen the interaction. Likewise, structure-function relationships can provide further information for improvement by noting how the hydrophobicity of a given compound affects the activity. The relationship

between uptake and activity is also an important one, and knowing the mechanism of uptake can provide the means with which to improve uptake. The knowledge of where within the cell the complex is being shuttled is a powerful tool, and the correlation between activity and subcellular localization will provide the researcher with the insight of how to make new therapeutics with improved effectiveness.

Targeted chemotherapy holds the potential to combat the severe side effects and acquired resistance associated with classical chemotherapeutics such as cisplatin. Many years of study have focused on achieving high potency for metal complex therapeutics, but such potency has been achieved. Just as the design of organic chemotherapeutics has shifted from potent alkylators and other inhibitors of DNA synthesis to far more tailored, subtle reagents, the design of novel metallotherapeutics now requires a targeted approach. There has really been a paradigm shift in next-generation chemotherapeutic drug design that focuses on specifically tailored therapies. The unique reactivity and coordination geometry of metal complexes make them the ideal scaffold for this new tailor-made design of targeted therapeutics. The examples discussed herein exemplify the enormous potential of this new strategy in transition metal chemotherapy and perhaps lay the groundwork for this burgeoning new field.

1.8 References

- 1 Zhang, C. X.; Lippard, S. J. *Curr. Opin. Chem. Biol.* **2003**, *7*, 481-489.
- 2 Mansour, V. H.; Rosenberg, B.; Vancamp, L.; Trosko, J. E. *Nature* **1969**, *222*, 385-386.
- 3 Wheate, N. J.; Walker, S.; Craig, G. E.; Oun, R. *Dalton Trans.* **2010**, *39*, 8113-8127.
- 4 Kelland, L. R.; Sharp, S. Y.; O'Neill, C. F.; Raynaud, F. I.; Beale, P. J.; Judson, I. *R. J. Inorg. Biochem.* **1999**, *77*, 111-115.
- 5 Boulikas, T.; Vougiouka, M. *Oncol. Rep.* **2004**, *11*, 559-595.
- 6 Jamieson, E. R.; Lippard, S. J. *Chem. Rev.* **1999**, *99*, 2467-2498.
- 7 Alessio, E.; Mestroni, G.; Bergamo, A.; Sava, B. *Curr. Top. Med. Chem.*, **2004**, *4*, 1525-1535.
- 8 Hartinger, G. C.; Zorbas-Seifried, S.; Jakupec, M. A.; Kynast, B.; Zorbas, H.; Keppler, B. K. *J. Inorg. Biochem.* **2006**, *100*, 891-904.
- 9 Gianferrara, T.; Bratsos, I.; Alessio, E. *Dalton Trans.* **2009**, *37*, 7588-7598.
- 10 Reslova, S. *Chem. Biol. Interact.* **1971**, *4*, 66-70.
- 11 Harder, H. C.; Rosenberg, B. *Int. J. Cancer* **1970**, *6*, 207-216.
- 12 Stone, P. J.; Kelman, A. D.; Sinex, F. M. *J. Mol. Biol.* **1976**, *104*, 793-801.
- 13 Ushay, H. M.; Tullius, T. D.; Lippard, S. J.; *Biochemistry* **1981**, *20*, 3744-3748.
- 14 Pinto, A. L.; Lippard, S. J. *Biochim. Biophys. Acta* **1985**, *780*, 167-180.
- 15 Takahara, P. M.; Rosenzweig, A. C.; Frederick, C. A.; Lippard, S. J. *Nature* **1995**, *377*, 649-652.

- 16 Wang, D.; Lippard, S. J. *Nat. Rev. Drug Discov.* **2005**, *4*, 307-320.
- 17 Bond, P. J.; Langridge, R.; Jennette, K. W.; Lippard, S. J. *Proc. Natl. Acad. Sci. U.S.A.* **1975**, *72*, 4825-4829.
- 18 Wang, A. H. J.; Nathans, J.; van der Marel, G.; van Boom, J. H.; Rich, A. *Nature* **1978**, *276*, 471-474.
- 19 Barton, J. K.; Danishefsky, A. T.; Goldberg, J. M. *J. Am. Chem. Soc.* **1984**, *106*, 2172-2176.
- 20 Kielkopf, C. L.; Erkkila, K. E.; Hudson, R. P.; Barton, J. K.; Rees, D. C. *Nat. Struct. Biol.* **2000**, *7*, 117-121.
- 21 Odom, D. T.; Parker, C. S.; Barton, J. K. *Biochemistry* **1999**, *38*, 5155-5163.
- 22 Song, H.; Kaiser, J. T.; Barton, J. K. *Nat. Chem.* **2012**, *4*, 615-620.
- 23 Dupureur, C. M.; Barton, J. K. *J. Am. Chem. Soc.* **1994**, *116*, 10286-10287.
- 24 Dupureur, C. M.; Barton, J. K. *Inorg. Chem.* **1997**, *36*, 33-43.
- 25 Holmlin, R. E.; Stemp, E. D. A.; Barton, J. K. *Inorg. Chem.* **1998**, *37*, 29-34.
- 26 Niyazi, H.; Hall, J. P.; O'Sullivan, K.; Winter, G.; Sorensen, T.; Kelly, J. M.; Cardin, C. J. *Nat. Chem.* **2012**, *4*, 621-628.
- 27 Hall, J. P.; O'Sullivan, K.; Naseer, A.; Smith, J. A.; Kelly, J. M.; Cardin, C. J. *Proc. Natl. Acad. Sci. U.S.A.* **2011**, *108*, 17610-17614.
- 28 Jackson, B. A.; Barton, J. K. *J. Am. Chem. Soc.* **1997**, *119*, 12986-12987.
- 29 Jackson, B. A.; Alekseyev, V. Y.; Barton, J. K. *Biochemistry* **1999**, *38*, 4655-4662.
- 30 Jackson, B. A.; Barton, J. K. *Biochemistry* **2000**, *39*, 6176-6182.

- 31 Pierre, V. C.; Kaiser, J. T.; Barton, J. K. *Proc. Natl. Acad. Sci. U.S.A.* **2007**, *104*, 429-434.
- 32 Barton, J. K. *Science* **1986**, *233*, 727-734.
- 33 Zeglis, B. M.; Pierre, V. C.; Kaiser, J. T.; Barton, J. K. *Biochemistry* **2009**, *48*, 4247-4253.
- 34 Wong, E.; Giandomenico, C. M. *Chem. Rev.* **1999**, *99*, 2451-2466.
- 35 Guo, Z.; Sadler, P. J. *Angew. Chem. Int. Ed.* **1999**, *38*, 1512-1531.
- 36 Gill, M. R.; Thomas, J. A. *Chem. Soc. Rev.* **2012**, *41*, 3179-3192.
- 37 Dwyer, F. P.; Gyarfas, E. C.; Rogers, W. P.; Koch, J. H. *Nature* **1952**, *170*, 190-191.
- 38 Novakova, O.; Kasparikova, J.; Vrana, O.; van Vliet, P. M.; Reedijk, J.; Brabec, V. *Biochemistry* **1995**, *34*, 12369-12378.
- 39 Tan, C.; Lai, S.; Wu, S.; Hu, S.; Zhou, L.; Chen, Y.; Wang, M.; Zhu, Y.; Lian, W.; Peng, W.; Ji, L.; Xu, A. *J. Med. Chem.* **2010**, *53*, 7613-7624.
- 40 Hackenberg, F.; Oehninger, L.; Alborzina, H.; Can, S.; Kitanovic, I.; Geldmacher, Y.; Kokoschka, M.; Wolfl, S.; Ott, I.; Sheldrick, W. S. *J. Inorg. Biochem.* **2011**, *105*, 991-999.
- 41 Geldmacher, Y.; Rubbiani, R.; Wfelmeier, P.; Prokop, A.; Ott, I.; Sheldrick, W. S.; *J. Organomet. Chem.* **2011**, *696*, 1023-1031.
- 42 Bieda, R.; Ott, I.; Gust, R.; Sheldrick, W. S. *Eur. J. Inorg. Chem.* **2009**, *2009*, 3821-3831.

- 43 Bieda, R.; Ott, I.; Dobroschke, M.; Prokop, A.; Gust, R.; Sheldrick, W. S. *J. Inorg. Biochem.* **2009**, *103*, 698-708.
- 44 Scharwitz, M. A.; Ott, I.; Geldmacher, Y.; Gust, R.; Sheldrick, W. S. *J. Organomet. Chem.* **2008**, *693*, 2299-2309.
- 45 Dobroschke, M.; Geldmacher, Y.; Ott, I.; Harlos, M.; Kater, L.; Wagner, L.; Gust, R.; Sheldrick, W. S.; Prokop, A. *ChemMedChem* **2009**, *4*, 177-187.
- 46 Noffke, A. L.; Habtemariam, A.; Pizarro, A. M.; Sadler, P. J. *Chem. Commun.* **2012**, *48*, 5219-5246.
- 47 Yan, Y. K.; Melchart, M.; Habtemariam, A.; Sadler, P. J. *Chem. Commun.* **2005**, *38*, 4764-4776.
- 48 Morris, R. E.; Aird, R. E.; Murdoch, P. del S.; Chen, H.; Cummings, J.; Hughes, N. D.; Parsons, S.; Parkin, A.; Boyd, G.; Jodrell, D. I.; Sadler, P. J. *J. Med. Chem.* **2001**, *44*, 3616-3621.
- 49 Aird, R. E.; Cummings, J.; Ritchie, A. A.; Muir, M.; Morris, R. E.; Chen, H.; Sadler, P. J.; Jodrell, D. I. *Br. J. Cancer* **2002**, *86*, 1652-1657.
- 50 Chen, H.; Parkinson, J. A.; Morris, R. E.; Sadler, P. J. *J. Am. Chem. Soc.* **2003**, *125*, 173-186.
- 51 Wang, F.; Bella, J.; Parkinson, J. A.; Sadler, P. J. *J. Biol. Inorg. Chem.* **2005**, *10*, 147-155.
- 52 Novakova, O.; Chen, H.; Vrana, O.; Rodger, A.; Sadler, P. J.; Brabec, V. *Biochemistry* **2003**, *42*, 11544-11554.

- 53 Hart, J. R.; Glebov, O.; Ernst, R. J.; Kirsch, I. R.; Barton, J. K. *Proc. Natl. Acad. Sci. U.S.A.* **2006**, *103*, 15359-15363.
- 54 Ernst, R. J.; Song, H.; Barton, J. K. *J. Am. Chem. Soc.* **2009**, *131*, 2359-2366.
- 55 Ernst, R. J.; Komor, A. C.; Barton, J. K. *Biochemistry* **2011**, *50*, 10919-10928.
- 56 Carethers, J. M.; Hawn, M. T.; Chauhan, D. P.; Luce, M. C.; Marra, G.; Koi, M.; Boland, C. R. *J. Clin. Invest.* **1996**, *98*, 199-206.
- 57 Robinson, J. W. *Anal. Chem.* **1960**, *32*, 17A-29A.
- 58 Robinson, J. W. *Anal. Chem.* **1961**, *33*, 1067-1071.
- 59 Brouwers, E. E. M.; Tibben, M.; Rosing, H.; Schellens, J. H. M.; Beijnen, J. H. *Mass Spec. Rev.* **2008**, *27*, 67-100.
- 60 Harrison, R. J. E. *Aust. J. Chem.* **2009**, *62*, 90-90.
- 61 Frenandez-Moreira, V.; Thorp-Greenwood, F. L.; Coogan, M. P. *Chem. Commun.* **2010**, *46*, 186-202.
- 62 Gately, D. P.; Howell, S. B. *Br. J. Cancer* **1993**, *67*, 1171-1176.
- 63 Timmer-Bosscha, H.; Mulder, N. H.; de Vries, E. G. E. *Br. J. Cancer* **1992**, *66*, 227-238.
- 64 Andrews, P. A.; Velury, S.; Mann, S. C.; Howell, S. B. *Cancer Res.* **1988**, *48*, 68-73.
- 65 Harlos, M.; Ott, I.; Gust, R.; Alborzina, H.; Wolfl, S.; Kromm, A.; Sheldrick, W. *S. J. Med. Chem.* **2008**, *51*, 3924-3933.

- 66 Burgarcic, T.; Novakova, O.; Halamikova, A.; Zerzankova, L.; Vrana, O.; Kasparikova, J.; Habtemariam, A.; Parsons, S.; Sadler, P. J.; Brabec, V. J. *J. Med. Chem.* **2008**, *51*, 5310-5319.
- 67 Louie, M-W.; Choi, A. W-T.; Liu, H-W.; Chan, B. T-N.; Lo, K. K-W. *Organometallics* **2012**, *31*, 5844-5855.
- 68 Puckett, C. A.; Ernst, R. J.; Barton, J. K. *Dalton Trans.* **2010**, *39*, 1159-1170.
- 69 Aderem, A.; Underhill, D. M. *Annu. Rev. Immunol.* **1999**, *17*, 593-623.
- 70 Doherty, G. J.; McMahon, H. T. *Annu. Rev. Biochem.* **2009**, *78*, 857-902.
- 71 Conner, S. D.; Schmid, S. L. *Nature* **2003**, *422*, 37-44.
- 72 Paulsen, I. T. *Curr. Op. Microbiol.* **2003**, *6*, 446-451.
- 73 Schinkel, A. H.; Jonker, J. W. *Adv. Drug Deliv. Rev.* **2003**, *55*, 3-29.
- 74 Neyfakh, A. A. *Mol. Microbiol.* **2002**, *44*, 1123-1130.
- 75 Barban, S.; Schulze, H. *J. Biol. Chem.* **1961**, *236*, 1887-1890.
- 76 Slater, C. *Methods Enzymol.* **1967**, *10*, 48-57.
- 77 Shapiro, H. M. *Methods* **2000**, *21*, 271-279.
- 78 Mizuno, N.; Sugiyama, Y. *Drug Metabol. Pharmacokin.* **2002**, *17*, 93-108.
- 79 Steinman, R. M.; Mellman, I. S.; Muller, W. A.; Cohn, Z. A. *J. Cell Biol.* **1983**, *96*, 1-27.
- 80 Cooper, A.; Shaul, Y. *J. Biol. Chem.* **2006**, *281*, 16563-16569.
- 81 Smart, J.; Anderson, R. G. *Methods Enzymol.* **2002**, *353*, 131-139.
- 82 West, M. A.; Bretscher, M. S.; Watts, C. *J. Cell. Biol.* **1989**, *109*, 2731-2739.
- 83 Binks, S. P.; Dobrota, M. *Biochem. Pharmacol.* **1990**, *40*, 1329-1336.

- 84 Arnesano, F.; Natile, G. *Coord. Chem. Rev.* **2009**, *253*, 2070-2081.
- 85 Holzer, A. K.; Samimi, G.; Katano, K.; Naerdemann, W.; Lin, X.; Safaei, R.; Howell, S. B. *Mol. Pharmacol.* **2004**, *66*, 817-823.
- 86 Puckett, C. A.; Barton, J. K. *Biochemistry* **2008**, *47*, 11711-11716.
- 87 Pisani, M. J.; Fromm, P. D.; Mulyana, Y.; Clarke, R. J.; Korner, H.; Heimann, K.; Collins, J. G.; Keene, F. R. *ChemMedChem* **2011**, *6*, 848-858.
- 88 Matson, M.; Svensson, F. R.; Norden, B.; Lincoln, P. *J. Phys. Chem. B.*, **2011**, *115*, 1706-1711.
- 89 Friedman, A. E.; Chambron, J-C.; Sauvage, J-P.; Turro, N. J.; Barton, J. K. *J. Am. Chem. Soc.* **1990**, *112*, 4960-4962.
- 90 Groessl, M.; Zava, O.; Dyson, P. J. *Metallomics* **2011**, *3*, 591-599.
- 91 Hoenger, A.; McIntosh, J. R. *Curr. Op. Cell Biol.* **2009**, *21*, 89-96.
- 92 Van Rijt, S. H.; Mukherjee, A.; Pizarro, A. M.; Sadler, P. J. *J. Med. Chem.* **2010**, *53*, 840-849.
- 93 Thomas, P. J.; Midgley, P. A. *Top. Catal.* **2002**, *21*, 109-138.
- 94 Werner, H. W. *Surf. Interface Anal.* **2003**, *35*, 859-879.
- 95 Wedlock, L. E.; Kilburn, M. R.; Cliff, J. B.; Filgueira, L.; Saunders, M.; Berners-Price, S. J. *Metallomics* **2011**, *3*, 917-925.
- 96 Gorlich, D.; Mattaj, I. W. *Science* **1996**, *271*, 1513-1518.
- 97 Kirin, S. I.; Ott, I.; Gust, R.; Mier, W.; Weyhermuller, T.; Metzler-Nolte, N. *Angew. Chem. Int. Ed.* **2008**, *47*, 955-959.
- 98 Brunner, J.; Barton, J. K. *Biochemistry* **2006**, *45*, 12295-12302.

- 99 Puckett, C. A.; Barton, J. K. *J. Am. Chem. Soc.* **2009**, *131*, 8738-8739.
- 100 Wang, D.; Lippard, S. J. *Nat. Rev. Drug Discovery* **2005**, *4*, 307-317.
- 101 Decatris, M. P.; Sundar, S.; O'Byrne, K. J. *Cancer Treat. Rev.* **2004**, *30*, 53-81.
- 102 Ang, W. H.; Dyson, P. J. *Eur. J. Inorg. Chem.* **2006**, *2006*, 4003-4018.
- 103 Beltran, B.; Casado, P.; Rodríguez-Prados, J-C.; Cutillas, P. R. *J. Proteomics* **2012**, *77*, 492-503.
- 104 Feng, L. *et al.*, *J. Am. Chem. Soc.* **2011**, *133*, 5976-5986.
- 105 Kunick, C.; Ott, I. *Angew. Chem. Int. Ed.* **2010**, *49*, 5226-5227.
- 106 Koblinski, J. E.; Ahram, M.; Sloane, B. F. *Clin. Chim. Acta.* **2000**, *291*, 113-135.
- 107 Meggers, E. *Chem. Commun.* **2009**, *9*, 1001-1010.
- 108 Casini, A. *et al.*, *J. Med. Chem.* **2008**, *51*, 6773-6781.
- 109 Guidi, F. *et al.*, *J. Inorg. Biochem.* **2013**, *118*, 94-99.
- 110 Holst, F. *et al.*, *Nat. Genet.* **2007**, *39*, 655-660.
- 111 Vessières, A.; Top, S.; Beck, W.; Hillard, E.; Jaouen, G. *Dalton Trans.* **2006**, *4*, 529-541.
- 112 Pigeon, P.; Top, S.; Vessières, A.; Huché, M.; Hillard, E.; Salomon, E.; Jaouen, G. *J. Med. Chem.* **2005**, *48*, 2814-2821.
- 113 Gogvadze, V.; Orrenius, W.; Zhivotovsky, B. *Trends Cell Biol.* **2008**, *18*, 166-173.
- 114 Wisnovsky, S. P.; Wilson, J. J.; Radford, R. J.; Pereira, M. P.; Laposa, R. R.; Lippard, S. J.; Kelley, S. O. *Chem. Biol.* **2013**, *20*, 1323-1328.
- 115 Loeb, L. A. *Cancer Res.* **2001**, *61*, 3230-3239.

- 116 Bhattacharya, N. P.; Skandalis, A.; Ganesh, A.; Groden, J.; Meuth, M. *Proc. Natl. Acad. Sci. U.S.A.* **1994**, *91*, 6319-6323.
- 117 Iyer, R. R.; Pluciennik, A.; Burdett, V.; Modrich, P. L. *Chem. Rev.* **2006**, *106*, 302-323.
- 118 Carethers, J. M.; Hawn, M. T.; Chauhan, D. P.; Luce, M. C.; Marra, G.; Koi, M.; Boland, C. R. *J. Clin. Invest.* **1996**, *98*, 199-206.

Chapter 2: Selective Cytotoxicity of Rhodium Metalloinsertors in Mismatch Repair-Deficient Cells[‡]

2.1 Introduction

The cell has evolved a complex replication mechanism containing multiple checkpoints in order to minimize the incorporation of errors during replication and correct errors that result from chemical damage to DNA after replication.¹ Left uncorrected, these DNA defects will lead to mutations in subsequent rounds of replication.^{2,3} The mismatch repair (MMR) pathway provides one such checkpoint and increases the fidelity of DNA replication ~1000-fold.⁴ Not surprisingly, defects in this pathway have been associated with several types of cancer. For example, about 18% of solid tumors and 15% of sporadic colorectal cancer cases have been found to exhibit MMR deficiencies.^{5,6} Furthermore, many commonly used chemotherapeutics, such as cisplatin, DNA alkylating agents, and anti-metabolites, have decreased effectiveness against MMR-deficient cancer cells.⁷ In fact, repeated chemotherapeutic treatments with these agents enrich tumors with MMR-deficient cells.^{8,9} Undeniably, then, the synthesis and study of small molecules that possess the ability to specifically target DNA defects may afford progress in the development of new cancer diagnostics and therapeutics that are specific for MMR-deficient cancers.

The Barton laboratory has previously developed a class of compounds, called rhodium metalloinsertors (**Figure 2.1**), that target DNA mismatches *in vitro* with high specificity and affinity.¹⁰ The first generation compound, $[\text{Rh}(\text{bpy})_2(\text{chrysi})]^{3+}$ (chrysi =

[‡] Adapted with permission from Ernst, R. J.; Komor, A.C.; Barton, J. K. Selective Cytotoxicity of Rhodium Metalloinsertors in Mismatch Repair-Deficient Cells. *Biochemistry* **2011**, *50*, 10919-10928. © 2011 ACS. *Acknowledgements*: Russell Ernst performed the flow cytometry experiments; I assisted with all metalloinsertor synthesis and all cell culture assays.

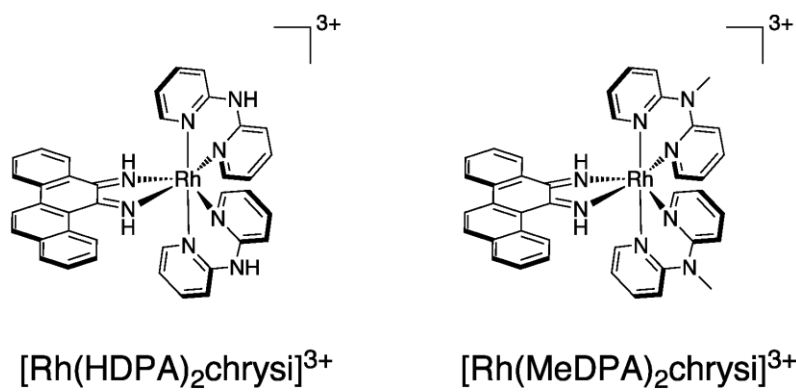


Figure 2.1 Chemical structures of rhodium metalloinsertors $[\text{Rh}(\text{HDPA})_2\text{chrysi}]^{3+}$ and $[\text{Rh}(\text{MeDPA})_2\text{chrysi}]^{3+}$.

chrysen-5,6-quinonediimine), binds 80% of DNA mismatches in all sequence contexts and preferentially targets thermodynamically destabilized mismatches over matched base pairs by a factor of over 1000.¹¹ Specifically, it has been shown to bind only at the single mismatch site in a 2725 base-pair plasmid.¹² Additional work focused on incorporating nitrogen atoms into the intercalating ligand in order to increase π -stacking stabilization and led to the development of the second generation compound, $[\text{Rh}(\text{bpy})_2(\text{phzi})]^{3+}$ (phzi = benzo [*a*] phenazine-5,6-quinonediimine). This complex exhibits a 50-fold increase in binding affinity compared to $[\text{Rh}(\text{bpy})_2(\text{chrysi})]^{3+}$ without a loss in selectivity, allowing for mismatch detection at nanomolar Rh concentrations.¹³ The binding mode of these mismatch-specific complexes was determined through the 1.1 Å resolution crystal structure of $[\text{Rh}(\text{bpy})_2(\text{chrysi})]^{3+}$ bound to an AC mismatch. The structure revealed the chrysi ligand to insert from the minor groove with ejection of both mismatched bases.¹⁴ NMR studies of $[\text{Rh}(\text{bpy})_2(\text{chrysi})]^{3+}$ bound to a CC mismatch further confirmed this binding mode for the complex at mismatched sites in solution.¹⁵ Additional crystal structures of the Rh complex bound to different mismatches¹⁶ as well as of a Ru complex bound by insertion to a mismatched site¹⁷ established the generality of metalloinsertion. It is noteworthy that these studies represented the first illustration of the insertion binding mode, originally proposed by L. S. Lerman in the early 1960's.¹⁸

Confocal microscopy and flow cytometry studies with $[\text{Ru}(\text{L})_2\text{dppz}]^{2+}$ (dppz=dipyrido[3,2-*a*:2',3'-*c*]phenazine) analogues have demonstrated that cellular accumulation occurs through passive diffusion, facilitated by the negative potential difference across the cell membrane.^{19,20} Taken together, the observations that (i) rhodium metalloinsertors are capable of recognizing mismatches with high selectivity and

(ii) analogous ruthenium complexes accumulate within cells and nuclei form a sound basis for the hypothesis that rhodium metalloinsertors recognize mismatched DNA within cells and predict that these complexes should selectively target MMR-deficient cells, which harbor ~1,000 fold more mismatches than MMR-proficient cells.

In an effort to characterize the *in cellulo* effects of these metalloinsertors, several cell assay experiments have been undertaken on the isogenic cell lines HCT116N and HCT116O. The HCT116 parent cell line is a human colorectal carcinoma line deficient in the *hMLH1* gene. This gene encodes for part of the mismatch repair (MMR) machinery; consequently, this cell line is MMR deficient. The HCT116N cell line has been transfected with human chromosome 3 (ch3), which restores MMR proficiency, while the HCT116O cell line has been transfected with human chromosome 2 (ch2), leaving it MMR deficient.²¹ These rhodium metalloinsertors have been found to selectively inhibit DNA synthesis in the MMR-deficient HCT116O cell line over the MMR-proficient HCT116N cell line,²² as measured by an ELISA assay for DNA synthesis.²³ Significantly, the binding affinities of the metalloinsertors were found to correlate directly with the selectivity of the rhodium complexes for the MMR-deficient cell line, lending credence to the idea that these complexes target DNA mismatches *in cellulo* as well as in the test tube.²⁴

However, the proliferation assay does not distinguish between senescence and cell death, and therefore is insufficient to demonstrate cytotoxicity. Here, we show that rhodium metalloinsertors are preferentially cytotoxic to the MMR-deficient HCT116O cell line. This rhodium-induced death is shown to be necrotic rather than apoptotic, and is preceded by cell cycle arrest at the G1/S-phase boundary. This observation is

consistent with activation of the DNA damage response by rhodium metalloinsertors.

2.2 Experimental Protocols

2.2.1 Materials

RhCl_3 was purchased from Pressure Chemical, Inc. (Pittsburgh, PA). $[\text{Rh}(\text{NH}_3)_5\text{Cl}]\text{Cl}_2$ was obtained from Strem Chemical, Inc. (Newburyport, MA). 2,2'-dipyridylamine (HDPA) and Sephadex ion exchange resin were obtained from Sigma-Aldrich (St. Louis, MO). Sep-Pak C_{18} solid phase extraction cartridges were purchased from Waters Chemical Co. (Milford, MA). Media and supplements were purchased from Invitrogen (Carlsbad, CA). The 3-[4,5-dimethylthiazol-2-yl]-2,5-diphenyl tetrazolium bromide (MTT) labeling reagent and acidified lysis buffer (10% SDS in 10 mM HCl) were purchased in kit format from Roche Molecular Biochemicals (Mannheim, Germany). Z-VAD-FMK caspase inhibitor was purchased from Promega. All PARP inhibitors were purchased from Santa Cruz Biotechnology, Inc. All commercial materials were used as received.

2.2.2 Synthesis of Metal Complexes

2.2.2.1 $[\text{Rh}(\text{NH}_3)_6][\text{OTf}]_3$

$[\text{Rh}(\text{NH}_3)_6][\text{OTf}]_3$ was prepared according to an adaptation of previously described procedures.^{25,26} A 100 mL schlenk flask was charged with $[\text{Rh}(\text{NH}_3)_5\text{Cl}]\text{Cl}_2$ (2.045 g, 7.0 mmol) and put under an Ar atmosphere. HOTf (10 g, 66.6 mmol) was added to the tan solid, and the resulting orange solution was purged with Ar for 1 m, then heated to 100° C for 2 h. Et_2O (40 mL) at -78° C was poured onto the red solution, and the resulting orange precipitate was collected on a medium frit. The collected precipitate was transferred to a 250 mL oven-dried schlenk flask and cooled to -78° C in a dry ice/acetone

bath. The flask was evacuated and refilled with $\text{NH}_3(\text{g})$, which condensed in the flask to afford a deep orange solution, which was stirred at -78°C . After 15 m, the flask was disconnected from the $\text{NH}_3(\text{g})$ tank, opened up to the atmosphere, and allowed to warm to ambient temperature. The resulting yellow solid was crystallized from water (20 mL) to afford colorless crystals. Yield: 3.166 g, 71.5 %. ^1H NMR (300 MHz, d_6 -DMSO): δ 3.62 (s, 18H). ESI-MS (cation): m/z calc. 503.0 (M-OTf⁺), obs. 502.7.

2.2.2.2 $[\text{Rh}(\text{NH}_3)_4(\text{chrysi})]\text{Cl}_3$

$[\text{Rh}(\text{NH}_3)_4(\text{chrysi})]^{3+}$ was prepared according to an adaptation of previously described procedures.²⁴ $[\text{Rh}(\text{NH}_3)_6][\text{OTf}]_3$ (0.50 g, 0.77 mmol) and chrysene-5,6-dione (0.200 g, 0.77 mmol) were dissolved in a 1:9 mixture of water:acetonitrile (500 mL). A 1M solution of NaOH (3 mL) was added to the orange solution, and the reaction was allowed to stir at ambient temperature for 3 h, at which time a 1M solution of HCl (3 mL) was added to neutralize the reaction mixture. The acetonitrile was evaporated *in vacuo*, and the resulting red solution was loaded onto a SPE cartridge, eluted with 25% acetonitrile in 0.1% TFA_(aq), and lyophilized to give a red solid. The chloride salt can be obtained from a Sephadex QAE anion exchange column equilibrated with 0.1M MgCl_2 . Yield: 0.072 g, 18%. ^1H NMR (300 MHz, d_6 -DMSO): δ 13.46 (s, 1H); 12.33 (s, 1H); 8.90 (t, $J = 8.0$ Hz, 1 H); 8.72 (d, $J = 8.4$ Hz, 1H); 8.51 (m, 2H); 8.38 (d, $J = 8.6$ Hz, 1H); 8.17 (t, $J = 6.8$ Hz, 1 H); 7.71-7.90 (m, 4H); 4.68 (br s, 3H); 4.53 (br s, 3H); 3.98 (br s, 6H). ESI-MS (cation): m/z calc. 522.07 (M-NH₃-H+TFA⁺), obs. 522.1. UV-Vis (H_2O , pH 7): 260 nm (60,900 $\text{M}^{-1} \text{cm}^{-1}$), 325 nm (12,600 $\text{M}^{-1} \text{cm}^{-1}$), 410 nm (12,000 $\text{M}^{-1} \text{cm}^{-1}$).

2.2.2.3 N-methyl-N-(pyridin-2-yl)pyridin-2-amine (MeDPA)

To a slurry of sodium hydride (70 mg, 2.9 mmol) in THF (10 ml) was added HDPa (500 mg, 2.9 mmol) in 5 ml THF at 0 °C under 1 atm Ar. The reaction was purged with argon for 15 min, and the appropriate 1-bromoalkane (3.8 mmol) was added dropwise and warmed to ambient temperature. The reaction was stirred an additional 18 h under argon at reflux temperature. The reaction mixture was extracted with dilute sodium bicarbonate, and the aqueous phase was extracted with CH₂Cl₂ (3 x 40 ml). The organic fractions were combined and dried over magnesium sulfate, and the solvent was removed *in vacuo*. These ligands were purified via flash chromatography (SiO₂, 1:9 EtOAc:hexanes). Yield: 23%. ¹H-NMR (CDCl₃, 300 MHz): δ 8.35 (d, *J* = 5.0 Hz, 2H); 7.53 (m, 2H); 7.17 (d, *J* = 8.4 Hz, 2H); 6.86 (m, 2H); 3.62 (s, 3H). ESI-MS (cation): *m/z* calc. 186.1 (M+H⁺), obs. 186.

2.2.2.4 [Rh(XDPA)₂(chrysi)]Cl₃ (X=H, Me)

[Rh(XDPA)₂chrysi]Cl₃ was prepared according to an adaptation of previously described procedures.²⁴ A 500 mL round bottomed flask was charged with [Rh(NH₃)₄(chrysi)]Cl₃ (80.5 mg, 0.15 mmol) and XDPA (0.4 mmol), and 1:1 EtOH:H₂O (250 mL) was added. The resulting red solution was allowed to reflux overnight after which time the solvent was removed *in vacuo*. The red solid was redissolved in H₂O (10 mL), filtered, and purified via flash chromatography (C₁₈-SiO₂, 17:3 0.1% TFA (aq): MeCN). The chloride salt can be obtained from a Sephadex QAE anion exchange column equilibrated with 0.1M MgCl₂.

[Rh(HDPA)₂(chrysi)]Cl₃: Yield: 74.0 mg, 61%. ESI-MS (cation): *m/z* calc. 699.2 (M-2H⁺), 350.1 (M-H²⁺), obs. 699.1, 350.3. ¹H NMR (300 MHz, (CD₃)₂SO): δ 12.84 (s,

1H); 12.34 (s, 1H); 11.78 (s, 1H); 10.32 (d, $J = 8.7$ Hz, 1H); 8.63 (d, $J = 6.9$ Hz, 1H); 8.40 (d, $J = 8.4$ Hz, 1H); 8.31 (d, $J = 9.3$ Hz, 1H); 8.14 (m, 2H); 8.07 (d, $J = 8.7$ Hz, 1H); 8.04 (d, $J = 5.4$ Hz, 1H); 7.94 (m, 4H); 7.77 (m, 5H); 7.58 (m, 2H); 7.48 (d, $J = 8.1$ Hz, 1H); 7.41 (d, $J = 8.4$ Hz, 1H); 7.32 (s, 1H); 7.14 (m, 2H); 7.04 (t, $J = 6.8$ Hz, 1H); 6.98 (t, $J = 6.9$ Hz, 1H); 6.81 (t, $J = 6.5$ Hz, 1H). UV-Vis (H₂O, pH 7): 290 nm (42,200 M⁻¹ cm⁻¹), 320 nm (23,000 M⁻¹ cm⁻¹), 440 nm (8,800 M⁻¹ cm⁻¹).

[Rh(MeDPA)₂chrysi]Cl₃: Yield: 0.103 g, 84%. ¹H NMR (500 MHz, CD₃CN): δ 14.39 (s, 1H); 10.66 (d, $J = 8.8$ Hz, 1H); 9.56 (d, $J = 7.9$ Hz, 1H); 9.30 (d, $J = 6.0$ Hz, 1H); 8.14-8.21 (m, 3H); 8.16 (t, $J = 7.2$ Hz, 1H); 8.02 (d, $J = 8.8$ Hz, 1H); 7.87-7.93 (m, 4H); 7.85 (d, $J = 8.0$ Hz, 1H); 7.77 (d, $J = 8.6$ Hz, 1H); 7.67-7.74 (m, 2H); 7.60 (m, 2H), 7.50 (m, 2H); 7.35 (d, $J = 8.4$ Hz, 1H); 7.15 (t, $J = 5.7$ Hz, 1H); 7.06-7.11 (m, 3H); 6.92 (t, $J = 6.0$ Hz, 1H); 4.07 (s, 3H); 3.82 (s, 3H). ESI-MS (cation): m/z calc. 727.2 (M-2H⁺), 364.1 (M-H²⁺), obs. 727.1, 364.3. UV-Vis (H₂O, pH 7): 295 nm (55,000 M⁻¹ cm⁻¹), 320 nm (39,700 M⁻¹ cm⁻¹), 390 nm (14,000 M⁻¹ cm⁻¹).

2.2.3 Cell Culture

HCT116N and HCT116O cells were grown in RPMI medium 1640 supplemented with: 10% FBS; 2 mM L-glutamine; 0.1 mM nonessential amino acids; 1 mM sodium pyruvate; 100 units/mL penicillin; 100 μ g/mL streptomycin; and 400 μ g/mL geneticin (G418). Cells were grown in tissue culture flasks and dishes (Corning Costar, Acton, MA) at 37°C under 5% CO₂ and humidified atmosphere.

2.2.3.1 ICP-MS Assay for Cellular Rhodium Levels

Each cell line was treated with 10 μ M of [Rh(bpy)₂chrysi]³⁺, [Rh(HDPA)₂chrysi]³⁺, or [Rh(NH₃)₄chrysi]³⁺ for 48 hours. After rhodium incubation, the

cells were harvested from adherent culture by trypsinization, washed with cold PBS, and counted by hemacytometer. The samples were pelleted and resuspended in 1% HNO₃ (v/v), homogenized by three freeze/thaw cycles in liquid nitrogen, and analyzed for rhodium content on an HP-4500 ICP-MS unit. Rhodium counts were normalized to the number of cells counted in each sample before lysate preparation. Standard errors for three independent experiments are shown.

2.2.3.2 Cellular Proliferation ELISA

HCT116N and HCT116O cells were plated in 96-well plates at 2,000 cells/well and allowed 24 hours to adhere. The cells were then incubated with rhodium for the durations specified. For incubation less than 72 hours, the Rh-containing media was replaced with fresh media, and the cells were grown for the remainder of the 72-hour period. Cells were labeled with BrdU 24 hours before analysis. The BrdU incorporation was quantified by antibody assay according to established procedures.^{23,27} Cellular proliferation was expressed as the ratio of the amount of BrdU incorporated by the treated cells to that of the untreated cells.

2.2.3.3 MTT Cytotoxicity Assay

Cytotoxicity assays were performed as described in the literature.²⁸ HCT116N and HCT116O cells were plated in 96-well plates at 50,000 cells/well and incubated with rhodium for the durations specified. After rhodium incubation, cells were labeled with MTT for 4 hours at 37°C under 5% CO₂ and humidified atmosphere. The resulting formazan crystals were dissolved with solubilizing reagent (purchased from Roche) according to the manufacturer's instructions. The dissolved formazan was quantified as the absorbance at 570 nm minus the background absorbance at 690 nm. Percent viability

was determined as the ratio of the amount of formazan in the treated cells to that of the untreated cells. For caspase inhibition assays, Z-VAD-FMK was added to a final concentration of 20 μ M. For poly-ADP ribose polymerase (PARP) assays, the inhibitor 3,4-Dihydro-5[4-(1-piperindinyl)butoxy]-1(2H)-isoquinoline (DPQ) was added to a final concentration of 0, 25, or 50 μ M; the inhibitor 3-aminobenzamide (3-AB) was added to a final concentration of 0, 2, or 3 mM; the inhibitor 4-amino-1,8-naphthalimide (4-AN) was added to a final concentration of 0, 10, or 20 μ M; and the inhibitor 2-((*R*)-2-Methylpyrrolidin-2-yl)-1*H*-benzimidazole-4-carboxamide (ABT-888) was added to a final concentration of 0, 5, or 10 μ M.

2.2.4 Cell Cycle Distribution Flow Cytometry Assay

Cells were harvested from adherent culture by trypsinization and washed with cold PBS. The resultant pellet was resuspended in PBS (chilled to 4 °C), and ice-cold ethanol was added dropwise to a final concentration of 70% (v/v), with continuous gentle agitation. Cells were fixed at 4°C for 30 minutes and stored for up to one week. Prior to analysis, the fixed cells in 70% ethanol were diluted 1:3 in cold PBS and centrifuged at 1,400 x g for 5 minutes. The resultant pellet was washed twice and resuspended in ice-cold PBS. Ribonuclease was added to a final concentration of 30 μ g/mL and the cells were incubated overnight at 4 °C. The next day propidium iodide was added to a final concentration of 20 μ g/mL and cells were analyzed by flow cytometry. Data analysis was performed using the FloJo software package (v 8.7.1).

2.2.5 Cell Death Mode Flow Cytometry Assay

Cell death was characterized by a dye exclusion assay.²⁹ After 24-, 48-, or 72-hour incubation with rhodium, cells were harvested from adherent culture by

trypsinization, washed with cold PBS, and centrifuged at 2,000 rpm for 5 minutes. The resultant pellets were resuspended in PBS to a concentration of 10^6 cells/mL and stained with propidium iodide to a final concentration of $1\mu\text{g/mL}$ and with YO-PRO-1 to a final concentration of 200 nM for 30 minutes prior to analysis by flow cytometry.

2.3 Results

2.3.1 ICP-MS of whole cell lysates

Each cell line was treated with $10\mu\text{M}$ of $[\text{Rh}(\text{bpy})_2\text{chrysi}]^{3+}$, $[\text{Rh}(\text{HDPA})_2\text{chrysi}]^{3+}$, or $[\text{Rh}(\text{NH}_3)_4\text{chrysi}]^{3+}$ for 48 hours. Whole cell lysates were analyzed for rhodium levels by ICP-MS (**Figure 2.2**). As expected, the HDPA complex exhibits a higher degree of cellular uptake than the other complexes. This supports the notion that the early activity displayed by the complex in the ELISA assay results from accelerated uptake.²⁴ It should be noted that these treatment conditions directly reflect those used previously.

2.3.2 MTT cytotoxicity assay

The cytotoxicities of $[\text{Rh}(\text{HDPA})_2\text{chrysi}]^{3+}$ and $[\text{Rh}(\text{MeDPA})_2\text{chrysi}]^{3+}$ were determined by MTT assay.²⁸ Briefly, reduction of the MTT reagent by mitochondrial enzymes leads to the production of formazan, which can then be dissolved in acidified SDS to produce a characteristic absorbance at 570 nm. This absorbance reflects the relative metabolic activity, which in turn reflects the percentage of viable cells in each sample. HCT116N and HCT116O cells were plated and treated with 0-25 μM of $[\text{Rh}(\text{bpy})_2\text{chrysi}]^{3+}$, $[\text{Rh}(\text{HDPA})_2\text{chrysi}]^{3+}$, or $[\text{Rh}(\text{MeDPA})_2\text{chrysi}]^{3+}$ for 48 or 72 hours. The results are shown in **Figure 2.3**. At 48 hours $[\text{Rh}(\text{HDPA})_2\text{chrysi}]^{3+}$ and $[\text{Rh}(\text{MeDPA})_2\text{chrysi}]^{3+}$ clearly display an enhanced toxicity in the MMR-deficient

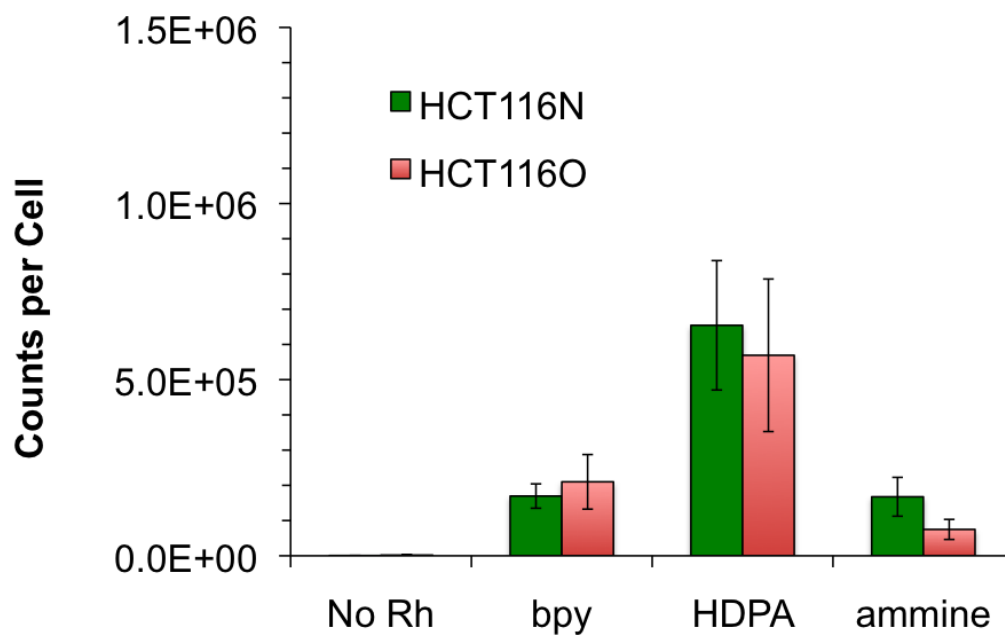


Figure 2.2 ICP-MS assay for rhodium accumulation. Normalized rhodium counts for whole cell lysates treated with 0 or 10 μM $[\text{Rh}(\text{bpy})_2\text{chrysi}]^{3+}$, $[\text{Rh}(\text{HDPA})_2\text{chrysi}]^{3+}$, or $[\text{Rh}(\text{NH}_3)_4\text{chrysi}]^{3+}$ for 48 hours. Standard error bars for three trials are shown. Cellular concentrations were determined by counting on hemacytometer prior to lysis. Rhodium counts were normalized to total cells per sample.

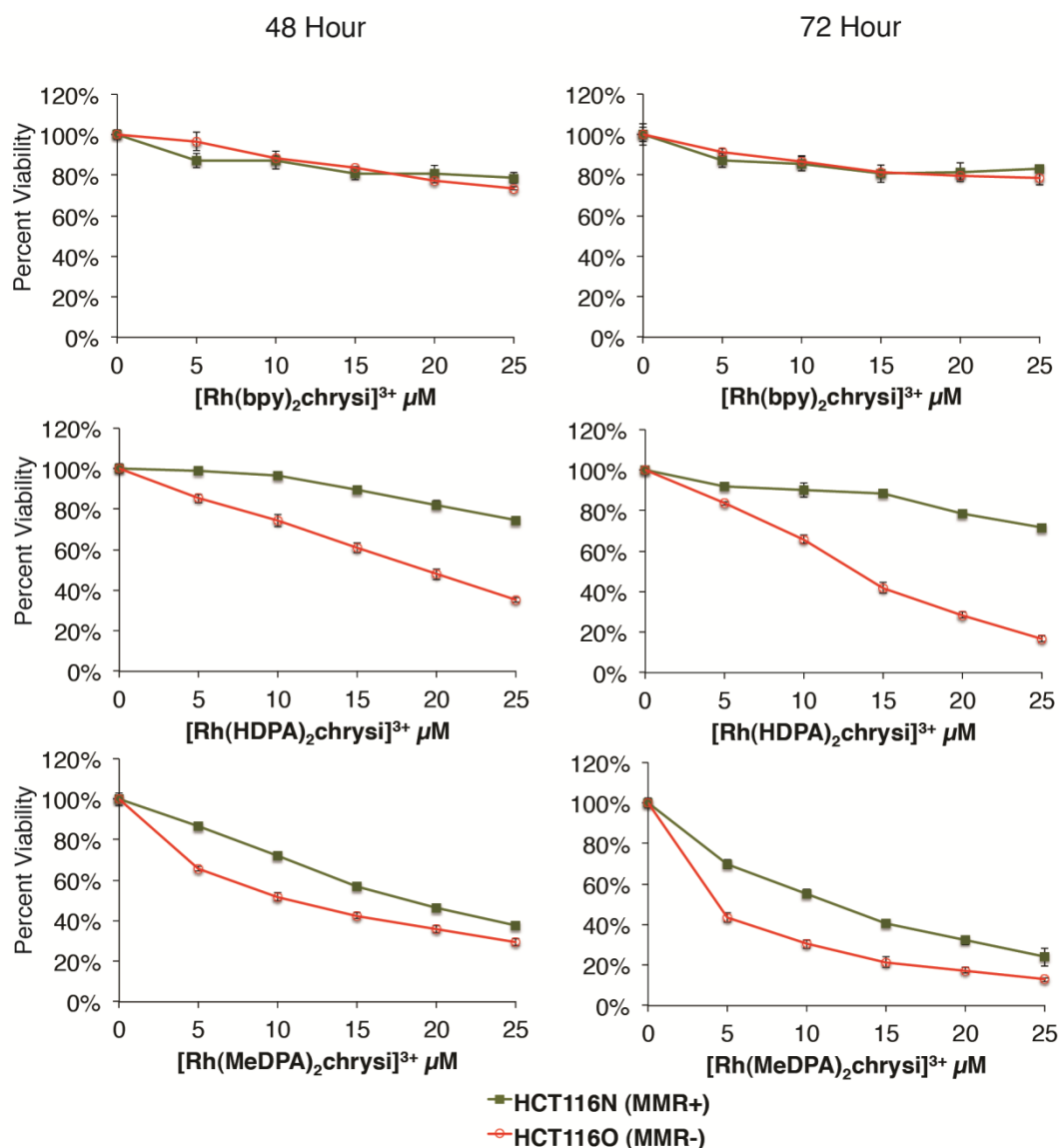


Figure 2.3 Selective toxicity of $[\text{Rh}(\text{HDPA})_2\text{chrysi}]^{3+}$ and $[\text{Rh}(\text{MeDPA})_2\text{chrysi}]^{3+}$ in MMR-deficient cells. HCT116N and HCT116O cells were plated in 96-well format at densities of 5×10^4 cells/well and treated with 0 – 25 μM of $[\text{Rh}(\text{bpy})_2\text{chrysi}]^{3+}$, $[\text{Rh}(\text{HDPA})_2\text{chrysi}]^{3+}$, or $[\text{Rh}(\text{MeDPA})_2\text{chrysi}]^{3+}$. After 48–72 hours, the cells were labeled with MTT for 4 hours. While the first generation complex $[\text{Rh}(\text{bpy})_2\text{chrysi}]^{3+}$ is non-toxic up to 72 hours, the dipyriddyamine derivatives $[\text{Rh}(\text{HDPA})_2\text{chrysi}]^{3+}$ and $[\text{Rh}(\text{MeDPA})_2\text{chrysi}]^{3+}$ exhibit toxicity specifically in the MMR-deficient HCT116O cell line at 48 hours.

HCT116O cell line versus the HCT116N cell line. For example, 72 hours after treatment with 20 μM $[\text{Rh}(\text{HDPA})_2\text{chrysi}]^{3+}$, the number of viable HCT116N cells is $80 \pm 5.2\%$ of untreated controls, whereas the number of viable HCT116O cells is $37 \pm 4.4\%$ of untreated controls. $[\text{Rh}(\text{MeDPA})_2\text{chrysi}]^{3+}$ also shows differential toxicity against the HCT116O cell line in this assay comparable to that of $[\text{Rh}(\text{HDPA})_2\text{chrysi}]^{3+}$.

2.3.3 Cell cycle distribution

Given the observation that the complexes inhibit DNA synthesis, a flow cytometry assay was performed to determine if the cytotoxicity of $[\text{Rh}(\text{HDPA})_2\text{chrysi}]^{3+}$ is accompanied by disruption of the cell cycle. MMR-proficient HCT116N and MMR-deficient HCT116O cells were treated with 20 μM $[\text{Rh}(\text{HDPA})_2\text{chrysi}]^{3+}$ for 24 or 48 h. After treatment, cells were stained with propidium iodide (PI) and analyzed by flow cytometry. The PI fluorescence reports the amount of DNA in each cell and follows a bimodal distribution, where the first peak contains cells with one copy of the genome, i.e., cells in G0/G1-phase, and the second peak contains cells with two copies of the genome, i.e., cells in G2- or M-phase. Cells in S-phase occupy the region between the two peaks. **Figure 2.4** shows these distributions for both cell lines, with or without rhodium treatment. In both cases, a decrease in the area under the curve between the peaks can be seen, indicating a depletion of the S-phase populations. Fitting the raw distributions to G1-, S-, or G2/M-phases confirms the depletion of the S-phase population, concomitant with an increase in the G1-phase population. Notably, at this concentration of $[\text{Rh}(\text{HDPA})_2\text{chrysi}]^{3+}$ large differentials in both the ELISA and MTT assay were observed. The changes to the cell cycle are more pronounced in the mismatch-repair-deficient HCT116O cell line, which continues to grow aggressively at 48 hours (> 50%

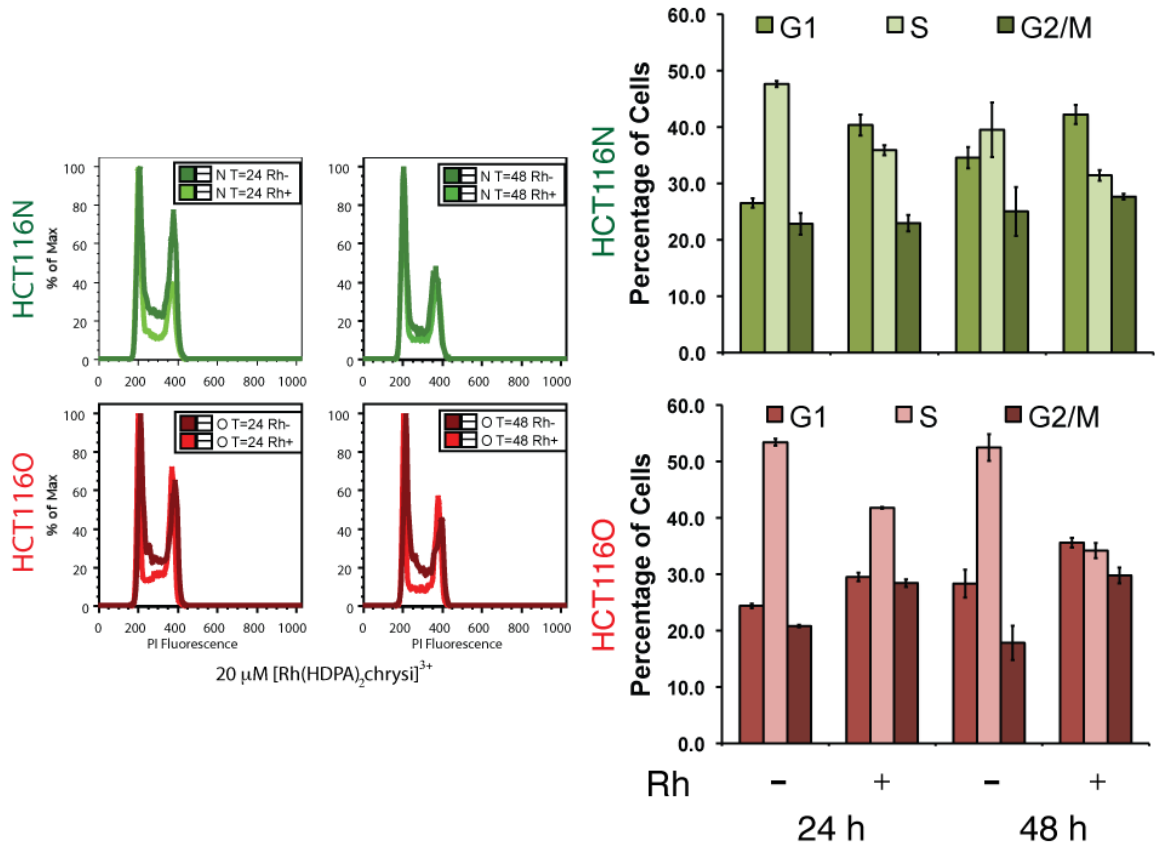


Figure 2.4 Cell cycle distribution assay. HCT116N (top) and HCT116O (bottom) cells were treated with $20 \mu\text{M}$ $[\text{Rh}(\text{HDPA})_2\text{chrysi}]^{3+}$ for 24 or 48 hours. After fixation and staining with PI, cells were analyzed by flow cytometry. The raw distributions were analyzed for cell cycle phase using commercially available software. Upon rhodium treatment, the S-phase population is depleted, with a concomitant increase in the G1-phase population.

S-phase) in the absence of rhodium treatment, whereas growth of the HCT116N cell line slows slightly as the density of the culture increases. Furthermore, the HCT116O cell line also shows a significant increase in the G2/M population as well as the G1 population.

2.3.4 Mode of cell death

To characterize the cell death occurring in response to rhodium treatment, a dye exclusion flow cytometry assay was employed.²⁹ The assay differentiates between live cells, dead cells, and cells undergoing apoptosis or necrosis through concurrent staining with propidium iodide (a dead-cell-permeable dye) and YO-PRO-1 (an apoptotic-cell-permeable dye). By plotting the fluorescence of the YO-PRO-1 channel against the PI channel, a pattern emerges. Healthy cells are seen in the lower lefthand corner of the plot. Apoptotic cells exhibit higher YO-PRO-1 fluorescence, but still exclude propidium iodide, placing them in the upper lefthand quadrant of the pattern. Dead cells admit both dyes and are therefore seen in the upper righthand quadrant of the image. Upon flow cytometry analysis, cells can be classified as live, apoptotic, necrotic, or dead by defining regions in the fluorescence plane corresponding to each category.

The HCT116N and HCT116O cell lines were incubated with 0–25 μM of $[\text{Rh}(\text{HDPA})_2\text{chrysi}]^{3+}$ for 24–72 hours. After harvesting the cells and staining with both PI and YO-PRO-1, the cells were analyzed by flow cytometry to obtain raw fluorescence data. Representative data for 20 μM rhodium treatment for 72 hours are shown in **Figure 2.5**. YO-PRO-1 fluorescence is shown on the y-axis, and PI fluorescence is shown on the x-axis. The color scale represents the number of cells, with blue indicating fewer cells at a given pair of fluorescence levels, and orange representing a greater number of cells at a given pair of fluorescence levels. The raw data were analyzed by gating the fluorescence

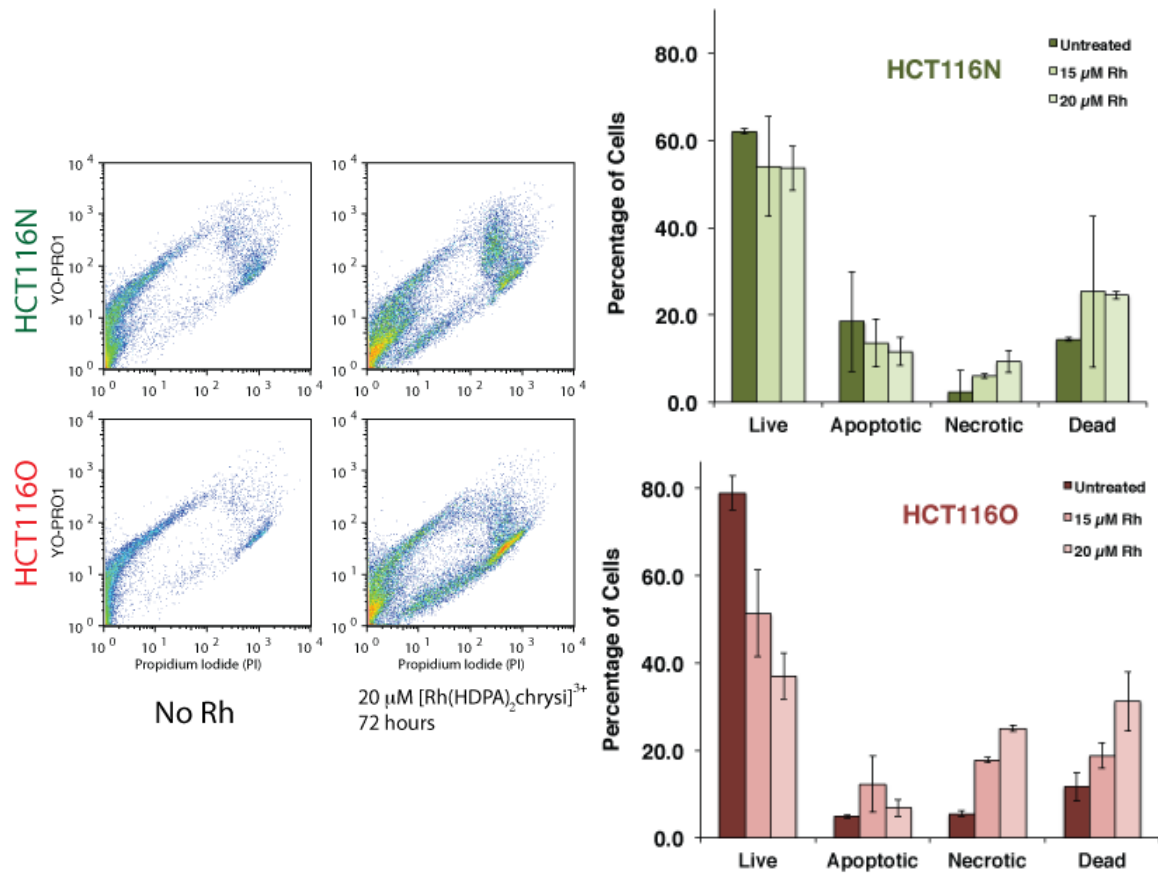


Figure 2.5 Flow cytometry assay of cell death. (Left) HCT116N and HCT116O cells were treated with 20 μM $[\text{Rh}(\text{HDPA})_2\text{chrysi}]^{3+}$ for 72 hours. Rhodium treatment causes cells to move away from the origin, along the necrotic pathway (lower branch of pattern). The effect is more pronounced in the HCT116O cell line. (Right) HCT116N and HCT116O cells were treated with 15 μM or 20 μM $[\text{Rh}(\text{HDPA})_2\text{chrysi}]^{3+}$ for 72 hours. Rhodium treatment causes a sharp decrease in the live population of the HCT116O cell line with a corresponding increase in the necrotic and dead cell populations. Minimal effect is seen in the HCT116N cell line. Thus, $[\text{Rh}(\text{HDPA})_2\text{chrysi}]^{3+}$ preferentially induces necrosis in the MMR-deficient HCT116O cell line.

events into one of four categories, depending on the fluorescence levels of the two dyes. **Figure 2.5** also shows histograms of live, apoptotic, necrotic, and dead cells for the HCT116N and HCT116O cell lines based on the flow cytometry. Rhodium treatment was either 15 or 20 μM $[\text{Rh}(\text{HDPa})_2\text{chrysi}]^{3+}$ for 72 hours. As before, rhodium treatment alone induces necrosis preferentially in the MMR-deficient HCT116O cell line; there is no significant change in the percentage of cells in the apoptotic region in either cell line. The effect is significantly more pronounced in the MMR-deficient HCT116O cell line, which drops from $79 \pm 3.8 \%$ to $37 \pm 5.3 \%$ after treatment with 20 μM $[\text{Rh}(\text{HDPa})_2\text{chrysi}]^{3+}$, versus the MMR-proficient HCT116N cell line, which shows a minimal decrease in live cells from $62 \pm 0.6 \%$ to $54 \pm 5.1 \%$ after treatment with 20 μM $[\text{Rh}(\text{HDPa})_2\text{chrysi}]^{3+}$.

2.3.5 Caspase inhibition

As a complement to the dye exclusion flow cytometry assay, the MTT cytotoxicity assay was repeated in the absence and presence of the pan-caspase inhibitor Z-VAD-FMK.³⁰ This inhibitor works by irreversibly binding to the active site of caspases. As before, the HCT116N and HCT116O cell lines were treated with 0 – 30 μM of the $[\text{Rh}(\text{HDPa})_2\text{chrysi}]^{3+}$ complex for 24 – 72 hours. In addition, each treatment was also combined with the inhibitor at a final concentration of 20 μM (**Figure 2.6**). As before, the rhodium complex exhibited selective toxicity in the repair-deficient HCT116O cell line, with cell viability dropping to $9.7 \pm 4.4 \%$ after treatment with 30 μM metal complex for 72 hours, versus $63 \pm 5.7 \%$ viability in the repair-proficient HCT116N cell line. Addition of the caspase inhibitor at 20 μM offered no protection from rhodium to the HCT116N cell line ($63 \pm 5.7 \%$ without inhibitor, $52 \pm 9.8 \%$ with

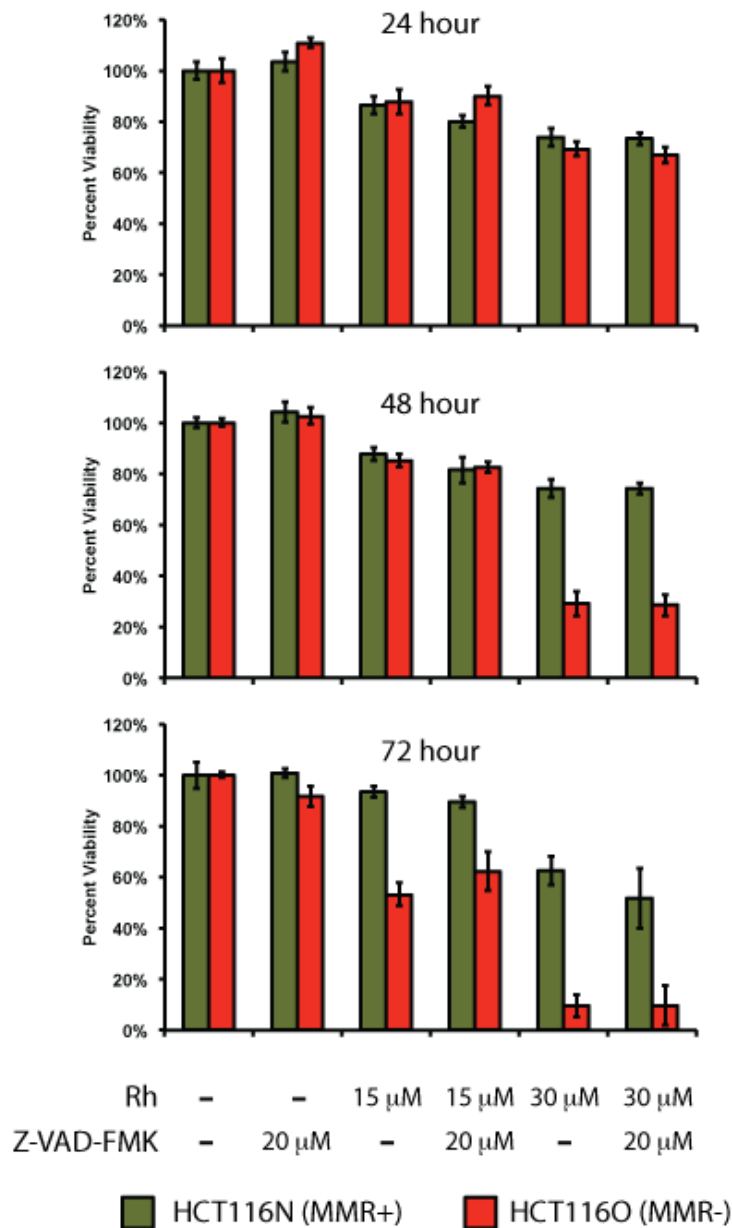


Figure 2.6 Caspase inhibition assay. HCT116N and HCT116O cells were plated in 96-well format at densities of 5×10^4 cells/well and treated with 0 – 30 μ M of $[\text{Rh}(\text{HDP A})_2\text{chrysi}]^{3+}$ with or without 20 μ M of the pan-caspase inhibitor Z-VAD-FMK. After 24 – 72 hours, the cells were labeled with MTT for 4 hours. The resulting formazan crystals were dissolved by addition of 10% SDS acidified with 10 mM HCl, and absorbance was measured at 570 nm. The caspase inhibitor confers no protection from rhodium-induced toxicity in either cell line.

inhibitor) or to the HCT116O cell line (9.7 ± 4.4 % without inhibitor, 9.8 ± 7.8 % with inhibitor). At a final concentration of 40 μ M, the caspase inhibitor provided some protection from rhodium to the HCT116O cell line (16 ± 10 % without inhibitor, 28 ± 3.7 % with inhibitor), but this difference was small in relation to the differential between the HCT116N and HCT116O cell lines and roughly within error (data not shown).

2.3.6 PARP inhibition

The MTT cytotoxicity assay was also repeated in conjunction with a panel of poly-ADP ribose polymerase (PARP) inhibitors: DPQ, 3-AB, 4-AN, and ABT-888.³¹⁻³⁴ As before, the HCT116N and HCT116O cell lines were treated with 0 or 20 μ M of the $[\text{Rh}(\text{HDPA})_2\text{chrysi}]^{3+}$ complex for 72 hours, with or without one of the four inhibitors. In each case, treatment with the inhibitor completely abolished the selective MMR-dependent effects of the rhodium compound (**Figure 2.7**), as determined by the difference between the percentage of viable cells in the HCT116N cell line and the percentage of viable cells in the HCT116O cell line. For example, in the case of the compound DPQ, this difference was 43 ± 2.7 % without inhibitor and 0.6 ± 3.0 % with inhibitor. Similar results are seen with each of the other three compounds as well; taken together, these data implicate PARP in the MMR-dependent response to $[\text{Rh}(\text{HDPA})_2\text{chrysi}]^{3+}$.

2.4 Discussion

2.4.1 Uptake

The direct correlation between the binding affinity of rhodium metalloinsertors for DNA mismatches and the differential in their activity between the HCT116N and HCT116O cell lines fails to predict the high selective activity of $[\text{Rh}(\text{HDPA})_2\text{chrysi}]^{3+}$.

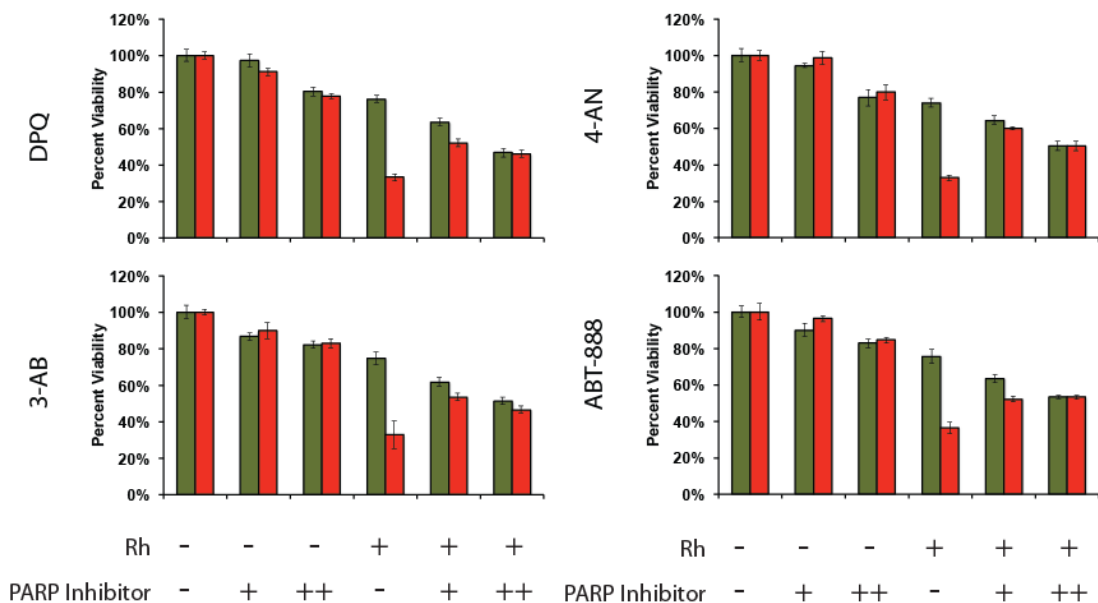


Figure 2.7 PARP inhibition assay. HCT116N and HCT116O cells were plated in 96-well format at densities of 5×10^4 cells/well and treated with 0 μM (“-”) or 20 μM (“+”) of $[\text{Rh}(\text{HDP A})_2\text{chrysi}]^{3+}$ with or without PARP inhibitor (“-” = 0 μM DPQ, 3-AB, 4-AN, or ABT-888; “+” = 25 μM DPQ, 2 mM 3-AB, 10 μM 4-AN, or 5 μM ABT-888; “++” = 50 μM DPQ, 3 mM 3-AB, 20 μM 4-AN, or 10 μM ABT-888). After 72 hours, the cells were labeled with MTT for 4 hours. The resulting formazan crystals were dissolved by addition of 10% SDS acidified with 10 mM HCl, and absorbance was measured at 570 nm. All four PARP inhibitors confer protection from rhodium-induced MMR-dependent toxicity, reducing the differential activity significantly.

In light of the shorter incubations required for this complex, it seemed likely that accelerated cellular uptake is a contributing factor in the increased cellular response. As $[\text{Rh}(\text{HDPA})_2\text{chrysi}]^{3+}$ is not luminescent, another method was needed to examine its cellular uptake. The high atomic mass and monoisotopic distribution of rhodium make the cellular accumulation of rhodium metalloinsertors well suited to analysis by inductively coupled plasma – mass spectrometry (ICP-MS).³⁵⁻³⁷ ICP-MS affords a direct comparison of the cellular accumulation of a series of rhodium metalloinsertors after treatments similar to those applied in ELISA assays for activity. The highest levels of cellular accumulation are clearly seen for the complex bearing the HDPA ligand, which was expected in light of the previous observation that $[\text{Rh}(\text{HDPA})_2\text{chrysi}]^{3+}$ exhibits increased anti-proliferative activity against the HCT116 cell lines at shorter incubation times than other rhodium metalloinsertors. Significant activity is seen with $[\text{Rh}(\text{HDPA})_2\text{chrysi}]^{3+}$ in as little as 12 hours, while $[\text{Rh}(\text{bpy})_2\text{chrysi}]^{3+}$ and $[\text{Rh}(\text{NH}_3)_4\text{chrysi}]^{3+}$ display no activity at this incubation time.

2.4.2 Cytotoxicity

Rhodium metalloinsertors have shown differential anti-proliferative activity in an ELISA assay for DNA synthesis. This assay directly reports on the amount of BrdU label incorporated during DNA replication, and, as such, does not distinguish between cells that are viable but not replicating, e.g, G0 cells that have exited the cell cycle, and cells that are inviable, or dead. Therefore, this assay can be used to determine *inhibitory*, but not *cytotoxic* activity. In contrast, the MTT assay reports directly on cell viability as measured by metabolic activity, with the action of mitochondrial reductases catalyzing the cleavage of the labeling agent MTT. Here cells that are viable still produce signal,

i.e, formazan absorbance, whether or not they are actively dividing. Thus, this assay can distinguish between senescence and true cell death, and the effects observed in response to rhodium treatment are truly cytotoxic. Importantly, the concentration ranges and incubation times of the treatments applied in the MTT assays for $[\text{Rh}(\text{HDPa})_2\text{chrysi}]^{3+}$ and the closely related complex $[\text{Rh}(\text{MeDPA})_2\text{chrysi}]^{3+}$ (0 – 25 μM , 24 – 72 hours) are identical to those that inhibit DNA synthesis as seen by ELISA.

Accordingly, the result that $[\text{Rh}(\text{HDPa})_2\text{chrysi}]^{3+}$ and $[\text{Rh}(\text{MeDPA})_2\text{chrysi}]^{3+}$ trigger cell death selectively in the MMR-deficient HCT116O cell line versus the MMR-proficient HCT116N cell line (as measured by MTT assay) represents a significant advance in the development of these complexes as anti-cancer agents; clearly, these agents are more potent than previously considered. Although $[\text{Rh}(\text{bpy})_2\text{chrysi}]^{3+}$ does not appear to be selectively toxic at these concentrations, it is likely that this is due to differences in the kinetics of cellular uptake, rather than fundamental differences in its mode of action as compared to $[\text{Rh}(\text{HDPa})_2\text{chrysi}]^{3+}$, since both bind DNA mismatches with equal affinity.²⁴ For either activity assay, the complex must first accumulate within the cell, and then cellular response must be triggered. While $[\text{Rh}(\text{HDPa})_2\text{chrysi}]^{3+}$ displays activity in ELISA after 12 h incubations, $[\text{Rh}(\text{bpy})_2\text{chrysi}]^{3+}$ requires 48 h or more to show significant differential activity. In light of the higher levels of rhodium accumulation seen by ICP-MS after treatment with the HDPa complex *versus* the bpy complex, it seems likely that accumulation of the bpy complex is delayed by ~36 h relative to the HDPa complex. Cellular responses that occur quickly after accumulation, such as the inhibition of DNA synthesis, can still be observed within the 72-hour timeframe of the ELISA assay, and both complexes display activity. However, a lag time

will exist between the inhibition of DNA synthesis and the onset of cell death, and when combined with the slow uptake of $[\text{Rh}(\text{bpy})_2\text{chrysi}]^{3+}$, ($t > 48$ h), cell death is delayed accordingly and cannot be observed within the timeframe of the MTT assay (also 72 h).

The fact that the $[\text{Rh}(\text{MeDPA})_2\text{chrysi}]^{3+}$ complex displays differential toxicity against the HCT116O cell lines comparable to that of the $[\text{Rh}(\text{HDPA})_2\text{chrysi}]^{3+}$ complex suggests that it shares the accelerated uptake of the HDPA complex. This was certainly expected, as the complexes are almost identical, but does not address the question of uptake mechanism, and clearly refutes the hypothesis that accelerated uptake requires a hydrogen-bonding interaction with the bridging secondary amine of the HDPA ligand. More importantly, this suggests that selective toxicity as a function of MMR-competency is a general property of rhodium metalloinsertors with dipyridylamine ancillary ligands, and establishes these ligands as the basis for the development of the next generation of complexes.

2.4.3 Cell Cycle Distribution

Flow cytometry analysis reveals that cell death is preceded by disruption of the cell cycle. Treatment with 20 μM $[\text{Rh}(\text{HDPA})_2\text{chrysi}]^{3+}$ for 24 hours leads to a marked depletion of the S-phase population with a concomitant increase in the G1 population. These data suggest that the G1/S-phase DNA damage checkpoint may be activated in response to rhodium treatment. In the case of the HCT116O line, the G2/M-phase population also increases in response to rhodium treatment. This could represent a secondary checkpoint activation occurring at the G2/M-phase transition, and might signal a “two-alarm fire” that accompanies the enhanced activity against this cell line.

2.4.4 Necrotic Mode of Cell Death

The biochemical events associated with apoptosis have been extensively studied.³⁸ An extensive network of regulatory proteins controls the initiation of this process in response to both internal and external signals.³⁹ Upon activation, the cascade of initiator and effector caspases cleaves a variety of substrates to bring about the morphological changes associated with this mode of cell death, including nuclear condensation and fragmentation, plasma membrane blebbing, decomposition of the cell into apoptotic bodies, and ultimately, the engulfment of these bodies by neighboring cells through phagocytosis.⁴⁰ Importantly, apoptotic cells retain their membrane integrity until the very last stages of this process, preventing release of cytokines and thus avoiding inflammation. By comparison, both the causes and the progression of necrosis are much less defined at the molecular level, and this mode of cell death is most frequently characterized by morphological criteria.⁴⁰⁻⁴² Perhaps the most reliable marker of necrosis then, is the early rupture of the plasma membrane, in direct contrast to apoptosis. These differences in membrane integrity enable the facile characterization of cell death by flow cytometry. The admission of the dead cell stain propidium iodide by the HCT116 cell lines upon rhodium treatment reveals that cell death proceeds through a necrotic, rather than apoptotic pathway. This conclusion is supported by the observation that the caspase inhibitor Z-VAD-FMK is unable to block rhodium-induced toxicity in the MTT assay, indicating that death occurs in a caspase-independent fashion.

It is interesting to consider that rhodium metalloinsertors selectively induce necrosis in MMR-deficient cells. Traditionally, necrotic cell death has been considered to be “accidental”, occurring mainly in response to non-physiological insults.^{43,44} More

recently however, the notion that necrosis may in fact be an ancestral mode of programmed cell death has gained attention in the literature and community of cell death research.^{40,41,45} Hitomi et al. screened an siRNA library covering the mouse genome and identified 432 gene knockdowns that blocked the induction of necrosis.⁴⁶ Chan et al. found anti-necrotic proteins encoded in the genomes of several viruses.⁴⁷ While these studies present some of the most compelling evidence for the notion that necrosis is in fact a regulated process, several other groups are also working to provide a molecular definition for the process as has been done for apoptosis.^{44,45}

Thompson and co-workers have reported that the DNA repair protein poly ADP-ribose polymerase-1 (PARP-1) mediates the induction of necrosis in response to DNA damage by the alkylator MNNG.⁴⁸ Upon activation at sites of DNA damage, PARP-1 covalently modifies itself with long chains of ADP-ribose polymers in order to recruit downstream components of the repair machinery.⁴⁹ As a result, PARP-1 along with PARP-2 has attracted much attention as a therapeutic target recently, and several specific and potent inhibitors of the enzyme are currently in clinical trials.⁵⁰ Here, treatment with a panel of PARP-1 inhibitors confers protection from MMR-dependent toxicity, abolishing differential activity between the HCT116 cell lines by Rh. This result strongly suggests that PARP activation is required for the differential biological effects of rhodium metalloinsertors. Importantly, the fact that each of the four PARP inhibitors on the panel abolishes differential activity argues against the notion that off-target effects of any particular inhibitor are responsible for blocking rhodium activity. Although the role of PARP in regulating necrosis is still emerging, the requirement for PARP activation is consistent with the notion that these rhodium complexes elicit a damage response upon

binding to DNA mismatches. This is supported by flow cytometry analysis, which reveals that cell death is preceded by disruption of the cell cycle. Upon rhodium treatment, there is a sharp decline in the population of cells that are actively synthesizing DNA. This observation suggests that the G1/S-phase DNA damage checkpoint is activated.

As necrosis triggers a pro-inflammatory response by releasing cytokines, selective induction of necrosis in cancerous tissues may be a way to activate the immune system against cancer cells and ultimately improve efficacy of a therapeutic agent.⁵¹ One accepted trigger of necrosis is bioenergetic catastrophe, i.e, severe ATP depletion.^{43,44} Rhodium metalloinsertors might trigger such a catastrophe by targeting mitochondrial DNA. Previously, it was thought that damaged mitochondrial genomes would simply be degraded and replaced by the replication of undamaged DNA.⁵² However, emerging research has uncovered DNA repair processes in mitochondria, including mismatch repair capability.^{52,53} As lipophilic cations, rhodium metalloinsertors likely accumulate in mitochondria,⁵⁴⁻⁵⁹ as we have seen with analogous ruthenium complexes in our laboratory.¹⁹ If mitochondrial DNA mismatches are in fact a target for rhodium metalloinsertors, then the resultant disruption of mitochondrial function would lead to energy depletion and necrosis. Future mechanistic work must explore the biochemical consequences of mismatch binding in nuclear DNA *versus* mitochondrial DNA. It should be noted that these mechanisms are not mutually exclusive; as such, both might contribute to the biological response to rhodium metalloinsertors.

2.4.5 General Implications

These studies support the notion that rhodium metalloinsertors bearing HDPA

ligands benefit from increased cellular accumulation, and thus provide an explanation for the observation that $[\text{Rh}(\text{HDPA})_2\text{chrysi}]^{3+}$ exceeds the activity predicted by its binding affinity for DNA mismatches. This increased uptake allows us to observe additional cellular responses to these agents, and, as a whole, a picture of the biological response to rhodium metalloinsertors, exemplified by $[\text{Rh}(\text{HDPA})_2\text{chrysi}]^{3+}$ in particular, is beginning to emerge (**Figure 2.8**). Over the course of the first 12 hours, the rhodium complex accumulates in cells, binding to either mitochondrial or genomic DNA mismatches. Within 24 hours, DNA synthesis is inhibited, and cells accumulate in G1-phase. Over the next 24–48 hours, the DNA damage response is likely activated, and ultimately leads to cell death by a caspase-independent, necrotic mechanism. These biological effects are more pronounced at each stage of the response in the MMR-deficient HCT116O cell line relative to the MMR-proficient HCT116N cell line, strongly suggesting that DNA mismatches are in fact the cellular target of rhodium metalloinsertors.

2.5 Conclusions

This work shows that dipyriddyamine ancillary ligands serve to accelerate the cellular uptake of rhodium metalloinsertors, triggering a selective cytotoxic effect as a function of MMR status and forming the foundation for the next generation of complex development. This new class of agents is significantly more potent than previously considered, and the work begun here on understanding their mechanism of action advances their development as novel anti-cancer agents.

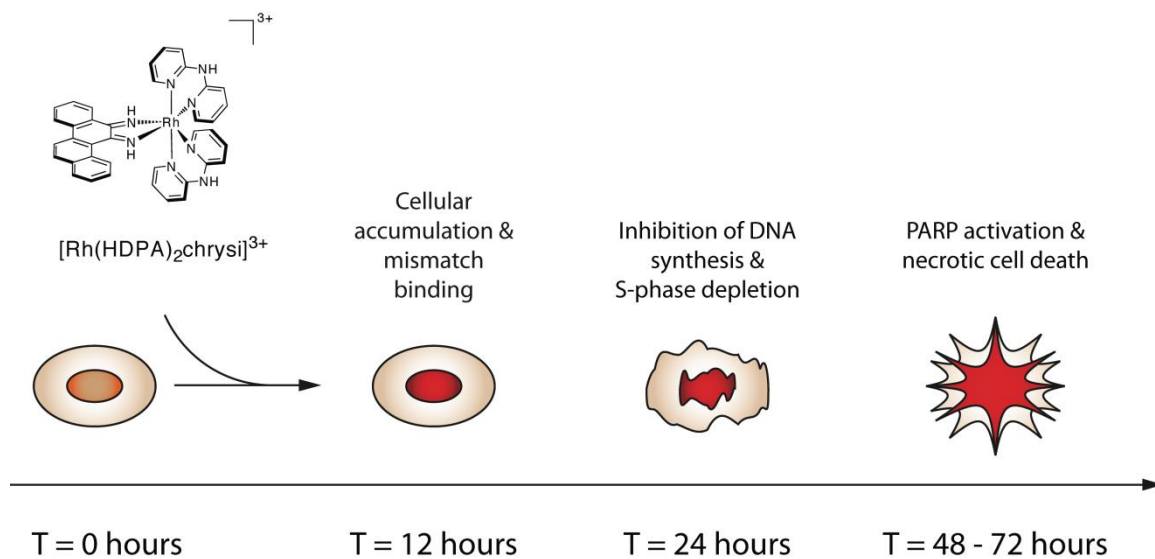


Figure 2.8 Model for the cellular response to rhodium metalloinsertors. Within 12 h of treatment with $[\text{Rh}(\text{HDPA})_2\text{chrysi}]^{3+}$, cellular accumulation is observed (**Figure 2.2**). Following cellular accumulation and mismatch binding, inhibition of DNA synthesis is observed (ELISA data not shown) concurrently with S-phase depletion (**Figure 2.4**). Finally, 48 to 72 h following rhodium treatment, PARP activation and necrotic cell death are observed (**Figure 2.5** and **Figure 2.7**).

2.6 References

- 1 Kunkel, T. A.; Erie, D. A. *Annu Rev. Biochem.* **2005**, *74*, 681-710.
- 2 Loeb, L. A. *Cancer Res.* **2001**, *61*, 3230-3239.
- 3 Bhattacharya, N. P.; Skandalis, A.; Ganesh, A.; Groden, J.; Meuth, M. *Proc. Natl. Acad. Sci. U.S.A.* **1994**, *91*, 6319-6323.
- 4 Iyer, R. R.; Pluciennik, A.; Burdett, V.; Modrich, P. L. *Chem. Rev.* **2006**, *106*, 302-323.
- 5 Arzimanoglou I. I.; Gilbers, F.; Barber, H. R. K. *Cancer* **1998**, *82*, 1808-1820.
- 6 Lawes, D. A.; SenGupta, S.; Boulos, P. B. *Eur. J. Surg. Oncol.* **2003**, *29*, 201-212.
- 7 Carethers, J. M.; Hawn, M. T.; Chauhan, D. P.; Luce, M. C.; Marra, G.; Koi, M.; Boland, C. R. *J. Clin. Invest.* **1996**, *98*, 199-206.
- 8 Fink, D.; Aebi, S.; Howell, S. B. *Clin. Cancer Res.* **1998**, *4*, 1-6.
- 9 Aebi, S.; Fink, D.; Gordon, R.; Kim, H. K.; Zheng, H.; Fink, J. L.; Howell, S. B. *Clin. Cancer Res.* **1997**, *3*, 1763-1767.
- 10 Jackson, B. A.; Barton, J. K. *J. Am. Chem. Soc.* **1997**, *119*, 12986-12987.
- 11 Jackson, B. A.; Barton, J. K. *Biochemistry* **2000**, *39*, 6176-6182.
- 12 Jackson, B. A.; Alekseyev, V. Y.; Barton, J. K. *Biochemistry* **1999**, *38*, 4655-4662.
- 13 Junicke, H.; Hart, J. R.; Kisko, J.; Glevob, O.; Kirsch, I. R.; Barton, J. K. *Proc. Natl. Acad. Sci. U.S.A.* **2003**, *100*, 3737-3741.

- 14 Pierre, V. C.; Kaiser, J. T.; Barton, J. K. *Proc. Natl. Acad. Sci. U.S.A.* **2007**, *104*, 429-434.
- 15 Cordier, C.; Pierre, V. C.; Barton, J. K. *J. Am. Chem. Soc.* **2007**, *129*, 12287-12295.
- 16 Zeglis, B. M.; Pierre, V. C.; Kaiser, J. T.; Barton, J. K. *Biochemistry* **2009**, *48*, 4247-4253.
- 17 Song, H.; Kaiser, J. T.; Barton, J. K. *Nat. Chem.* **2012**, *4*, 615-620.
- 18 Lerman, L. S. *J. Mol. Biol.* **1961**, *3*, 18-30.
- 19 Puckett, C. A.; Barton, J. K. *J. Am. Chem. Soc.* **2007**, *129*, 46-47.
- 20 Puckett, C. A.; Barton, J. K. *Biochemistry* **2008**, *47*, 11711-11716.
- 21 Koi, M.; Umar, A.; Chauhan, D. P.; Cherian, S. P.; Carethers, J. M.; Kunkel, T. A.; Boland, C. R. *Cancer Res.* **1994**, *54*, 4308-4312.
- 22 Hart, J. R.; Glebov, O.; Ernst, R. J.; Kirsch, I. R.; Barton, J. K. *Proc. Natl. Acad. Sci. U.S.A.* **2006**, *103*, 15359-15363.
- 23 Gratzner, H. G. *Science* **1982**, *218*, 474-475.
- 24 Ernst, R. J.; Song, H.; Barton, J. K. *J. Am. Chem. Soc.* **2009**, *131*, 2359-2366.
- 25 Dixon, N. E.; Lawrance, G. A.; Lay, P. A.; Sargeson, A. M. *Inorg. Chem.* **1983**, *22*, 846-847.
- 26 Dixon, N. E.; Lawrance, G. A.; Lay, P. A.; Sargeson, A. M. *Inorg. Chem.* **1984**, *23*, 2940-2947.

- 27 Reitmar, A. H.; Risley, R.; Bristow, R. G.; Wilson, T.; Ganesh, A.; Jang, A.; Peacock, J.; Benchimol, S.; Hill, R. P.; Mak, T. W.; Fishel, R.; Meuth, M. *Cancer Res.* **1997**, *57*, 3765-3771.
- 28 Mosmann, T. *J. Immunol. Methods* **1983**, *65*, 55–63.
- 29 Idziorek, T.; Estaquier, J.; DeBels, F.; Ameisen, J.-C. *J. Immunol. Methods* **1995**, *185*, 249-258.
- 30 Vandenabeele, P.; Vanden Berghe, T.; Festjens, N. *Science STKE* **2006**, *358*, pe44.
- 31 Costantino, G.; Macchiarulo, A.; Camaioni, E.; Pellicciari, R. *J. Med. Chem.* **2001**, *44*, 3786-3794.
- 32 Purnell, M. R.; Whish, W. J. D. *Biochem. J.* **1980**, *185*, 775-777.
- 33 Banasik, M.; Komura, H.; Shimoyama, M.; Ueda, K. *J. Biol. Chem.* **1992**, *267*, 1569-1575.
- 34 Donawho, C. K.; Luo, Y.; Luo, Y.; Penning, T. D.; Bauch, J. L.; Bouska, J. J.; Bontcheva-Diaz, V. D.; Cox, B. F.; DeWeese, T. L.; Dillehay, L. W.; *et. al.* *Clin. Cancer Res.* **2007**, *13*, 2728-2737.
- 35 Egger, E.; Rappel, C.; Jakupec, M. A.; Hartinger, C. G.; Heffeter, P.; Keppler, B. K. *J. Anal. At. Spectrom.* **2009**, *24*, 51–61.
- 36 Ghezzi, A.; Aceto, M.; Cassino, C.; Gabano, E.; Osella, D. *J. Inorg. Biochem.* **2004**, *98*, 73–78.
- 37 Kirin, S. I.; Ott, I.; Gust, R.; Mier, W.; Weyhermüller, T.; Metzler-Nolte, N. *Angew. Chem. Int. Ed.* **2008**, *47*, 955–959.

- 38 Kerr, J. F. R.; Wyllie, A. H.; Currie, A. R. *Br. J. Cancer* **1972**, *26*, 239-257.
- 39 Danial, N. N.; Korsmeyer, S. J. *Cell* **2004**, *116*, 205–219.
- 40 Edinger, A. L.; Thompson, C. B. *Curr. Op. in Cell Biol.* **2004**, *16*, 663-669.
- 41 Kroemer, G.; El-Deiry, W. S.; Golstein, P.; Peter, M. E.; Vaux, D.; Vandenabeele, P.; Zhivotovsky, B.; Blagosklonny, M. V.; Malorni, W.; Knight, R. A.; Piacentini, M.; Nagata, S.; Melino, G. *Cell Death and Differentiation* **2005**, *12*, 1463-1467.
- 42 Kroemer, G.; Galuzzi, L.; Vandenabeele, P.; Abrams, J.; Alnemri, E. S.; Baehrecke, E. H.; Blagosklonny, M. V.; El-Deiry, W. S.; Golstein, P.; Green, D. R.; Hengartner, M.; Knight, R. A.; Kumar, S.; Lipton, S. A.; Malorni, W.; Nunez, G.; Peter, M. E.; Tschopp, J.; Yuan, J.; Piacentini, M.; Zhivotovsky, B.; Melino, G. *Cell Death and Differentiation* **2009**, *16*, 3-11.
- 43 Golstein, P.; Kroemer, G. *Trends in Biochemical Sciences* **2007**, *32*, 37-43.
- 44 McCall, K. *Curr. Op. Cell Biology* **2010**, *22*, 882-888.
- 45 Galluzzi, L.; Kroemer, G. *Cell* **2008**, *135*, 1161-1163.
- 46 Hitomi, J.; Christofferson, D. E.; Ng, A.; Yao, J.; Degterev, A.; Xavier, R. J.; Yuan, J. *Cell* **2008**, *135*, 1311-1323
- 47 Chan, F. K.; Shisler, J.; Bixby, J. G.; Felices, M.; Zheng, L.; Appel, M.; Orenstein, J.; Moss, B.; Lenardo, M. J. *J of Biol. Chem.* **2003**, *278*, 51613-5162.
- 48 Zong, W. X.; Ditsworth, D.; Bauer, D. E.; Wang, Z. -Q.; Thompson, C. B. *Genes and Development* **2004**, *18*, 1272–1282.
- 49 Malanga, M.; Althaus, F. R. *Biochem. and Cell Biol.* **2005**, *83*, 354–364.
- 50 Annunziata, C. M.; O'Shaughnessy, J. *Clin. Cancer Res.* **2010**, *16*, 4517–4526.

- 51 Ricci, M. S.; Zong, W. X. *The Oncologist* **2006**, *11*, 342-357.
- 52 Boesch, P.; Weber-Lotfi, F.; Ibrahim, N.; Tarasenko, V.; Cosset, A.; Paulus, F.; Lightowlers, R. N.; Dietrich, A. *Biochimica et Biophysica Acta*. **2011**, *1813*, 186-200.
- 53 de Souza-Pinto, N. C.; Mason, P. A.; Hashiguchi, K.; Weissman, L.; Tian, J.; Guay, D.; Lebel, M.; Stevensner, T. V.; Rasmussen, L. J.; Bohr, V. A. *DNA Repair (Amst)*. **2009**, *8*, 704-719.
- 54 Napolitano, S. M.; Aprile, J. R. *Adv. Drug Delivery Rev.***2001**, *49*, 63–70.
- 55 Murphy, M. P.; Smith, R. A. J. *Adv. Drug Delivery Rev.***2000**, *41*, 235–250.
- 56 Rackham, O.; Nichols, S. J.; Leedman, P. J.; Berners-Price, S. J.; Filipovska, A. *Biochem. Pharmacol.* **2007**, *74*, 992–1002.
- 57 Liu, J. J.; Galettis, P.; Farr, A.; Maharaj, L.; Samarasinha, H.; McGechan, A. C.; Baguley, B. C.; Bowen, R. J.; Berners-Price, S. J.; McKeage, M. J. *J. Inorg. Biochem.* **2008**, *102*, 303–310.
- 58 Liberman, E. A.; Topali, V. P.; Tsofina, L. M.; Jasaitis, A. A.; Skulachev, V. P. *Nature* **1969**, *222*, 1076–1078.
- 59 Johnson, L. V.; Walsh, M. L.; Chen, L. B. *Proc. Natl. Acad. Sci. U.S.A.* **1980**, *77*, 990–994.

Chapter 3: Cell-Selective Biological Activity of Rhodium Metalloinsertors Correlates with Subcellular Localization[§]

3.1 Introduction

Recent work in the Barton laboratory discovered that the rhodium metalloinsertors that display activity at relatively short incubation times in the ELISA assay also show preferential cytotoxicity towards the MMR-deficient HCT116O cell line, inducing death *via* a necrotic pathway.¹ As one generally accepted trigger of necrosis is severe ATP depletion,^{2,3} this observation prompted the investigation of subcellular localization. These metalloinsertors may trigger necrosis through mitochondrial DNA targeting. As lipophilic cations, mitochondrial accumulation is a possibility;⁴ real-time monitoring of the cells with confocal microscopy could not be used to monitor organelle accumulation, however, since the rhodium complexes are not luminescent. Nonetheless, an understanding of the subcellular localization of these compounds is crucial for the development of next-generation metalloinsertors with improved selectivity for MMR-deficient cells.⁵ Rhodium uptake can be easily probed by inductively coupled plasma mass spectrometry (ICP-MS), as no interfering ion exists within the cell. The sensitivity of ICP-MS allows for biologically relevant concentrations of rhodium to be determined,⁶ and combined with organelle isolation procedures can be used to give estimates on the subcellular localization of our metalloinsertors.

There have been few studies to date investigating the subcellular localization of common therapeutic agents. Non-fluorescent organic molecules pose a particular problem

[§] Adapted with permission from Komor, A.C.; Schneider, C. J.; Weidmann, A. G.; Barton, J. K. Cell-Selective Biological Activity of Rhodium Metalloinsertors Correlates with Subcellular Localization *J. Am. Chem. Soc.* **2012**, *134*, 19223-19233. © 2012 American Chemical Society.

Acknowledgements: Curtis Schneider synthesized the $[\text{Rh}(\text{chrysi})(\text{phen})(\text{L})]\text{Cl}_3$ (L= HDPa, MeDPA, PrDPA) compounds, and Alyson Weidmann synthesized $[\text{Rh}(\text{DPaE})_2(\text{chrysi})]^{3+}$ and $[\text{Rh}(\text{PrDPA})_2(\text{chrysi})]^{3+}$.

in this regard owing to their lack of spectroscopic handle for detection unless the drug is tethered to a fluorescent tag. However, this process of appending a fluorescent molecule to a drug has been shown in itself to alter the subcellular localization of the compound.⁷ There have been instances where appending an organelle-specific peptide to a therapeutic agent resulted in drastically altered activity of the agent, which was attributed to altered subcellular localization.^{8,9} Fluorescent organic therapeutics, as well as metal-based therapeutics, do contain spectroscopic or spectrometric handles for detection, and can therefore be mapped within the cell. Doxorubicin, a chemotherapeutic that intercalates DNA, is one such fluorescent molecule. In one study, doxorubicin resistance was correlated with subcellular localization of the compound. Specifically, the subcellular distribution of the drug shifted from nuclear to cytosolic as drug resistance increased.¹⁰ Furthermore, in a study by Liu and coworkers on a series of Au(I) and Ag(I) bidentate pyridyl phosphine anticancer agents, it was observed that increased lipophilicity resulted in increased potency of the drug, with preferential accumulation of the drug in the mitochondria.¹¹ In a final study, ICP-MS was used to track the uptake and subcellular localization of cisplatin as well as two ruthenium-based chemotherapeutics currently in clinical trials, NAMI-A and KP1019. Reduced mitochondrial accumulation of cisplatin was observed in cisplatin resistant cells, while the ruthenium-based drugs were found to have different localization patterns than cisplatin that did not change from one cell type to the other.¹²

Here we correlate the selectivity of a variety of rhodium metalloinsertors that target MMR-deficient cells with the subcellular localization of the complexes. We find that all complexes studied are localized at a sufficient concentration in the nucleus for

mismatch binding. Furthermore, we find that, in general, higher levels of mitochondrial rhodium reduce the cell-selective biological activity of these metalloinsertors. These observations give credence to the theory that mismatches in genomic DNA are the ultimate target of our metalloinsertors and that this mismatch targeting is responsible for their unique cell-selective biological activity.

3.2 Experimental Protocols

3.2.1 Materials

Commercially available chemicals were used as received. The Rh complex $[\text{Rh}(\text{NH}_3)_5\text{Cl}]\text{Cl}_2$ was obtained from Strem Chemical, Inc. RhCl_3 was purchased from Pressure Chemical, Inc. All organic reagents and Sephadex ion-exchange resin were obtained from Sigma-Aldrich unless otherwise noted. Sep-pak C_{18} solid-phase extraction (SPE) cartridges were purchased from Waters Chemical Co. (Milford, MA). Media and supplements were purchased from Invitrogen (Carlsbad, CA). BrdU, antibodies, buffers, peroxidase substrate, MTT, and acidified lysis buffer (10% SDS in 10 mM HCl) solution were purchased in kit format from Roche Molecular biochemical (Mannheim, Germany). Phosphoramidites were purchased from Glen Research (Sterling, VA).

3.2.2 Oligonucleotide Synthesis

Oligonucleotides were synthesized on an Applied Biosystems 3400 DNA synthesizer using standard phosphoramidite chemistry. DNA was synthesized with a 5'-dimethoxytrityl (DMT) protecting group. The oligonucleotides were cleaved from the beads by reaction with concentrated ammonium hydroxide at 60° C overnight. The resulting free oligonucleotides were purified by HPLC using a C_{18} reverse-phase column (Varian, Inc.) on a Hewlett-Packard 1100 HPLC. The DMT group was removed by

reaction with 80% acetic acid for 15 min at ambient temperature. The DMT-free oligonucleotides were precipitated with absolute ethanol and purified again by HPLC. Positive identification of the oligonucleotides and their purity were confirmed by MALDI-TOF mass spectrometry. Quantification was performed on a Cary 100 Bio UV-Visible Spectrophotometer using the extinction coefficients at 260 nm (ϵ_{260}) estimated for single-stranded DNA.

3.2.3 Synthesis and Characterization of Metal Complexes

The complexes $[\text{Rh}(\text{bpy})_2(\text{chrysi})]^{3+}$, $[\text{Rh}(\text{HDP A})_2(\text{chrysi})]^{3+}$, $[\text{Rh}(\text{NH}_3)_4(\text{chrysi})]^{3+}$, $[\text{Rh}(\text{DIP})_2(\text{chrysi})]^{3+}$, $[\text{Rh}(\text{DP AE})_2(\text{chrysi})]^{3+}$, and $[\text{Rh}(\text{PrDP A})_2(\text{chrysi})]^{3+}$ were prepared according to published procedures.¹³⁻¹⁵

3.2.3.1 $[\text{Rh}(\text{chrysi})(\text{phen})(\text{NH}_3)_2]\text{Cl}_3$

$[\text{Rh}(\text{chrysi})(\text{phen})(\text{NH}_3)_2]\text{Cl}_3$ was prepared according to an adaptation of previously described procedures.¹⁶ A 1 L round bottomed flask was charged with $[\text{Rh}(\text{NH}_3)_4(\text{phen})][\text{OTf}]_3$ (0.500 g, 0.626 mmol) and chrysene-5,6-dione (0.162 g, 0.626 mmol), and 1:9 $\text{H}_2\text{O}:\text{MeCN}$ was added (400 mL). A 1M solution of NaOH (1.5 mL) was added to the orange solution. Over the next hour, the solution changed color from orange to red, after which time a 1M solution of HCl (1.5 mL) was added to quench the reaction. The MeCN was evaporated *in vacuo* and the resulting red solution was loaded onto a SPE cartridge, eluted with 25% acetonitrile in 0.1% $\text{TFA}_{(\text{aq})}$, and lyophilized to give a red solid. The chloride salt can be obtained from a Sephadex QAE anion exchange column equilibrated with 0.1M MgCl_2 . Yield: 0.536 g, 94%. ^1H NMR (300 MHz, $\text{d}_6\text{-DMSO}$): δ 13.59 (s, 1H); 13.43 (s, 1H); 9.56 (d, $J = 5.3$ Hz, 1 H); 9.16 (m, 2H); 8.93 (d, $J = 8.3$ Hz, 1H); 8.77 (d, $J = 5.3$ Hz, 1H); 8.35-8.57 (m, 7H); 8.23 (d, $J = 8.3$ Hz, 1H); 7.99 (m, 2H);

7.83 (m, 2H); 7.54 (t, $J = 7.6$ Hz, 1H); 4.95 (s, 3H); 4.79 (s, 3H). ESI-MS (cation): m/z calc. 571.13 ($M-2H^+$), obs. 570.9.

3.2.3.2 1,1-di(pyridin-2-yl)ethanol (DPE)

DPE was synthesized according to an adaptation of previously described procedures.¹⁷ A 250-mL oven dried schlenk flask was cooled to -78°C in a dry ice/acetone bath and charged with di(pyridin-2-yl)methanone (0.508 g, 2.8 mmol). Anhydrous Et_2O (50 mL) was added *via* cannula transfer, and the resulting yellow solution was allowed to stir for 10 m. A 1.6M solution of MeLi (5 mL) was then added dropwise over 15 m, during which time the solution turned deep purple. After 30 m of stirring at -78°C , sat. NH_4Cl (aq) (15 mL) was added. The resulting yellow solution was allowed to warm to ambient temperature, and was then extracted with Et_2O (3 x 50 mL). The organic fractions were combined and dried over magnesium sulfate, and the solvent was removed *in vacuo*. The ligand was further purified via flash chromatography (SiO_2 , 1:1 Et_2O :hexanes). Yield: 0.560 g, 100%. $^1\text{H-NMR}$ (CDCl_3 , 300 MHz): δ 8.57 (d, $J = 5.1$ Hz, 2H); 7.92 (d, $J = 6.9$ Hz, 2H); 7.80 (m, 2H); 7.27 (m, 2H); 6.60 (s, 1H); 2.08 (s, 3H). ESI-MS (cation): m/z calc. 201.09 ($M+H^+$), obs. 201.0.

3.2.3.3 N-alkyl-N-(pyridin-2-yl)pyridin-2-amine (alkyl = methyl or propyl; MeDPA, PrDPA)

To a slurry of sodium hydride (70 mg, 2.9 mmol) in THF (10 mL) was added HDPA (500 mg, 2.9 mmol) in THF (5 mL) at 0°C under 1 atm Ar. The reaction was purged with argon for 15 min, and the appropriate 1-bromoalkane (3.8 mmol) was added dropwise and warmed to ambient temperature. The reaction was stirred an additional 18 h under argon at reflux temperature. The reaction mixture was extracted with dilute sodium

bicarbonate, and the aqueous phase was extracted with CH_2Cl_2 (3 x 40 mL). The organic fractions were combined and dried over magnesium sulfate, and the solvent was removed *in vacuo*. These ligands were purified via flash chromatography (SiO_2 , 1:9 EtOAc:hexanes).

MeDPA: Yield: 23%. $^1\text{H-NMR}$ (CDCl_3 , 300 MHz): δ 8.35 (dd, 2H); 7.54 (t, 2H); 7.17 (d, 2H); 6.86 (t, 2H), 3.62 (s, 3H). ESI-MS (cation): m/z calc. 186.1 ($\text{M}+\text{H}^+$), obs. 186.

PrDPA: Yield: 25%. $^1\text{H NMR}$ (CDCl_3 , 300 MHz): δ 8.34 (d, $J = 7.7$ Hz, 2H); 7.57 – 7.45 (m, 2H); 7.06 (d, $J = 0.7$ Hz, 2H); 6.90 – 6.79 (m, 2H); 4.19 – 4.07 (m, 2H); 1.79 – 1.65 (m, 2H); 0.99 – 0.85 (m, 3H). ESI-MS (cation): m/z calc. 214.1 ($\text{M} + \text{H}^+$), obs. 214.

3.2.3.4 $[\text{Rh}(\text{NH}_3)_4(\text{phzi})]\text{Cl}_3$

$[\text{Rh}(\text{NH}_3)_6][\text{OTf}]_3$ (0.50 g, 0.77 mmol) and benzo[α]phenazine-5,6-dione (0.200 g, 0.77 mmol) were dissolved in a 1:5 mixture of water:acetonitrile (500 mL). A 1M solution of NaOH (1 mL) was added to the yellow solution and the reaction was allowed to stir at ambient temperature for 45 min, at which time a 1M solution of HCl (1 mL) was added to neutralize the reaction mixture. The MeCN was evaporated *in vacuo* and the resulting yellow solution was loaded onto a SPE cartridge, eluted with 25% acetonitrile in 0.1% $\text{TFA}_{(\text{aq})}$, and lyophilized to give a yellow solid. The chloride salt can be obtained from a Sephadex QAE anion exchange column equilibrated with 0.1M MgCl_2 . Yield: 0.45 g, 76%. $^1\text{H NMR}$ (300 MHz, d_6 -DMSO): δ 13.98 (s, 1H); 13.88 (s, 1H); 8.96 (d, $J = 7.8$ Hz, 1 H); 8.62 (d, $J = 7.6$ Hz, 1H); 8.34 (m, 2H); 7.92-8.21 (m, 4H); 4.48 (d, $J = 20.1$ Hz, 6 H); 3.79 (s, 6H). ESI-MS (cation): m/z calc. 524.07 ($\text{M-NH}_3+\text{TFA}^+$), obs.

523.8. UV-Vis (H₂O, pH 7): 250 nm (36,800 M⁻¹ cm⁻¹), 310 nm (20,800 M⁻¹, cm⁻¹), 340 nm (23,400 M⁻¹, cm⁻¹).

3.2.3.5 [Rh(chrysi)(phen)(L)]Cl₃ (L= HDPA, MeDPA, PrDPA)

Rh(chrysi)(phen)(NH₃)₂]Cl₃ (25 mg, 0.02 mmol) was reacted with L (0.022 mmol) in a 4:1 mixture of ethanol:water (10 mL). The bright red solution was refluxed overnight. The solvent was removed *in vacuo* and the resulting red solid dissolved in 0.1% TFA_(aq) (10 mL). The red solution was loaded onto a SPE cartridge and rinsed with copious amount of 0.1% TFA_(aq). The SPE cartridge was eluted with 10% acetonitrile in 0.1% TFA_(aq), and fractions were collected. The fractions containing product were identified by HPLC, combined, and lyophilized. The chloride salt can be obtained from a Sephadex QAE anion exchange column equilibrated with 0.1M MgCl₂.

[Rh(chrysi)(phen)(HDPA)]Cl₃: Yield: 17-28%. ESI-MS (cation): *m/z* calc 708.14 (M-2H⁺), obs. 708.2. UV-Vis (H₂O, pH 7): 303 nm (34,200 M⁻¹ cm⁻¹), 391 nm (8,000 M⁻¹, cm⁻¹), 440 nm (3,600 M⁻¹, cm⁻¹).

[Rh(chrysi)(phen)(MeDPA)]Cl₃: Yield: 12-32%. ¹H NMR (500 MHz, DMSO-*d*₆) δ 12.45 (s, 1H), 10.48 (s, 1H), 9.34 – 6.83 (m, 26H), 3.87 (s, 3H). ESI-MS (cation): *m/z* calc. 722.15 (M-2H⁺) 361.6 (M-H²⁺), obs. 722, 362. UV-Vis (H₂O, pH 7): 303 nm (55,500 M⁻¹ cm⁻¹), 391 nm (13,800 M⁻¹, cm⁻¹), 440 nm (5,700 M⁻¹, cm⁻¹).

[Rh(chrysi)(phen)(PrDPA)]Cl₃: Yield: 10-22%. ESI-MS: calc. 750.18 (M-2H⁺), 375.6 (M-H²⁺), obs. 750, 376. UV-Vis (H₂O, pH 7): 303 nm (53,500 M⁻¹ cm⁻¹), 391 nm (13,900 M⁻¹, cm⁻¹), 440 nm (9,900 M⁻¹, cm⁻¹).

3.2.3.6 [Rh(chrysi)(phen)(DPE)]Cl₂

A 125 mL round-bottomed flask was charged with [Rh(chrysi)(phen)(NH₃)₂]TFA₃ (62.0 mg, 0.068 mmol) and DPE (25.6 mg, 0.128 mmol) in ethanol (50 mL) to give a red solution. The reaction was heated to reflux (80° C) and stirred for 48 h. The ethanol solution was evaporated to dryness and dissolved in 0.1% TFA_(aq) (50 mL). The red solution was loaded onto a SPE cartridge and rinsed with copious amount of 0.1% TFA_(aq). The SPE cartridge was eluted with 10% acetonitrile in 0.1% TFA_(aq), and fractions were collected. The fractions containing product were identified by HPLC, combined, and lyophilized. The chloride salt can be obtained from a Sephadex QAE anion exchange column equilibrated with 0.1M MgCl₂. Yield: 30%. ESI-MS (cation): *m/z* calc. 737.15 (M-H⁺), 369.1 (M²⁺), obs. 737, 369. UV-Vis (H₂O, pH 7): 272 nm (102,100 M⁻¹ cm⁻¹), 303 nm (35,400 M⁻¹ cm⁻¹), 440 nm (10,600 M⁻¹ cm⁻¹). ¹H NMR (CD₃CN, 500 MHz): δ 15.10 (s, 1 H); 11.30 (s, 1 H); 9.62 (d, *J* = 5.5 Hz, 1H); 8.98 (d, *J* = 7.0 Hz, 1H); 8.92 (d, *J* = 8.0 Hz, 1H); 8.88 (m, 2H); 8.36 (m, 4H); 8.27 (d, *J* = 8.5 Hz, 1H); 8.21 (m, 1H); 8.13 (d, *J* = 8.5 Hz, 1H); 8.00 (m, 2H); 7.94 (d, *J* = 8.5 Hz, 1H); 7.73-7.78 (m, 4H); 7.62 (t, *J* = 8.0 Hz, 1H); 7.57 (d, *J* = 8.0 Hz, 1H); 7.50 (t, *J* = 7.0 Hz, 1H); 7.32 (d, *J* = 6.5 Hz, 1H); 7.14 (m, 1H); 6.95 (t, *J* = 7.5 Hz, 1H); 6.33 (t, *J* = 6.0 Hz, 1H); 1.98 (s, 3H).

3.2.4 Photocleavage Competition Titrations

The oligonucleotide was ³²P-labeled at the 5'-end by incubating DNA with ³²P-ATP and polynucleotide kinase (PNK) at 37°C for 2 h, followed by purification using gel electrophoresis. A small amount of the labeled DNA (less than 1% of the total amount of DNA) was added to 2 μM DNA in 100 mM NaCl, 20 mM NaP_i, pH 7.1 buffer. The DNA

hairpin was annealed by heating at 90°C for 10 min and cooling slowly to ambient temperature over a period of 2 h. Racemic solutions of non-photocleaving rhodium complex ranging from nanomolar to micromolar concentration, as well as a 4 μM $[\text{Rh}(\text{bpy})_2(\text{chrysi})]^{3+}$ solution were made in Milli-Q water. Annealed 2 μM DNA (10 μL), 4 μM $[\text{Rh}(\text{bpy})_2(\text{chrysi})]^{3+}$ (5 μL), and 5 μL of non-photocleaving Rh solution at each concentration were mixed in a microcentrifuge tube and incubated at 37 °C for 10 min. A light control ($\emptyset\text{Rh}$), in which the DNA was mixed with 10 μL of water and irradiated, and a dark control ($\emptyset\text{hv}$), in which the DNA was mixed with the highest concentration of rhodium complex without irradiation, were also prepared. The samples were then irradiated on an Oriel (Darmstadt, Germany) 1000-W Hg/Xe solar simulator (340-440 nm) for 5 min. The irradiated samples were dried and electrophoresed in a 20% denaturing polyacrylamide gel. The gel was then exposed to a phosphor screen, and the relative amounts of DNA in each band were quantitated by phosphorimagery (ImageQuant).

3.2.4.1 Binding Constant Determination

The fraction of DNA cleaved in each lane on the gel (See **Figure 3.1** for a typical autoradiogram) was normalized and plotted against the log of the concentration of rhodium complex. At least three photocleavage titrations were carried out for each racemic metal complex. The pooled data were fit to a sigmoidal curve using OriginPro 6.1 (**Figure 3.2**). The resulting midpoint value (i.e., the log of [rhodium complex] at the inflection point of the curve) was converted to units of concentration ($[\text{Rh}_{50\%}]$). The binding and dissociation constants of the non-photocleaving complex were calculated by

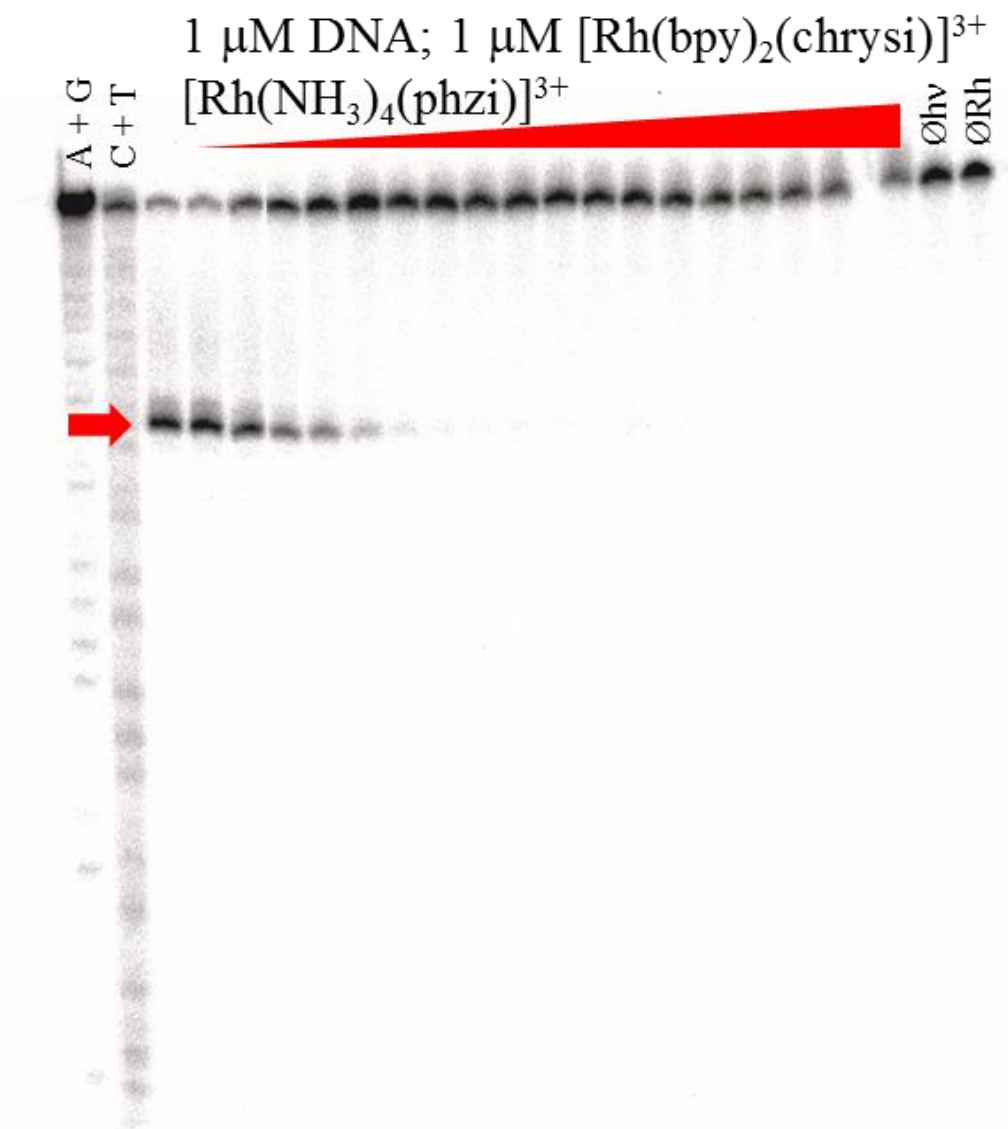


Figure 3.1 Binding affinities determined through DNA photocleavage. The DNA hairpin sequence is 5*'-GGCAGGCATGGCTTTTTGCCATCCCTGCC-3' (underline denotes the mismatch, asterisk denotes the radiolabel). Samples were irradiated and electrophoresed through a 20% denaturing PAGE gel. A light control (ØRh , without rhodium) and dark control (Øhv , without irradiation) were included. A representative autoradiogram of a photocleavage competition titration between 1 μM *rac*- $[\text{Rh}(\text{bpy})_2(\text{chrysi})]^{3+}$ and 0-100 μM $[\text{Rh}(\text{NH}_3)_4(\text{phzi})]^{3+}$ is shown. Arrow indicates the position of the mismatch.

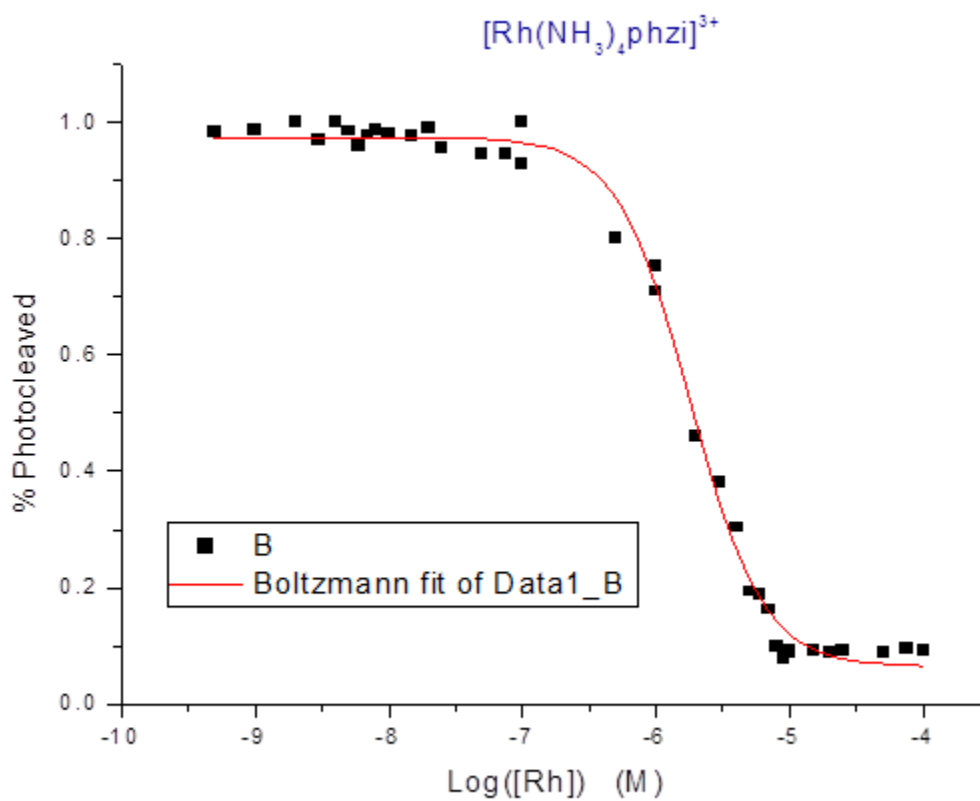


Figure 3.2 Representative sigmoidal curve for binding affinity determination. Shown is a plot of data pooled from photocleavage competition titrations between 1 μM *rac*- $[\text{Rh}(\text{bpy})_2(\text{chrysi})]^{3+}$ and 0-100 μM $[\text{Rh}(\text{NH}_3)_4(\text{phzi})]^{3+}$.

solving simultaneous equilibria involving DNA, $[\text{Rh}(\text{bpy})_2(\text{chrysi})]^{3+}$, and the complex in question in Mathematica 6.0.

3.2.5 Cell Culture

HCT116N and HCT116O cells were grown in RPMI medium 1640 supplemented with: 10% FBS; 2 mM L-glutamine; 0.1 mM nonessential amino acids; 1 mM sodium pyruvate; 100 units/mL penicillin; 100 $\mu\text{g}/\text{mL}$ streptomycin; and 400 $\mu\text{g}/\text{mL}$ Geneticin (G418). Cells were grown in tissue culture flasks (Corning Costar, Acton, MA) at 37 °C under 5% CO_2 and humidified atmosphere.

3.2.5.1 Cellular Proliferation ELISA

HCT116N and HCT116O cells were plated in 96-well plates at 2000 cells/well and allowed 24 h to adhere. The cells were then incubated with rhodium for the concentration and durations specified. For incubations less than 72 h, the Rh-containing media was replaced with fresh media, and the cells were grown for the remainder of the 72 h period. Cells were labeled with BrdU 24 h before analysis. The BrdU incorporation was quantified by antibody assay according to established procedures.¹⁸ Cellular proliferation was expressed as the ratio of the amount of BrdU incorporated by the treated cells to that of the untreated cells.

3.2.5.2 MTT Cytotoxicity Assay

Cytotoxicity assays were performed as described in the literature.¹⁹ HCT116N and HCT116O cells were plated in 96-well plates at 50,000 cells/well and incubated with rhodium for the durations specified. After rhodium incubation, cells were labeled with MTT for 4 h at 37°C under 5% CO_2 and humidified atmosphere. The resulting formazan crystals were dissolved with solubilizing reagent purchased from Roche according to the

manufacturer's instructions. The dissolved formazan was quantified as the absorbance at 570 nm minus the background absorbance at 690 nm. Percent viability was determined as the ratio of the amount of formazan in the treated cells to that of the untreated cells.

3.2.6 Nuclear Isolation Protocol

Approximately 10 million HCT116N/O cells were harvested from adherent culture by trypsinization, washed with cold PBS, and resuspended in 1 mL hypotonic buffer (20 mM TrisHCl pH 7.4, 10 mM NaCl, 3 mM MgCl₂). The resulting suspension was incubated on ice for 15 min. 50 μ L of a 10% NP-40 solution was added to the solution and immediately followed by vortexing at the highest setting for 10 seconds. The solution was then centrifuged at 3,000g for 10 min. The supernatant was discarded and the pellet saved as the nuclear fraction.

3.2.7 Mitochondrial Isolation Protocol

The followed protocol is an adaptation of that used by Ahmad, et al.²⁰ Approximately 20 million HCT116N/O cells were harvested from adherent culture by trypsinization, washed with cold PBS, and resuspended in 500 μ L mitochondrial extraction buffer (200 mM mannitol, 68 mM sucrose, 50 mM pipes, 50 mM KCl, 5 mM EGTA, 2 mM MgCl₂, 1 mM DTT, protease inhibitors). The resulting suspension was incubated on ice for 20 min, then homogenized by 35 passes through a 21-gauge needle and 1-mL syringe. The resulting lysate was centrifuged at 150g for 5 min. The supernatant was then transferred to a new microcentrifuge tube and centrifuged for an additional 10 min at 14,000g. The supernatant was discarded and the pellet saved as the mitochondrial fraction.

3.2.8 ICP-MS Assay for Whole-Cell Rhodium Levels

HCT116O cells were plated at 1×10^6 cells/well in a 6 well plate. The cells were allowed 24 h to adhere, then treated with 10 μ M of rhodium complex (except $[\text{Rh}(\text{DIP})_2(\text{chrysi})]^{3+}$, which was administered at 2 μ M). After the appropriate amount of time, the media was decanted, the cell monolayer washed with 3 mL PBS, and the cells lysed with 800 μ L of 1% SDS. The cell lysate was further lysed by sonication on a Qsonica Ultrasonic processor for 10 sec at 20% amplitude. 750 μ L of the lysate was then combined with 750 μ L of a 2% HNO_3 (v/v) solution, while the remainder of the lysate was quantified for protein by a bicinchoninic assay (BCA).²¹ The 1% HNO_3 solution was analyzed for rhodium content on an HP-4500 ICP-MS unit. Rhodium counts were normalized to the amount of protein determined from the BCA analysis (to obtain ng [Rhodium]/mg [protein] values). Standard errors for three independent experiments are shown. The experiment was repeated with HCT116N cells for one time point only to verify similar uptake of rhodium by the two cell lines.

3.2.9 ICP-MS Assay for Nuclear Rhodium Levels

HCT116O cells were plated at 10×10^6 cells/ plate in culture flasks and allowed 24 h to adhere. The cells were then treated with 10 μ M of rhodium complex (except $[\text{Rh}(\text{DIP})_2(\text{chrysi})]^{3+}$, which was administered at 2 μ M) for 24 h, harvested by trypsinization, and washed with PBS. The nuclear isolation protocol was then performed on the cells. The resulting pellet was resuspended in 800 μ L Milli-Q water and lysed by sonication on a Qsonica Ultrasonic processor for 10 sec at 40% amplitude. 750 μ L of the lysate was then combined with 750 μ L of a 2% HNO_3 (v/v) solution, while the remainder of the lysate was quantified for protein by a bicinchoninic assay (BCA).²¹ The resulting

1% HNO₃ solution was analyzed for rhodium content on an HP-4500 ICP-MS unit. Rhodium counts were normalized to the amount of protein determined from the BCA analysis (to obtain ng [Rhodium]/mg [protein]). The protein content was converted to number of nuclei by the conversion factor 3.28×10^{-8} mg [nuclear protein]/nuclei (found by counting nuclei with a hemacytometer followed by lysing and protein quantification). The rhodium concentrations were then divided by nuclei density to obtain ng of rhodium per nucleus. Standard errors for three independent experiments are shown. The experiment was repeated with HCT116N cells for one time point to verify similar uptake of rhodium by the two cell lines.

3.2.10 ICP-MS Assay for Mitochondrial Rhodium Levels

HCT116O cells were plated at 15×10^6 cells/ plate in culture flasks and allowed 24 h to adhere. The cells were then treated with 10 μ M of rhodium complex (except [Rh(DIP)₂(chrysi)]³⁺, which was administered at 2 μ M) for 24 h, harvested by trypsinization, and washed with PBS. The mitochondrial isolation protocol was then performed on the cells. The resulting pellet was resuspended in 800 μ L Milli-Q water and lysed by sonication on a Qsonica Ultrasonic processor for 10 sec at 40% amplitude. 750 μ L of the lysate was then combined with 750 μ L of a 2% HNO₃ (v/v) solution, while the remainder of the lysate was quantified for protein by a bicinchoninic assay (BCA).²¹ The resulting 1% HNO₃ solution was analyzed for rhodium content on an HP-4500 ICP-MS unit. Rhodium counts were normalized to the amount of protein determined from the BCA analysis (to obtain ng [Rhodium]/mg [protein] values). Standard errors for three independent experiments are shown. The experiment was repeated with HCT116N cells for one time point only to verify similar uptake of rhodium by the two cell lines.

3.3 Results

3.3.1 Binding Affinities for Metal Complexes at Single Base Mismatches

The binding constants of the various rhodium metalloinsertors at a CC mismatch in a 29-mer DNA hairpin with the sequence 5'-GGCAGGCCATGGCTTTTTGCCATCCCTGCC-3' (underline denotes the mismatch) were measured. The hairpin sequence allows cleavage site determination on either strand around the mismatch site. All newly synthesized rhodium complexes promote relatively little DNA cleavage upon irradiation, and, as such, their binding affinities were determined through binding competition titrations with 1 μM *rac*-[Rh(bpy)₂(chrysi)]³⁺, which does cleave DNA upon irradiation.²²⁻²⁴ A representative photocleavage titration can be found in **Figure 3.1**. The degree of photocleavage can be plotted against the log([Rh]) and fit to a sigmoidal curve (**Figure 3.2**). On the basis of the binding constant of [Rh(bpy)₂(chrysi)]³⁺, the binding constants of all subsequent complexes are then determined by solving simultaneous equilibria at the inflection point of the photocleavage titration curve. The results, along with those of all previously reported compounds,^{15,22,25} are shown in **Figure 3.3**. Interestingly, despite the variance in both the ancillary ligands and number of hydrogen-bond donors, all compounds (except the extremely bulky [Rh(DIP)₂(chrysi)]³⁺) exhibit binding affinities within essentially the same order of magnitude, varying from $2.3 \times 10^6 \text{ M}^{-1}$ to $4.4 \times 10^7 \text{ M}^{-1}$.

3.3.2 Quantitation of Inhibition of Cellular Proliferation using an Enzyme-Linked Immunosorbent Assay (ELISA)

An ELISA for DNA synthesis was used to quantify the effects of the metalloinsertors on the proliferation of HCT116N cells (MMR-proficient) and HCT116O

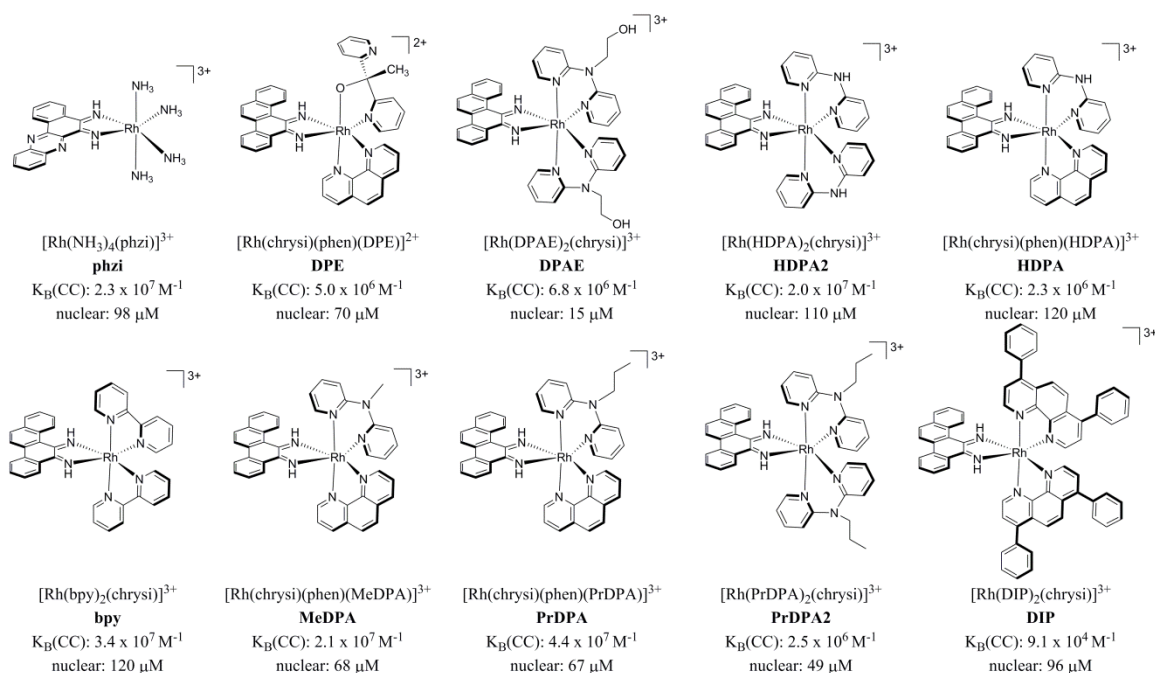


Figure 3.3 Chemical structures, binding affinities for CC mismatches, and approximated nuclear concentration of all compounds studied. Note all compounds are shown as the +3 complex. $\text{p}K_a$'s of the imine protons vary among complexes and thus the protonation state of the inserting ligand will vary at physiological pH among the complexes. Binding affinities for $[\text{Rh}(\text{DIP})_2(\text{chrysi})]^{3+}$, $[\text{Rh}(\text{HDPA})_2(\text{chrysi})]^{3+}$, $[\text{Rh}(\text{bpy})_2(\text{chrysi})]^{3+}$, $[\text{Rh}(\text{DPAE})_2(\text{chrysi})]^{3+}$, and $[\text{Rh}(\text{PrDPA})_2(\text{chrysi})]^{3+}$ are previously reported.^{13,15,22} All other compounds' DNA binding affinities were measured on the 29mer hairpin 5'-GGCAGGCATGGCTTTTTGCCATCCCTGCC-3' (underline denotes the mismatch) in a competition assay through photocleavage by $[\text{Rh}(\text{bpy})_2\text{chrysi}]^{3+}$. To determine nuclear rhodium concentrations, rhodium content was quantified by ICP-MS and first normalized to number of nuclei, then divided by the volume of the nucleus of a HCT116O cell, which was approximated as a sphere with radius 8 μm .²⁹ It is important to note that while the structures all illustrate the Δ isomers, all experiments were done with racemic mixtures.

cells (MMR-deficient). Both cell lines were incubated with 0-25 μM of each compound (except $[\text{Rh}(\text{DIP})_2(\text{chrysi})]^{3+}$ and $[\text{Rh}(\text{chrysi})(\text{phen})(\text{DPE})]^{2+}$, which were both administered at 0-5 μM concentrations due to increased potency). Incubations were performed for 1, 3, 6, 12 or 24 h. After the incubations, the medium containing Rh was replaced with fresh medium, and the cells were grown for the remainder of the 72 h period. The extent of cellular proliferation is expressed as the ratio of BrdU incorporated by the rhodium-treated cells as compared to untreated controls. Furthermore, we define differential inhibition as the difference in BrdU incorporation between the HCT116N and HCT116O cells. **Figure 3.4** and **Figure 3.5** show data for all compounds. Very little to no activity is seen for any of the compounds at 1- or 3-hour incubation times (data not shown).

Figure 3.6 summarizes the ELISA results for all compounds tested at 10 μM rhodium concentration and 24 h of incubation (Except $[\text{Rh}(\text{DIP})_2(\text{chrysi})]^{3+}$, which is shown at 2 μM), as these are the same conditions used for all ICP-MS experiments.^{15,25,26} There are four compounds with high selectivity for the MMR-deficient HCT116O cells ($[\text{Rh}(\text{NH}_3)_4(\text{phzi})]^{3+}$, $[\text{Rh}(\text{chrysi})(\text{phen})(\text{DPE})]^{2+}$, $[\text{Rh}(\text{DPAE})_2(\text{chrysi})]^{3+}$, and $[\text{Rh}(\text{HDP A})_2(\text{chrysi})]^{3+}$, all shown in different shades of blue), displaying differential inhibitions of $63 \pm 5\%$, $55 \pm 3\%$, $55 \pm 3\%$, and $52 \pm 2\%$, respectively. $[\text{Rh}(\text{chrysi})(\text{phen})(\text{HDP A})]^{3+}$ and $[\text{Rh}(\text{bpy})_2(\text{chrysi})]^{3+}$ exhibit modest selectivity with differential inhibitions of $27 \pm 2\%$ and $8 \pm 2\%$ at 24 h (shown in green in **Figure 3.6**). It should be noted that at longer incubation times the differential inhibition of $[\text{Rh}(\text{bpy})_2(\text{chrysi})]^{3+}$ increases.²⁵ $[\text{Rh}(\text{chrysi})(\text{phen})(\text{MeDPA})]^{3+}$, also shown in green, exhibits delayed biological activity. At 24 h incubation times, this complex does not

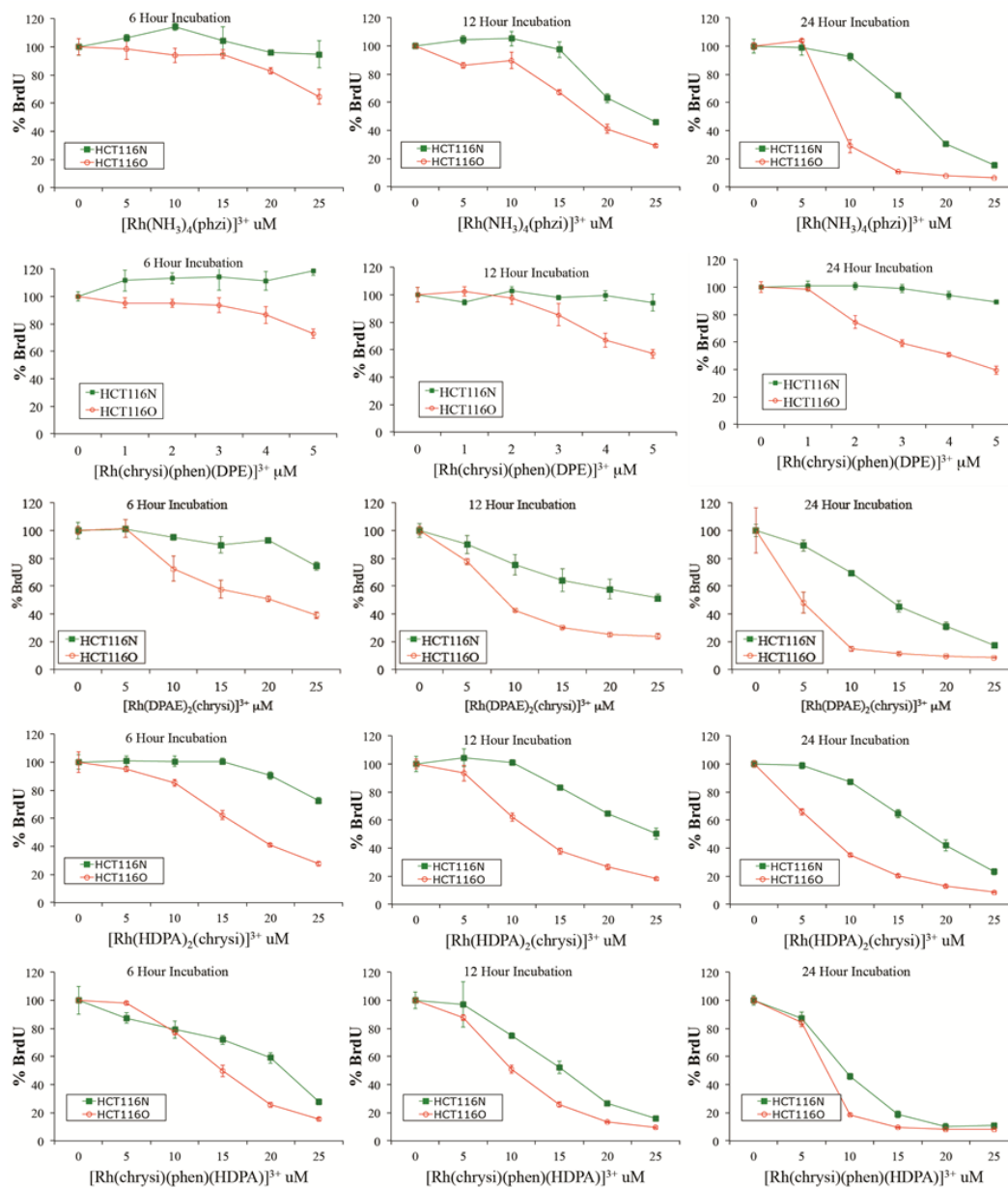


Figure 3.4 Inhibitory effects of (from top to bottom) $[\text{Rh}(\text{NH}_3)_4(\text{phzi})]^{3+}$, $[\text{Rh}(\text{chrysi})(\text{phen})(\text{DPE})]^{2+}$, $[\text{Rh}(\text{DPAE})_2(\text{chrysi})]^{3+}$, $[\text{Rh}(\text{HDPA})_2(\text{chrysi})]^{3+}$, and $[\text{Rh}(\text{chrysi})(\text{phen})(\text{HDPA})]^{3+}$ as a function of incubation time on cellular proliferation. Shown are plots of BrdU incorporation (a measure of DNA synthesis and therefore cellular proliferation) normalized to the BrdU incorporation of untreated cells as a function of rhodium concentration. Standard error bars for five trials are shown. 1- and 3-h plots are not shown, as no activity was observed.

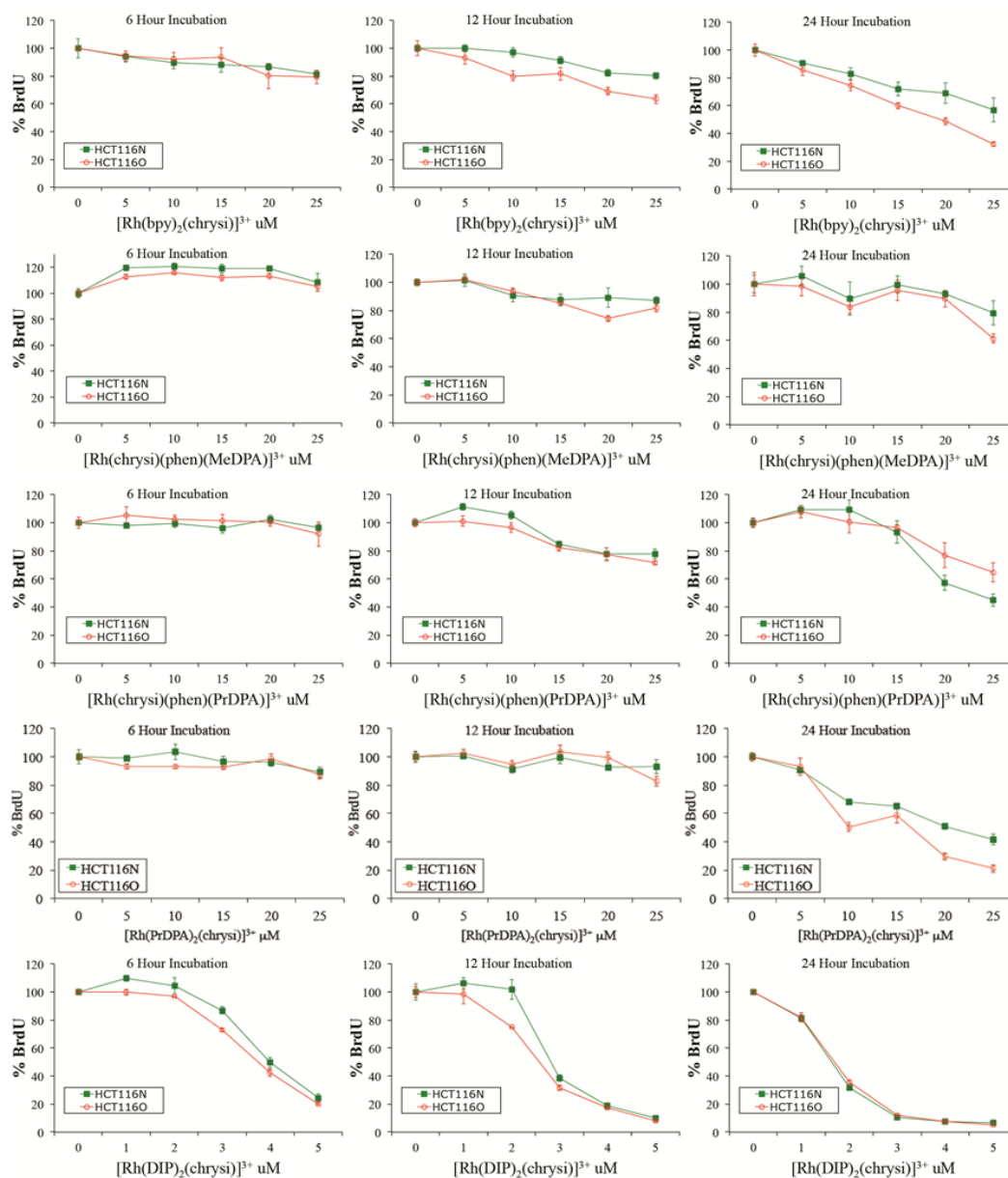


Figure 3.5 Inhibitory effects of (from top to bottom) $[\text{Rh}(\text{bpy})_2(\text{chrysi})]^{3+}$, $[\text{Rh}(\text{chrysi})(\text{phen})(\text{MeDPA})]^{3+}$, $[\text{Rh}(\text{chrysi})(\text{phen})(\text{PrDPA})]^{3+}$, $[\text{Rh}(\text{PrDPA})_2(\text{chrysi})]^{3+}$, and $[\text{Rh}(\text{PrDPA})_2(\text{chrysi})]^{3+}$ as a function of incubation time on cellular proliferation. Shown are plots of BrdU incorporation (a measure of DNA synthesis and therefore cellular proliferation) normalized to the BrdU incorporation of untreated cells as a function of rhodium concentration. Standard error bars for five trials are shown. 1- and 3-h plots are not shown, as no activity was observed.

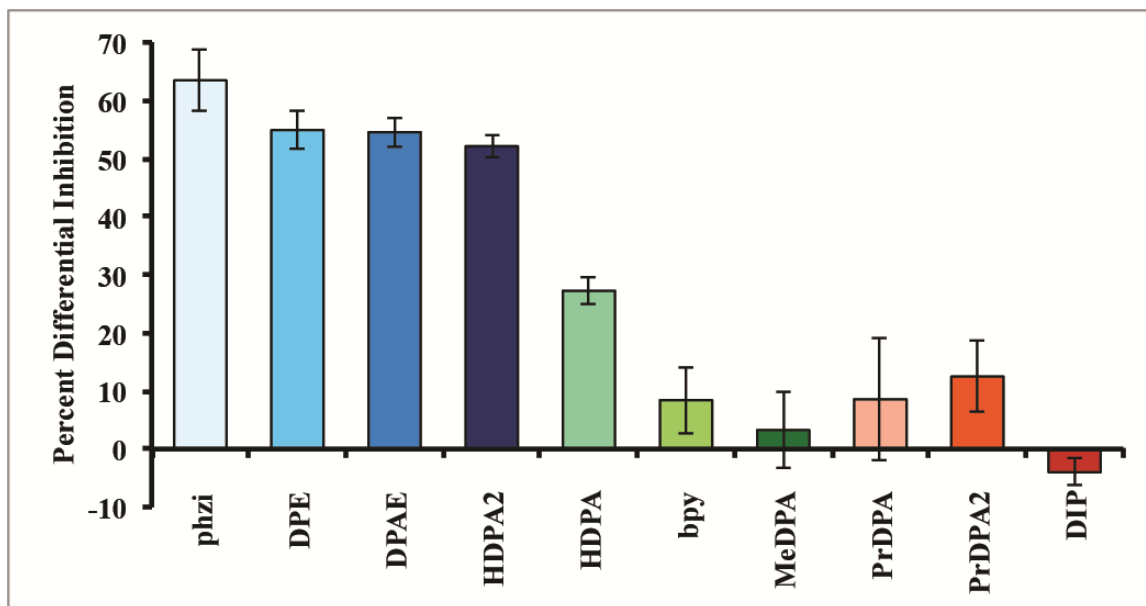


Figure 3.6 Inhibitory effects of rhodium metalloinsertors as a function of metalloinsertor identity. The percent differential inhibition is defined as the difference of the normalized percentages of cellular proliferation between the two cell lines, HCT116O versus HCT116N. ELISA analyses were performed as in **Figure 3.4** and **Figure 3.5**. Cells were incubated with 10 μM rhodium complex for 24 h (except $[\text{Rh}(\text{DIP})_2(\text{chrysi})]^{3+}$, which was administered at 2 μM).

display significant inhibition of DNA synthesis toward either cell line. The remaining compounds $[\text{Rh}(\text{chrysi})(\text{phen})(\text{PrDPA})]^{3+}$, $[\text{Rh}(\text{PrDPA})_2(\text{chrysi})]^{3+}$ and $[\text{Rh}(\text{DIP})_2(\text{chrysi})]^{3+}$, shown in red) exhibit no selectivity for the MMR-deficient HCT116O cell line, and inhibit DNA synthesis similarly in both cell lines. It should be noted that none of the complexes studied show a differential inhibition favoring the HCT116N cell line, although that is the common result for many DNA-damaging agents.

Many of these compounds exhibit accelerated activity in the ELISA assay, displaying substantial differential inhibition of DNA synthesis towards the HCT116O cell line at 6- or 12-h incubation times. Motivated by the previous observation that rhodium metalloinsertors which display accelerated activity in the ELISA assay exhibit preferential cytotoxicity towards the MMR-deficient HCT116O cell line,¹ we chose also to test all compounds for cytotoxicity in the MTT assay.

3.3.3 MTT Cytotoxicity Assay

The cytotoxic effects of all compounds were determined by MTT assay.¹⁹ Briefly, reduction of the MTT reagent by metabolically active cells leads to the production of formazan, which can then be dissolved in acidified SDS to produce a characteristic absorbance at 570 nm. This absorbance reflects the percentage of metabolically active cells in each sample. HCT116N and HCT116O cells were plated and treated with the various rhodium complexes at the concentrations indicated in **Figure 3.7** for 24, 48, or 72 h. Percent viability is defined as the ratio of the amount of formazan in the treated cells to that in the untreated cells, and differential cytotoxicity is defined as the difference between the percent viabilities of the two cell lines. The 72-h results are shown in **Figure 3.7**. These results are consistent with the ELISA assay results. The same four compounds

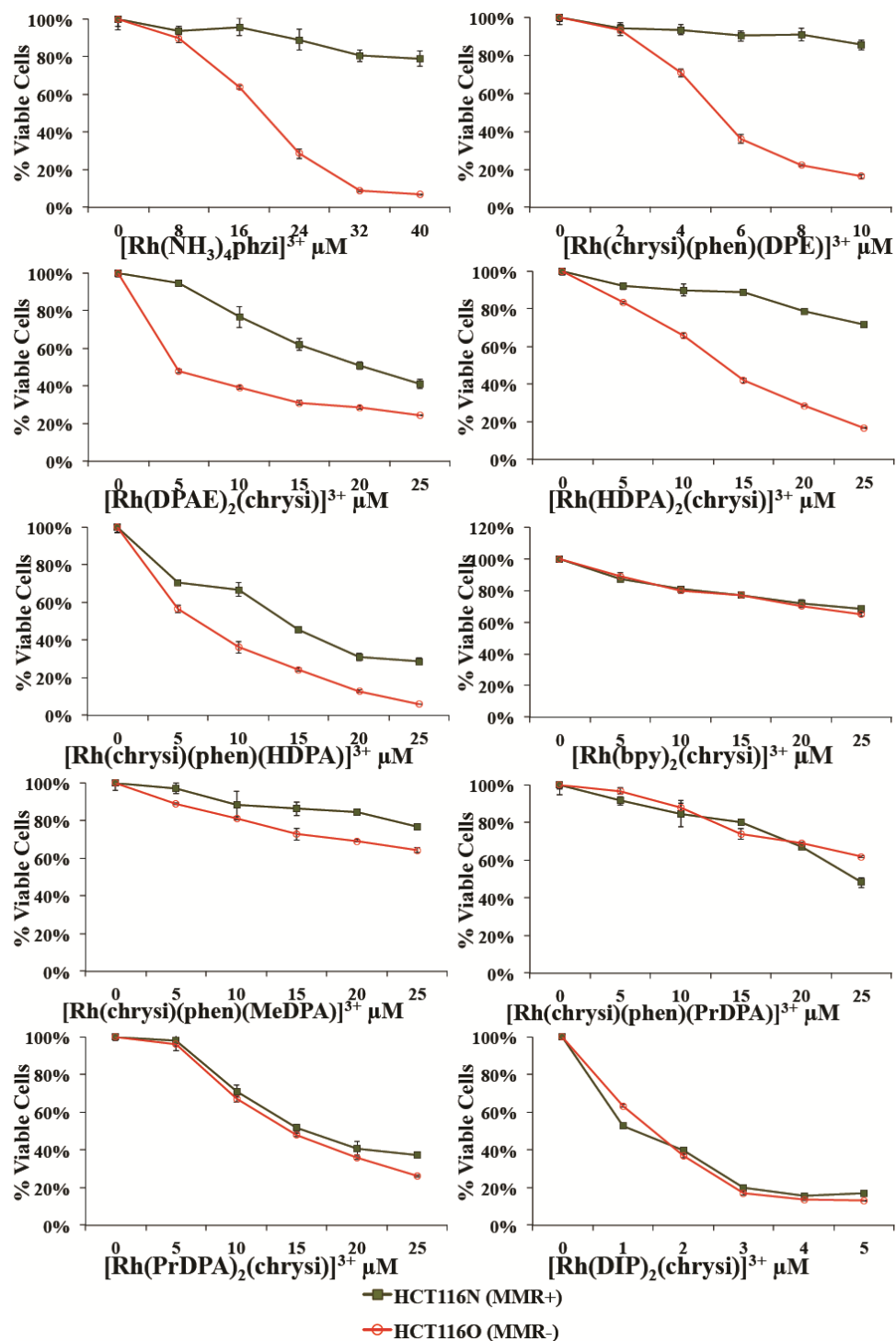


Figure 3.7 Differential cytotoxicities of rhodium metalloinsertors. HCT116N (green) and HCT116O (red) cells were plated in 96-well format at densities of 5×10^4 cells/well and treated with the concentrations of rhodium metalloinsertors indicated. After 72 hours, the cells were labeled with MTT for 4 hours.

that show the best differential inhibition of DNA synthesis in the ELISA assay ($[\text{Rh}(\text{NH}_3)_4(\text{phzi})]^{3+}$, $[\text{Rh}(\text{chrysi})(\text{phen})(\text{DPE})]^{2+}$, $[\text{Rh}(\text{DPAE})_2(\text{chrysi})]^{3+}$, and $[\text{Rh}(\text{HDPa})_2(\text{chrysi})]^{3+}$) exhibit highly selective cytotoxicities towards the MMR-deficient HCT116O cell line, $72 \pm 4\%$, $69 \pm 3\%$, $47 \pm 1\%$, and $55 \pm 1\%$, respectively (at their respective optimal concentrations). The compounds that exhibit delayed activity in the ELISA assay ($[\text{Rh}(\text{chrysi})(\text{phen})(\text{MeDPA})]^{3+}$ and $[\text{Rh}(\text{bpy})_2(\text{chrysi})]^{3+}$) do not display significant cytotoxicity toward either cell line in the MTT assay, consistent with previous observations.¹ The remaining compounds ($[\text{Rh}(\text{chrysi})(\text{phen})(\text{HDPa})]^{3+}$, $[\text{Rh}(\text{chrysi})(\text{phen})(\text{PrDPA})]^{3+}$, $[\text{Rh}(\text{PrDPA})_2(\text{chrysi})]^{3+}$, and $[\text{Rh}(\text{DIP})_2(\text{chrysi})]^{3+}$) exhibit either modest or no selective cytotoxicity towards the HCT116O cell line, consistent with their activities in the ELISA assay.

Despite our previous results²⁵ that rhodium metalloinsertors' biological activity correlates directly with their binding affinities, the metalloinsertors discussed herein have similar DNA binding affinities (except $[\text{Rh}(\text{DIP})_2(\text{chrysi})]^{3+}$), yet display biological activities that vary drastically. ICP-MS studies were undertaken in order to determine if the cellular uptake and distribution of these rhodium metalloinsertors could explain their variation in activities.

3.3.4 ICP-MS Assay for Whole-Cell Rhodium Levels

HCT116O cells were treated with 10 μM of each rhodium complex (except $[\text{Rh}(\text{DIP})_2(\text{chrysi})]^{3+}$, which was administered at 2 μM) for 1, 3, 6, 12, or 24 h. Whole cell lysates were analyzed for rhodium levels by ICP-MS and normalized to protein content (**Figure 3.8**). The experiment was repeated with HCT116N cells at 24 h to

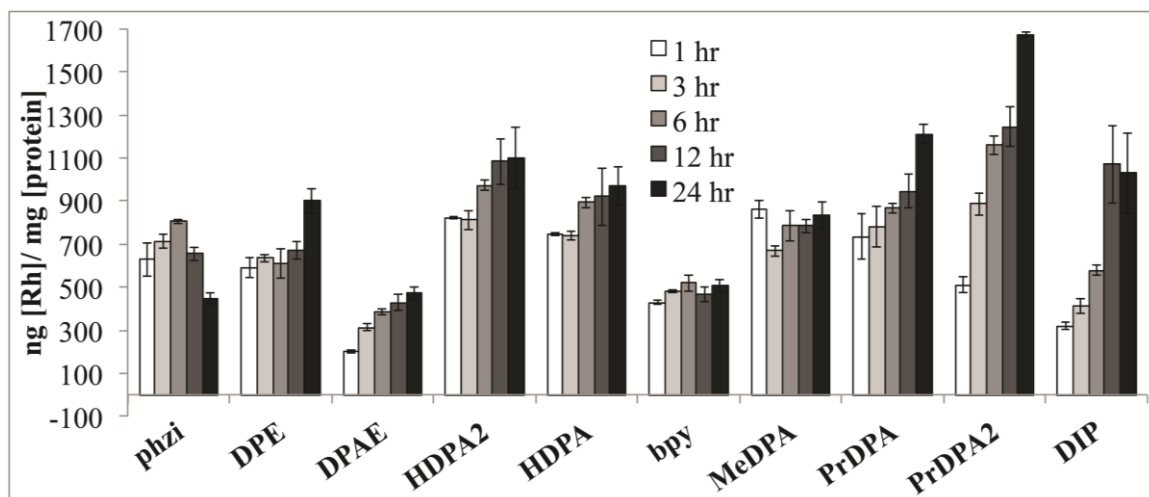


Figure 3.8 ICP-MS assay for whole-cell rhodium accumulation. HCT1160 cells were treated with 10 μM of each rhodium complex (except $[\text{Rh}(\text{DIP})_2(\text{chrysi})]^{3+}$, which was administered at 2 μM) for 1, 3, 6, 12, or 24 h. The cells were analyzed for rhodium content by ICP-MS. The rhodium counts were normalized to protein content, which was determined by a BCA assay. See **section 2.2.8**.

confirm that cellular uptake is not different for the HCT116 O versus N cells and to verify consistency in trends among the ten compounds.

There seem to be a variety of modes of uptake at play. The most lipophilic compounds $[\text{Rh}(\text{chrysi})(\text{phen})(\text{PrDPA})]^{3+}$, $[\text{Rh}(\text{PrDPA})_2(\text{chrysi})]^{3+}$, and $[\text{Rh}(\text{DIP})_2(\text{chrysi})]^{3+}$ exhibit gradual uptake into the HCT116O cells, suggestive of passive diffusion. This is consistent with previous studies conducted on luminescent $[\text{Ru}(\text{L})_2\text{dppz}]^{2+}$ (dppz = dipyrido[3,2- α :2',3'-c]phenazine) analogues, demonstrating cellular accumulation through passive diffusion, facilitated by the negative potential difference across the cell membrane,^{27,28} The two compounds that exhibit delayed biological activity in the ELISA assay $[\text{Rh}(\text{chrysi})(\text{phen})(\text{MeDPA})]^{3+}$ and $[\text{Rh}(\text{bpy})_2(\text{chrysi})]^{3+}$ exhibit no increase in cellular rhodium levels after initial uptake at 1 h. Furthermore, the two compounds with HDPA ligands exhibit an enhanced cellular uptake despite reduced lipophilicities. They show a very high initial uptake, followed by a slight increase over the next 23 hours. The MeDPA compound does not exhibit the increase in uptake that we had expected, given its enhanced lipophilicity compared to the HDPA analog. This suggests a completely different mechanism of uptake for the HDPA complex. The two compounds with PrDPA ligands do exhibit enhanced uptakes compared to their respective HDPA analogs at 24 h, but not nearly to the degree we would have expected based on lipophilicities. However, both the PrDPA compounds appear to be taken up through passive diffusion, unlike the HDPA compounds. Perhaps the fact that the HDPA ligand has the potential to form hydrogen bonds *in cellulo* is important to its path into the cell. The compounds that exhibit the highest selectivities in the biological assays $[\text{Rh}(\text{chrysi})(\text{phen})(\text{DPE})]^{2+}$, $[\text{Rh}(\text{DPAE})_2(\text{chrysi})]^{3+}$, and

[Rh(NH₃)₄(phzi)]³⁺) by no means have the highest overall rhodium levels. In fact, all three of them have among the lowest amount of rhodium uptake into cells.

3.3.5 ICP-MS Assay for Nuclear Rhodium Levels

The nuclear rhodium concentrations of all compounds were determined via ICP-MS. Briefly, HCT116O cells were treated with the various rhodium complexes for 24 h, the nuclei were isolated, and rhodium concentrations of the various samples were determined by ICP-MS and normalized to number of nuclei. The process was repeated with HCT116N cells to confirm that the two cell lines behave similarly and to verify consistency in trends among the ten compounds (data not shown). These numbers (in ng of rhodium per nuclei) can be used to estimate nuclear concentrations by approximating the nucleus of a HCT116O cell as a sphere with radius 4 μm.²⁹ The approximate nuclear rhodium concentrations, so determined, are reported in **Figure 3.3**.

As can be seen in **Figure 3.9**, there is little correlation between cell-selective activity and nuclear rhodium concentration. In fact, all nuclear rhodium concentrations except for that of [Rh(DPAE)₂(chrysi)]³⁺ are within a factor of two of each other and hardly vary among the 10 compounds. When we approximate the nuclear concentrations in molarity of the 10 compounds, all compounds are present in the nucleus at concentrations on the order of 10⁻⁵ to 10⁻⁴ M. These concentrations are all more than 2 orders of magnitude higher than the binding affinities for *in vitro* mismatch detection (yet below non-specific DNA binding levels²³). Thus, even estimating the error on these numbers to be an order of magnitude, all compounds are present in the nucleus at concentrations sufficient for mismatch binding.

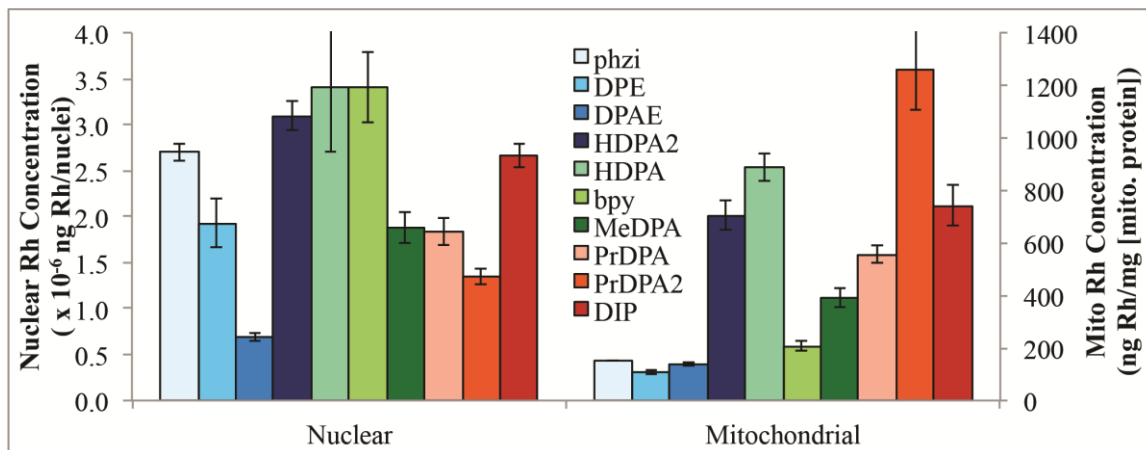


Figure 3.9 ICP-MS assay for nuclear and mitochondrial rhodium accumulation. HCT1160 cells were treated with 10 μM of each rhodium complex (except $[\text{Rh}(\text{DIP})_2(\text{chrysi})]^{3+}$, which was administered at 2 μM) for 24 h. The cells were harvested by trypsinization and appropriate organelle isolation procedures performed. The mitochondrial rhodium counts were normalized to protein content, which was determined by a BCA assay. The nuclear rhodium numbers were normalized to number of nuclei.

3.3.6 ICP-MS Assay for Mitochondrial Rhodium Levels

The mitochondrial rhodium concentrations of all compounds were determined via ICP-MS. Briefly, HCT116O cells were treated with the various rhodium complexes for 24 h, the mitochondria were isolated, and rhodium concentrations of the various samples were determined by ICP-MS and normalized to amount of protein. The results are summarized in **Figure 3.9** alongside the nuclear rhodium levels. The fact that the three compounds with the most cell-selective biological activity ($[\text{Rh}(\text{NH}_3)_4(\text{phzi})]^{3+}$, $[\text{Rh}(\text{chrysi})(\text{phen})(\text{DPE})]^{2+}$, and $[\text{Rh}(\text{DPAE})_2(\text{chrysi})]^{3+}$, shown in blue) have the lowest mitochondrial rhodium accumulation, 152 ± 3 ng [Rh]/ mg [mitochondrial protein], 106 ± 7 ng [Rh]/ mg [mitochondrial protein], and 141 ± 8 ng [Rh]/ mg [mitochondrial protein], respectively, is striking. This correlation indicates that the biological target of our rhodium metalloinsertors is genomic DNA rather than mitochondrial DNA.

Furthermore, the three compounds that exhibit no selectivity for the MMR-deficient HCT116O cell line in both biological assays ($[\text{Rh}(\text{chrysi})(\text{phen})(\text{PrDPA})]^{3+}$, $[\text{Rh}(\text{PrDPA})_2(\text{chrysi})]^{3+}$, and $[\text{Rh}(\text{DIP})_2(\text{chrysi})]^{3+}$, shown in red) display the highest levels of mitochondrial rhodium accumulation, 560 ± 30 ng [Rh]/ mg [mitochondrial protein], 1260 ± 150 ng [Rh]/ mg [mitochondrial protein] and 740 ± 70 ng [Rh]/ mg [mitochondrial protein], respectively. This result points to mitochondrial targeting as responsible for the promiscuous biological activity associated with these three compounds that detracts from the cell-selective activity. The two HDPA-containing compounds stray from the trends observed with the other eight compounds.

3.4 Discussion

3.4.1 Variations in Complexes Synthesized

The compounds displayed in **Figure 3.3** were initially synthesized in order to investigate the biological effects of varying the lipophilicity of the metalloinsertor. $[\text{Rh}(\text{HDPA})_2(\text{chrysi})]^{3+}$ has been shown to exhibit accelerated biological activity, as well as an enhanced selectivity for the MMR-deficient HCT116O cell line compared to that expected based solely on its binding affinity.^{1,25} By varying L in $[\text{Rh}(\text{chrysi})(\text{phen})(\text{L})]^{3+}$ from HDPA to MeDPA to PrDPA, we sought to examine the effect that changes in lipophilicity have on uptake and to determine if the proton associated with the HDPA ligand, which is not present in other compounds examined, might play some role in the enhanced activity and uptake of $[\text{Rh}(\text{HDPA})_2(\text{chrysi})]^{3+}$. The DPE ligand was originally intended as an analog of HDPA, but without the amine nitrogen which is capable of inverting its geometry. Its unexpected ligand coordination results in a distinctive Rh-O bond, which is the subject of future work. The chrysi analog of $[\text{Rh}(\text{NH}_3)_4(\text{phzi})]^{3+}$ was shown to exhibit excellent differential activity in the ELISA assay,²⁵ and therefore its phzi analog was synthesized both in the hopes of making a compound with increased efficacy, and to look at the biological effects of decreasing lipophilicity. The compounds $[\text{Rh}(\text{DPAE})_2(\text{chrysi})]^{3+}$ and $[\text{Rh}(\text{PrDPA})_2(\text{chrysi})]^{3+}$ were made as a matched pair to look at the biological effects of small structural changes to the ancillary ligands.

Surprisingly, all compounds exhibited binding affinities within the same order of magnitude (except $[\text{Rh}(\text{DIP})_2(\text{chrysi})]^{3+}$, which was included in the study as a reference compound with extreme lipophilicity, poor binding to mismatches, and no selectivity in our biological assays). The differences among these nine compounds in the ELISA and

MTT assays therefore arise from primarily biological effects rather than mismatch binding.

For all compounds, the cytotoxic effects seen in the MTT assay reflect the antiproliferative activity seen in the ELISA assay. Both compounds that exhibit delayed activity in the ELISA assay, $[\text{Rh}(\text{chrysi})(\text{phen})(\text{MeDPA})]^{3+}$ and $[\text{Rh}(\text{bpy})_2(\text{chrysi})]^{3+}$, do not show any significant cytotoxicity in the MTT assay. Furthermore, the four compounds with the largest differential inhibitions in the ELISA assay, $[\text{Rh}(\text{NH}_3)_4(\text{phzi})]^{3+}$, $[\text{Rh}(\text{chrysi})(\text{phen})(\text{DPE})]^{2+}$, $[\text{Rh}(\text{DPAE})_2(\text{chrysi})]^{3+}$, and $[\text{Rh}(\text{HDPA})_2(\text{chrysi})]^{3+}$, also show the largest differential cytotoxicities by the MTT assay. Finally, the three compounds with no differential activity in the ELISA assay, $[\text{Rh}(\text{chrysi})(\text{phen})(\text{PrDPA})]^{3+}$, $[\text{Rh}(\text{PrDPA})_2(\text{chrysi})]^{3+}$, and $[\text{Rh}(\text{DIP})_2(\text{chrysi})]^{3+}$, also show no differential cytotoxicity in the MTT assay. It is important to distinguish the absence of differential activity, where the compound shows no selectivity for one cell line over the other and affects both cell lines to the same degree, versus the absence of all activity, where the compound shows no appreciable biological effect on either cell line.

Significantly, the biological activities of these compounds vary dramatically despite their similar binding affinities. Interestingly, the effect of appending a lipophilic alkyl chain to the back of the HDPA ligand either significantly slows down all activity, as with the MeDPA derivative, or instead abolishes the selectivity of the compound for the MMR-deficient HCT116O cell line, as with the PrDPA derivatives. While the mechanism of inhibition is not yet fully understood, one possible scenario is protein recognition of the metalloinsertor-mismatch complex, generating a covalent protein-DNA lesion. Bulky tethers off the back of the metalloinsertor may inhibit the formation of such

a lesion, leading to the aforementioned observations. Yet another explanation for the results might be that the increased lipophilicity of the metalloinsertor enhances uptake into the cell but also alters the subcellular localization of the complex once it has entered the cell. This altered subcellular localization could be the reason for the lack of selectivity of the compound for one cell line over the other. Indeed, the least lipophilic compounds have the most selective biological activity, while the more lipophilic compounds exhibit no selective biological activity.

3.4.2 Metalloinsertor Uptake and Nuclear Accumulation

Table 3.1 displays qualitative nuclear and mitochondrial uptake properties, as well as the presence or absence of cell-selective biological activity for all ten metalloinsertors. Importantly, the biological effects seen in both assays can be explained by the subcellular localization of the metalloinsertors. If passive diffusion were the dominant mode of cellular uptake for these metalloinsertors,^{27,28} the more lipophilic compounds would be expected to have increased cellular uptake. And indeed, except for the HDPA compounds, the most lipophilic compounds do exhibit the greatest cellular accumulation. However, the more lipophilic compounds are in general associated with little differential biological activity; high accumulations of these metalloinsertors are toxic.

By altering L in $[\text{Rh}(\text{chrysi})(\text{phen})(\text{L})]^{3+}$ from HDPA to MeDPA to PrDPA, we do not observe an increase in uptake. In fact, the HDPA complex seems to show enhanced uptake in comparison with those that are more lipophilic. Furthermore, both compounds that possess HDPA ligands display both enhanced and accelerated uptake. This is likely due to additional uptake pathways facilitating the influx of complexes

Table 3.1 Qualitative nuclear^a and mitochondrial^b uptake properties, as well as the presence or absence of cell-selective biological activity^c for all ten metalloinsertors.

Compound	Nuclear Conc. ^a	Mito. Conc. ^b	Cell-Selective Activity ^c
[Rh(NH ₃) ₄ (phzi)] ³⁺	+	-	+
[Rh(chrysi)(phen)(DPE)] ³⁺	+	-	+
[Rh(DPAE) ₂ (chrysi)] ³⁺	+	-	+
[Rh(HDPA) ₂ (chrysi)] ³⁺	+	+	+
[Rh(chrysi)(phen)(HDPA)] ³⁺	+	+	+
[Rh(bpy) ₂ (chrysi)] ³⁺	+	+	-
[Rh(chrysi)(phen)(MeDPA)] ³⁺	+	+	-
[Rh(chrysi)(phen)(PrDPA)] ³⁺	+	+	-
[Rh(PrDPA) ₂ (chrysi)] ³⁺	+	+	-
[Rh(DIP) ₂ (chrysi)] ³⁺	+	+	-

^a Compound is considered to have “+” nuclear concentration if its nuclear concentration is sufficient for mismatch detection given its binding affinity. ^b Compound is considered to have “+” mitochondrial concentration if its mitochondrial rhodium concentration is ≥ 200 ng Rh/mg [mito protein]. ^cCompound is considered to have “+” cell-selective activity if its differential inhibition of DNA synthesis as measured by ELISA of the MMR-proficient line versus the MMR-deficient line is $\geq 25\%$ at 24 hr of incubation, 10 μ M compound concentration.

containing HDPA. Indeed, several bis(cyclometalated) iridium(III) polypyridine complexes have been shown to employ more than one mechanism of uptake,³⁰ and this may be the case for several of our metalloinsertors. In comparing $[\text{Rh}(\text{PrDPA})_2(\text{chrysi})]^{3+}$ to $[\text{Rh}(\text{DPAE})_2(\text{chrysi})]^{3+}$, it appears that by altering the methyl group of PrDPA to an alcohol, uptake is decreased by a factor of four, yet only the DPAE compound has cell-selective activity. Lastly, the most polar compound, $[\text{Rh}(\text{NH}_3)_4(\text{phzi})]^{3+}$, displays a peak in uptake at 3 hours, after which cellular rhodium levels seem to decrease steadily. This is most likely caused by an efflux mechanism, that is, pumping the complex out of the cell.

The ATP-binding cassette protein ABCG2 has been reported to be overexpressed in HCT116 cells,³¹ is known to exhibit substrate promiscuity,³² and may be responsible. Contrary to what would be expected, three of the four compounds with high activity have among the lowest cellular uptake at 24 hours, while the three compounds with no cell-selective activity have among the highest cellular uptake at 24 hours. It appears as though increased cellular uptake is actually detrimental to the unique cell-selective behavior of our metalloinsertors.

Significantly, the nuclear rhodium concentrations vary only slightly among the ten compounds. Importantly, by approximating the nucleus of an HCT116O cell as a sphere with diameter 8 μm ,²⁹ all of our metalloinsertors are present in the nucleus at sufficient concentrations for mismatch binding, given their *in vitro* binding affinities (**Figure 3.3**). Moreover, all metalloinsertors are below non-specific DNA binding concentrations,²³ which precludes non-specific DNA binding as a possible cause of the non-selective toxicity seen with 3 of our metalloinsertors. The only difference between the two cell lines is the presence of a functional copy of the MLH1 gene in the HCT116N

cell line, which encodes for an MMR protein found in the nucleus.³³ Therefore, any interactions the rhodium complexes have with the cell that are not associated with the nucleus may account for their nonspecific biological activity. Consequently, if nuclear DNA were the only cellular target for these metalloinsertors, then all compounds should exhibit similar differential activity due to their similar nuclear concentrations. However, these metalloinsertors could also interact with mitochondrial DNA, or become sequestered in lipid membranes throughout the cell (including the nuclear membrane, which would cause the nuclear rhodium concentration of such a complex to appear higher than it actually is), both of which would result in nonspecific biological activity.

3.4.3 Mitochondrial Accumulation of Rhodium Metalloinsertors

Importantly, the metalloinsertors that display highly cell-selective biological activity are generally associated with lower mitochondrial rhodium accumulation (**Figure 3.9**, complexes shown in blue), while the metalloinsertors that display non-selective toxicity show larger mitochondrial rhodium accumulation (**Figure 3.9**, complexes shown in red). These observations suggest that it is nuclear DNA targeting of our metalloinsertors that is responsible for their cell-selective biological activities rather than mitochondrial DNA targeting.

The two compounds $[\text{Rh}(\text{DPAE})_2(\text{chrysi})]^{3+}$ and $[\text{Rh}(\text{PrDPA})_2(\text{chrysi})]^{3+}$ exhibit this phenomenon quite simply.¹⁵ The only structural difference between the two compounds is the substitution of the methyl group of the PrDPA ligand for a primary alcohol in the DPAE ligand. While this substitution is structurally minute, the consequences of such a substitution are extreme from a biological standpoint. This substitution causes a large increase in polarity for the DPAE complex, as can be

quantified by a decrease in the logP values from -1.0 to -1.5.¹⁵ Significantly, this increase in polarity is accompanied by an increase in cell-selective biological activity. While the more lipophilic $[\text{Rh}(\text{PrDPA})_2(\text{chrysi})]^{3+}$ complex exhibits no selectivity for the MMR-deficient cell line, the more polar $[\text{Rh}(\text{DPAE})_2(\text{chrysi})]^{3+}$ complex is highly selective for the MMR-deficient line over the MMR-proficient line. Furthermore, this small structural change results in dramatic changes in uptake and localization of the compounds. While the more lipophilic $[\text{Rh}(\text{PrDPA})_2(\text{chrysi})]^{3+}$ complex has about a four-fold greater uptake into the cell than the polar $[\text{Rh}(\text{DPAE})_2(\text{chrysi})]^{3+}$ complex, it exhibits a ten-fold greater mitochondrial accumulation than the DPAE complex, and only a two-fold greater nuclear accumulation. This suggests that the non-selective behavior of $[\text{Rh}(\text{PrDPA})_2(\text{chrysi})]^{3+}$ is caused by increased mitochondrial accumulation.

It should be noted, however, that mitochondrial accumulation is not always associated with non-selective toxicity. The presence of the HDPA ligand enhances and accelerates uptake significantly, and even leads to increased mitochondrial accumulation, yet complexes containing HDPA show high selective biological activities. In fact, it has recently been reported that changes in polarity can affect whether mitochondria-targeted peptides simply accumulate in the mitochondrial matrix or disrupt the mitochondrial membrane activity and result in apoptosis.³⁴ Furthermore, while the antimetabolite methotrexate normally exhibits toxicity towards mammalian cells, when it is conjugated to a mitochondrial-penetrating peptide, the altered subcellular localization reduces its toxicity by three orders of magnitude.⁸

3.4.4 General Implications for Design

This work supports the hypothesis that nuclear DNA mismatch binding is responsible for the unique cell-selective biological activity of our rhodium metalloinsertors. Indeed, out of ten compounds studied, all ten exhibit sufficient nuclear uptake for mismatch binding. Furthermore, the fact that the three compounds that are not selective for the MMR-deficient cell line have enhanced mitochondrial accumulation indicates that mitochondrial mismatch DNA targeting is not responsible for cell-selective behavior (**Figure 3.10**). As the only difference between the two cell lines is a functional copy of the MLH1 gene, a gene which encodes for a nuclear MMR protein, the cell-selective behavior of our metalloinsertors must be related to this MMR deficiency. As the mitochondria are the location of oxidative phosphorylation, where reactive oxygen species are unavoidably formed as byproducts, mitochondrial DNA has higher levels of oxidative damage than nuclear DNA.³⁵ While these DNA defects could very well be targets of our metalloinsertors, mtDNA repair pathways do exist,³⁶ and in most cases are distinct from their nuclear counterparts.³⁷ Specifically, the nuclear MMR proteins MSH2, MSH3, MSH6, and MLH1 have been shown to be absent from the mitochondria.³⁸ The targeting of defects in mitochondrial DNA therefore cannot be responsible for the unique cell-selective behavior of our metalloinsertors. Instead, mitochondrial uptake appears to be associated with nonspecific toxicity.

3.5 Conclusion

In this work, all compounds tested are present in the nucleus at sufficient concentrations for mismatch detection. However, the more lipophilic compounds, which display enhanced uptake into the cells, tend to localize more in the mitochondria, thus

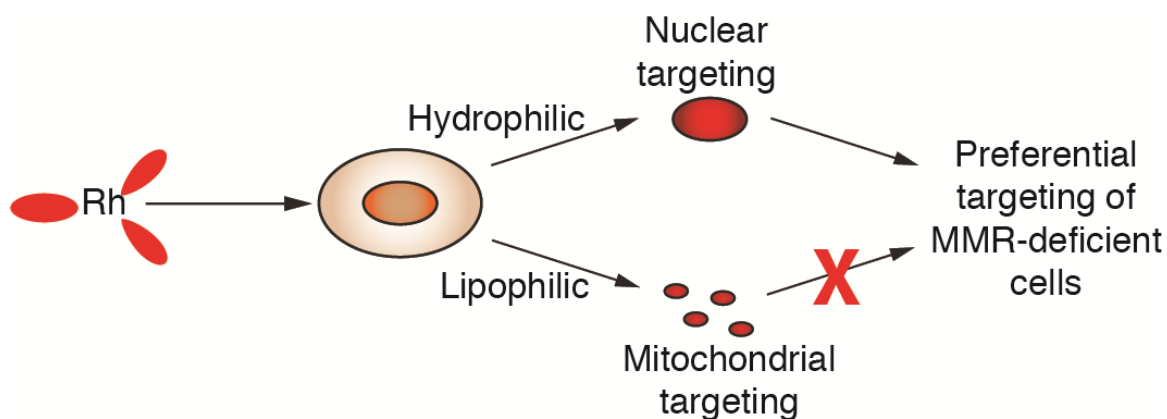


Figure 3.10 Model for the requirements for MMR-deficient cell-selectivity by rhodium metalloinsertors. All metalloinsertors localize to the nucleus in sufficient concentrations for mismatch binding. This genomic mismatch binding is thought to be responsible for the unique preferential targeting of MMR-deficient cells by rhodium metalloinsertors. If the compound is sufficiently lipophilic, mitochondrial targeting will occur, which will abolish any cell-selective activity resulting from nuclear localization.

giving rise also to nonspecific biological activity. While the more polar compounds, $[\text{Rh}(\text{NH}_3)_4(\text{phzi})]^{3+}$, $[\text{Rh}(\text{chrysi})(\text{phen})(\text{DPE})]^{2+}$, and $[\text{Rh}(\text{DPAE})_2(\text{chrysi})]^{3+}$, do not have the largest amount of cellular rhodium, there is consequently a smaller amount of rhodium in the mitochondria. This, coupled with sufficient nuclear rhodium for mismatch binding, gives rise to high MMR-deficient cell-selective biological activities for these three compounds. It seems that by increasing lipophilicity in an effort to increase uptake *via* passive diffusion, the subcellular localization is altered, leading to a larger amount of cellular rhodium residing in the mitochondria and less selectivity for the MMR-deficient cell line. This tradeoff in uptake for selectivity is in contrast to current strategies to improve the efficacy of cisplatin by increasing uptake of the drug.^{39,40} More generally, these results highlight that the relative accumulation of the complexes in different organelles needs to be considered, not simply cellular accumulation.

Most importantly, these data support the notion that the cell-specific activity we observe is caused by nuclear DNA mismatch targeting by our metalloinsertors. This exciting new result gives us key information in designing the next generation of rhodium metalloinsertors as cell-specific chemotherapeutics.

3.6 References

- 1 Ernst, R. J.; Komor, A. C.; Barton, J. K. *Biochemistry* **2011**, *50*, 10919-10928.
- 2 Golstein, P.; Kroemer, G. *Trends Biochem.* **2007**, *32*, 37-43.
- 3 McCall, K. *Curr. Opin. Cell Biol.* **2010**, *22*, 882-888.
- 4 Napolitano, S. M.; Aprille, J. R. *Adv. Drug Delivery Rev.* **2001**, *49*, 63-70.
- 5 Klein, A. V.; Hambley, T. W. *Chem. Rev.* **2009**, *109*, 4911-4920.
- 6 Ghezzi, A.; Aceto, M.; Cassino, C.; Gabano, E.; Osella, D. *J. Inorg. Biochem.* **2004**, *98*, 73-78.
- 7 Puckett, C. J.; Barton, J. K. *J. Am. Chem. Soc.* **2009**, *131*, 8738-8739.
- 8 Pereira, M. P.; Kelley, S. O. *J. Am. Chem. Soc.* **2011**, *133*, 3260-3263.
- 9 Meyer-Losic, F.; Quinonero, J.; Dubois, V.; Alluis, B.; Dechambre, M.; Michel, M.; Cailler, F.; Fernandez, A.-M.; Trouet, A.; Kearsy, J. *J. Med. Chem.* **2006**, *49*, 6908-6916.
- 10 Keizer, H. G.; Schuurhuis, G. J.; Broxterman, H. J.; Lankelma, J.; Schoonen, W. G. E. J.; Rijn, J. v.; Pinedo, H. M.; Joenje, H. *Cancer Res.* **1989**, *49*, 2988-2993.
- 11 Liu, J. L.; Galettis, P.; Farr, A.; Maharaj, L.; Samarasingha, H.; McGechan, A. C.; Baguley, B. C.; Bowen, R. J.; Berners-Price, S. J.; McKeage, M. J. *J. Inorg. Biochem.* **2008**, *102*, 303-310.
- 12 Groessl, M.; Zava, O.; Dyson, P. J. *Metallomics* **2011**, *3*, 591-599.
- 13 Ernst, R. J.; Song, H.; Barton, J. K. *J. Am. Chem. Soc.* **2009**, *131*, 2359-2366.
- 14 Zeglis, B. M.; Barton, J. K. *Nat. Protocols* **2007**, *2*, 357-371.
- 15 Weidmann, A. G.; Komor, A. C.; Barton, J. K. *Philos. Trans. R. Soc. A.*, **2013**, *371*, 20120117.

- 16 Muerner, H.; Jackson, B. A.; Barton, J. K. *Inorg. Chem.* **1998**, *37*, 3007-3012.
- 17 Basu, A.; Bhaduri, S.; Sapre, N. Y.; Jones, P. G. *J. Chem. Soc., Chem. Commun.* **1987**, *22*, 1724-1725.
- 18 Reitmar, A. H.; Risley, R.; Bristow, R. G.; Wilson, T.; Ganesh, A.; Jang, A.; Peacock, J.; Benchimol, S.; Hill, R. P. *Cancer Res.* **1997**, *57*, 3765-3771.
- 19 Mosmann, T. *J. Immunol. Methods* **1983**, *65*, 55-63.
- 20 Ahmad, K. A.; Iskandar, K. B.; Hirpara, J. L.; Clement, M-V.; Pervaiz, S. *Cancer Res.* **2004**, *64*, 7867-7878.
- 21 Smith, P. K.; Krohn, R. I.; Hermanson, G. T.; Mallia, A. K.; Gartner, F. H.; Provenzano, M. D.; Fujimoto, E. K.; Goetze, N. M.; Olson, B. J.; Klenk, D. C. *Anal. Biochem.* **1985**, *150*, 76-85.
- 22 Jackson, B. A.; Barton, J. K. *J. Am. Chem. Soc.* **1997**, *119*, 12986-12987.
- 23 Jackson, B. A.; Barton, J. K. *Biochemistry* **2000**, *39*, 6176-6182.
- 24 Jackson, B. A.; Alekseyev, V. Y.; Barton, J. K. *Biochemistry* **1999**, *38*, 4655-4662.
- 25 Ernst, R. J.; Song, H.; Barton, J. K. *J. Am. Chem. Soc.* **2009**, *131*, 2359-2366.
- 26 ELISA data on five of these compounds have been reported previously in ref. 15 and 25. However, the ELISA data reported here were obtained in parallel under the same conditions for all ten metalloinsertors to verify trends.
- 27 Puckett, C. A.; Barton, J. K. *J. Am. Chem. Soc.* **2007**, *129*, 46-47.
- 28 Puckett, C. A.; Barton, J. K. *Biochemistry* **2008**, *47*, 11711-11716.
- 29 Fujioka, A.; Terai, K.; Itoh, R. E.; Aoki, N.; Nakamura, T.; Kuroda, S.; Nishida, E.; Matsuda, M. *J. Biol. Chem.* **2006**, *281*, 8917-8926.

- 30 Zhang, Y.; Lo, K. K-W. *Inorg. Chem.* **2009**, *48*, 6011-6025.
- 31 Candeil, L.; Gourdiere, I.; Peyron, D.; Vezzio, N.; Copois, V.; Bibeau, F.; Orsetti, B.; Scheffer, G. L.; Ychou, M.; Khan, Q. A.; Pommier, Y.; Pau, B.; Martineau, P.; Del Rio, M. *Int. J. Cancer* **2004**, *109*, 848-854.
- 32 Eckford, P. D. W.; Sharom, F. J. *Chem. Rev.* **2009**, *109*, 2989-3011.
- 33 Fink, D.; Nebel, S.; Aebi, S.; Zheng, H.; Kim, H. K.; Christen, R. D.; Howell, S. B. *Cancer* **1997**, *76*, 890-893.
- 34 Horton, K. L.; Pereira, M. P.; Stewart, K. M.; Fonseca, S. B.; Kelley, S. O. *ChemBioChem* **2012**, *13*, 476-485.
- 35 Yakes, F. M.; Van Houten, B. *Proc. Natl. Acad. Sci. USA* **1997**, *94*, 514-519.
- 36 Tomkinson, A. E.; Bonk, R. T.; Linn, S. *J. Biol. Chem.* **1988**, *263*, 12532-12537.
- 37 Liu, P.; Demple, B. *Environ. Mol. Mutagen.* **2010**, *51*, 417-426.
- 38 de Souza-Pinto, N. C.; Mason, P. A.; Hashiguchi, K.; Weissman, L.; Tian, J.; Guay, D.; Lebel, M.; Stevensner, T. V.; Rasmussen, L. J.; Bohr, V. A. *DNA Repair* **2009**, *8*, 704-719.
- 39 Fuertes, M. A.; Alonso, C.; Perez, J. M. *Chem. Rev.* **2003**, *103*, 645-662.
- 40 Gately, D. P.; Howell, S. B. *Br. J. Cancer* **1993**, *67*, 1171-1176.

Chapter 4: An Inducible, Isogenic Cancer Cell Further Validates Rhodium Metalloinsertors as Selective Chemotherapeutic Agents**

4.1 Introduction

Genome instability is a hallmark of cancer cells and can lead to numerical or structural changes to chromosomes (chromosome instability, or CIN), or nucleotide mismatch repair (MMR) deficiency (MIN).¹ While CIN can result from loss of function of a number of cellular pathways, MIN results specifically from defects in the MMR system and is identifiable by the gain or loss of mono-, di- or tri-nucleotide repeat sequences, referred to as microsatellite instability (MSI).² Replication errors such as polymerase slippage generate small insertion-deletion loops (IDLs) or single base mismatches in the DNA. DNA damage can also modify bases to cause mismatches. In human cells that are MMR-proficient, heterodimers that contain the bacterial MutS homolog MSH2 bind a mismatch, and then heterodimers that contain the bacterial MutL homolog MLH1 associate with the protein-DNA complex to mediate the recruitment of repair factors that excise the mismatch and restore the correct DNA sequence. MMR-deficient cells are unable to correct mismatches, and this results in incorporation of errors into the DNA template and a mutator phenotype.

MMR deficiency is strongly linked with cancer. Germ line mutation of MMR genes, particularly MLH1 or MSH2, is the basis of hereditary non-polyposis colorectal cancer (HNPCC), or Lynch syndrome, which confers susceptibility to colorectal cancer

** Adapted from Bailis, J. M.; Gordon, M. L.; Gurgel, J. L.; Komor, A. C.; Barton, J. K.; Kirsch, I. R. An Inducible, Isogenic Cancer Cell Line System for Targeting the State of Mismatch Repair Deficiency *PLoS ONE* **2013**, *10*, e78726.

Acknowledgements: Julie Bailis developed the inducible cell line and performed all cell culture experiments; I confirmed MLH1 knockdown upon doxycycline treatment in our laboratory and supplied all metalloinsertors.

but also to other specific cancer types including endometrial and ovarian cancer.^{3,4} Mutation or hypermethylation of MMR genes in somatic cells is associated with ~15% of sporadic colorectal cancers, as well as ~10-15% of ovarian, endometrial and gastric cancers.⁵ MMR deficiency and MSI have also been identified in up to 20% of leukemias in patients that relapse or develop the disease as a consequence of prior chemotherapeutic treatment.⁶

MMR deficiency and MSI also occur in primary lung cancer associated with smoking or exposure to chromium.⁷⁻⁹ Cancers with MSI have been reported to be resistant to several standard-of-care chemotherapeutic agents, such as the antimetabolite 5-fluorouracil (5-FU), the platinum compounds cisplatin and carboplatin, the alkylating drug temozolomide, and the topoisomerase inhibitor etoposide.¹⁰ Inactivation of the MMR pathway may allow cells to tolerate certain types of DNA damage without initiating a pathway of programmed cell death.¹¹

One challenge to identifying therapies for MMR-deficient cancers is that the molecular targets and clinical phenotypes resulting from inactivation of MMR genes are variable. MMR deficiency can lead to frameshift mutations in genes that contain repeat sequences in the DNA, and at least 30 genes have been identified as potential targets of MSI, including the oncogenes BRAF and KRAS, and the DNA damage response genes MRE11, BRCA1 and ATR.^{12,13} Efforts to identify novel therapeutic targets that exhibit synthetic lethality with MMR-deficient cancer cells have revealed different genetic interactions with loss of function of MLH1 compared to loss of function of MSH2,¹⁴ even though the MLH1 and MSH2 proteins function in the same biochemical pathway. Together, these observations support the idea that cancers with MSI represent a

multifaceted, heterogeneous set of diseases. In consideration of the complexity of MSI tumors, the end phenotype or “state” of mismatch repair deficiency itself has previously been proposed as a target for chemotherapeutics.^{15,16}

In the current effort described here, the goal was to develop tools to enable studies of induced mismatch repair deficiency. A completely isogenic cell line system in which expression of the MMR gene MLH1 can be switched on or off using shRNA is described. The lung adenocarcinoma NCI-H23, a cell line selected based on relatively high levels of MLH1 that could be reversibly inactivated by shRNA, is used as a model. In this study, MMR deficiency in the NCI-H23 cell line system is induced and results in MSI and increased resistance to DNA-damaging agents. As a potential step toward developing a therapeutic that targets the end “state” of MMR deficiency, this cell line system is used to further validate rhodium metalloinsertors as chemotherapeutic agents.

4.2 Experimental Protocols

4.2.1 Antibodies and Western Blots

Protein lysates were prepared in lysis buffer (50mM HEPES, 1% Triton X-100, 150mM NaCl, 1mM EGTA, 10% glycerol, 1mM DTT) to which phosphatase and protease inhibitors (20mM β -glycerophosphate, 100mM sodium fluoride, 0.5mM PMSF, 0.1mM sodium orthovanadate, 10ug/ml leupeptin) were added. Lysates were cleared by centrifugation and then analyzed by SDS-PAGE on 4-12% Bis-Tris gels (Invitrogen), followed by immunoblotting. Primary antibodies used were against MLH1 (Becton Dickinson #551091), MSH2 (Becton Dickinson #556349), GAPDH (Abcam #ab9484), phosphorylated histone H2AX (Millipore #05-636) or tubulin (Cell Signaling #2148). Primary antibodies were detected by secondary antibodies conjugated to IRDye700 or

IRDye800 (LiCOR) and visualized with the LiCOR Odyssey. Each western blot experiment was carried out at least twice, on independent days.

4.2.2 Cell Viability Assays

Cells grown in the absence or presence of doxycycline were plated at 2,000-5,000 cells per well in 96-well plates and allowed to incubate overnight. Cells were then treated with compounds in a dose response for 4 days. Cell viability was assessed using a Cell Titer Glo assay (Promega) for ATP metabolism. Cell viability assays were performed in duplicate in at least 3 independent experiments.

Phase contrast imaging of cells during the proliferation experiments was carried out using an IncuCyte with a 20X objective (Essen BioScience).

Colony-forming assays were used to further assess cell viability following compound treatment. Cells grown in the absence or presence of doxycycline were plated at 500-2,000 cells per well of a 6-well plate and allowed to incubate overnight. Cells were treated with compounds in a dose response for 24h, and then media was aspirated and replaced with fresh media that did not contain compound. Colonies were visualized with crystal violet stain at 10-12 d.

SA-beta-galactosidase (SA- β -gal) production was assessed using a histochemical stain for beta-galactosidase activity at pH 6.0 (Sigma-Aldrich). Cells were untreated or treated with compounds as indicated for 3d, and then cells were fixed, stained for SA- β -gal and imaged using a Zeiss Axio inverted microscope equipped with a color camera.

4.2.3 Statistical Analysis

For the cell viability assays, paired t tests were used to compare half maximal inhibitory (IC₅₀) values or median lethal dose (LD₅₀) from multiple experiments and

determine p values. p values less than 0.05 were considered statistically significant. Statistical analysis was done with Graph Pad Prism software.

4.2.4 Synthesis of Chemical Compounds

Synthesis of $[\text{Rh}(\text{DIP})_2\text{chrysi}]^{3+}$ has been described.¹⁷ $[\text{Rh}(\text{HDPA})_2\text{chrysi}]^{3+}$ and $[\text{Rh}(\text{chrysi})(\text{phen})(\text{DPE})]^{2+}$ were synthesized as previously described (2.2.2.4 and 3.2.3.6, respectively).^{18,19} Cisplatin, doxorubicin, etoposide, 6-thioguanine and temozolomide were obtained from Sigma-Aldrich and dissolved in DMSO or water.

4.3 Results

4.3.1 Inhibition of MLH1 by shRNA Reduces MLH1 Protein Levels

The NCI-H23 lung adenocarcinoma cell line is proficient for mismatch repair and contains relatively high levels of the MMR proteins MLH1 and MSH2.²⁰ With the goal of generating a matched system that induces MMR deficiency and allows direct comparison to MMR-proficient cells, our collaborators at Amgen transduced NCI-H23 cells with lentivirus containing inducible shRNA to MLH1, and cells that stably integrated the construct into the genome were selected and expanded. Two subclones of this new cell line, labeled 4-10 and 4-13, were obtained from Amgen and tested for MLH1 inhibition following doxycycline treatment. Under normal growth conditions, the integrated shRNA was not active and MLH1 continued to be expressed. However, following addition of doxycycline to the media, shRNA was induced, which sequentially led to near complete (>90%) inhibition of the MLH1, as measured by Western blot analysis of protein lysates (Figure 4.1).

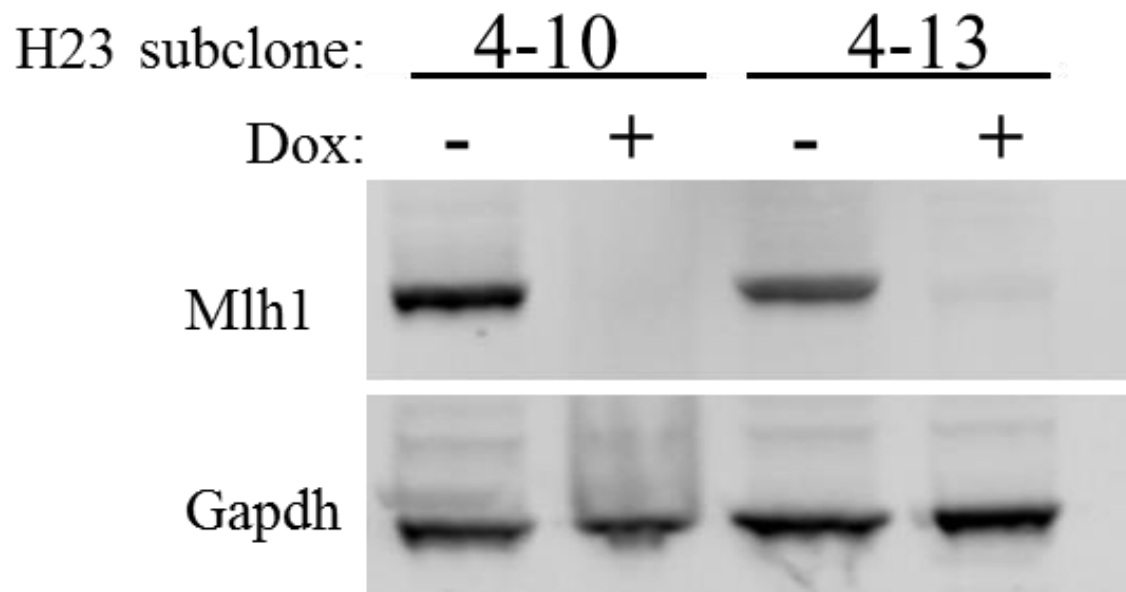


Figure 4.1 MLH1 shRNA expression is inducible. NCI-H23 subclones 4-10 and 4-13 were induced for MLH1 shRNA by splitting into two cultures, one maintained in inducing conditions (+ Dox) and the other grown in the absence of doxycycline (- Dox). Protein lysates were prepared and analyzed by SDS-PAGE, followed by immunoblotting for expression of the MLH1 protein. GAPDH was used as a control for equal protein loading across samples.

4.3.2 MLH1-Deficient NCI-H23 Subclones Exhibit Increased Resistance to Chemotherapeutic Drugs

We next tested whether induced MMR deficiency would cause resistance to DNA damaging agents. We directly compared the MMR-deficient NCI-H23 subclones to MMR-proficient cells from the same subclone that were obtained by allowing the cells to re-express MLH1. The MMR-deficient and MMR-proficient subclones were treated with the topoisomerase inhibitor etoposide or the alkylating agent temozolomide, and cell viability was assessed after 4 d (**Figure 4.2** and **Figure 4.3**). The MMR-proficient subclones (shRNA uninduced) did not show a significant difference in sensitivity to the compounds compared to parental NCI-H23 cells that were either untreated or treated with doxycycline ($p=0.33$) (**Figure 4.2**). For each matched pair of cells (for example, subclone 4-10 uninduced compared to 4-10 induced), the MLH1-deficient cells were consistently at least two-fold more resistant to these compounds than the isogenic MLH1-proficient cells, a finding that is statistically significant ($p=0.03$ for cells treated with etoposide, and $p=0.009$ for cells treated with temozolomide). The MLH1-deficient subclones were also more resistant to the crosslinking agent cisplatin ($p=0.02$), the purine analog 6-thioguanine ($p=0.05$), and another topoisomerase inhibitor, doxorubicin ($p=0.04$) (**Figure 4.4**). The approximately two-fold difference in viability of MMR-deficient cells versus MMR-proficient cells *in vitro* in response to chemotherapeutic agents has been reported previously and shown to translate to drug resistance *in vivo*.^{4,10} To confirm that the differential effect on viability is due to the presence or absence of MLH1, we used different shRNA sequences, 362 and 2239, to inhibit MLH1 expression and then characterized cell sensitivity to chemotherapeutic drugs. We observed that the MLH1-

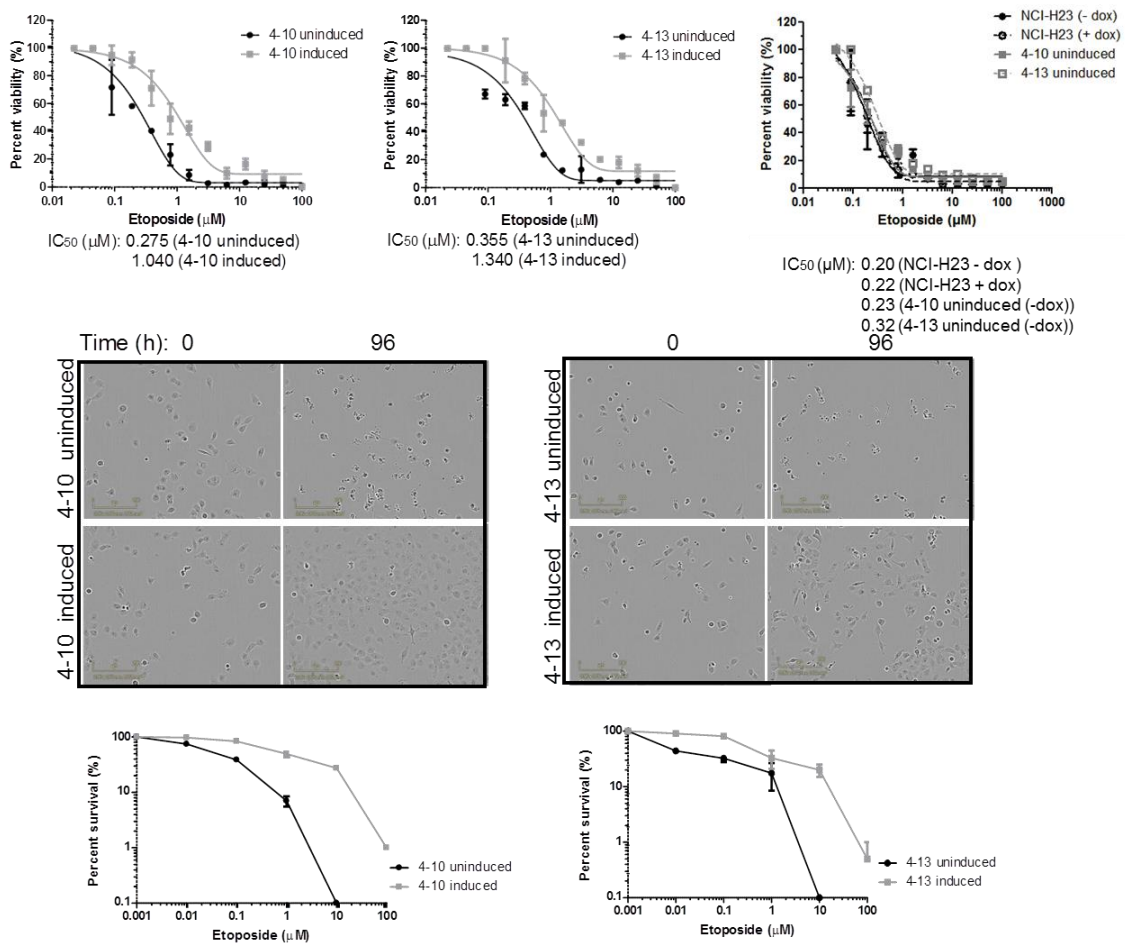


Figure 4.2 NCI-H23 subclones that were uninduced or induced for MLH1 shRNA were treated with etoposide. (Top) Cells were treated at the concentrations indicated, and cell viability was assessed at 4d using a Cell Titer Glo assay. The graphs indicate the relative survival for duplicate samples from a single experiment. (Middle) Representative phase contrast images of cells treated with 390 μ M etoposide during the viability experiments. 0h and 96h time points are shown. (Bottom) Cells were treated with etoposide for 24h at the concentrations indicated, and colony-forming ability after compound washout was assessed. The graphs display percent survival at 10d for duplicate samples of compound treated cells.

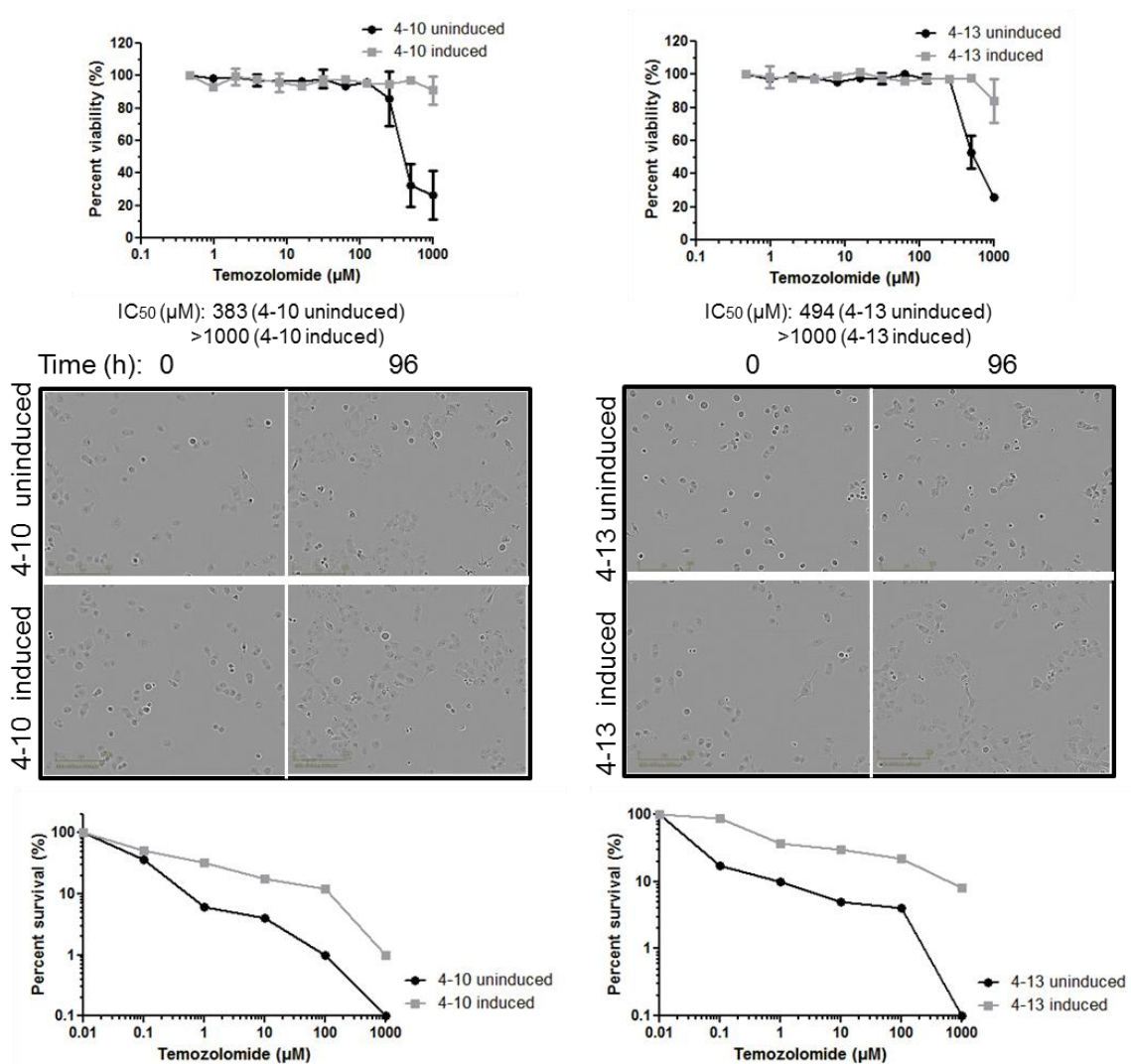


Figure 4.3 NCI-H23 subclones that were uninduced or induced for MLH1 shRNA were treated with temozolomide. (Top) Cells were treated at the concentrations indicated, and cell viability was assessed at 4d using a Cell Titer Glo assay. The graphs indicate the relative survival for duplicate samples from a single experiment. (Middle) Representative phase contrast images of cells treated with 500 μ M temozolomide during the viability experiments. 0h and 96h time points are shown. (Bottom) Cells were treated with temozolomide for 24h at the concentrations indicated, and colony-forming ability after compound washout was assessed. The graphs display percent survival at 10d for duplicate samples of compound treated cells.

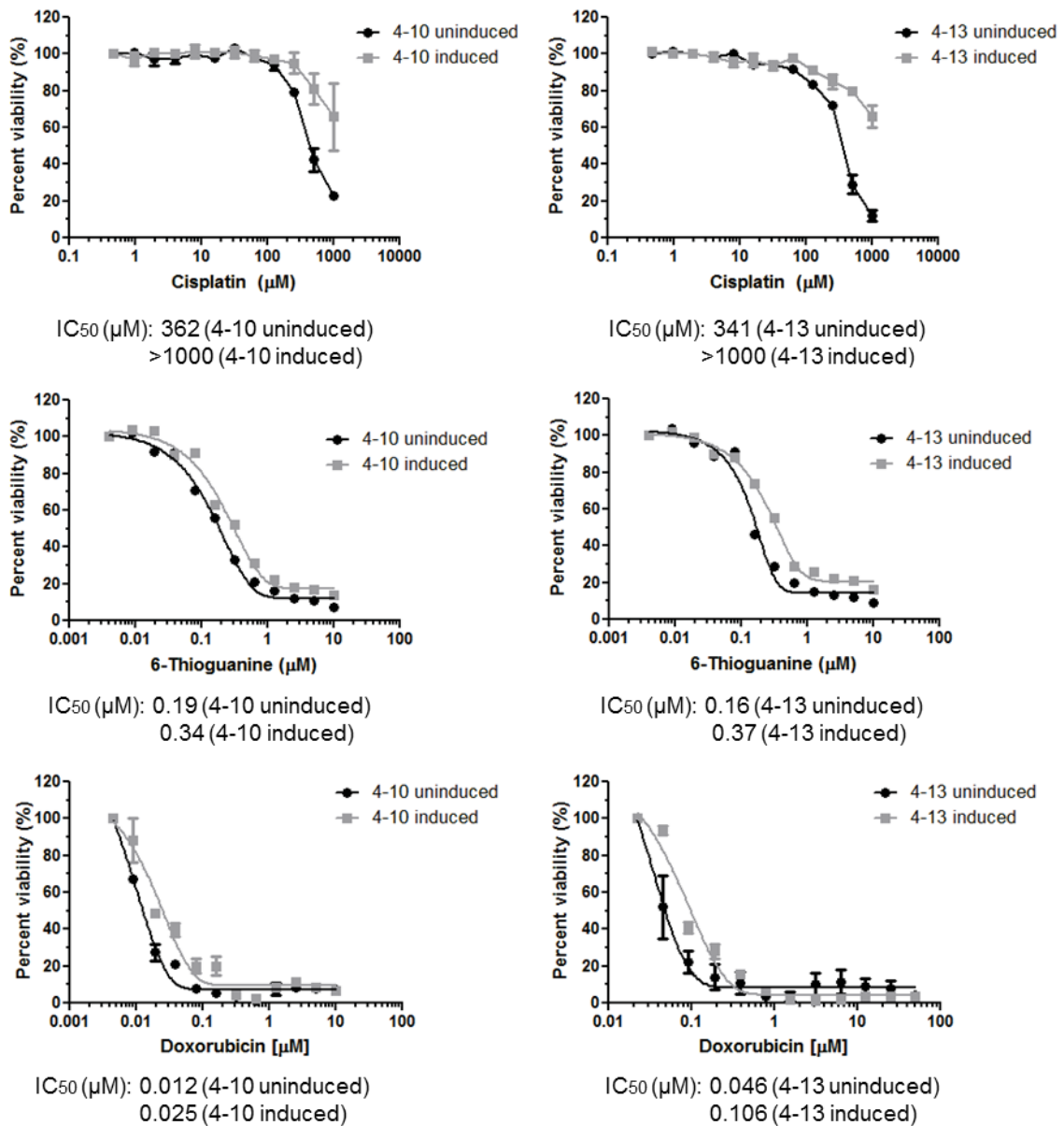


Figure 4.4 MLH1-deficient NCI-H23 subclones display increased resistance to DNA-damaging drugs. NCI-H23 subclones that were uninduced or induced for MLH1 shRNA were treated with (top) cisplatin, (middle) 6-thioguanine or (bottom) doxorubicin as indicated, and then cell viability was assessed after 4d using a Cell Titer Glo assay. The graphs indicate the relative survival for duplicate samples from a single experiment.

deficiency resulting from induction of these independent shRNA triggers led to a similar increase in resistance to chemotherapeutic drugs relative to the NCI-H23 cells that expressed MLH1 ($p=0.001$) (**Figure 4.5**).

To explore the differential sensitivity to the compounds in more detail, we imaged cells over the 4d treatment period of the cell viability assay and examined cell count and morphology. At the 0h time point, the cells are in growth phase and appear healthy by phase contrast imaging. However by 96h, the differences between the uninduced and induced subclones were apparent: most of the MLH1-proficient cells had undergone cell death after treatment with the DNA damaging agents, whereas the MLH1-deficient cells continued to proliferate (**Figure 4.2** and **Figure 4.3**).

We further investigated cell survival following compound treatment using clonogenic assays. Cells were treated with etoposide or temozolomide for 24h, and recovery from compound treatment was assessed by colony formation after 10d. The MLH1-deficient NCI-H23 subclones were more resistant to compound treatment than the isogenic cells proficient for MLH1 (**Figure 4.2** and **Figure 4.3**), showing a significant difference in the LD_{50} values ($p=0.03$ for etoposide, and $p=0.04$ for temozolomide). Together, these results demonstrate a differential response to DNA damage that is based solely on the presence or absence of MLH1.

4.3.3 MLH1-Deficient NCI-H23 Subclones Display Increased Sensitivity to Rhodium Metalloinsertor Compounds

We previously described metal complexes that noncovalently bind DNA mismatches with high affinity specificity, due to thermodynamic destabilization of the mismatched base pairs.²¹ We initially demonstrated that this class of compounds

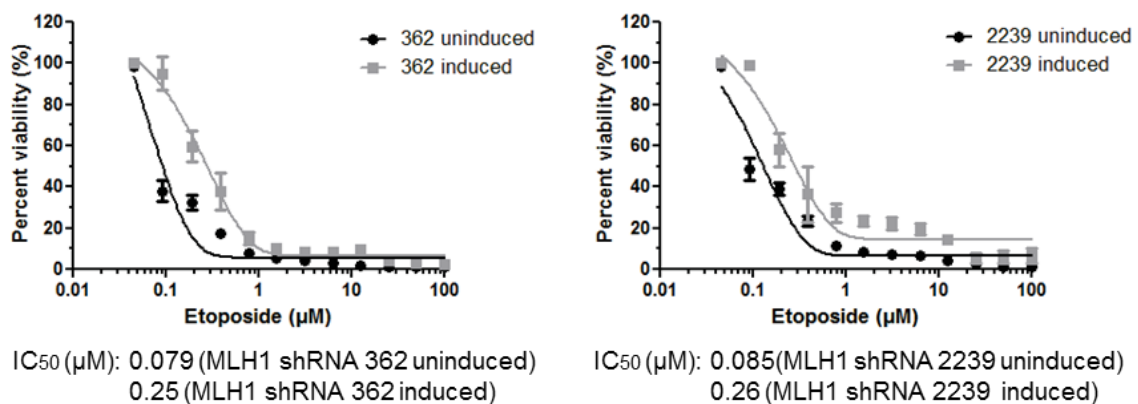


Figure 4.5 Independent MLH1 shRNA constructs confer differential sensitivity to compounds. NCI-H23 cells transduced with (left) MLH1 shRNA 362 or (right) shRNA 2239 were divided into two cultures, and grown in conditions that were uninduced (MLH1-proficient) or induced for MLH1 shRNA (MLH1-deficient). The cells were treated with etoposide, and cell viability was assessed after 4d using a Cell Titer Glo assay. Percent viability of duplicate samples from a representative experiment is shown.

preferentially inhibits the proliferation of MMR-deficient cells, using a matched HCT116 colorectal cancer cell line system and a genetic knockout system.¹⁶⁻¹⁹ This earlier work was the foundation and motivation for the creation of the isogenic cell lines described in the current study and led us to test whether rhodium metalloinsertor compounds would also preferentially inhibit the viability of these cells when MMR deficiency was induced.

In our inducible cell line system, the rhodium metalloinsertor compound $[\text{Rh}(\text{chrysi})(\text{phen})(\text{DPE})]^{2+}$ preferentially inhibited the viability of induced MLH1-deficient NCI-H23 subclones, with at least a three-fold change in the cellular IC_{50} in a 4d Cell Titer Glo assay relative to the MLH1-proficient subclones ($p=0.001$) (**Figure 4.6**). Another rhodium metalloinsertor compound, $[\text{Rh}(\text{HDP A})_2\text{chrysi}]^{3+}$ also preferentially inhibited proliferation of MLH1-deficient cells (**Figure 4.7**), with a two- to three-fold change in cellular IC_{50} values ($p=0.003$). To confirm that the difference resulted from MLH1 deficiency rather than an off-target effect of the shRNA, we used additional, independent MLH1 shRNA constructs to downregulate MLH1 in NCI-H23 cells and confirmed the result ($p=0.007$) (**Figure 4.8**). In contrast, a related compound that exhibits only weak binding to mismatched DNA, $[\text{Rh}(\text{DIP})_2\text{chrysi}]^{3+}$,¹⁹ did not display a differential effect on cell viability of the uninduced and induced NCI-H23 clones ($p=0.30$) (**Figure 4.7**). Together, our data support the hypothesis that downregulation of MLH1 increases cell sensitivity to the rhodium metalloinsertor compounds.

We examined the cellular morphology of the NCI-H23 subclones treated with $[\text{Rh}(\text{chrysi})(\text{phen})(\text{DPE})]^{2+}$ during the time course of the proliferation assays, using phase contrast imaging. Cells from the MLH1-proficient and MLH1-deficient subclones appeared healthy and in growth phase at the 0h time point. By 96h, the uninduced

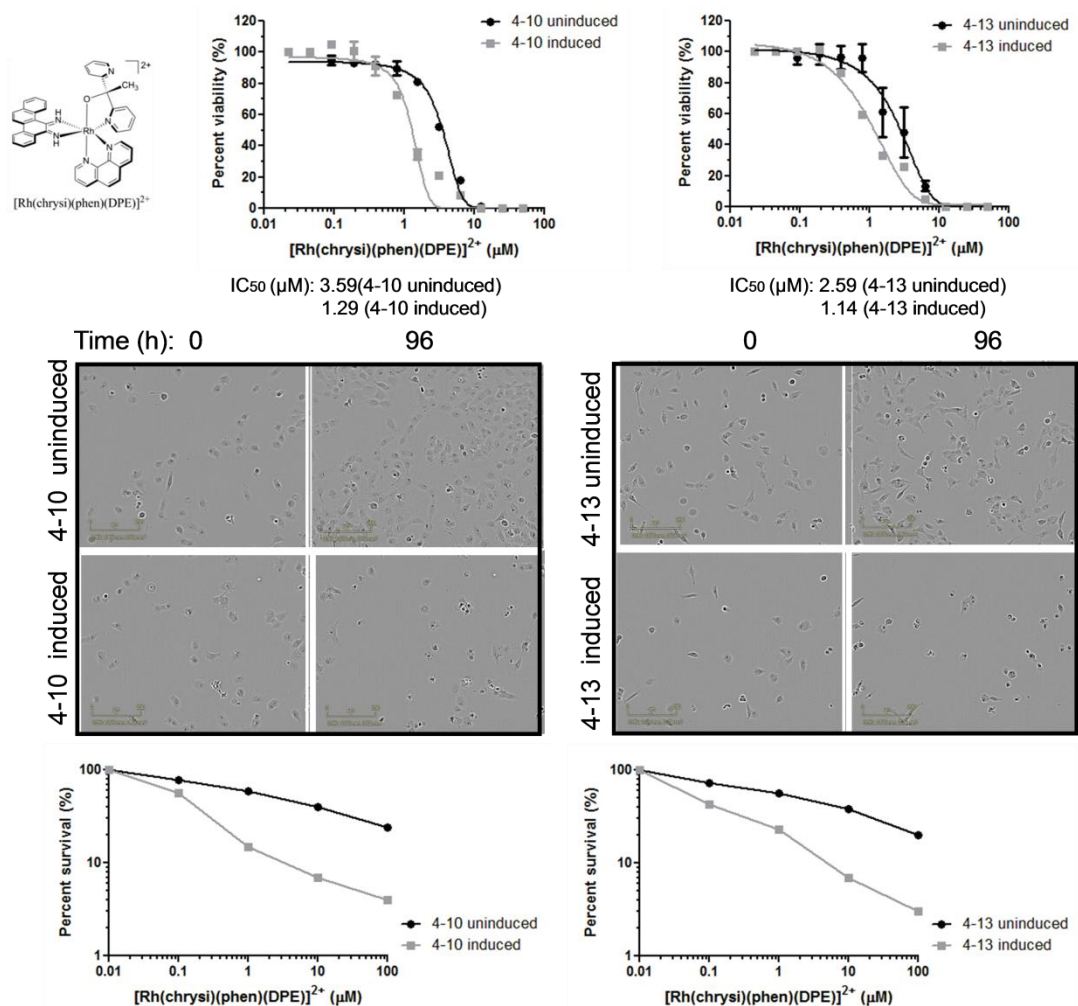


Figure 4.6 MLH1-deficient NCI-H23 cells display increased cell sensitivity to rhodium metalloinsertor compounds. NCI-H23 subclones that were uninduced or induced for MLH1 shRNA were treated with the rhodium metalloinsertor compound $[\text{Rh}(\text{chrysi})(\text{phen})(\text{DPE})]^{2+}$. (Top) Cells were treated at concentrations indicated, and cell viability was assessed after 4d using a Cell Titer Glo assay. Percent viability of duplicate samples from a single experiment is shown. (Middle) Representative phase contrast images of cells treated with 5 μM $[\text{Rh}(\text{chrysi})(\text{phen})(\text{DPE})]^{2+}$ at 0h and 96h during the cell viability assay are shown. (Bottom) Cells were treated with $[\text{Rh}(\text{chrysi})(\text{phen})(\text{DPE})]^{2+}$ for 24h, and then assayed for colony formation after 10d. The graphs show percent survival of duplicate samples of compound treated cells.

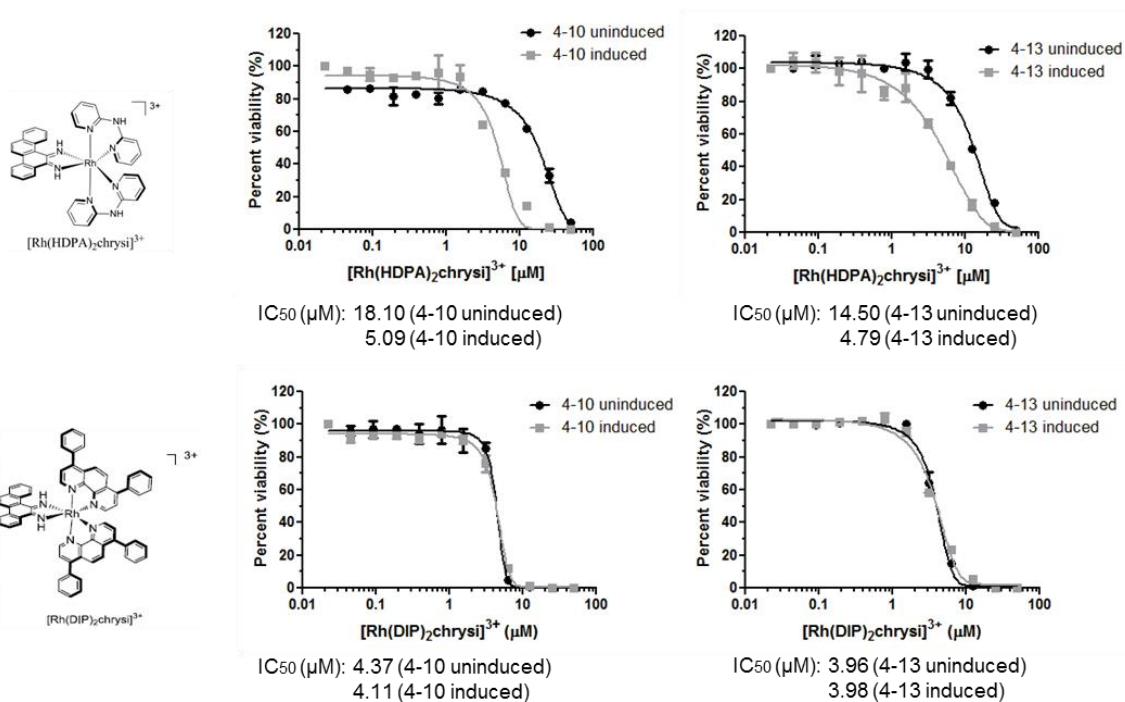


Figure 4.7 MLH1-deficient NCI-H23 cells display increased cell sensitivity only to rhodium metalloinsertors that exhibit DNA mismatch binding. (Top Left) Chemical structure of $[\text{Rh}(\text{HDPA})_2\text{chrysi}]^{3+}$. (Top Right) NCI-H23 subclones that were uninduced or induced for MLH1 shRNA were treated with $[\text{Rh}(\text{HDPA})_2\text{chrysi}]^{3+}$ as indicated, and cell viability was assessed after 4d using a Cell Titer-Glo assay. (Bottom Left) Chemical structure of $[\text{Rh}(\text{DIP})_2\text{chrysi}]^{3+}$. (Bottom Right) NCI-H23 subclones that were uninduced or induced for MLH1 shRNA were treated with $[\text{Rh}(\text{DIP})_2\text{chrysi}]^{3+}$ as indicated, and cell viability was assessed after 4d using a Cell Titer-Glo assay. Percent viability from duplicate samples of a single experiment is shown.

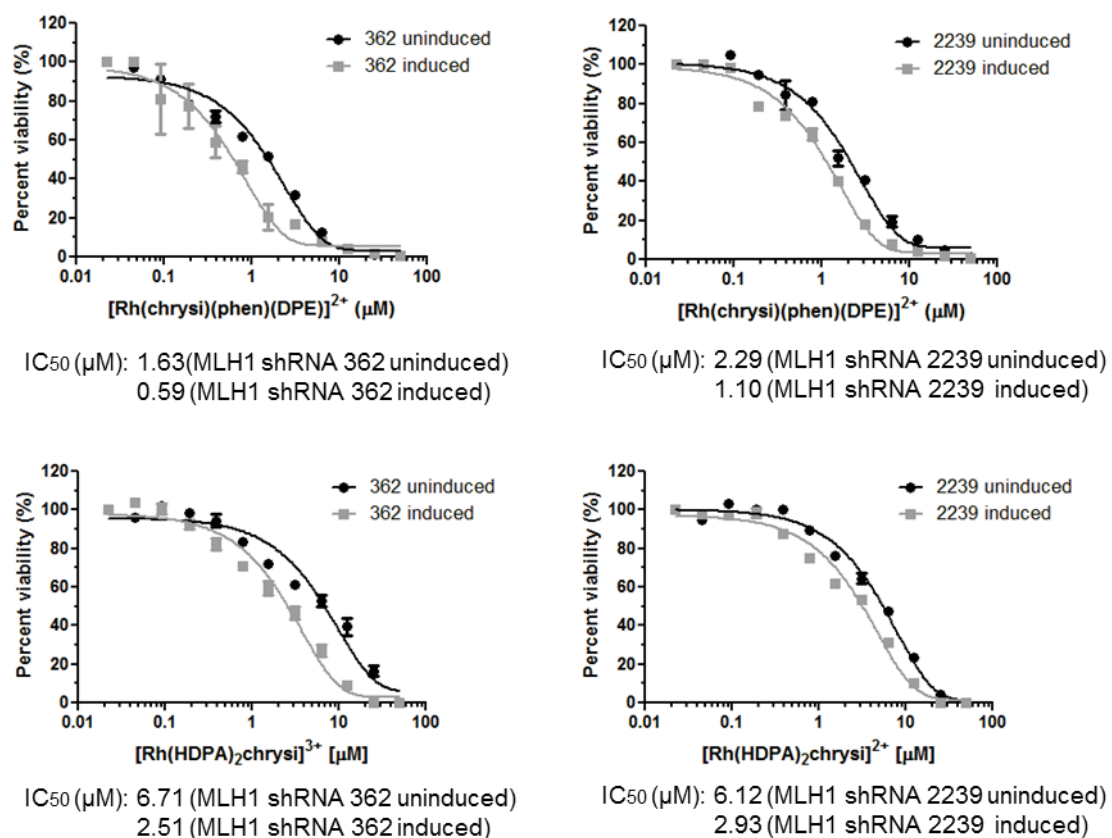


Figure 4.8 Independent MLH1 shRNA constructs confer differential sensitivity to rhodium metalloinsertors. NCI-H23 cells transduced with MLH1 shRNA 362 or MLH1 shRNA 2239 were divided into two cultures, and grown in conditions that were uninduced (MLH1-proficient) or induced for MLH1 shRNA (MLH1-deficient). (Top) Cells were treated with $[\text{Rh}(\text{DPE})(\text{phen})\text{chrysi}]^{2+}$, and cell viability was assessed after 4d using a Cell Titer Glo assay. (Bottom) Cells were treated with $[\text{Rh}(\text{HDPA})_2\text{chrysi}]^{3+}$, and cell viability was assessed after 4d using a Cell Titer Glo assay. Percent viability from duplicate samples of a single experiment is shown.

MLH1-proficient cells had continued to proliferate, but fewer cells appeared to be undergoing mitosis, suggesting a cell cycle delay or arrest (**Figure 4.6**). The cells did not appear to be undergoing senescence, as evidenced by lack of SA-beta-galactosidase production (data not shown). In contrast, most of the MLH1-deficient cells either failed to proliferate, or had undergone cell death by 96h (**Figure 4.6**). We verified that this differential effect was due to the absence or presence of MSI in the cells by assessing MLH1 protein levels in cells treated with rhodium metalloinsertor compounds (**Figure 4.9**). The previously demonstrated effect of shRNA induction on MLH1 protein expression was not altered following treatment with the rhodium compounds (**Figure 4.9**).

We also confirmed the increased sensitivity of the MLH1-deficient NCI-H23 subclones to the rhodium metalloinsertor compounds using clonogenic assays. After 24h treatment with $[\text{Rh}(\text{chrysi})(\text{phen})(\text{DPE})]^{2+}$, the MLH1-deficient NCI-H23 subclones formed fewer colonies than the isogenic MLH1-proficient subclones, exhibiting a significant difference in LD_{50} values ($p=0.009$) (**Figure 4.6**). The differential sensitivity of the MLH1-deficient subclones to the rhodium metalloinsertor compounds is consistent with the hypothesis that these compounds exert their effects through binding to DNA mismatches that are present in MMR-deficient cells.

4.4 Discussion

4.4.1 Generation of Isogenic Cell Lines

The MMR pathway maintains genome stability by promoting the recognition and repair of single base mismatches and small insertion-deletion loops in the DNA that result from replication errors or DNA damage. Loss of function of the MMR pathway

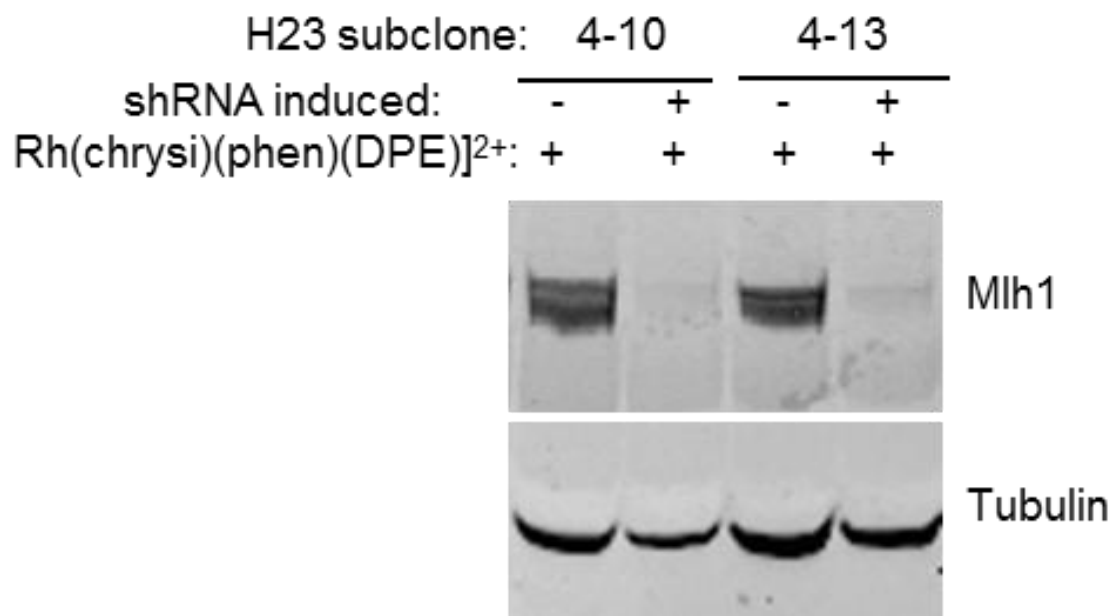


Figure 4.9 Treatment of NCI-H23 subclones with rhodium metalloinsertor compounds does not alter MSI status. MLH1-proficient and MLH1-deficient NCI-H23 subclones were treated with 5uM [Rh(DPE)(phen)chrysi]³⁺ for 24h, and then protein lysates were prepared and analyzed for MLH1 protein levels as a marker for MSI. Levels of tubulin were also assessed as a control for protein loading.

increases the prevalence of cellular mutations and can cause or contribute to cancer. The mechanism of carcinogenesis resulting from inherited MMR deficiency has been well studied, particularly in colorectal cancer,^{4,22} and has been modeled in cell line systems such as HCT116O cells, which are MLH1-deficient but contain an extra copy of Chromosome 2, and HCT116N cells, in which the MLH1 deficiency is complemented by an extra copy of Chromosome 3 that contains wild type MLH1.²³ In other cancer types, such as in lung cancer, MMR deficiency can be promoted by carcinogen exposure.⁷⁻⁹ Chemotherapeutic treatment also may promote MMR deficiency, leading to secondary leukemias.⁶ The cell line system we describe provides the first example of an isogenic model for induced MMR deficiency that can be reversibly switched on or off at the level of control of gene expression. It provides a model to study questions about induced MMR deficiency and to allow identification of molecules that might offer therapeutic benefit in MMR-deficient cancers.

This new cell line system is complementary to matched cell line systems commonly used to study MMR, such as the MMR-deficient cancer cell lines HCT116 or Hec59, which are complemented by an extra copy of the chromosome containing wild type MLH1 or MSH2, respectively.^{23,24} In these models, the MMR-proficient cells and MMR-deficient cells are generated as different clones, and are chromosomally distinct from each other and the parental cell line. These differences may result in changes in chromosome stability or gene expression that are not solely due to MMR deficiency.^{25,26} Matched normal cell systems, such as MMR-deficient embryonic kidney cells 293T compared to 293T cells engineered to overexpress MLH1,²⁷ or wild-type mouse embryonic fibroblasts (MEFs) compared to MSH2-deficient MEFs²⁸ may not be ideal

models to study MMR function in cancer. MEFs may be less sensitive to defects in DNA repair than cancer cells, and have been reported to exhibit a much lower mutation rate than MMR-deficient cancer cells.^{25,29}

4.4.2 Implications for Chemotherapy

There is currently no targeted therapy for patients with MMR-deficient cancers. In patients with colorectal cancers, the standard of care remains adjuvant-combined chemotherapy that includes the nucleoside inhibitor 5-fluorouracil (5-FU), even though multiple clinical studies have now shown that MMR-deficient tumors might not benefit from 5-FU treatment.^{4,22} In addition to defects in DNA damage recognition and repair,¹¹ MMR-deficient colorectal tumors display distinct features such as localization to the proximal colon, decreased metastasis, increased number of tumor infiltrating lymphocytes, and near-diploid DNA content of the cells.³⁰ These characteristics may contribute to the better overall prognosis reported for patients with MMR-deficient colorectal cancer when compared on a stage-by-stage basis to patients with MMR-proficient cancers.³¹ However, there is still a need for therapeutics that will be efficacious in MMR-deficient tumors.

Synthetic lethality screens have identified several potential therapeutic targets for MMR-deficient cancer cells. Methotrexate, an inhibitor of dihydrofolate reductase, was reported to show synthetic lethality in MSH2-deficient cancer cells³² and is currently in clinical trials for MSH2-deficient colorectal cancers (www.clinicaltrials.gov; Identifier: NCT00952016). Inhibition of DNA polymerases, Pol B and Pol G, caused synthetic sickness or synthetic lethality in cancer cells deficient for MSH2 or MLH1, respectively.³² MMR-deficient colorectal cancer cells were also reported to be

preferentially sensitive to inhibitors of cytosine-based nucleoside analogs such as cytarabine,³³ the PI3 kinase/Akt pathway,³⁴ and the PTEN-induced putative kinase PINK1.³⁵ A disadvantage of the synthetically lethal interactions identified is that in several cases, these appear to be specific for a single gene mutation (for example, MSH2), and do not necessarily apply to other deficiencies in the pathway. It remains to be determined whether the proposed mechanistic basis for these synthetically lethal interactions will translate to efficacy in patients with genotypic and phenotypic tumor heterogeneity.

We previously considered targeting the end “state” of genomic instability.¹⁵ We have demonstrated that rhodium metalloinsertor compounds can bind DNA mismatches and preferentially inhibit the proliferation of MMR-deficient cells, including the MLH1-deficient HCT116 colorectal cancer cell line.¹⁶⁻¹⁹ Here we verify and extend our previous observations by demonstrating, in a completely isogenic system, preferential sensitivity of cells induced for MMR deficiency to rhodium metalloinsertor compounds. The differential activity of the compounds in MMR-deficient cells correlates with their binding affinity to DNA mismatches *in vitro*.¹⁷ Recently, the differential cellular activity of these compounds has also been shown to correlate with their accumulation in the cell nucleus.¹⁹ Together, these observations support the model that rhodium metalloinsertor compounds act directly on DNA mismatches in genomic DNA. The metal complexes enter cells by passive diffusion and bind non-covalently to mismatched DNA due to the thermodynamic destabilization of mispaired nucleosides.²¹ This mechanism of mismatched base pair recognition is distinct from the checkpoint surveillance process normally used by cells, which involves proteins associated with the replication fork

during S phase.³⁶ MMR-deficient cells show a 100- to 1000-fold increase in spontaneous mutation rate compared to that of MMR-proficient cells, which is estimated at 1×10^{-9} to 1×10^{-10} per cell.^{24,37} It is provocative that the rhodium metalloinsertor compounds have the ability to recognize this number of DNA mismatches, and differentially inhibit the proliferation of MMR-deficient cells *in vitro*, in the context of ~6 billion correctly paired bases. We speculate that this differential effect may translate to even greater therapeutic benefit *in vivo*.

4.5 Conclusion

It is striking that the MLH1-deficient cells, which show increased resistance to DNA-damaging agents, are preferentially sensitive to rhodium metalloinsertor compounds. We have observed differential effects for this class of compounds consistently across multiple experiments and in different assays for cell proliferation. The differential effect on cell proliferation observed with the rhodium metalloinsertor compounds cannot be explained simply by the growth rate of the MLH1-deficient NCI-H23 subclones, which is similar for the MLH1-proficient and the MLH1-deficient cells. We do not yet understand the molecular mechanism of the preferential sensitivity of MMR-deficient cells to rhodium metalloinsertor compounds. The compounds might interfere with cellular DNA replication or transcription. However, the metal complexes bind noncovalently to mismatched DNA, suggesting that the compounds may dissociate during the DNA unwinding that occurs during replication. It is possible that the compounds might also associate with proteins adjacent to a DNA mismatch. Alternatively, the replication fork may not be able to synthesize through mismatched DNA bound with a metal complex. Current studies are focused on addressing these

hypotheses, and also on improving the potency and drug-like properties of the current series of rhodium metalloinsertor compounds for applications in cancer therapy.

4.6 References

- 1 Lengauer, C.; Kinzler, K. W.; Vogelstein, B. *Nature* **2007**, *386*, 623-627.
- 2 Jiricny, J. *Nat. Rev. Mol. Cell Biol.* **2006**, *7*, 335-346.
- 3 Hewish, M.; Lord, C. J.; Martin, S. A.; Cunningham, D.; Ashworth, A. *Nat. Rev. Clin. Oncol.* **2010**, *7*, 197-208.
- 4 Boland, C. R.; Goel, A. *Gastroenterology* **2010**, *138*, 2073-2087.
- 5 Lawes, D. A.; SenGupta, S.; Boulos, P. B. *Eur. J. Surg. Oncol.* **2003**, *29*, 201-212.
- 6 Diouf, B.; Cheng, Q.; Krynetskaia, N. F.; Yang, W.; Cheok, M.; et al. *Nat. Med.* **2011**, *17*, 1298-1303.
- 7 Takahashi, Y.; Kondo, K.; Hirose, T.; Nakagawa, H.; Tsuyuguchi, M.; et al. *Mol Carcinog* **2005**, *42*, 150-158.
- 8 Castagnaro, A.; Marangio, E.; Verduri, A.; Chetta, A.; D'Ippolito, R.; et al. *Exp. Lung. Res.* **2007**, *33*, 289-301.
- 9 Ali, A. H.; Kondo, K.; Namura, T.; Senba, Y.; Takizawa, H.; et al. *Mol. Carcinog.* **2011**, *50*, 89-99.
- 10 Fink, D.; Aebi, S.; Howell, S. B. *Clin. Cancer Res.* **1998**, *4*, 1-6.
- 11 Davis, T. W.; Wilson-Van Patten, C.; Meyers, M.; Kunugi, K. A.; Cuthill, S.; et al. *Cancer Res.* **1998**, *58*, 767-778.
- 12 Miquel, C.; Jacob, S.; Grandjouan, S.; Aime, A.; Viguier, J.; et al. *Oncogene* **2007**, *26*, 5919-5926.
- 13 Bilbao, C.; Ramirez, R.; Rodriguez, G.; Falcon, O.; Leon, L.; et al. *Eur. J. Cancer* **2010**, *46*, 2821-2827.

- 14 Martin, S. A.; Lord, C. J.; Ashworth, A. *Clin. Cancer Res.* **2010**, *16*, 5107-5113.
- 15 Roschke, A. V.; Lababidi, S.; Tonon, G.; Gehlhaus, K. S.; Bussey, K.; et al. *Proc. Natl. Acad. Sci. U. S. A.* **2005**, *102*, 2964-2969.
- 16 Hart, J. R.; Glebov, O.; Ernst, R. J.; Kirsch, I. R.; Barton, J. K. *Proc. Natl. Acad. Sci. U. S. A.* **2006**, *103*, 15359-15363.
- 17 Ernst, R. J.; Song, H.; Barton, J. K. *J. Am. Chem. Soc.* **2009**, *131*, 2359-2366.
- 18 Ernst, R. J.; Komor, A. C.; Barton, J. K. *Biochemistry* **2011**, *50*, 10919-10928.
- 19 Komor, A. C.; Schneider, C. J.; Weidmann, A. G.; Barton, J. K. *J. Am. Chem. Soc.* **2012**, *134*, 19223-19233.
- 20 Taverna, P.; Liu, L.; Hanson, A. J.; Monks, A.; Gerson, S. L. *Cancer Chemother. Pharmacol.* **2000**, *46*, 507-516.
- 21 Komor, A. C.; Barton, J. K. *Chem. Commun.* **2013**, *49*, 3617-3630.
- 22 Vilar, E.; Gruber, S. B. *Nat. Rev. Clin. Oncol.* **2010**, *7*, 153-162.
- 23 Koi, M.; Umar, A.; Chauhan, D. P.; Cherian, S. P.; Carethers, J. M.; et al. *Cancer Res.* **1994**, *54*, 4308-4312.
- 24 Umar, A.; Koi, M.; Risinger, J. I.; Glaab, W. E.; Tindall, K. R.; et al. *Cancer Res.* **1997**, *57*, 3949-3955.
- 25 Reitmair, A. H.; Risley, R.; Bristow, R. G.; Wilson, T.; Ganesh, A.; et al. *Cancer Res.* **1997**, *57*, 3765-3771.
- 26 Campbell, M. R.; Wang, Y.; Andrew, S. E.; Liu, Y. *Oncogene* **2006**, *25*, 2531-2536.
- 27 Cejka, P.; Stojic, L.; Mojas, N.; Russell, A. M.; Heinemann, K.; et al. *EMBO J.* **2003**, *22*, 2245-2254.

- 28 Kucherlapati, M. H.; Lee, K.; Nguyen, A. A.; Clark, A. B.; Hou, H. Jr.; et al. *Gastroenterology* **2010**, *138*, 993-1002 e1001.
- 29 Yasin, S. L.; Rainbow, A. J. *Int. J. Oncol.* **2011**, *39*, 719-726.
- 30 Thibodeau, S. N.; Bren, G.; Schaid, D. *Science* **1993**, *260*, 816-819.
- 31 Sinicrope, F. A.; Rego, R. L.; Foster, N.; Sargent, D. J.; Windschitl, H. E.; et al. *Am. J. Gastroenterol.* **2006**, *101*, 2818-2825.
- 32 Martin, S. A.; McCarthy, A.; Barber, L. J.; Burgess, D. J.; Parry, S.; et al. *EMBO Mol. Med.* **2009**, *1*, 323-337.
- 33 Hewish, M.; Martin, S. A.; Elliott, R.; Cunningham, D.; Lord, C. J.; et al. *Br. J. Cancer* **2013**, *108*, 983-992.
- 34 Vilar, E.; Mukherjee, B.; Kuick, R.; Raskin, L.; Misek, D. E.; et al. *Clin. Cancer Res.* **2009**, *15*, 2829-2839.
- 35 Martin, S. A.; Hewish, M.; Sims, D.; Lord, C. J.; Ashworth, A. *Cancer Res.* **2011**, *71*, 1836-1848.
- 36 Hombauer, H.; Srivatsan, A.; Putnam, C. D.; Kolodner, R. D. *Science* **2011**, *334*, 1713-1716.
- 37 Phear, G.; Bhattacharyya, N. P.; Meuth, M. *Mol. Cell Biol.* **1996**, *16*, 6516-6523.

Chapter 5: An Unusual Ligand Coordination Gives Rise to a New Family of Rhodium Metalloinsertors with Improved Selectivity and Potency

5.1 Introduction

Recently in the Barton laboratory, a family of ten metalloinsertors with varying lipophilicities yet similar mismatch binding affinities was synthesized. Their abilities to preferentially target MMR-deficient cells over MMR-proficient cells were found to vary drastically.¹ One metalloinsertor in particular, $[\text{Rh}(\text{chrysi})(\text{phen})(\text{DPE})]^{2+}$ (**Figure 5.1**), was found to possess enhanced potency and selectivity compared to the others. Crystallization of the compound revealed the solid state structure shown in **Figure 5.2**; the DPE ligand was discovered to coordinate to the rhodium center *via* one pyridine ring and the alcohol oxygen, in contrast to all other previously reported metalloinsertors, which coordinate *via* two pyridine rings (**Figure 5.3**). It was hypothesized that this new ligand coordination environment was responsible for the enhanced biological activity of this compound, and we thus sought to synthesize a family of compounds inspired by this new ligand scaffold.

In this report, we describe the discovery of an unusual ligand coordination for the rhodium metalloinsertor $[\text{Rh}(\text{chrysi})(\text{phen})(\text{DPE})]^{2+}$ and subsequent development of a family of compounds based on this new type of ligand. The family of compounds has been found to possess enhanced potency and cell selectivity in our cell assays. All compounds have binding affinities that range from 2.6 to $5.5 \times 10^6 \text{ M}^{-1}$, and, furthermore, it has been discovered that the amount of intracellular rhodium required for optimal biological activity for this family of compounds is ≥ 5 times lower than that of previously

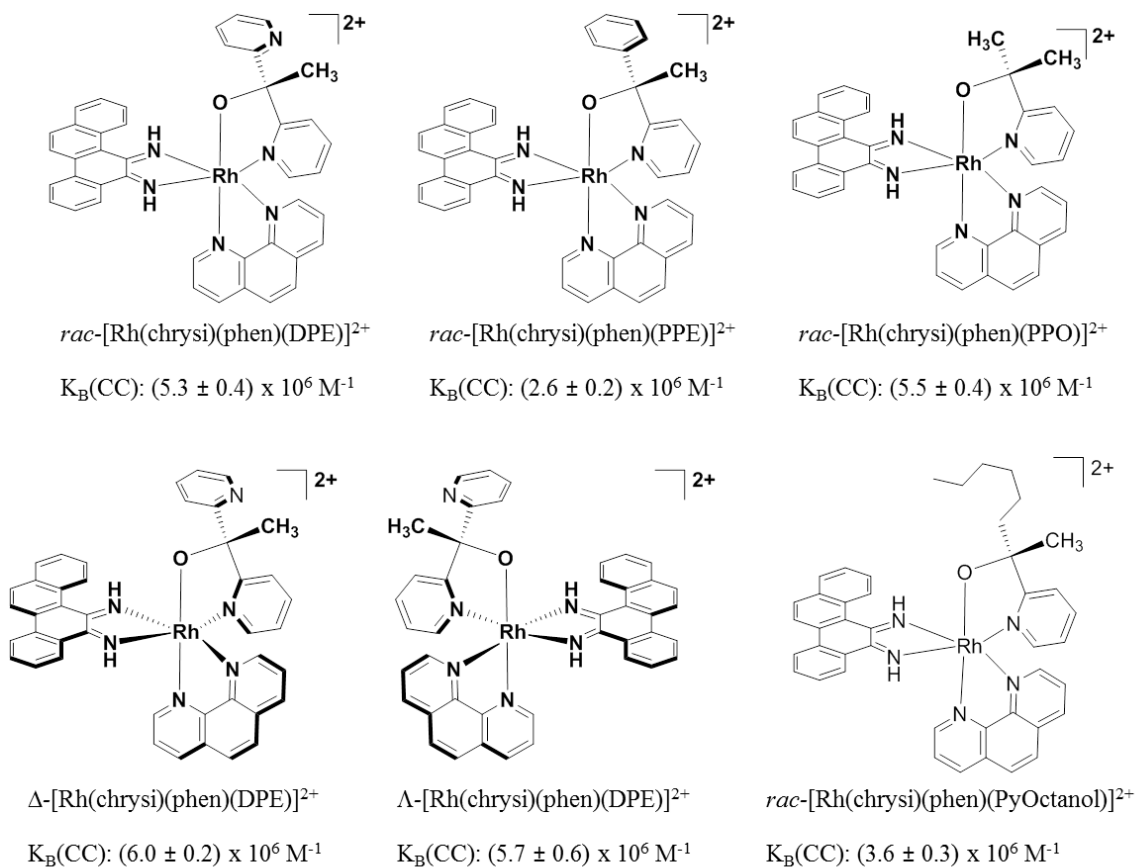


Figure 5.1 Chemical structures and binding affinities for CC mismatches of all compounds studied.

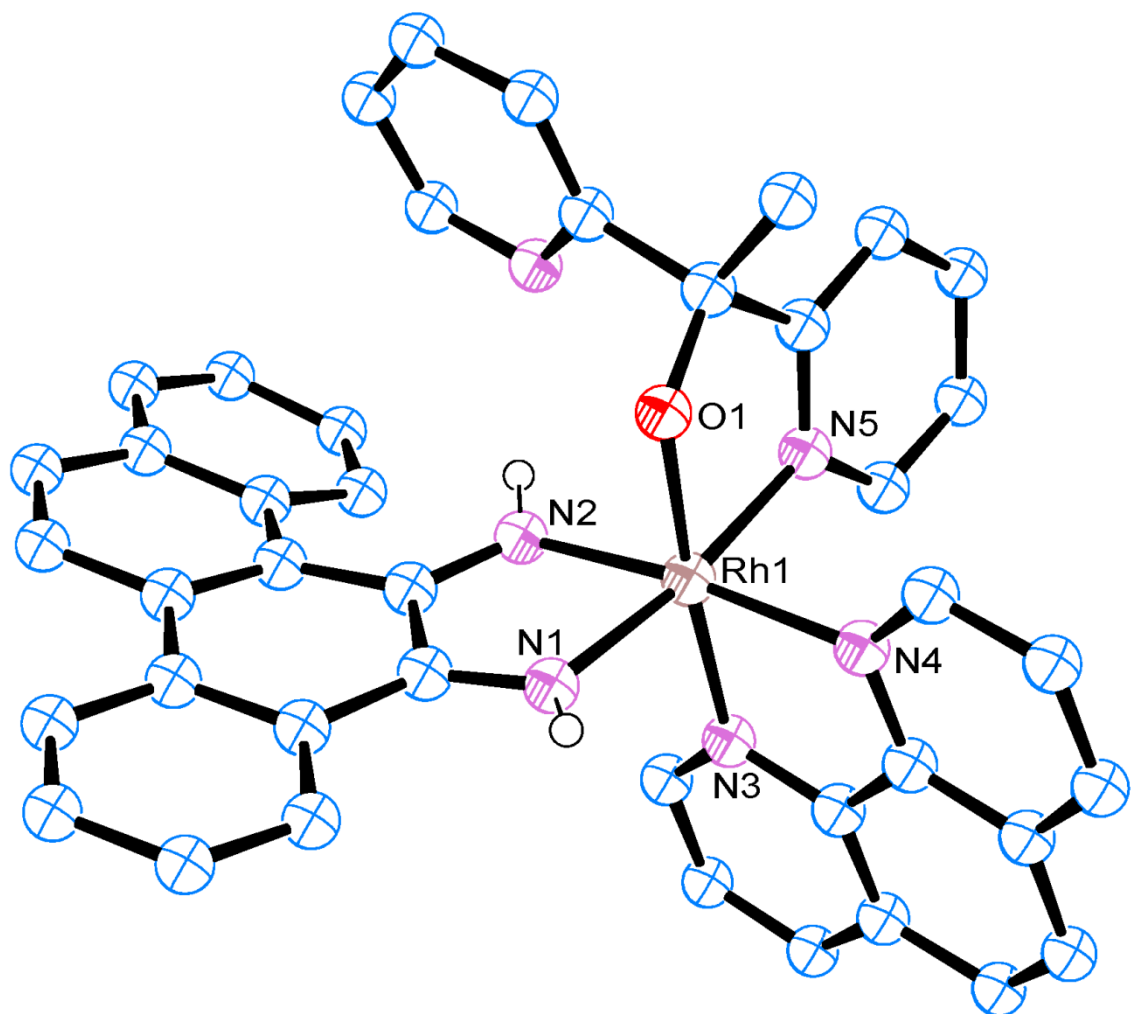


Figure 5.2 X-ray crystal structure of [Rh(chrysi)(phen)(DPE)]Cl₂. Displacement of ellipsoids are drawn at 50% probability. For clarity, chloride atoms and hydrogen atoms (except imine protons) have been omitted. Selected bond lengths (Å): Rh-O 1.996, Rh-N1 2.006, Rh-N2 1.987, Rh-N3 2.046, Rh-N4 2.059, Rh-N5 2.031.

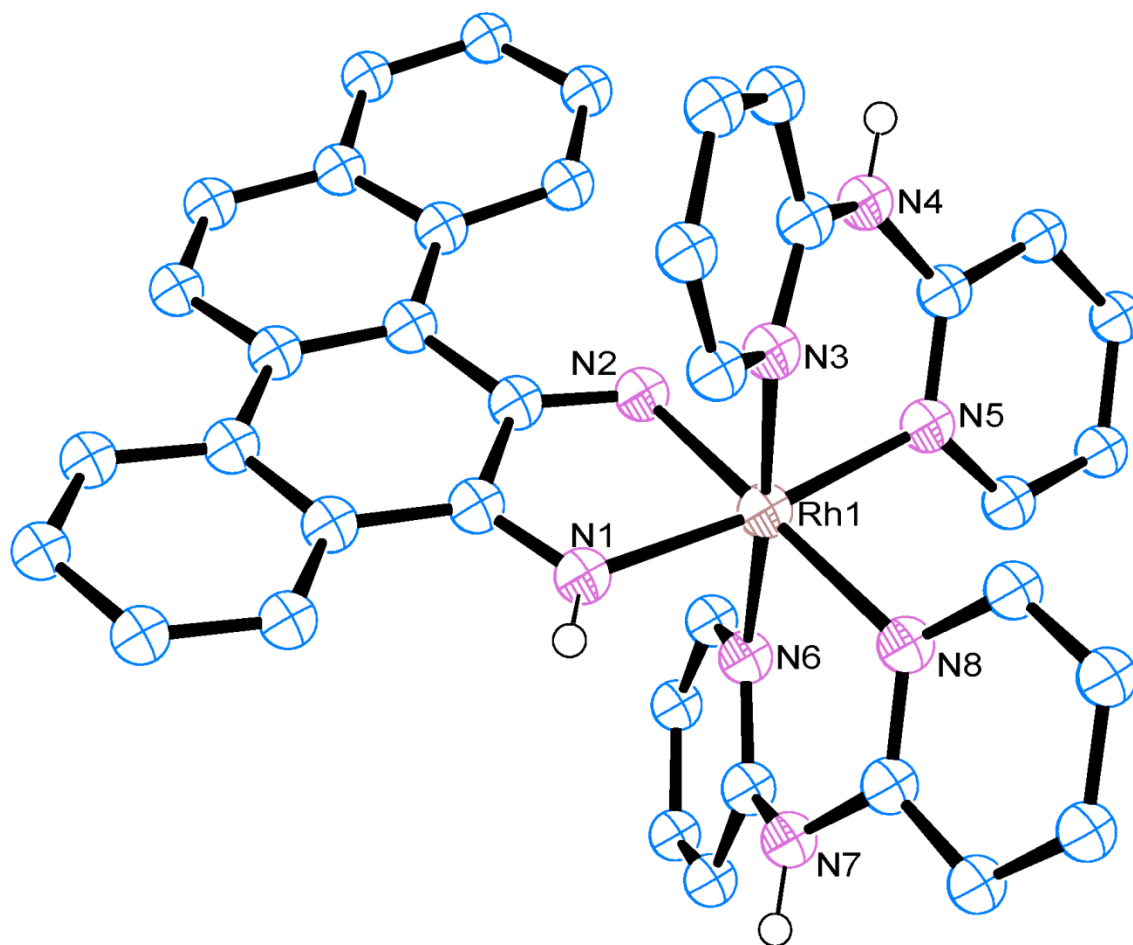


Figure 5.3 X-ray crystal structure of [Rh(HDPA)₂(chrysi)]Cl₂. Displacement of ellipsoids are drawn at 50% probability. For clarity, chloride atoms and hydrogen atoms (except the imine proton) have been omitted. Selected bond lengths (Å): Rh-N1 2.002, Rh-N2 1.974, Rh-N3 2.042, Rh-N5 2.045, Rh-N6 2.041, Rh-N8 2.114.

reported metalloinsertors (thus making them significantly more potent). Enantiomeric separation of $[\text{Rh}(\text{chrysi})(\text{phen})(\text{DPE})]^{2+}$ has led to the discovery that for this family, both Δ and Λ enantiomers bind to DNA with equal affinity and demonstrate comparable cell-selective activity, hinting at a possible different DNA mismatch binding conformation than previous metalloinsertors.

5.2 Experimental Protocols

5.2.1 Materials

Commercially available chemicals were used as received. All organic reagents and Sephadex ion-exchange resin were obtained from Sigma-Aldrich unless otherwise noted. Sep-pak C_{18} solid-phase extraction (SPE) cartridges were purchased from Waters Chemical Co. (Milford, MA). Media and supplements were purchased from Invitrogen (Carlsbad, CA). BrdU, antibodies, buffers, peroxidase substrate, MTT, and acidified lysis buffer (10% SDS in 10 mM HCl) solution were purchased in kit format from Roche Molecular biochemical (Mannheim, Germany). Phosphoramidites were purchased from Glen Research (Sterling, VA).

5.2.2 Oligonucleotide Synthesis

Oligonucleotides were synthesized on an Applied Biosystems 3400 DNA synthesizer using standard phosphoramidite chemistry. DNA was synthesized with a 5'-dimethoxytrityl (DMT) protecting group. The oligonucleotides were cleaved from the beads by reaction with concentrated ammonium hydroxide at 60° C overnight. The resulting free oligonucleotides were purified by HPLC using a C_{18} reverse-phase column (Varian, Inc.) on a Hewlett-Packard 1100 HPLC. The DMT group was removed by reaction with 80% acetic acid for 15 min at ambient temperature. The DMT-free

oligonucleotides were precipitated with absolute ethanol and purified again by HPLC. Positive identification of the oligonucleotides and their purity were confirmed by MALDI-TOF mass spectrometry. Quantification was performed on a Cary 100 Bio UV-Visible Spectrophotometer using the extinction coefficients at 260 nm (ϵ_{260}) estimated for single-stranded DNA.

5.2.3 Synthesis and Characterization of Ligands and Metal Complexes

The complexes $[\text{Rh}(\text{bpy})_2(\text{chrysi})]^{3+}$ and $[\text{Rh}(\text{HDPA})_2(\text{chrysi})]^{3+}$ were prepared according to published procedures.^{2,3} $[\text{Rh}(\text{chrysi})(\text{phen})(\text{NH}_3)_2]^{3+}$ was prepared from $[\text{Rh}(\text{phen})(\text{NH}_3)_4]\text{OTf}_3$ and 5,6-chrysenequinone following an adaptation of the methods described by Mürner et. al (3.2.3.1).⁴ The ligand 1,1-di(pyridin-2-yl)ethanol (DPE) was synthesized according to an adaptation of published procedures (3.2.3.2).⁵ $[\text{Rh}(\text{chrysi})(\text{phen})(\text{DPE})]^{2+}$ was synthesized as previously described (3.2.3.6).¹

5.2.3.1 1-R-1-(pyrid-2-yl) ethanol (R = phenyl, methyl, hexyl; PPE, PPO, PyOctanol)

The appropriate ketone $\text{py}(\text{CO})(\text{L})$ (8.3 mmol) was dissolved in dry diethyl ether (100 mL) in an oven-dried 250 mL schlenk flask under Ar. The solution was cooled to -78°C and MeLi (12.9 mL of a 1.6M solution) was added slowly over 15 min. The resulting yellow solution was allowed to stir at -78°C for 1 h and then warmed to ambient temperature. Next, saturated NH_4Cl (aq) (30 mL) was added to quench the reaction, and the resulting solution was extracted with EtOAc (3 x 75 mL), dried over Na_2SO_4 , and the solvent evaporated *in vacuo*. The crude product was purified via flash chromatography (SiO_2 , 1:1 EtOAc: CH_2Cl_2 for L=Me and hexyl, 1:3 EtOAc: CH_2Cl_2 for L=Ph) to afford a light yellow oil.

PPE: Yield: 97%. ^1H NMR (CDCl_3 , 300 MHz): δ 8.52 (d of m, $J = 5.1$ Hz, 1 H); 7.65 (t of d, $J = 7.8$ Hz, 1.8 Hz, 1 H); 7.48 (m, 2H); 7.31 (m, 3H); 7.17-7.26 (m, 2H); 5.85 (s, 1H); 1.94 (s, 3H).

PPO: Yield: 55% ^1H NMR NMR (CDCl_3 , 300 MHz): δ 8.52 (d of m, $J = 4.8$ Hz, 1 H); 7.71 (t of m, $J = 7.8$ Hz, 1 H); 7.38 (d of m, $J = 8.1$ Hz, 1H); 7.21 (t of m, $J = 6.2$ Hz, 1H); 5.08 (s, 1H); 1.54 (s, 6H).

PyOctanol: Yield: 35% ^1H NMR NMR (CDCl_3 , 300 MHz): δ 8.51 (d of m, $J = 6.0$ Hz, 1 H); 7.71 (t of m, $J = 9.0$ Hz, 1 H); 7.32 (d of m, $J = 9.0$ Hz, 1H); 7.20 (t of m, $J = 6.0$ Hz, 1H); 5.18 (s, 1H); 1.78 (m, 2H); 1.51 (s, 3H); 1.19 (m, 6H); 0.82 (m, 5H).

5.2.3.2 [Rh(chrysi)(phen)(L)]Cl₂ (L = PPE, PPO, PyOctanol)

[Rh(chrysi)(phen)(NH₃)₂]TFA₃ (62.3 mg, 0.092 mmol) and L (0.138 mmol) were dissolved in 1:12 H₂O:EtOH (90 mL). The resulting red solution was heated to 98°C and allowed to reflux for 18 hours. The resulting solution was dried *in vacuo*, redissolved in H₂O (10 mL), filtered, and purified via flash chromatography (C₁₈-SiO₂, 17:3 0.1% TFA (aq): MeCN). All compounds but [Rh(chrysi)(phen)(PyOctanol)]²⁺ were synthesized as a mixture of diastereomers; only the diastereomers of [Rh(chrysi)(phen)(DPE)]²⁺ were resolvable *via* HPLC (17:3 0.1% TFA (aq): MeCN to 1:1 0.1% TFA (aq): MeCN gradient over 45 m). The chloride salt can be obtained from a Sephadex QAE anion exchange column equilibrated with 0.1M MgCl₂.

[Rh(chrysi)(phen)(PPE)]Cl₂: Yield: 80%. ESI-MS (cation): m/z calc 736.2 (M - 1H⁺), 368.6 (M²⁺), obs. 736.0, 368.8. UV-Vis (H₂O, pH 7): 270 nm (165,800 M⁻¹ cm⁻¹), 300 nm (56,300 M⁻¹ cm⁻¹), 430 nm (16,100 M⁻¹ cm⁻¹). ^1H NMR (CD₃CN, 600 MHz): δ 15.45 (s, 1 H); 14.38 (s, 1 H); 11.76 (s, 1 H); 11.08 (s, 1 H); 9.71 (d, $J = 5.2$ Hz, 1H);

9.49 (d, $J = 5.2$ Hz, 1H); 9.12 (d, $J = 5.6$ Hz, 1H); 8.99 (d, $J = 9.0$ Hz, 1H); 8.94 (m, 2H); 8.88 (m, 3H); 8.81 (d, $J = 8.0$ Hz, 1H); 8.46 (d, $J = 8.0$ Hz, 1H); 8.35-8.39 (m, 4H); 8.29-8.33 (m, 3H); 8.20-8.25 (m, 4H); 8.14 (t, $J = 8.0$ Hz, 1H); 8.10 (m, 2H); 8.03 (m, 1H); 7.99 (m, 1H); 7.92 (d, $J = 7.5$ Hz, 1H); 7.89 (d, $J = 8.5$ Hz, 1H); 7.83 (m, 1H); 7.68-7.80 (m, 5H); 7.64 (m, 1H); 7.55-7.60 (m, 4H); 7.52 (m, 2H); 7.40 (d, $J = 5.7$ Hz, 1H); 7.28-7.34 (m, 4H); 7.23 (t, $J = 6.6$ Hz, 1H); 7.16 (m, 3H); 6.61 (t, $J = 6.6$ Hz, 2H); 6.33 (t, $J = 6.6$ Hz, 1H); 2.49 (s, 3H); 2.13 (s, 3H) (1:1 mixture of diastereomers). Crystals suitable for X-ray diffraction were obtained from vapor diffusion of diethyl ether into a concentrated solution of [Rh(chrysi)(phen)(PPE)]Cl₂ dissolved in methanol.

[Rh(chrysi)(phen)(PPO)]Cl₂: Yield: 40%. ESI-MS (cation): m/z calc 674.1 (M - 1H⁺), 337.6 (M²⁺), obs. 674.0, 337.7. UV-Vis (H₂O, pH 7): 270 nm (122,400 M⁻¹ cm⁻¹), 300 nm (41,600 M⁻¹ cm⁻¹), 430 nm (12,300 M⁻¹ cm⁻¹). ¹H NMR (CD₃CN, 500 MHz): δ 13.29 (br s, 1.7 H); 11.68 (br s, 1 H); 9.61 (d, $J = 5.2$ Hz, 1H); 9.54 (d, $J = 5.2$ Hz, 1.7H); 9.09 (d, $J = 5.5$ Hz, 1H); 8.93 (m, 5.4H); 8.88 (m, 2.7H); 8.30-8.42 (m, 12.5H); 8.26 (m, 1H); 8.23 (m, 1.7H); 8.14 (m, 4.4H); 7.93-8.04 (m, 11.5H); 7.74-7.85 (m, 5.4H); 7.55 (m, 4.4H); 7.49 (t, $J = 8.0$ Hz, 1H); 7.21 (m, 2H); 7.13 (m, 1H); 7.09 (m, 2.7H); 2.00 (s, 3H); 1.96 (s, 5.1H); 1.67 (s, 3H); 1.66 (s, 5.1H); (1:1.7 mixture of diastereomers). Crystals suitable for X-ray diffraction were obtained from vapor diffusion of diethyl ether into a concentrated solution of [Rh(chrysi)(phen)(PPO)]Cl₂ dissolved in isopropanol.

[Rh(chrysi)(phen)(PyOctanol)]Cl₂: Yield: 10%. ESI-MS (cation): m/z calc 744.2 (M - 1H⁺), 372.6 (M²⁺), obs. 744.1, 372.8. ¹H NMR (CD₃CN, 500 MHz): δ 15.00 (s, 1 H); 12.80 (s, 1 H); 9.55 (d, $J = 5.0$ Hz, 1H); 9.12 (d, $J = 8.0$ Hz, 1H); 9.09 (d, $J = 5.5$ Hz, 1H); 8.94 (d, $J = 8.9$ Hz, 1H); 8.88 (d, $J = 8.5$ Hz, 1H); 8.85 (d, $J = 8.5$ Hz, 1H);

8.32-8.44 (m, 5H); 8.17 (m, 2H); 8.08 (m, 1H); 7.91 (t, $J = 7.0$ Hz, 1H); 7.86 (t, $J = 8.0$ Hz, 1H); 7.80 (m, 2H); 7.54 (t, $J = 7.5$ Hz, 1H); 7.41 (d, $J = 8.0$ Hz, 1H); 7.31 (d, $J = 6.0$ Hz, 1H); 7.05 (t, $J = 7.0$ Hz, 1H); 1.74 (s, 3H); 1.55 (m, 2H); 0.71-0.96 (m, 11H).

Crystals suitable for X-ray diffraction were obtained from vapor diffusion of diethyl ether into a concentrated solution of $[\text{Rh}(\text{chrysi})(\text{phen})(\text{DPE})]\text{Cl}_2$ dissolved in ethanol.

Crystals of $[\text{Rh}(\text{HDPA})_2(\text{chrysi})]\text{Cl}_2$ (one chrysi immine deprotonated) suitable for X-ray diffraction were obtained from vapor diffusion of diethyl ether into a concentrated solution of $[\text{Rh}(\text{HDPA})_2(\text{chrysi})]\text{Cl}_2$ dissolved in ethanol.

5.2.3.3 Enantiomeric Separation

1.5 mL of a 2 mM solution of $[\text{Rh}(\text{chrysi})(\text{phen})(\text{DPE})]^{2+}$ was injected, 30 μL at a time, onto an Astec® CYCLOBOND® I 2000 Chiral HPLC Column that was heated to 40° C. An isocratic method of 50% acetonitrile, 50% 100 mM KPF_6 was used to separate the two enantiomers. An automatic fraction collector was used to collect each peak separately. The resulting dilute solutions were loaded onto a SPE cartridge and rinsed with copious amount of 0.1% $\text{TFA}_{(\text{aq})}$. The SPE cartridge was eluted with 10% acetonitrile in 0.1% $\text{TFA}_{(\text{aq})}$. The chloride salts were obtained from a Sephadex QAE anion exchange column equilibrated with 0.1M MgCl_2 . Circular dichroism spectra were taken on an Aviv 62DS spectropolarimeter in a 1 mm path length cell.

5.2.4 X-Ray Structure Determination

5.2.4.1 $[\text{Rh}(\text{HDPA})_2(\text{chrysi})]\text{Cl}_2$

Low-temperature diffraction data (ϕ - and ω -scans) were collected on a Bruker Kappa diffractometer coupled to a Apex II CCD detector with graphite monochromated

Mo K_{α} radiation ($\lambda = 0.71073 \text{ \AA}$) for the structure of $[\text{Rh}(\text{HDP A})_2(\text{chrysi})]\text{Cl}_2$. The structure was solved by direct methods using SHELXS⁶ and refined against F^2 on all data by full-matrix least squares with SHELXL-2013⁷ using established refinement techniques.⁸ All non-hydrogen atoms were refined anisotropically. All hydrogen atoms were included into the model at geometrically calculated positions and refined using a riding model. The isotropic displacement parameters of all hydrogen atoms were fixed to 1.2 times the U value of the atoms they are linked to (1.5 times for methyl groups).

$[\text{Rh}(\text{HDP A})_2(\text{chrysi})]\text{Cl}_2$ crystallizes in the monoclinic space group $P2_1/n$ with one molecule in the asymmetric unit along with two molecules of methanol. One of the two chloride ions was disordered over two positions and refined with the help of similarity restraints on the displacement parameters. The occupancies of the two components refined to 0.930(4):0.070(4). The coordinates for the hydrogen atoms bound to N1, N4, N7, O1S, O1T, and O1W were located in the difference Fourier synthesis and refined semi-freely with the help of a distance restraint. The N-H distances were restrained to be 0.91(4) \AA for N1, 0.88(4) \AA for N4, N7 and 0.84(4) \AA for all O-H bonds.

5.2.4.2 $[\text{Rh}(\text{chrysi})(\text{phen})(\text{DPE})]\text{Cl}_2$

Low-temperature diffraction data (ϕ - and ω -scans) were collected on a Bruker Kappa diffractometer coupled to an Apex II CCD detector with graphite-monochromated Mo K_{α} radiation ($\lambda = 0.71073 \text{ \AA}$) for the structure of $[\text{Rh}(\text{chrysi})(\text{phen})(\text{DPE})]\text{Cl}_2$. The structure was solved by direct methods using SHELXS⁶ and refined against F^2 on all data by full-matrix least squares with SHELXL-2013⁷ using established refinement techniques.⁸ All non-hydrogen atoms were refined anisotropically. Unless otherwise noted, all hydrogen atoms were included into the model at geometrically calculated

positions and refined using a riding model. The isotropic displacement parameters of all hydrogen atoms were fixed to 1.2 times the U value of the atoms they are linked to (1.5 times for methyl groups).

[Rh(chrysi)(phen)(DPE)]Cl₂ crystallizes in the triclinic space group $P\bar{1}$ with one molecule in the asymmetric unit along with two chloride anions, two waters, and two molecules of ethanol. Each of the ethanol molecules were disordered over three positions. They were refined with the help of similarity restraints on the 1,2- and 1,3-distances and displacement parameters as well as rigid bond restraints for anisotropic displacement parameters. The occupancies of the two disordered ethanol molecules were freely refined to 0.509(3):0.261(3):0.229(3) and 0.453(3):0.295(3):0.252(3), respectively. Additional residual electron density is located near each of the disordered ethanol molecules. However, the refinement of additional ethanol positions was unsuccessful, and the current model represents the best model which led to a stable refinement. The coordinates for the hydrogen atoms bound to N1, N2, O1W and O2W were located in the difference Fourier synthesis and refined semi-freely with the help of a distance restraint. The N-H and O-H distances were restrained to be 0.88(4) Å and 0.84(4) Å, respectively. The hydrogen atoms bound to oxygen in the ethanol molecules could not be found and were included at geometrically calculated positions and refined using a riding model.

5.2.4.3 [Rh(chrysi)(phen)(PPE)]Cl₂

Low-temperature diffraction data (ϕ - and ω -scans) were collected on a Bruker Kappa diffractometer coupled to an Apex II CCD detector with graphite-monochromated Mo K_{α} radiation ($\lambda = 0.71073$ Å) for the structure of [Rh(chrysi)(phen)(PPE)]Cl₂. The structure was solved by direct methods using

SHELXS⁶ and refined against F^2 on all data by full-matrix least squares with SHELXL-2013⁸ using established refinement techniques.⁸ All non-hydrogen atoms were refined anisotropically. Unless otherwise noted, all hydrogen atoms were included into the model at geometrically calculated positions and refined using a riding model. The isotropic displacement parameters of all hydrogen atoms were fixed to 1.2 times the U value of the atoms they are linked to (1.5 times for methyl groups). All disordered atoms were refined with the help of similarity restraints on the 1,2-distances and displacement parameters as well as rigid bond restraints for anisotropic displacement parameters.

[Rh(chrysi)(phen)(PPE)]Cl₂ crystallizes in the triclinic space group $P\bar{1}$ with one molecule in the asymmetric unit along with two chloride anions and four molecules of methanol. One of the methanol molecules hydrogen-bonds to the ruthenium molecule and was not disordered. The three other methanol molecules were modeled as disordered. For the second methanol, only the methyl group was disordered over two positions with the occupancy of the two components refined to 0.841(7):0.159(7). The third methanol was completely disordered over two positions with occupancies of 0.792(6):0.208(6). The fourth methanol was disordered over three positions with occupancies 0.0615(3):0.234(3):0.151(3). The coordinates for the hydrogen atoms bound to N1, N2, and O1M were located in the difference Fourier synthesis and refined semi-freely with the help of a distance restraint. The N-H and O-H distances were restrained to be 0.88(4) Å and 0.84(4) Å, respectively. The hydrogen atoms for the remaining methanol positions could not be located and were included at geometrically calculated positions and refined using a riding model.

5.2.4.4 [Rh(chrysi)(phen)(PPO)]Cl₂

Low-temperature diffraction data (ϕ - and ω -scans) were collected on a Bruker three-circle diffractometer coupled to a Bruker Smart 1000 CCD detector with graphite monochromated Mo K_{α} radiation ($\lambda = 0.71073 \text{ \AA}$) for the structure of compound ack013. The structure was solved by direct methods using SHELXS⁶ and refined against F^2 on all data by full-matrix least squares with SHELXL-2013⁷ using established refinement techniques.⁸ All non-hydrogen atoms were refined anisotropically. All hydrogen atoms were included into the model at geometrically calculated positions and refined using a riding model. The isotropic displacement parameters of all hydrogen atoms were fixed to 1.2 times the U value of the atoms they are linked to (1.5 times for methyl groups).

Compound ack013 crystallizes in the triclinic space group $P\bar{1}$ with one molecule in the asymmetric unit along with two chloride anions, one molecule of diethyl ether, and one molecule of isopropyl alcohol. The coordinates for the hydrogen atoms bound to N1, N2, and O1T were located in the difference Fourier synthesis and refined semi-freely with the help of a distance restraint. The N-H and O-H distance were restrained to be 0.88(4) \AA and 0.84(4) \AA , respectively.

5.2.5 Metalloinsertor pH Titrations

25 μM solutions of $[\text{Rh}(\text{chrysi})(\text{phen})(\text{DPE})]^{2+}$ or $[\text{Rh}(\text{HDPA})_2(\text{chrysi})]^{3+}$ (3 mL, in 0.1 M NaCl) were prepared and absorption-spectra measured on a Cary 100 Bio UV-Visible Spectrophotometer. The pHs of the solutions and their blanks were adjusted (and monitored by an internal electrode) from approximately 4.5 to 10.5 and back *via* titration with either 6mM NaOH or 10 mM HCl. After each acid or base addition, an absorption spectrum was taken. A single wavelength was selected for each metal complex where a

large change was observed over the course of the titration. The absorbance at this wavelength was then plotted as a function of pH to generate a titration curve. The pK_a of each metal complex was determined from the inflection point of this sigmoidal curve. The data from three separate experiments were pooled to determine average pK_a values.

In addition, 25 μM solutions of 1:1 $[\text{Rh}(\text{chrysi})(\text{phen})(\text{DPE})]^{2+}:\text{DNA}$ or $[\text{Rh}(\text{HDPA})_2(\text{chrysi})]^{3+}:\text{DNA}$ (3 mL, in 100 mM NaCl, 20 mM NaP_i , pH 7.1 buffer) were prepared and absorption-spectra measured on a Cary 100 Bio UV-Visible Spectrophotometer. The DNA hairpin 5'-GGCAGGCATGGCTTTTTGCCATCCCTGCC-3' (underline denotes the CC mismatch) was used.

5.2.6 Photocleavage Competition Titrations

The oligonucleotide 3' - GCG ATG CAG ATA TAC CTA CTA GGA TTC ACT GTC ATG-5' was ^{32}P -labeled at the 5'-end by incubating DNA with ^{32}P -ATP and polynucleotide kinase (PNK) at 37°C for 2 h, followed by purification using gel electrophoresis. A small amount of the labeled DNA (less than 1% of the total amount of DNA) was added to 2 μM unlabeled DNA and its corresponding unlabeled complement (with a CC mismatch incorporated at the underlined site) in 100 mM NaCl, 20 mM NaP_i , pH 7.1 buffer. The duplex DNA was annealed by heating at 90°C for 10 min and cooling slowly to ambient temperature over a period of 2 h. Solutions of non-photocleaving rhodium complex ranging from nanomolar to micromolar concentration, as well as a 4 μM $[\text{Rh}(\text{bpy})_2(\text{chrysi})]^{3+}$ solution were made in Milli-Q water. Annealed 2 μM DNA (10 μL), 4 μM $[\text{Rh}(\text{bpy})_2(\text{chrysi})]^{3+}$ (5 μL), and 5 μL of non-photocleaving Rh solution at each concentration were mixed in a microcentrifuge tube and incubated at 37 °C for 10 min. A light control ($\emptyset\text{Rh}$), in which the DNA was mixed with 10 μL of water and

irradiated, and a dark control (\emptyset hv), in which the DNA was mixed with the highest concentration of rhodium complex without irradiation, were also prepared. The samples were then irradiated on an Oriel (Darmstadt, Germany) 1000-W Hg/Xe solar simulator (340-440 nm) for 15 min. The samples were dried and electrophoresed in a 20% denaturing polyacrylamide gel. The gel was then exposed to a phosphor screen, and the relative amounts of DNA in each band were quantitated by phosphorimagery (ImageQuant).

5.2.6.1 Binding Constant Determination

The fraction of DNA cleaved in each lane on the gel (See **Figure 5.4** for a typical autoradiogram) was normalized and plotted against the log of the concentration of rhodium complex. The data were fit to a sigmoidal curve using OriginPro 6.1 (**Figure 5.5**). The resulting midpoint value (i.e., the log of [rhodium complex] at the inflection point of the curve) was converted to units of concentration ($[\text{Rh}_{50\%}]$). The binding and dissociation constants of the non-photocleaving complex were calculated by solving simultaneous equilibria involving DNA, $[\text{Rh}(\text{bpy})_2(\text{chrysi})]^{3+}$, and the complex in question in Mathematica 6.0. The data from at least three photocleavage titrations were averaged for each metal complex to give an average binding affinity.

5.2.7 Covalent DNA binding assay

A 6.0 μM solution (250 μL) of the DNA hairpin 5'-GGCAGGCATGGCTTTTTGCCATCCCTGCC-3' (underline denotes the CC mismatch) in either in 100 mM NaCl, 20 mM NaP_i , pH 7.1 buffer or 100 mM NaCl, 20 mM NaP_i , 5 mM glutathione buffer (to mimic the reducing environment of the cell) was added to a 6.0 μM solution of $[\text{Rh}(\text{bpy})_2(\text{chrysi})]^{3+}$, $[\text{Rh}(\text{HDPA})_2(\text{chrysi})]^{3+}$, or

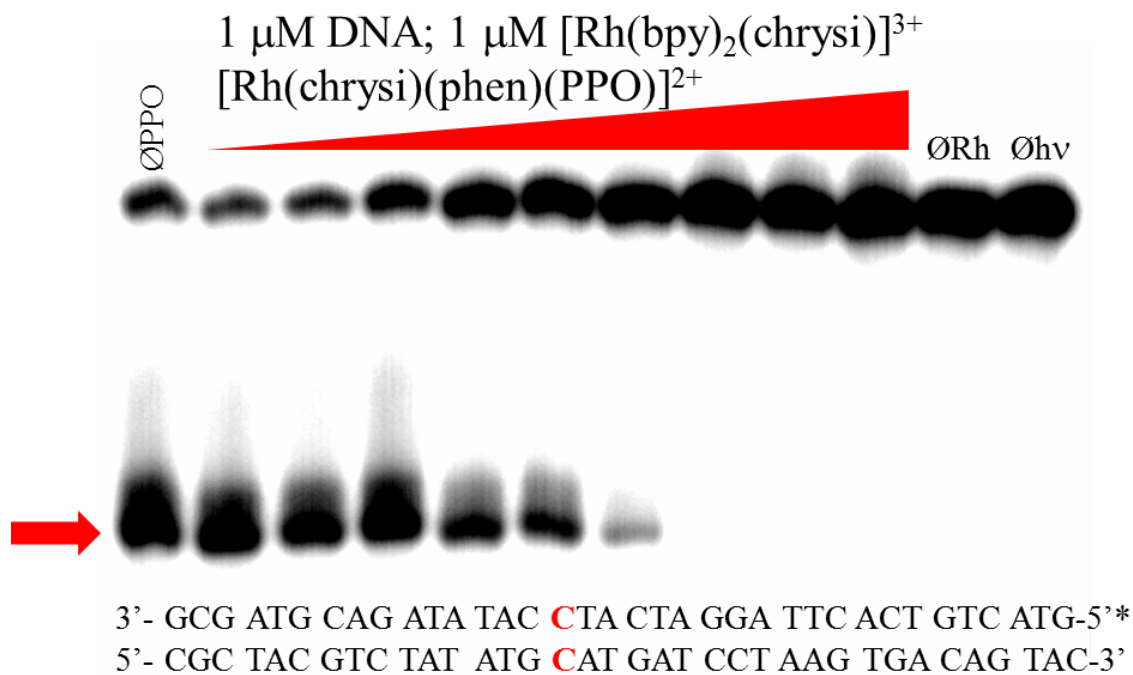


Figure 5.4 Binding affinities determined through DNA photocleavage. The DNA sequence is as shown (red denotes the mismatch, asterisk denotes the radiolabel). Samples were irradiated and electrophoresed through a 20% denaturing PAGE gel. A light control (ØRh , without rhodium) and dark control (Øhv , without irradiation) were included. A representative autoradiogram of a photocleavage competition titration between 1 μM *rac*- $[\text{Rh}(\text{bpy})_2(\text{chrysi})]^{3+}$ and 0-100 μM $[\text{Rh}(\text{chrysi})(\text{phen})(\text{PPO})]^{2+}$ is shown. Arrow indicates the position of the mismatch.

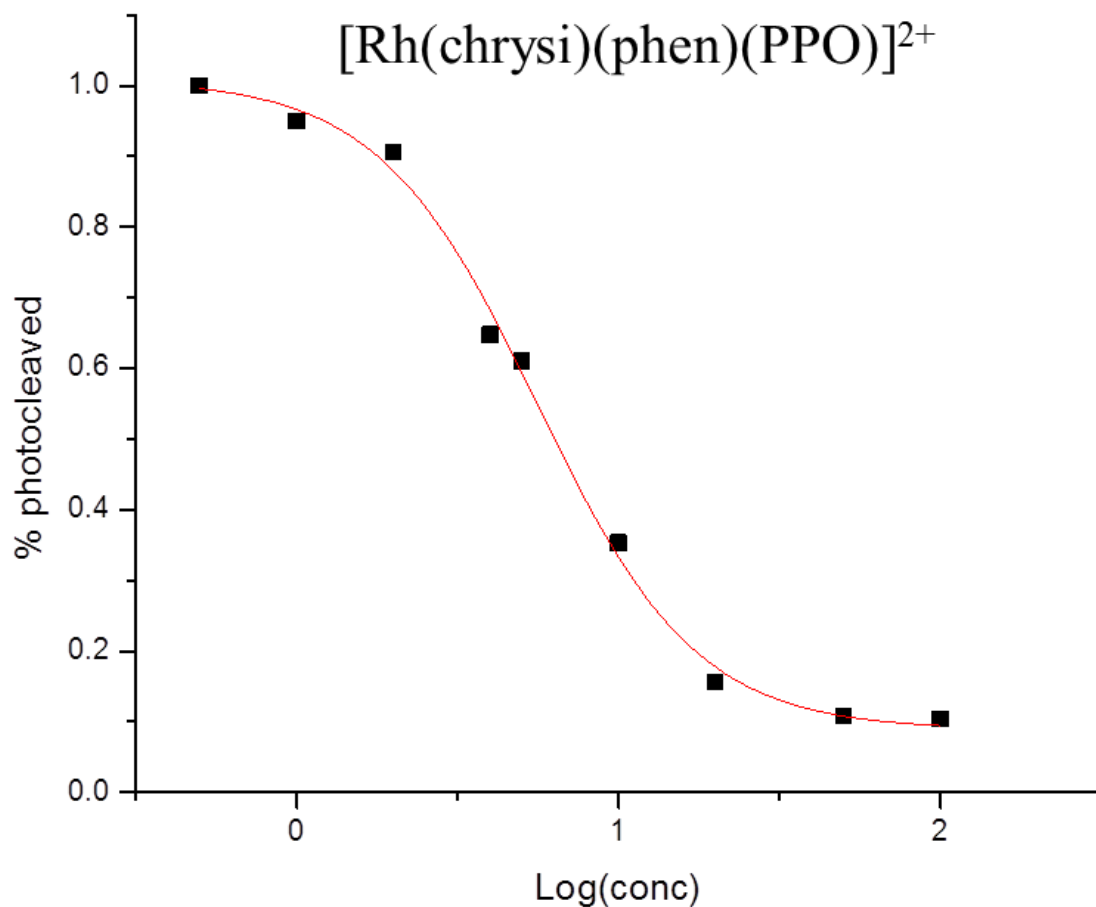


Figure 5.5 Representative sigmoidal curve for binding affinity determination. Shown is a plot of data from the photocleavage competition titration between 1 μM *rac*- $[\text{Rh}(\text{bpy})_2(\text{chrysi})]^{3+}$ and 0-100 μM $[\text{Rh}(\text{chrysi})(\text{phen})(\text{PPO})]^{3+}$ shown in **Figure 5.4** for binding constant determination.

[Rh(chrysi)(phen)(PPE)]²⁺ (250 μ L). The resulting solution was allowed to incubate at 37° C for 30 min, followed by a 10-min incubation at 90° C. A 3.0 M solution of NaOAc (50 μ L) was added, followed by EtOH (1.5 mL) in order to precipitate the DNA. The resulting solution was vortexed and incubated on dry ice for 1.5 h, after which time it was spun at 14,000 rpm for 12 min. The supernatant was discarded, and the pellet dissolved in water (100 μ L). A 3.0 M solution of NaOAc (10 μ L) was added, followed by EtOH (300 μ L) in order to precipitate the DNA. The resulting solution was vortexed and incubated on dry ice for 1.5 h, after which time it was spun at 14,000 rpm for 12 min. The supernatant was discarded, and the pellet dissolved in water (500 μ L). An electronic absorption (UV-Vis) spectrum was then taken of the resulting solution on a Cary 100 Bio UV-Visible Spectrophotometer.

5.2.8 Circular Dichroism Study of Δ/Λ -[Rh(chrysi)(phen)(DPE)]²⁺ Bound to Mismatched DNA

50.0 μ M solutions of the DNA hairpin 5'-GGCAGGCCATGGCTTTTTGCCATCCCTGCC-3' (underline denotes the CC mismatch) and Δ - and Λ -[Rh(chrysi)(phen)(DPE)]²⁺ (200 μ L in 100 mM NaCl, 20 mM NaPi, pH 7.1 buffer) were prepared, and CD spectra were taken on an Aviv 62DS spectropolarimeter in a 1 mm path length cell. 100 μ L of each metal complex solution was then added to 100 μ L of the DNA solution, and CD spectra were immediately recorded. After 30 m, additional CD spectra were recorded to confirm that no changes in the spectra occurred.

5.2.9 Cell Culture

HCT116N and HCT116O cells were grown in RPMI medium 1640 supplemented with: 10% FBS; 2 mM L-glutamine; 0.1 mM nonessential amino acids; 1 mM sodium

pyruvate; 100 units/mL penicillin; 100 µg/mL streptomycin; and 400 µg/mL Geneticin (G418). Cells were grown in tissue culture flasks (Corning Costar, Acton, MA) at 37 °C under 5% CO₂ and humidified atmosphere.

5.2.9.1 Cellular Proliferation ELISA

HCT116N and HCT116O cells were plated in 96-well plates at 2000 cells/well and allowed 24 h to adhere. The cells were then incubated with rhodium for the concentration and durations specified. For incubations less than 72 h, the Rh-containing media was replaced with fresh media, and the cells were grown for the remainder of the 72-h period. Cells were labeled with BrdU 24 h before analysis. The BrdU incorporation was quantified by antibody assay according to established procedures.⁹ Cellular proliferation was expressed as the ratio of the amount of BrdU incorporated by the treated cells to that of the untreated cells.

5.2.9.2 MTT Cytotoxicity Assay

Cytotoxicity assays were performed as described in the literature.¹⁰ HCT116N and HCT116O cells were plated in 96-well plates at 50,000 cells/well and incubated with rhodium for the durations specified. After rhodium incubation, cells were labeled with MTT for 4 h at 37°C under 5% CO₂ and humidified atmosphere. The resulting formazan crystals were dissolved with solubilizing reagent purchased from Roche according to the manufacturer's instructions. The dissolved formazan was quantified as the absorbance at 570 nm minus the background absorbance at 690 nm. Percent viability was determined as the ratio of the amount of formazan in the treated cells to that of the untreated cells.

5.2.9.3 Cell Death Mode Flow Cytometry Assay

Cell death was characterized by a dye exclusion assay.¹¹ After 24-, 48-, or 72-h incubation with rhodium, cells were harvested from adherent culture by trypsinization, washed with cold PBS, and centrifuged at 2,000 rpm for 5 minutes. The resultant pellets were resuspended in PBS to a concentration of 10^6 cells/mL and stained with propidium iodide to a final concentration of 1 μ g/mL and with YO-PRO-1 to a final concentration of 50 nM for 30 minutes prior to analysis by flow cytometry.

5.2.10 ICP-MS Assay for Whole-Cell Rhodium Levels

HCT116O cells were plated at 1×10^6 cells/well in a 6 well plate. The cells were allowed 24 h to adhere, then treated with 10 μ M [Rh(HDPA)₂(chrysi)]Cl₃, 5 μ M [Rh(chrysi)(phen)(DPE)]Cl₂, 1 μ M [Rh(chrysi)(phen)(PPE)]Cl₂, or 0.5 μ M [Rh(chrysi)(phen)(PPO)]Cl₂. After 24 h, the media was decanted, the cell monolayer washed with 3 mL PBS, and the cells lysed with 800 μ L of 1% SDS. The cell lysate was sonicated on a Qsonica Ultrasonic processor for 10 sec at 20% amplitude. 750 μ L of the lysate was then combined with 750 μ L of a 2% HNO₃ (v/v) solution, while the remainder of the lysate was quantified for protein by a bicinchoninic assay (BCA).¹² The 1% HNO₃ solution was analyzed for rhodium content on an HP-4500 ICP-MS unit. Rhodium counts were normalized to the amount of protein determined from the BCA analysis (to obtain ng [Rhodium]/mg [protein] values). Standard errors for three independent experiments are shown. The experiment was repeated with HCT116N cells to verify similar uptake of rhodium by the two cell lines.

5.3 Results

5.3.1 Synthesis and Characterization of Compounds

Single crystals of $[\text{Rh}(\text{chrysi})(\text{phen})(\text{DPE})]\text{Cl}_2$ were grown from a vapor diffusion of diethyl ether into a concentrated solution of the complex in ethanol. The solved structure revealed the DPE ligand to coordinate *via* an oxygen instead of the second pyridine nitrogen. In order to assess the generality of this coordination environment (and determine if the solid state structure of $[\text{Rh}(\text{chrysi})(\text{phen})(\text{DPE})]\text{Cl}_2$ is the same as its solution structure), we synthesized a phenyl (PPE) derivative and a methyl (PPO) derivative. Both ligands are notable in their lack of a second nitrogen to coordinate to the rhodium center. These new compounds can be synthesized *via* analogous methods and in decent yields. Single crystals grown of both compounds confirmed the generality of this unusual ligand coordination (**Figure 5.6** and **Figure 5.7**).

These compounds were also designed to ascertain the importance of both the ligand coordination environment (the presence of a Rh-O bond) and the bulky “dangling” pyridine group with regards to the enhanced potency and cell-selective activity of the parent compound. An additional compound with a greasy hexyl group appended to this ligand scaffold was also synthesized to assess the effects of lipophilicity on the biological activity of this family of compounds.

In order to determine the acidity constants of the imine protons in $[\text{Rh}(\text{chrysi})(\text{phen})(\text{DPE})]^{2+}$ as compared to $[\text{Rh}(\text{HDPA})_2(\text{chrysi})]^{3+}$, pH spectroscopic titrations were performed. It has previously been demonstrated that the visible absorbance changes which occur as the pH of a rhodium complex solution is titrated can be used for the determination of the pK values of the compounds.¹³ As can be seen in **Figure 5.8** and

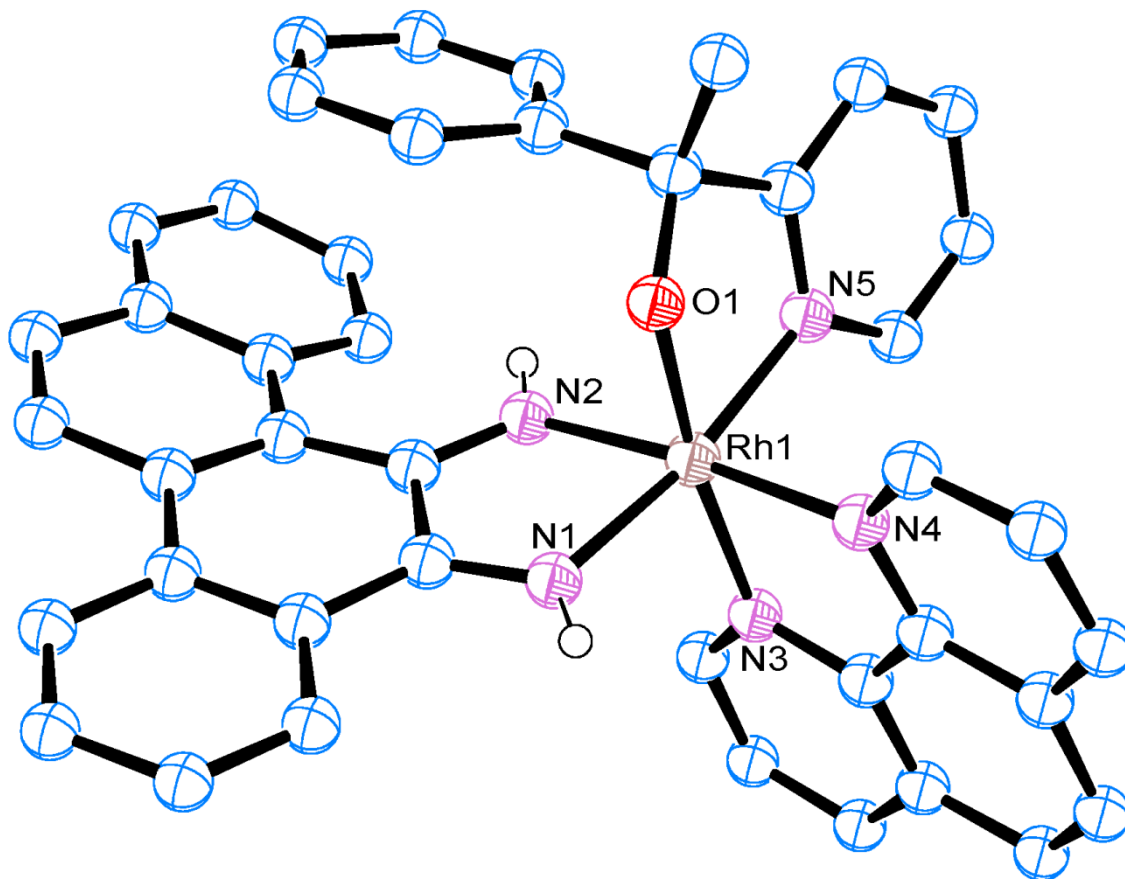


Figure 5.6 X-ray crystal structure of [Rh(chrysi)(phen)(PPE)]Cl₂. Displacement of ellipsoids are drawn at 50% probability. For clarity, chloride atoms and hydrogen atoms (except imine protons) have been omitted. Selected bond lengths (Å): Rh-O 1.983, Rh-N1 1.991, Rh-N2 1.993, Rh-N3 2.053, Rh-N4 2.037, Rh-N5 2.034.

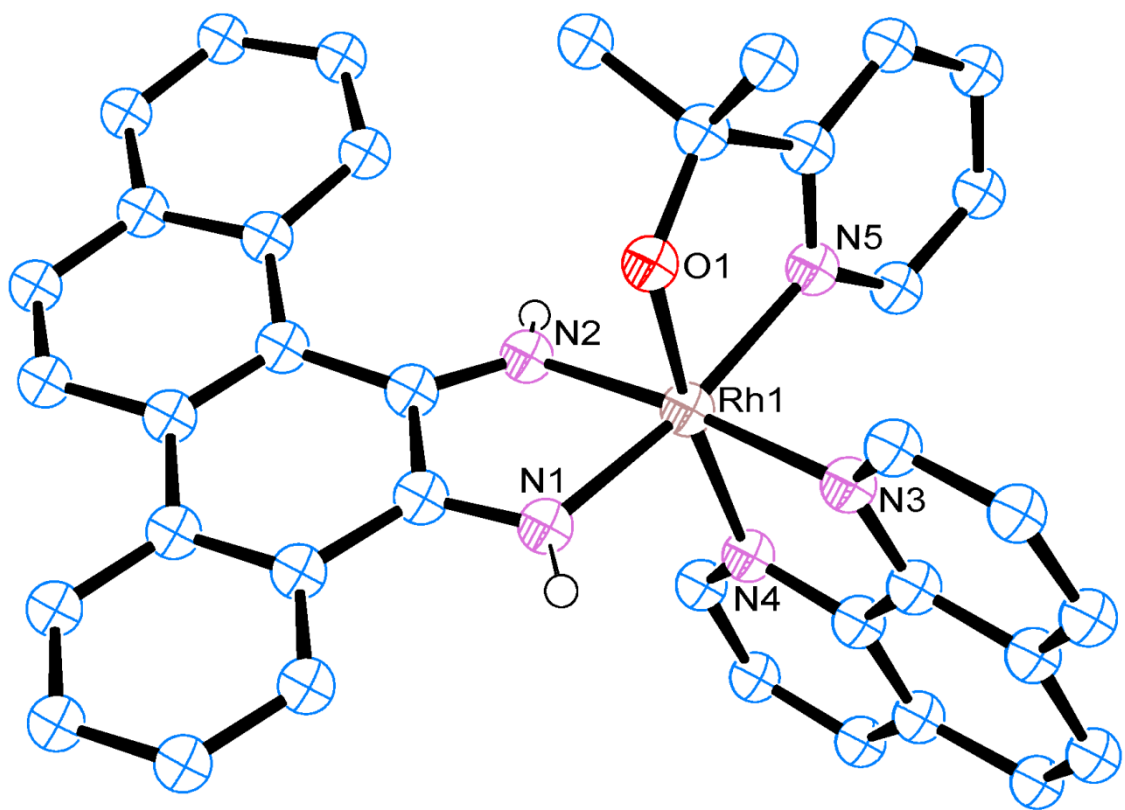


Figure 5.7 X-ray crystal structure of [Rh(chrysi)(phen)(PPO)]Cl₂. Displacement of ellipsoids are drawn at 50% probability. For clarity, chloride atoms and hydrogen atoms (except imine protons) have been omitted. Selected bond lengths (Å): Rh-O 1.973, Rh-N1 1.980, Rh-N2 1.994, Rh-N3 2.039, Rh-N4 2.067, Rh-N5 2.041.

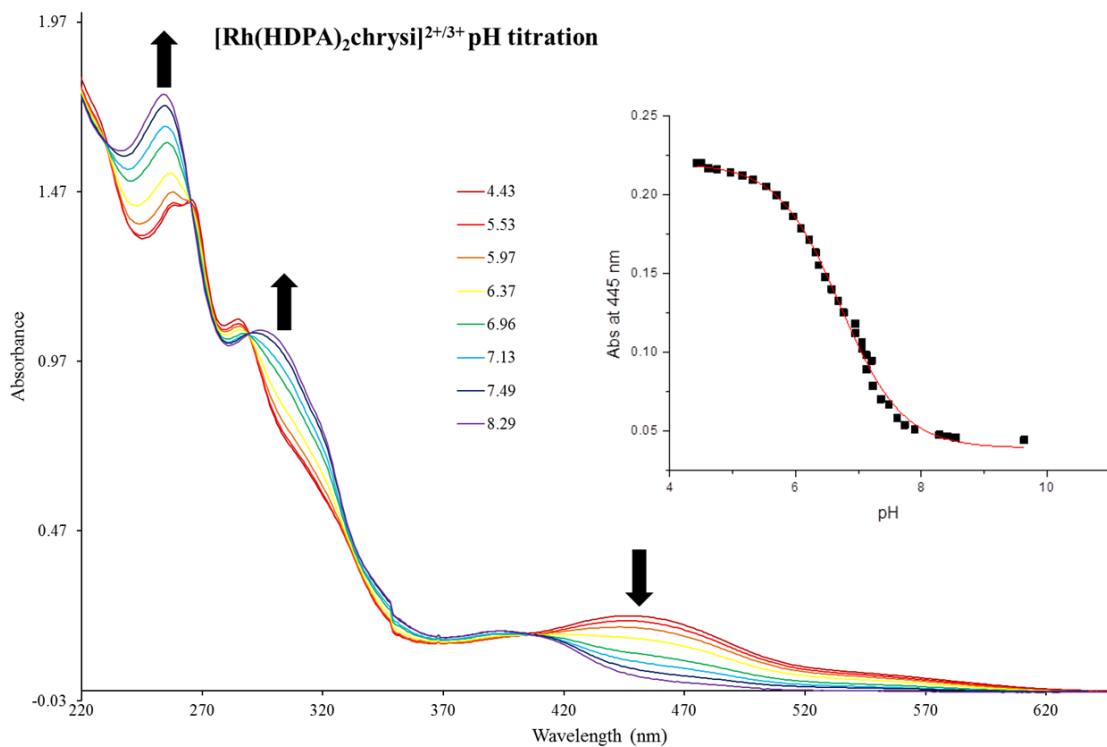


Figure 5.8 pH titration of $[\text{Rh}(\text{HDPA})_2(\text{chrysi})]^{3+}$. Shown are absorption spectra of a 25 μM solution of $[\text{Rh}(\text{HDPA})_2(\text{chrysi})]^{3+}$ as the pH changes from 4.5 (red) to 8.5 (purple). The black arrows exhibit the direction in which the various bands change as the pH increases. (Inset) The absorbance at 445 nm was plotted as a function of pH and fit to a sigmoidal curve. The pK_a was determined from the inflection point of this curve.

Figure 5.9, as the pH of the solution increases from 4.5 to 10.5, the band around 440 nm (which corresponds to an MLCT from the Rh center to the chrysi ligand) undergoes a blue shift. When the absorbance at the λ_{\max} of this band is plotted as a function of pH, a titration curve can be constructed, and the pK_a value of each metal complex is determined from the inflection point of the curve (**Figure 5.8** and **Figure 5.9**, insets). The pK_a values for $[\text{Rh}(\text{HDPA})_2(\text{chrysi})]^{3+}$ and $[\text{Rh}(\text{chrysi})(\text{phen})(\text{DPE})]^{2+}$ are 7.0 ± 0.5 and 8.7 ± 0.2 , respectively. This reflects a difference in equilibrium constants of almost 2 orders of magnitude, quite possibly due to the negative charge of the DPE ligand as compared to HDPA.

In order to ascertain the protonation state of $[\text{Rh}(\text{chrysi})(\text{phen})(\text{DPE})]^{2+}$ and $[\text{Rh}(\text{HDPA})_2(\text{chrysi})]^{3+}$ upon DNA binding, mismatched DNA was added to both compounds in a 1:1 ratio and absorption spectra recorded. As can be seen in **Figure 5.10**, $[\text{Rh}(\text{chrysi})(\text{phen})(\text{DPE})]^{2+}$ binds to mismatched DNA with a fully protonated chrysi ligand. On the basis of the hypochromicity, it is clear that the chrysi ligand is pi-stacking with the DNA bases. It appears that with $[\text{Rh}(\text{HDPA})_2(\text{chrysi})]^{3+}$, on the other hand, there are a mixture of protonation states upon DNA binding. The 400 nm that corresponds to the deprotonated species has a much larger hypochromicity than the 445 nm band.

All three crystallographically characterized compounds are synthesized as a mixture of diastereomers (See NMR characterization), and only the diastereomers of $[\text{Rh}(\text{chrysi})(\text{phen})(\text{DPE})]^{2+}$ were able to be resolved *via* HPLC. Therefore, this compound was chosen for enantiomeric studies. The enantiomers of $[\text{Rh}(\text{chrysi})(\text{phen})(\text{DPE})]^{2+}$ were resolved *via* HPLC and characterized *via* circular dichroism spectroscopy (**Figure**

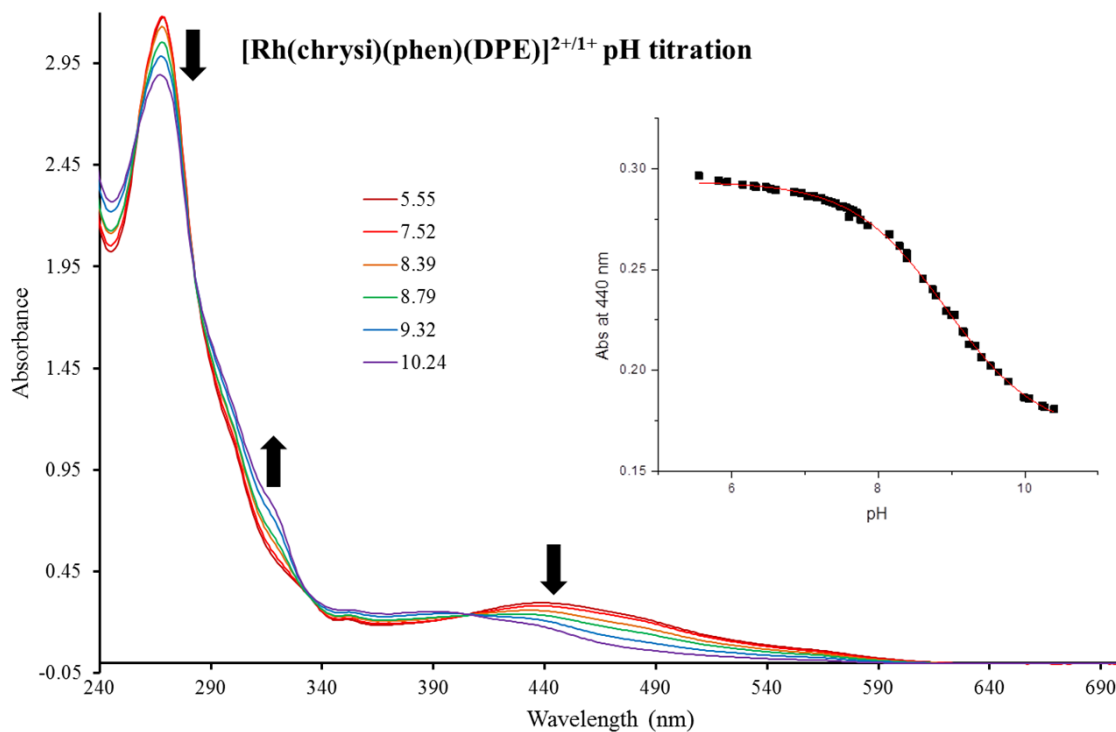


Figure 5.9 pH titration of $[\text{Rh}(\text{chrysi})(\text{phen})(\text{DPE})]^{2+}$. Shown are absorption spectra of a 25 μM solution of $[\text{Rh}(\text{chrysi})(\text{phen})(\text{DPE})]^{2+}$ as the pH changes from 5.5 (red) to 10.2 (purple). The black arrows exhibit the direction in which the various bands change as the pH increases. (Inset) The absorbance at 440 nm was plotted as a function of pH and fit to a sigmoidal curve. The pK_a was determined from the inflection point of this curve.

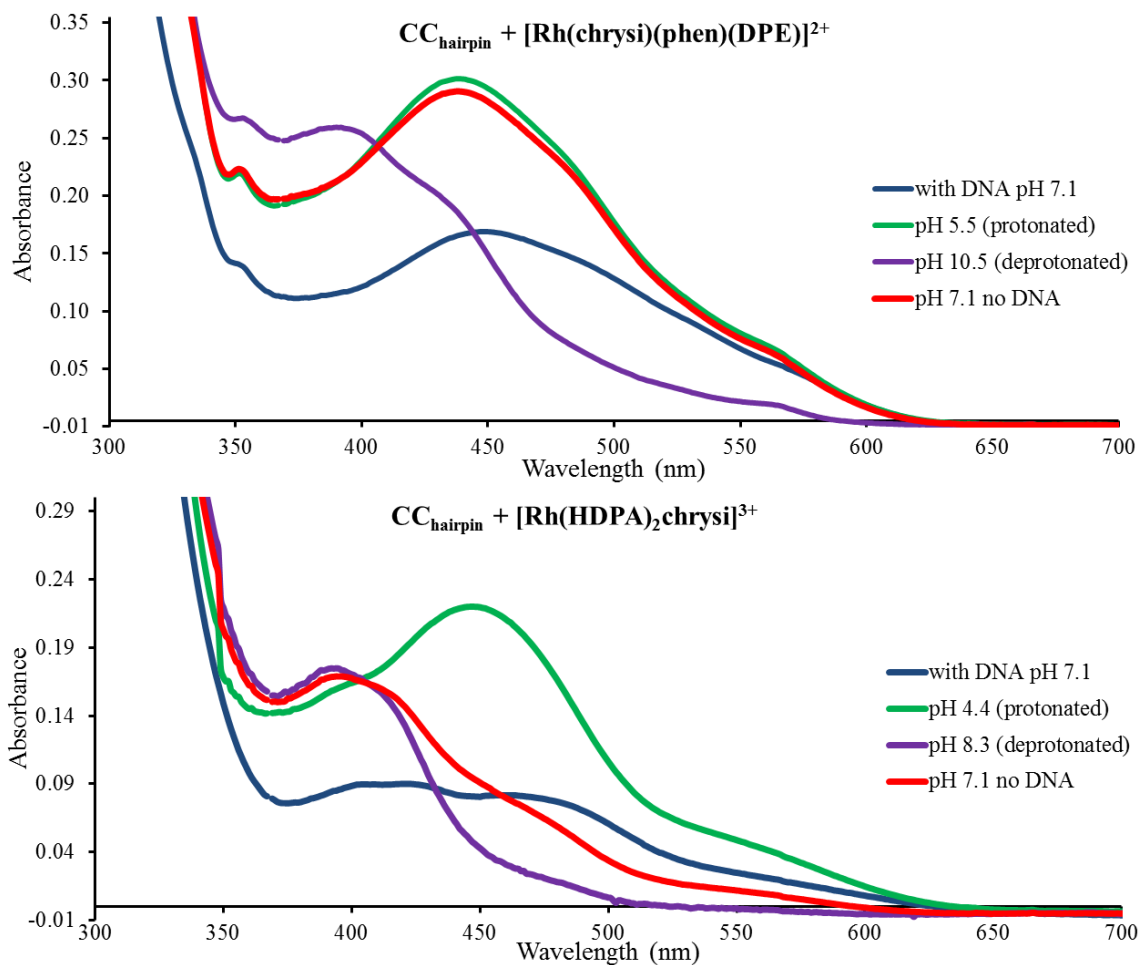


Figure 5.10 Absorption spectra of $[\text{Rh}(\text{chrysi})(\text{phen})(\text{DPE})]^{2+}$ and $[\text{Rh}(\text{HDPA})_2(\text{chrysi})]^{3+}$ bound to mismatched DNA. Shown in blue are absorption spectra of 25 μM solutions of $[\text{Rh}(\text{chrysi})(\text{phen})(\text{DPE})]^{2+}$ and $[\text{Rh}(\text{HDPA})_2(\text{chrysi})]^{3+}$ with 25 μM of the DNA hairpin 5'-GGCAGGCATGGCTTTTTGCCATCCCTGCC-3' (underline denotes the CC mismatch). The absorption spectra of the fully protonated species are shown in green, those of the fully deprotonated species are in purple, and those of the compounds at pH 7.1 with no DNA are shown in red.

5.11). HPLC analysis of the purified fractions confirmed >95% ee of the Δ isomer, and ~90% ee of the Λ isomer (data not shown). Furthermore, the enantiomers are stable in aqueous solution for up to 1 month; no interconversion of the enantiomers is observed in either neutral buffer or buffer with 5 mM glutathione.

5.3.2 Binding Affinities for Metal Complexes at Single Base Mismatches

The new family of compounds promotes no DNA cleavage upon irradiation, and, as such, their binding affinities were determined through binding competition titrations with 1 μ M *rac*-[Rh(bpy)₂(chrysi)]³⁺, which does cleave DNA upon irradiation.¹⁴⁻¹⁶ A synthetic 36-mer oligonucleotide was synthesized with a complement featuring a cytosine across from a central cytosine (underlined) to form a mismatched strand of duplex DNA: 3' - GCG ATG CAG ATA TAC CTA CTA GGA TTC ACT GTC ATG - 5'. A representative photocleavage titration can be found in **Figure 5.3**. The degree of photocleavage can be plotted against the log([Rh]) and fit to a sigmoidal curve (**Figure 5.4**). On the basis of the binding constant of [Rh(bpy)₂(chrysi)]³⁺, the binding constants of all subsequent complexes are then determined by solving simultaneous equilibria at the inflection point of the photocleavage titration curve. The results are shown in **Figure 5.1**. All racemic mixtures of compounds exhibit binding affinities within a factor of two of each other, varying from 2.6 to 5.5 x 10⁶ M⁻¹. Most interesting, however, is the observation that the two enantiomers of [Rh(chrysi)(phen)(DPE)]²⁺ bind to mismatched DNA with the same affinity (6.0 x 10⁶ M⁻¹ and 5.7 x 10⁶ M⁻¹ for Δ and Λ , respectively). This is in direct contrast to [Rh(bpy)₂(chrysi)]³⁺, in which only the Δ isomer binds to mismatched DNA.¹⁴

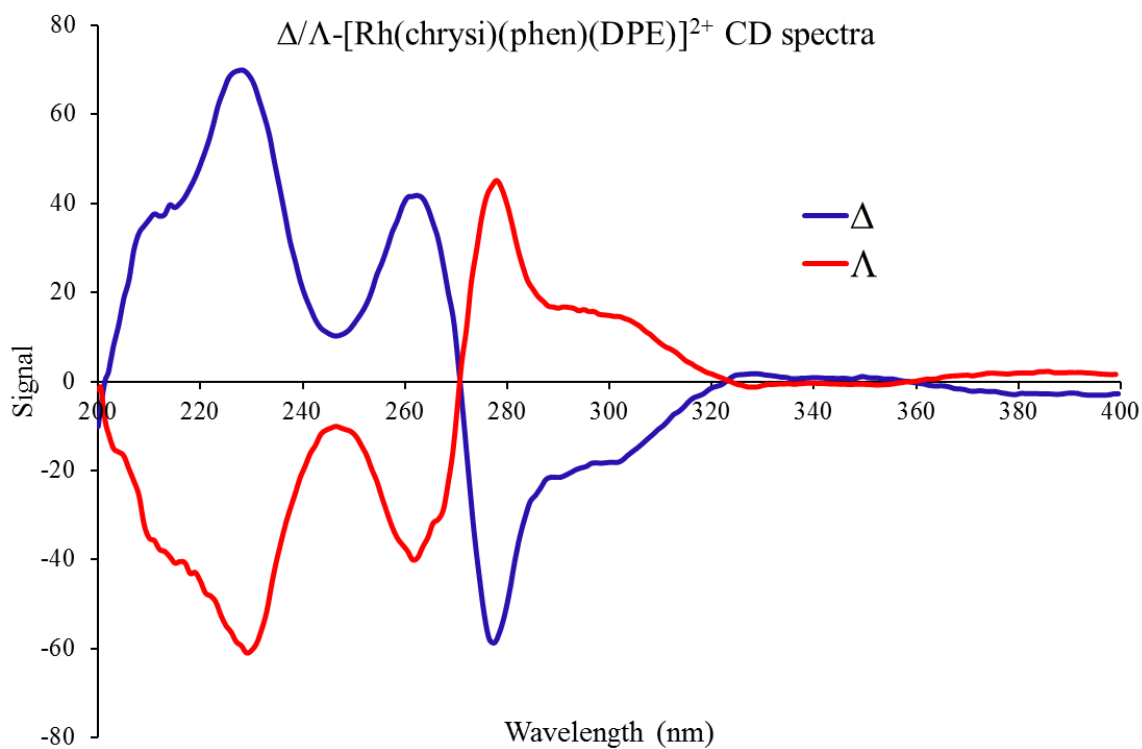


Figure 5.11 Circular dichroism (CD) spectra of Δ - and Λ - [Rh(chrysi)(phen)(DPE)]²⁺ in water (blue and red, respectively). $\Delta\epsilon$ values for Δ - [Rh(chrysi)(phen)(DPE)]²⁺: 229 nm (77 M⁻¹ cm⁻¹), 262 nm (46 M⁻¹ cm⁻¹), 277 nm (-64 M⁻¹ cm⁻¹), 295 nm (-21 M⁻¹ cm⁻¹). $\Delta\epsilon$ values for Λ - [Rh(chrysi)(phen)(DPE)]²⁺: 229 nm (-82 M⁻¹ cm⁻¹), 262 nm (-53 M⁻¹ cm⁻¹), 277 nm (61 M⁻¹ cm⁻¹), 295 nm (22 M⁻¹ cm⁻¹).

In order to ascertain if racemization of the two enantiomers occurs upon DNA binding, circular dichroism spectra were taken of the two enantiomers before and after addition to mismatched DNA. As can be seen in **Figure 5.12**, the CD spectra of the two metalloinsertor-mismatched DNA complexes are distinct from each other, even after 30 min of incubation (the average time frame of a competition gel titration, wherein both enantiomers bind to DNA). This confirms that both enantiomers bind to mismatched DNA without racemization.

5.3.3 Covalent DNA Binding

The ability of $[\text{Rh}(\text{chrysi})(\text{phen})(\text{PPE})]^{2+}$ to bind covalently to DNA was assessed *via* UV-Vis spectroscopy. In the event that the Rh-O bond is labile, it is possible for the complexes to bind covalently to DNA. In order to determine if covalent binding occurs, $[\text{Rh}(\text{bpy})_2(\text{chrysi})]^{3+}$, $[\text{Rh}(\text{HDPA})_2(\text{chrysi})]^{3+}$, or $[\text{Rh}(\text{chrysi})(\text{phen})(\text{PPE})]^{2+}$ were incubated with mismatched DNA under either neutral conditions (phosphate buffer), or a reducing environment (5 mM glutathione in phosphate buffer) for 30 min. The DNA was then denatured in order to release any noncovalently attached rhodium complex and precipitated out of solution. UV-Vis spectra of the various samples of precipitated DNA revealed no covalent DNA binding by any of the three complexes (**Figure 5.13**) under either neutral or reducing conditions; covalent DNA binding would result in a characteristic rhodium metalloinsertor MLCT band around 400 nm. Furthermore, the absorbance at 260 nm of the various samples confirmed comparable yields of DNA precipitation.

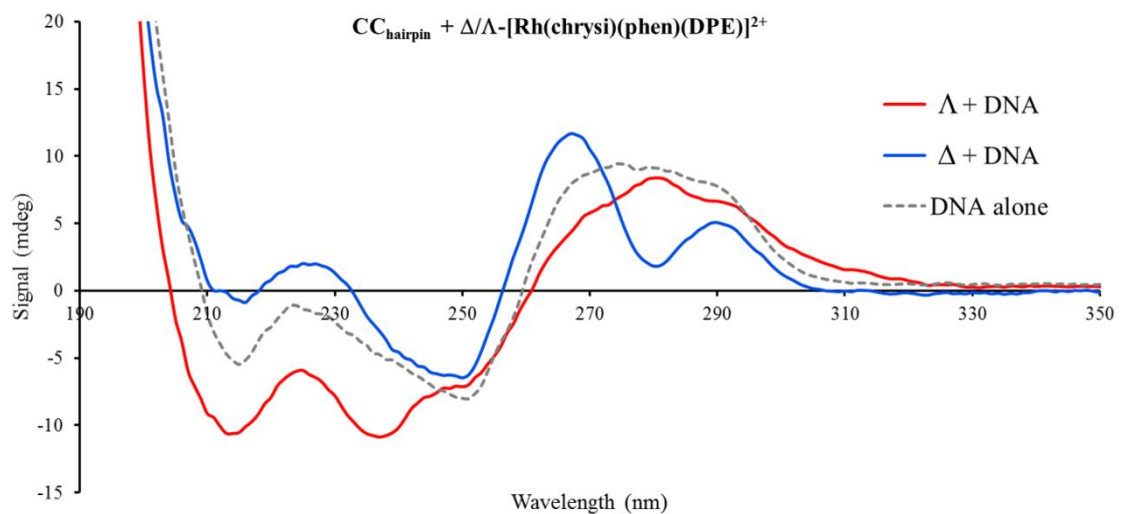


Figure 5.12 Circular dichroism (CD) spectra of Δ - and Λ - $[\text{Rh}(\text{chrysi})(\text{phen})(\text{DPE})]^{2+}$ bound to mismatched DNA. Shown are spectra of 25 μM solutions of Δ - and Λ - $[\text{Rh}(\text{chrysi})(\text{phen})(\text{DPE})]^{2+}$ in 100 mM NaCl, 20 mM NaPi, pH 7.1 buffer bound to the DNA hairpin 5'-GGCAGGCATGGCTTTTTGCCATCCCTGCC-3' (underline denotes the CC mismatch), and the DNA hairpin alone (Δ in blue, Λ in red, DNA alone in grey).

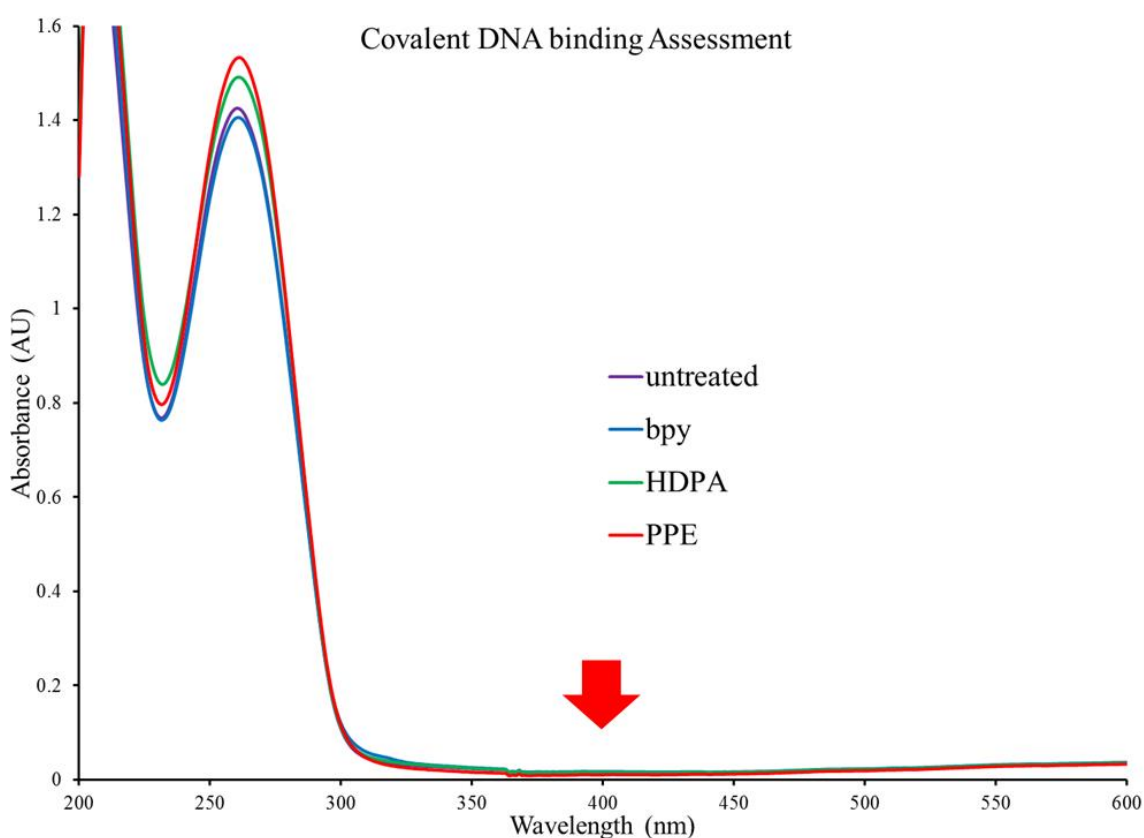


Figure 5.13 Assessment of the ability of $[\text{Rh}(\text{chrysi})(\text{phen})(\text{PPE})]^{2+}$ to bind covalently to mismatched DNA. A 29-mer hairpin with a CC mismatch was incubated with water, $[\text{Rh}(\text{chrysi})(\text{phen})(\text{PPE})]^{2+}$, $[\text{Rh}(\text{bpy})_2(\text{chrysi})]^{3+}$, or $[\text{Rh}(\text{HDPA})_2(\text{chrysi})]^{3+}$ (latter two compounds were included as control compounds that do not covalently bind to DNA). Following DNA melting and precipitation, a UV-Vis spectra was taken of the various samples. The absence of a band around 400 nm (indicated with red arrow) indicates that no Rh complex was still bound (this MLCT band is a characteristic band in all Rh-chrysi compounds).

5.3.4 Quantitation of Inhibition of Cellular Proliferation using an Enzyme-Linked Immunosorbent Assay (ELISA)

An ELISA for DNA synthesis was used to quantify the effects of the new family of metalloinsertors on the proliferation of HCT116N cells (MMR-proficient) and HCT116O cells (MMR-deficient). Both cell lines were incubated with the concentrations of compounds shown in **Figure 5.14**. The compound $[\text{Rh}(\text{HDPA})_2(\text{chrysi})]^{3+}$ was included as a control with which to compare the potencies and cell-selectivities of the new compounds. Cisplatin (*cis*-diamminedichloroplatinum) and MNNG (methylnitronitrosoguanidine) were also included as prototypical, FDA-approved chemotherapeutic agents that exhibit decreased effectiveness against MMR-deficient cancer cells.¹⁷ Incubations were performed for 24 h, after which time the medium containing the chemotherapeutic was replaced with fresh medium, and the cells were grown for the remainder of the 72-h period. The extent of cellular proliferation is expressed as the ratio of BrdU incorporated by the treated cells as compared to untreated controls. Furthermore, we define differential inhibition as the difference in BrdU incorporation between the HCT116N and HCT116O cells. The results are shown in **Figure 5.14**.

Clearly, the new family of compounds has significantly enhanced potency as compared to the earlier generation metalloinsertor; concentrations required for optimal differential activity are reduced from 10 μM for $[\text{Rh}(\text{HDPA})_2(\text{chrysi})]^{3+}$ (our previously most potent compound) to 3 μM ($[\text{Rh}(\text{chrysi})(\text{phen})(\text{DPE})]^{2+}$), 1 μM ($[\text{Rh}(\text{chrysi})(\text{phen})(\text{PPE})]^{2+}$), and 300 nM ($[\text{Rh}(\text{chrysi})(\text{phen})(\text{PPO})]^{2+}$). These compounds are also more potent than the FDA-approved chemotherapeutics in these

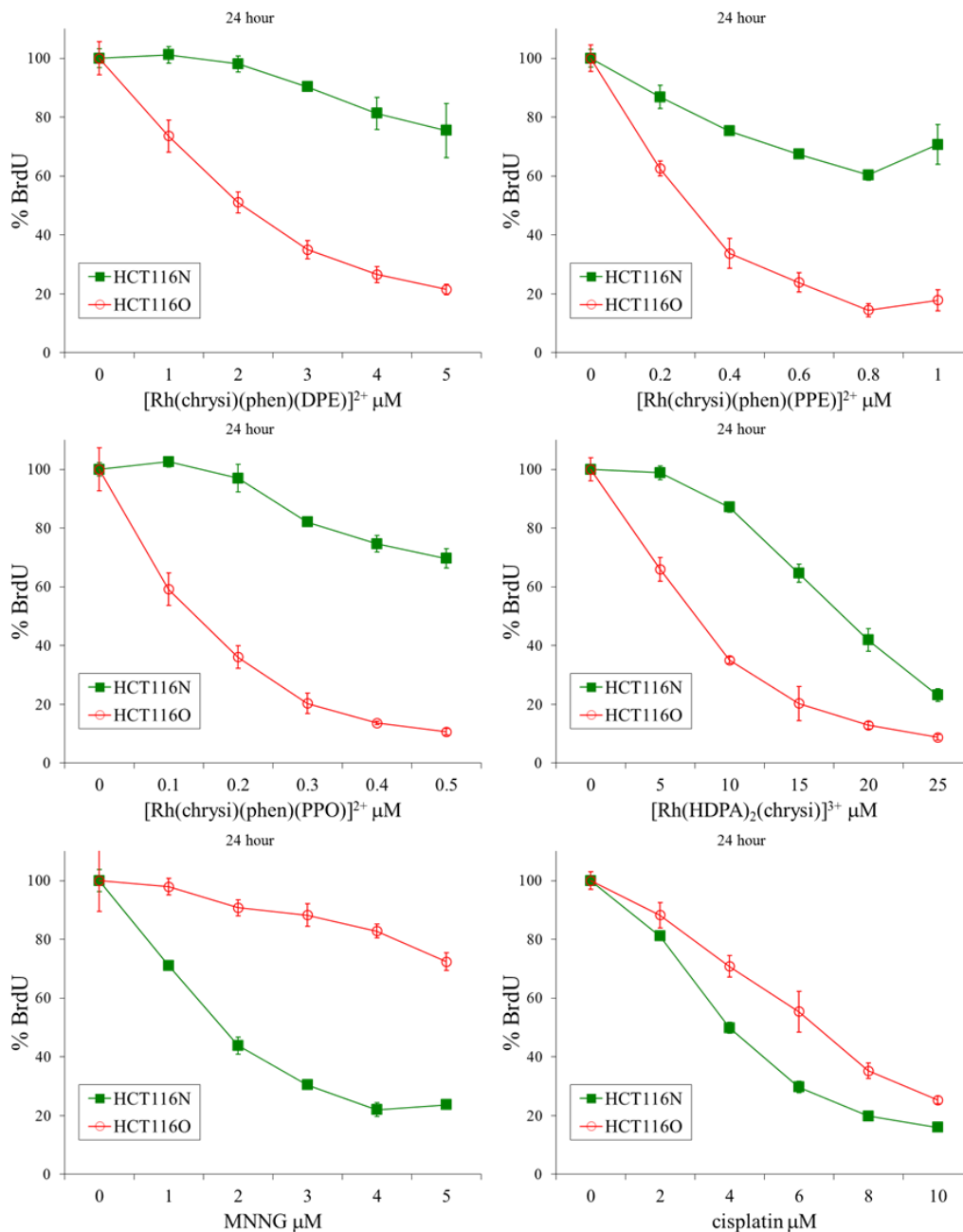


Figure 5.14 Inhibitory effects of rac - $[Rh(\text{chrysi})(\text{phen})(\text{DPE})]^{2+}$, rac - $[Rh(\text{chrysi})(\text{phen})(\text{PPE})]^{2+}$, rac - $[Rh(\text{chrysi})(\text{phen})(\text{PPO})]^{2+}$, $[Rh(\text{HDPA})_2(\text{chrysi})]^{3+}$, MNNG, and cisplatin. Shown are plots of BrdU incorporation (a measure of DNA synthesis and therefore cellular proliferation) normalized to the BrdU incorporation of untreated cells as a function of rhodium concentration. Standard error bars for five trials are shown.

assay conditions, which require 4 μM and 6 μM for optimal biological activity of MNNG and cisplatin, respectively. In addition, the enhanced cell-selectivity that was observed previously with $[\text{Rh}(\text{chrysi})(\text{phen})(\text{DPE})]^{2+}$ is conserved across the entire family. At their optimal concentrations, their differential inhibition are $55 \pm 2\%$, $53 \pm 7\%$, and $62 \pm 2\%$ for the DPE, PPE, and PPO derivatives, respectively. These MMR-deficient cell-selectivities far surpass the MMR-proficient cell-selectivity of cisplatin ($25 \pm 3\%$), which translates to drug resistance in the clinic, an issue that is currently a major epidemic with respect to cancer treatment.¹⁸

5.3.5 MTT Cytotoxicity Assay

The cytotoxic effects of all compounds were determined by MTT assay.¹⁰ Briefly, reduction of the MTT reagent by metabolically active cells leads to the production of formazan, which can then be dissolved in acidified SDS to produce a characteristic absorbance at 570 nm. This absorbance reflects the percentage of metabolically active cells in each sample. HCT116N and HCT116O cells were plated and treated with the various rhodium complexes at the concentrations indicated in **Figure 5.15** for 72 h. Percent viability is defined as the ratio of the amount of formazan in the treated cells to that in the untreated cells, and differential cytotoxicity is defined as the difference between the percent viabilities of the two cell lines. The results are shown in **Figure 5.15**. All four compounds in this new family display differential cytotoxicity in excess of 50%, and three compounds exhibit maximal activity at sub-micromolar concentrations. Specifically, the differential cytotoxicities and optimal concentrations of $[\text{Rh}(\text{chrysi})(\text{phen})(\text{DPE})]^{2+}$, $[\text{Rh}(\text{chrysi})(\text{phen})(\text{PPE})]^{2+}$, $[\text{Rh}(\text{chrysi})(\text{phen})(\text{PPO})]^{2+}$, and $[\text{Rh}(\text{chrysi})(\text{phen})(\text{PyOctanol})]^{2+}$ are $76 \pm 2\%$ at 6 μM , $66 \pm 2\%$ at 720 nM, $66 \pm 3\%$ at

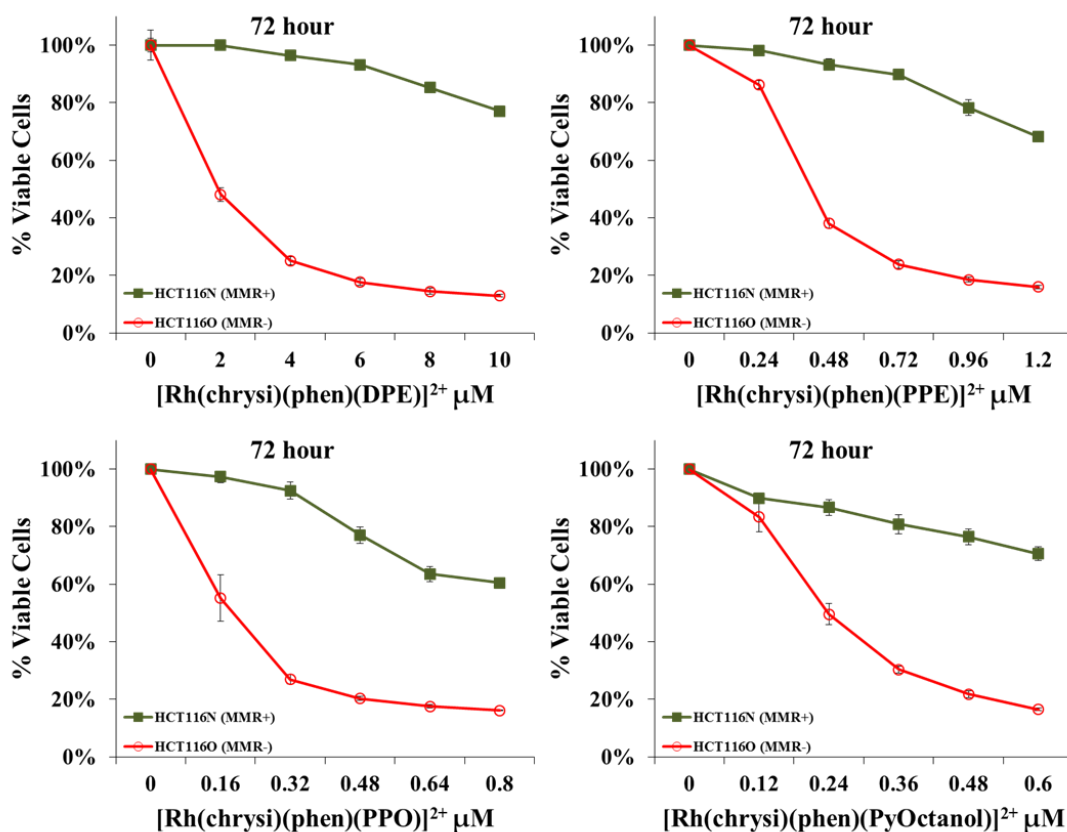


Figure 5.15 Differential cytotoxicities of rac -[Rh(chrysi)(phen)(DPE)]²⁺, rac -[Rh(chrysi)(phen)(PPE)]²⁺, rac -[Rh(chrysi)(phen)(PPO)]²⁺, and rac -[Rh(chrysi)(phen)(PyOctanol)]²⁺. HCT116N (green) and HCT116O (red) cells were plated in 96-well format at densities of 5×10^4 cells/well and treated with the concentrations of rhodium metalloinsertors indicated. After 72 hours, the cells were labeled with MTT for 4 hours.

320 nM, and $55 \pm 3\%$ at 480 nM, respectively. This is an increase in cytotoxic potency of almost two orders of magnitude as compared to $[\text{Rh}(\text{HDPA})_2(\text{chrysi})]^{3+}$ (25 μM required for optimal cytotoxicity). Furthermore, this is the only instance of a metalloinsertor with a greasy ancillary ligand retaining the cell-selective activity unique to our compounds.

The cell-selective cytotoxicities of the two enantiomers of $[\text{Rh}(\text{chrysi})(\text{phen})(\text{DPE})]^{2+}$ were also assessed, and the results are shown in **Figure 5.16**. Just as both enantiomers bind with equal affinity to DNA mismatches, both enantiomers display equal cell-selectivity; their differential cytotoxicities are $78 \pm 1\%$ and $75 \pm 2\%$ for Δ and Λ , respectively. This is again in direct contrast to $[\text{Rh}(\text{bpy})_2(\text{chrysi})]^{3+}$, in which case only the Δ isomer displays differential activity.¹⁹

5.3.6 ICP-MS Assay for Whole-Cell Rhodium Levels

HCT116O and HCT116N cells were treated with each rhodium complex at the concentrations indicated for 24 h. Whole cell lysates were analyzed for rhodium levels by ICP-MS and normalized to protein content (**Figure 5.17**). These concentrations roughly correspond to the concentrations necessary for optimal biological activity in the 24-h ELISA for the four different complexes. Therefore, the intracellular rhodium concentrations in this experiment reflect the amount of rhodium required for an optimal biological response. It is striking that the new family of compounds require significantly less intracellular rhodium to elicit a biological response than the prototypical $[\text{Rh}(\text{HDPA})_2(\text{chrysi})]^{3+}$ compound; specifically, the new compounds exhibit comparable biological activity to $[\text{Rh}(\text{HDPA})_2(\text{chrysi})]^{3+}$ with only $20 \pm 2\%$ ($[\text{Rh}(\text{chrysi})(\text{phen})(\text{DPE})]^{2+}$), $15 \pm 5\%$ ($[\text{Rh}(\text{chrysi})(\text{phen})(\text{PPE})]^{2+}$), or $13 \pm 2\%$ ($[\text{Rh}(\text{chrysi})(\text{phen})(\text{PPO})]^{2+}$) of the amount of intracellular rhodium.

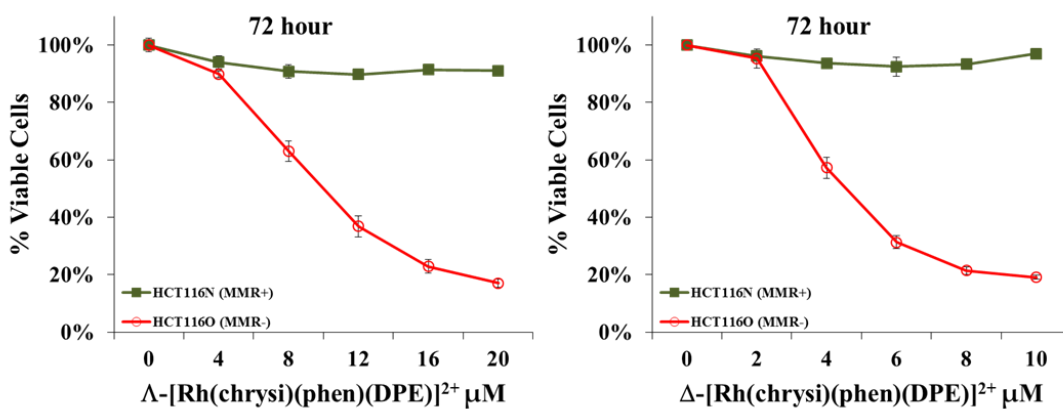


Figure 5.16 Differential cytotoxicities of Δ - and Λ -[Rh(chrysi)(phen)(DPE)]²⁺. HCT116N (green) and HCT116O (red) cells were plated in 96-well format at densities of 5×10^4 cells/well and treated with the concentrations of rhodium metalloinsertors indicated. After 72 hours, the cells were labeled with MTT for 4 hours.

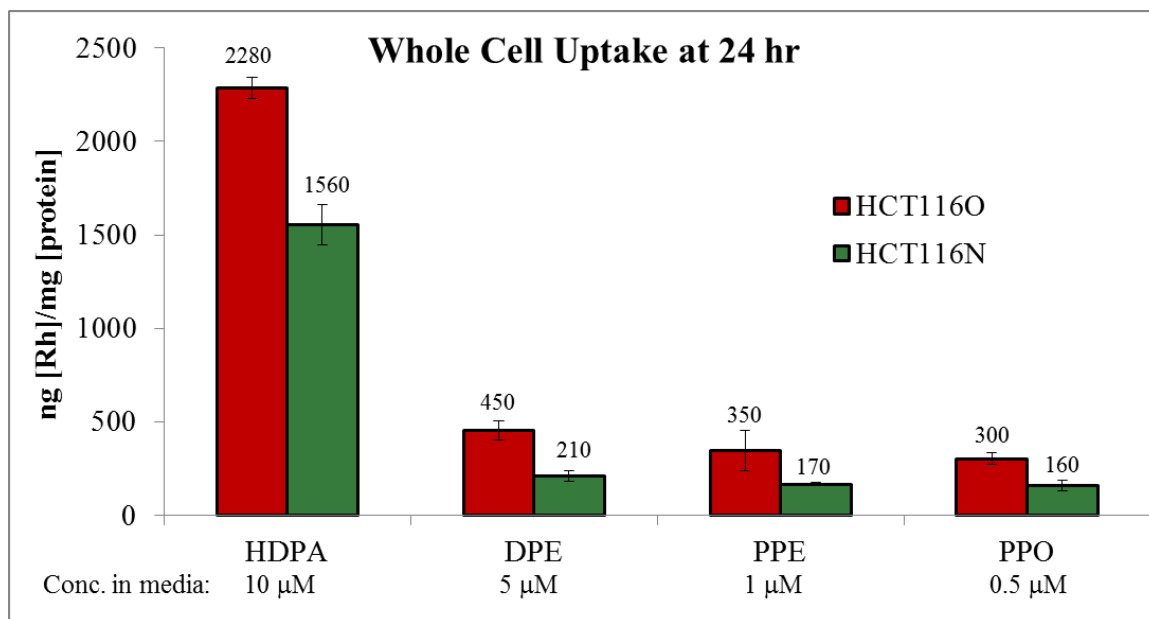


Figure 5.17 ICP-MS assay for whole-cell rhodium accumulation. HCT116O and HCT116N cells were treated with $[\text{Rh}(\text{HDPA})_2(\text{chrysi})]^{3+}$, $[\text{Rh}(\text{chrysi})(\text{phen})(\text{DPE})]^{2+}$, $[\text{Rh}(\text{chrysi})(\text{phen})(\text{PPE})]^{2+}$, or $[\text{Rh}(\text{chrysi})(\text{phen})(\text{PPO})]^{2+}$ at the concentrations shown for 24 h. The cells were analyzed for rhodium content by ICP-MS. The rhodium counts were normalized to protein content, which was determined by a BCA assay. See **Section 5.2.10**. It should be noted that because the rhodium concentrations are normalized to protein content, rather than number of cells, the concentrations from the two cell lines cannot be directly compared to one another.

5.3.7 Mode of cell death

To characterize the cell death occurring in response to rhodium treatment, a dye-exclusion flow cytometry assay was employed.¹¹ The assay differentiates between live cells, dead cells, and cells undergoing apoptosis or necrosis through concurrent staining with propidium iodide (a dead-cell-permeable dye) and YO-PRO-1 (an apoptotic-cell-permeable dye). By plotting the fluorescence of the YO-PRO-1 channel against the PI channel, a pattern emerges. Healthy cells are seen in the lower lefthand corner of the plot. Apoptotic cells exhibit higher YO-PRO-1 fluorescence, but still exclude propidium iodide, placing them in the upper lefthand quadrant of the pattern. Dead cells admit both dyes and are therefore seen in the upper righthand quadrant of the image. Upon flow cytometry analysis, cells can be classified as live, apoptotic, necrotic, or dead by defining regions in the fluorescence plane corresponding to each category.

The HCT116N and HCT116O cell lines were incubated with 0 – 0.5 μM of $[\text{Rh}(\text{chrysi})(\text{phen})(\text{PPO})]^{2+}$ for 72 h. After harvesting the cells and staining with both PI and YO-PRO-1, the cells were analyzed by flow cytometry to obtain raw fluorescence data. Representative data for 20 μM rhodium treatment for 72 h are shown in **Figure 5.18**. YO-PRO-1 fluorescence is shown on the y-axis, and PI fluorescence is shown on the x-axis. The color scale represents the number of cells, with blue indicating fewer cells at a given pair of fluorescence levels, and orange representing a greater number of cells at a given pair of fluorescence levels.

The raw data were analyzed by gating the fluorescence events into one of four categories, depending on the fluorescence levels of the two dyes. **Figure 5.18** also shows histograms of live, apoptotic, necrotic, and dead cells for the HCT116N and HCT116O

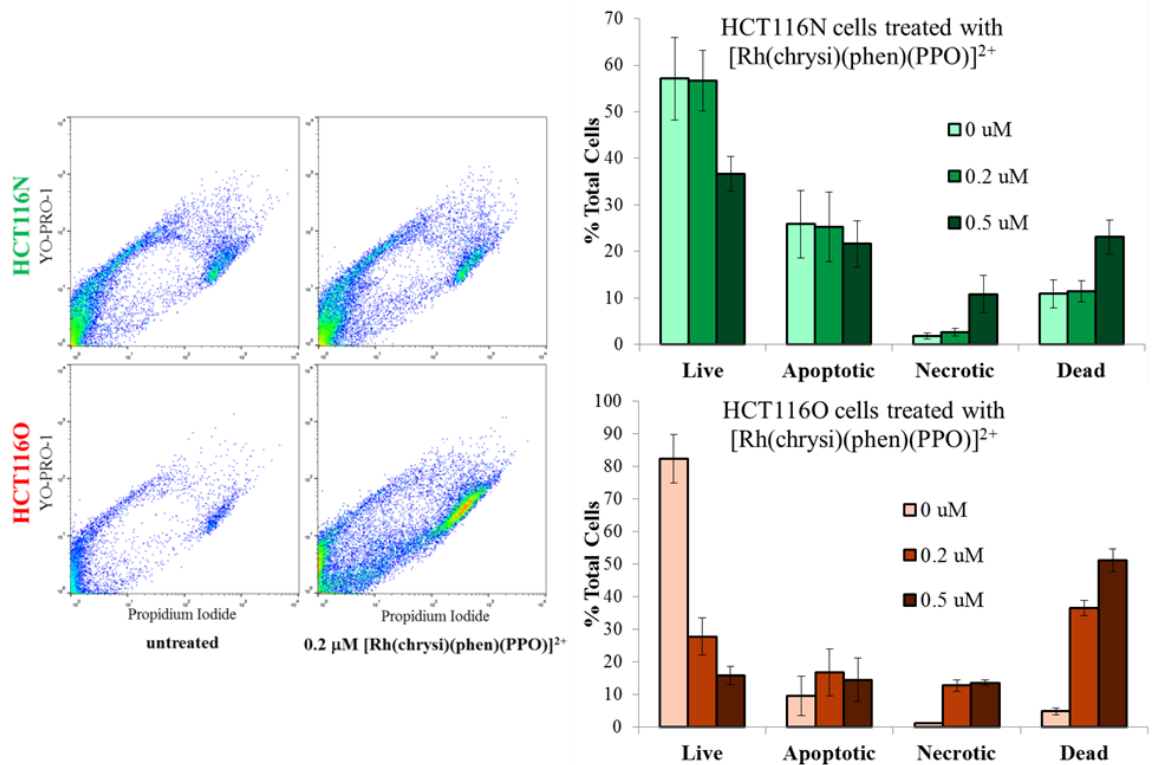


Figure 5. 18 Flow cytometry assay of cell death. (Right) HCT116N and HCT116O cells were treated with 0.2 μM $[\text{Rh}(\text{chrysi})(\text{phen})(\text{PPO})]^{2+}$ for 72 hours. Rhodium treatment causes cells to move away from the origin, along the necrotic pathway (lower branch of pattern). The effect is more pronounced in the HCT116O cell line. (Right) HCT116N and HCT116O cells were treated with 0.2 μM or 0.5 μM $[\text{Rh}(\text{chrysi})(\text{phen})(\text{PPO})]^{2+}$ for 72 hours. Rhodium treatment causes a sharp decrease in the live population of the HCT116O cell line with a corresponding increase in the necrotic and dead cell populations. Less of an effect is seen in the HCT116N cell line. Thus, $[\text{Rh}(\text{chrysi})(\text{phen})(\text{PPO})]^{2+}$ preferentially induces necrosis in the MMR-deficient HCT116O cell line.

cell lines based on the flow cytometry. Rhodium treatment was either 0.2, 0.5, or 1 μM $[\text{Rh}(\text{chrysi})(\text{phen})(\text{PPO})]^{2+}$ for 72 h. As with $[\text{Rh}(\text{HDPA})_2\text{chrysi}]^{3+}$,²⁰ $[\text{Rh}(\text{chrysi})(\text{phen})(\text{PPO})]^{2+}$ treatment induces necrosis preferentially in the MMR-deficient HCT116O cell line; the number of necrotic cells increases from 1.2 ± 0.1 % to 13 ± 2 % after treatment with 0.2 μM $[\text{Rh}(\text{chrysi})(\text{phen})(\text{PPO})]^{2+}$. There is no significant change in the percentage of cells in the apoptotic region in either cell line following metalloinsertor treatment (26 ± 7 % vs. 25 ± 7 % for the HCT116N cell line, and 10 ± 6 % vs. 17 ± 7 % for the HCT116O cell line). The effect of rhodium treatment is significantly more pronounced in the MMR-deficient HCT116O cell line, in which live cells drop from 82 ± 7 % to 28 ± 6 % after treatment with 0.2 μM $[\text{Rh}(\text{chrysi})(\text{phen})(\text{PPO})]^{2+}$, versus the MMR-proficient HCT116N cell line, which shows no decrease in live cells (57 ± 9 % versus 57 ± 7 %) after treatment with 0.2 μM $[\text{Rh}(\text{chrysi})(\text{phen})(\text{PPO})]^{2+}$.

5.4 Discussion

5.4.1 *In Vitro* Characterization

The DPE ligand was originally designed to coordinate to the Rh center *via* the two pyridine rings, resulting in a tertiary alcohol as a site of conjugation. The solid state structure of $[\text{Rh}(\text{chrysi})(\text{phen})(\text{DPE})]^{2+}$ was both a surprise and a revelation to us when it revealed the true coordination to include an axial Rh-O bond. The driving force of this unexpected ligand coordination is believed to be the formation of a 5-membered ring, as opposed to the 6-membered ring that would form if the second pyridine ring coordinated.²¹ As this compound exhibited enhanced potency and maximal cell-selectivity,¹ we sought to investigate this new ligand coordination and determine its role

in the biological activity of $[\text{Rh}(\text{chrysi})(\text{phen})(\text{DPE})]^{2+}$. In order to assess the generality of this ligand coordination, we synthesized the analogous $[\text{Rh}(\text{chrysi})(\text{phen})(\text{PPE})]^{2+}$ compound, which lacks the second pyridine and thus has no possible coordination site beyond the oxygen. The resulting compound with a phenyl group dangling off the back of the compound was thus made and exhibited a comparable DNA mismatch binding affinity. An additional compound with a dangling methyl group was then synthesized in order to determine if the steric bulk of the dangling group was responsible for its biological activity ($[\text{Rh}(\text{chrysi})(\text{phen})(\text{PPO})]^{2+}$), and, finally, we appended a hexyl group off the back of the ligand ($[\text{Rh}(\text{chrysi})(\text{phen})(\text{PyOctanol})]^{2+}$) to assess the effects of lipophilicity on this new family of compounds. All compounds exhibit binding affinities within a factor of 2 of each other, indicating that the size of the steric bulk of the dangling group has no effect on DNA mismatch binding.

We hypothesized that perhaps the Rh-O bond is labile, resulting in covalent DNA binding following Rh-O cleavage of the inserted complex. The ensuing covalent lesion could be more efficiently recognized by the machinery of the cell.²² However, even under an extremely reducing environment (5 mM glutathione), there is no evidence of covalent DNA binding.

Spectrophotometric titrations reveal that the acidity of the chrysi imine proton of $[\text{Rh}(\text{chrysi})(\text{phen})(\text{DPE})]^{2+}$ (pK_a of 8.7) varies significantly from that of $[\text{Rh}(\text{bpy})_2(\text{chrysi})]^{3+}$ (pK_a of 5.2¹³) and $[\text{Rh}(\text{HDPA})_2(\text{chrysi})]^{3+}$ (pK_a of 7.0). This can most likely be explained by the negative charge on the DPE ligand; a more basic environment is required to deprotonate the 2+ $[\text{Rh}(\text{chrysi})(\text{phen})(\text{DPE})]^{2+}$ species than the 3+ $[\text{Rh}(\text{HDPA})_2(\text{chrysi})]^{3+}$ species. Furthermore, in the case of $[\text{Rh}(\text{bpy})_2(\text{chrysi})]^{3+}$, the

chrysi imine proton must be deprotonated in order for the molecule to bind to mismatched DNA.²⁴ As can be seen in **Figure 5.2**, when both imine nitrogens are protonated, the chrysi ligand is not planar, which, in effect, prevents proper pi-stacking with the base pairs adjacent to the mismatched site. Despite this fact, $[\text{Rh}(\text{chrysi})(\text{phen})(\text{DPE})]^{2+}$ still binds to mismatched DNA with a fully protonated chrysi ligand, as can be seen in **Figure 5.10**. The significant amount of hypochromicity seen upon DNA binding confirms that not only does this compound bind to the DNA, but there is significant pi-stacking between the DNA and the chrysi ligand. These observations suggest a different mechanism of mismatch binding for this new family of compounds as compared to $[\text{Rh}(\text{bpy})_2(\text{chrysi})]^{3+}$.

In order to further characterize the compounds, the enantiomers of $[\text{Rh}(\text{chrysi})(\text{phen})(\text{DPE})]^{2+}$ were separated by HPLC. In the case of a labile Rh-O bond, racemization of the enantiomers could occur over time.²³ However, samples of both enantiomers in aqueous solution in light exhibited no racemization over a month, as confirmed by chiral HPLC and CD. Furthermore, the two enantiomers do not racemize upon DNA binding (**Figure 5.12**), and, in fact, exhibit distinct CD spectra when bound to DNA, providing direct evidence that both enantiomers do indeed bind to mismatches. Even more interestingly, both the Δ and Λ isomers of $[\text{Rh}(\text{chrysi})(\text{phen})(\text{DPE})]^{2+}$ bind to mismatched DNA with equal affinity. In fact, **Figure 5.19** compares models of Δ - $[\text{Rh}(\text{chrysi})(\text{phen})(\text{DPE})]^{2+}$, Λ - $[\text{Rh}(\text{chrysi})(\text{phen})(\text{DPE})]^{2+}$, Δ - $[\text{Rh}(\text{chrysi})(\text{phen})(\text{PPE})]^{2+}$, and Δ - $[\text{Rh}(\text{chrysi})(\text{phen})(\text{PPO})]^{2+}$ bound to a mismatched site in DNA. Preserving the DNA conformation from the crystal structure of $[\text{Rh}(\text{bpy})_2(\text{chrysi})]^{3+}$ bound to an AC mismatch,²⁴ we simply overlaid the chrysi ligands of the crystal structures of the various

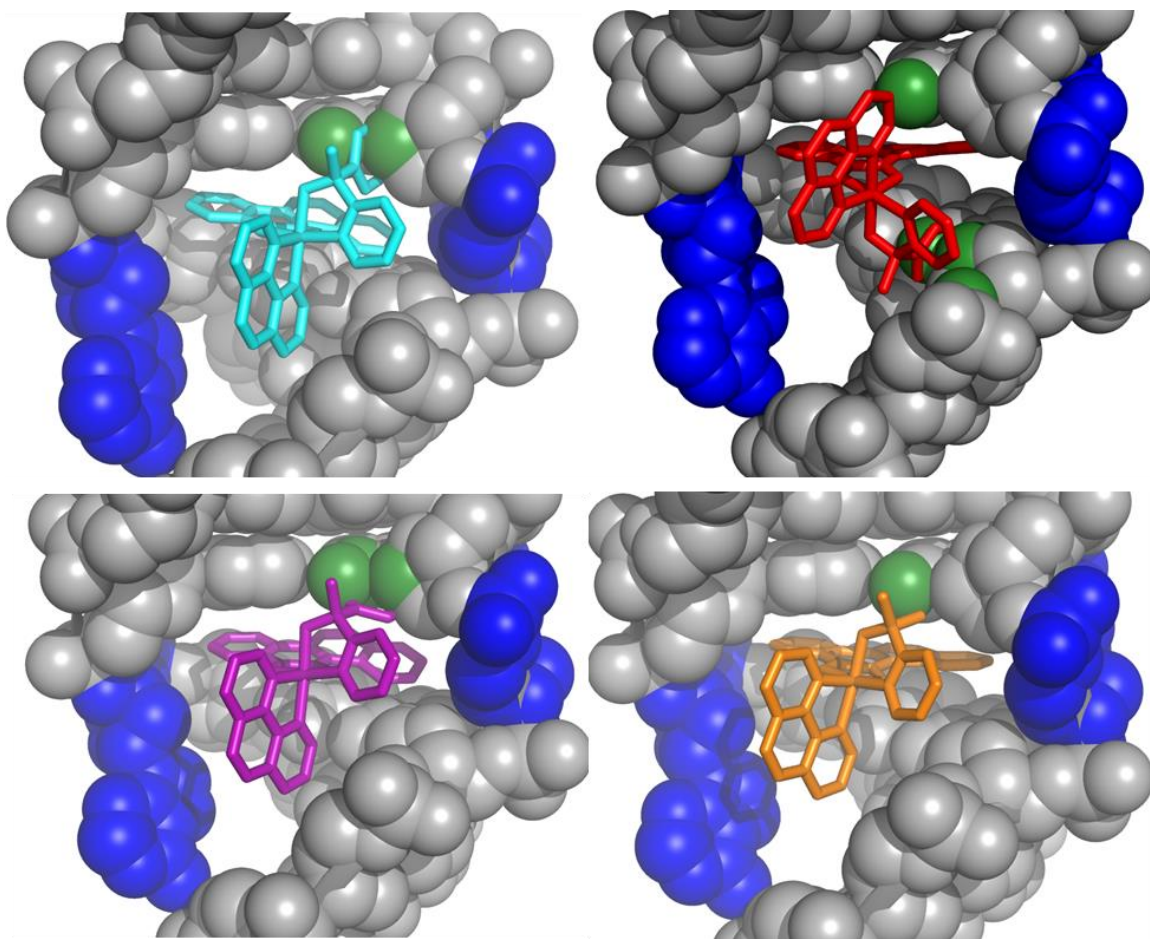


Figure 5.19 Modeling of new family of compounds bound to mismatched DNA. Crystal structures of Δ -[Rh(chrysi)(phen)(DPE)]²⁺ (top left, cyan), Λ -[Rh(chrysi)(phen)(DPE)]²⁺ (top right, red), Δ -[Rh(chrysi)(phen)(PPE)]²⁺ (bottom left, purple), and Δ -[Rh(chrysi)(phen)(PPO)]²⁺ (bottom right, orange) modeled into the crystal structure of [Rh(bpy)₂(chrysi)]³⁺ bound to an AC mismatch. The metalloinsertors are shown bound to the DNA (gray) from the minor groove at the mismatch site with the bases (blue) ejected and their chrysi ligands stacked fully with the adjacent base pairs. In all cases, steric clashing (shown in green) occurs between the ancillary ligand(s) and the DNA.

new compounds with that of Δ -[Rh(bpy)₂(chrysi)]³⁺. **Figure 5.19** shows that there is the potential for significant steric clashing between the dangling group and the DNA backbone for the Δ enantiomers of the DPE and PPE compounds, which is partially alleviated for the PPO complex. Even considering free rotation of the aromatic group around the quaternary C-aromatic C bond of both ligands, this steric clash cannot be diminished. Given the similarity in binding affinities of the various compounds, it is clear that this cannot be the same binding conformation for this new family of compounds. In addition, there is even more steric clashing between the ancillary ligands of the Λ -[Rh(chrysi)(phen)(DPE)]²⁺ complex and the DNA backbone, as would be expected given the complete lack of DNA binding of Λ -[Rh(bpy)₂(chrysi)]³⁺. These models clearly imply that the binding mode of this new family of complexes must be structurally distinct from that of [Rh(bpy)₂(chrysi)]³⁺.

5.4.2 *In Cellulo* Characterization

We sought to explore the biological effects of the different dangling groups of the ancillary ligand. As can be seen from **Figure 5.15**, all four complexes exhibit the MMR-deficient cell-selective activity that is unique to rhodium metalloinsertors. Thus, appending additional steric bulk off the back of the complexes does not inhibit cellular processing of the rhodium-DNA lesion that results from mismatch binding. In addition, the fact that [Rh(chrysi)(phen)(PyOctanol)]²⁺ retains its cell-selectivity is very surprising given our recent results that the more lipophilic metalloinsertors localize to the mitochondria, which in effect abolishes their cell-selectivity.¹ One explanation is that the ancillary PyOctanol ligand falls off either prior to uptake or following cellular uptake. The variance in potencies of the four different compounds negates the former, and our

result showing the lack of racemization of the $[\text{Rh}(\text{chrysi})(\text{phen})(\text{DPE})]^{2+}$ compound over a month in a reducing aqueous environment negates the latter. As expected, given its mismatch binding affinity, Λ - $[\text{Rh}(\text{chrysi})(\text{phen})(\text{DPE})]^{2+}$ also displayed cell-selective activity in the MTT assay.

Encouraged by the enhanced potencies of the new complexes as compared to our earlier generation compounds, we measured their antiproliferative activity alongside two FDA-approved chemotherapeutics that display decreased effectiveness against MMR-deficient cancers in the clinic.¹⁷ As can clearly be seen in **Figure 5.14**, the new compounds are both more selective and more potent than both classic chemotherapeutics. This is very exciting, given that for many years, the focus of numerous laboratories has been on the preparation of more potent analogues of cisplatin.^{25,26} However, a new strategy based upon selectivity has recently emerged, and focus has shifted towards the preparation of chemotherapeutics that are more selective than cisplatin owing to a design strategy where the complex interacts with a specific biological target found prominently in cancer cells.²⁷ This new family of compounds has fulfilled both of these criteria, and efforts are currently in motion to test these compounds *in vivo*.

In order to further characterize the biological activity of the compounds, we assessed cellular uptake of the various compounds and compared them to that of $[\text{Rh}(\text{HDPA})_2\text{chrysi}]^{3+}$. **Figure 5.17** displays the intracellular rhodium concentrations of the various complexes required to produce the same biological effect. It is important to note that the new family of compounds require from 7.5- to 5- fold less intracellular rhodium as compared to $[\text{Rh}(\text{HDPA})_2\text{chrysi}]^{3+}$ to evoke the same cellular response. This may be an indication that the Rh-DNA lesion being formed by the new family of

compounds is more readily recognized by the cell's machinery, and thus fewer lesions are required for cytotoxicity. Furthermore, the three complexes with Rh-O bonds exhibit similar intracellular rhodium concentrations; they vary less than 1.5-fold from each other. This is despite a 10-fold difference in the rhodium concentration of the media between $[\text{Rh}(\text{chrysi})(\text{phen})(\text{DPE})]^{2+}$ and $[\text{Rh}(\text{chrysi})(\text{phen})(\text{PPO})]^{2+}$. This clearly demonstrates that the latter compound has more efficient uptake than the DPE parental compound. This property is especially valuable in considering these compounds for *in vivo* work; many antitumor agents are limited in their applications due to chronic side effects. In particular, doxorubicin is one of the most effective chemotherapies against leukemia and lymphomas,²⁸ yet causes congestive heart failure at a rate that is directly correlated with the total amount of drug administered.^{29,30}

Finally, we evaluated the mode of cell death caused by treatment of HCT116 cells with the new compound $[\text{Rh}(\text{chrysi})(\text{phen})(\text{PPO})]^{2+}$ as a representative member of the new family. The admission of the dead-cell stain propidium iodide by the HCT116 cell lines upon rhodium treatment reveals that cell death proceeds through a necrotic, rather than apoptotic pathway, similar to $[\text{Rh}(\text{HDPa})_2\text{chrysi}]^{3+}$ treatment.²⁰ If there is a different Rh-DNA lesion being formed by the new family of compounds, then it is not different enough to evoke a significantly altered cellular response. The observations that significantly less intracellular rhodium is required to elicit the same biological response as our previous generation compounds, and the appendage of a greasy hexyl group off the ancillary ligand ($[\text{Rh}(\text{chrysi})(\text{phen})(\text{PyOctanol})]^{2+}$) does not abolish cell-selectivity¹ lend credence to the theory that this new family of compounds is distinct from our earlier generation metalloinsertors. Further evidence to support this hypothesis is the observation

that *both* the Δ and Λ enantiomers bind to mismatches in DNA with equal affinity, yet do not interconvert with each other. Whatever the reason, the enhanced potency and selectivity of these new compounds make them suitable candidates for the next step in chemotherapeutic development.

5.5 Conclusion

Here we have described a family of rhodium metalloinsertors with a new ancillary ligand coordination. These compounds all contain a Rh-O bond axial to their inserting chrysi ligand. This new ligand coordination has been found to be responsible for the enhanced potency and selectivity towards MMR-deficient cancer cells that we observe with these compounds. Models of the compounds bound to mismatched DNA imply a different binding mode than our earlier generation compounds, which may account for their biological activity. We are now focusing our studies on structurally characterizing their DNA-bound conformation. Furthermore, this new ligand scaffold is very amenable to conjugation, and thus effort will be made to further enhance their potency and selectivity by conjugating these new types of compounds to cell-penetrating peptides and antibodies.

5.6 References

- 1 Komor, A. C., Schneider, C. J., Weidmann, A. G., Barton, J. K. *J. Am. Chem. Soc.* **2012**, *134*, 19223-19233.
- 2 Ernst, R. J.; Song, H.; Barton, J. K. *J. Am. Chem. Soc.* **2009**, *131*, 2359-2366.
- 3 Zeglis, B. M.; Barton, J. K. *Nat. Protocols* **2007**, *2*, 357-371.
- 4 Muerner, H.; Jackson, B. A.; Barton, J. K. *Inorg. Chem.* **1998**, *37*, 3007-3012.
- 5 Basu, A.; Bhaduri, S.; Sapre, N. Y.; Jones, P. G. *J. Chem. Soc., Chem. Commun.* **1987**, *22*, 1724-1725.
- 6 Sheldrick, G. M. *Acta Cryst.* **1990**, *A46*, 467-473.
- 7 Sheldrick, G. M. *Acta Cryst.* **2008**, *A64*, 112-122.
- 8 Müller, P. *Crystallography Reviews* **2009**, *15*, 57-83.
- 9 Reitmar, A. H.; Risley, R.; Bristow, R. G.; Wilson, T.; Ganesh, A.; Jang, A.; Peacock, J.; Benchimol, S.; Hill, R. P. *Cancer Res.* **1997**, *57*, 3765-3771.
- 10 Mosmann, T. *J. Immunol. Methods* **1983**, *65*, 55-63.
- 11 Idziorek, T.; Estaquier, J.; DeBels, F.; Ameisen, J.-C. *J. Immunol. Methods* **1995**, *185*, 249-258.
- 12 Smith, P. K.; Krohn, R. I.; Hermanson, G. T.; Mallia, A. K.; Gartner, F. H.; Provenzano, M. D.; Fujimoto, E. K.; Goetze, N. M.; Olson, B. J.; Klenk, D. C. *Anal. Biochem.* **1985**, *150*, 76-85.
- 13 Jackson, B. A.; Henling, L. M.; Barton, J. K. *Inorg. Chem.* **1999**, *38*, 6218-6224.
- 14 Jackson, B. A.; Barton, J. K. *J. Am. Chem. Soc.* **1997**, *119*, 12986-12987.
- 15 Jackson, B. A.; Barton, J. K. *Biochemistry* **2000**, *39*, 6176-6182.

- 16 Jackson, B. A.; Alekseyev, V. Y.; Barton, J. K. *Biochemistry* **1999**, *38*, 4655-4662.
- 17 Carethers, J. M.; Hawn, M. T.; Chauhan, D. P.; Luce, M. C.; Marra, G.; Koi, M.; Boland, C. R. *J. Clin. Invest.* **1996**, *98*, 199-206.
- 18 Fink, D.; Aebi, S.; Howell, S. B. *Clin. Cancer Res.* **1998**, *4*, 1-6.
- 19 Junicke, H.; Hart, J. R.; Kisko, J.; Glevob, O.; Kirsch, I. R.; Barton, J. K. *Proc. Natl. Acad. Sci. U.S.A.* **2003**, *100*, 3737-3741.
- 20 Ernst, R. J.; Komor, A. C.; Barton, J. K. *Biochemistry* **2011**, *50*, 10919-10928.
- 21 Hancock, R. D.; Wade, P. W.; Ngwenya, M. P.; deSousa, A. S.; Damu, K. V. *Inorg. Chem.* **1990**, *29*, 1968-1974.
- 22 Jamieson, E. R.; Lippard, S. J. *Chem. Rev.* **1999**, *99*, 2467-2498.
- 23 Cimolino, M. C.; Shipley, N. J.; Linck, R. G. *Inorg. Chem.* **1980**, *19*, 3291-3295.
- 24 Pierre, V. C.; Kaiser, J. T.; Barton, J. K. *Proc. Natl. Acad. Sci. U.S.A.* **2007**, *104*, 429-434.
- 25 Wheate, N. J.; Walker, S.; Craig, G. E.; Oun, R. *Dalton Trans.* **2010**, *39*, 8113-8127.
- 26 Kelland, L. R.; Sharp, S. Y.; O'Neill, C. F.; Raynaud, F. I.; Beale, P. J.; Judson, I. *R. J. Inorg. Biochem.* **1999**, *77*, 111-115.
- 27 Weidmann, A. G.; Komor, A. C.; Barton, J. K. *Comments in Inorg. Chem.* **2014**, DOI: 10.1080/02603594.2014.890099.
- 28 Young, R. C.; Ozols, R. F.; Myers, C. E. *New Engl. J. Med.* **1981**, *305*, 139-153.
- 29 Cortes, E. P.; Lutman, G.; Wanka, J.; Wang, J. J.; Pickren, J.; Wallace, J.; Holland, J. F. *Cancer Treat. Rep.* **1975**, *6*, 215-225.

- 30 Von Hoff, D. D.; Layard, M. W.; Basa, P.; Davis, H. L.; Von Hoff, A. L.;
Rozencweig, M.; Muggia, F. M. *Ann. Intern. Med.* **1979**, *91*, 710-717.

Chapter 6: Conclusion

The motivation behind the work in this thesis is the biological consequences of lesions in DNA. If they are left uncorrected, they will ultimately lead to mutations in our DNA, which leads to mutations in the corresponding proteins. About 80-90% of protein mutations that are responsible for human disease are caused by the substitution, deletion, or insertion of only a single nucleotide. Clearly, the design and study of drugs that can recognize such lesions is incredibly important for the future development of cures and treatments for these diseases.

My work focused on DNA mismatches in particular, which are recognized and fixed *in vivo* by the mismatch repair (MMR) pathway. However, inactivation of this pathway leads to a large increase in the number of mismatches in a given cell, resulting in an increased rate of mutagenesis and predisposition to cancer. Cancers that display MMR deficiencies are notoriously difficult to treat; the current standard-of-care treatment is adjuvant chemotherapy with 5-fluorouracil (5-FU), despite multiple studies showing its ineffectiveness against these cancers.

The observation in 1999 that rhodium metalloinsertors can bind selectively and with high affinity to DNA mismatch opened up an entire new avenue of research in the Barton laboratory. Their mismatch binding characteristics were studied extensively in the test tube until 2006, when the first cell work on rhodium metalloinsertors showed that after treatment for 72 h with 0 - 25 μM , these compounds can selectively inhibit growth in MMR-deficient cells for isogenic MMR-proficient cells. My thesis has focused on enhancing the biological activity of these compounds, so that one day (hopefully soon), they can be tested in the clinic.

My work with Russell Ernst showing that later-generation compounds can actively kill cancer cells rather than just inhibit growth was the start of this journey. I have since shown that localization to the nucleus, the site of mismatches in genomic DNA, is required for their unique activity. Through our collaboration with Amgen I have also been able to further validate these compounds by showing that their unique cell-selective targeting is observed across multiple experiments and cell lines. Most recently, I have been able to increase their activity from inhibition of growth at 0 - 25 μM metalloinsertor to cytotoxicity at 0 - 500 nM metalloinsertor, potency that surpasses even FDA-approved chemotherapeutics.

It has been especially gratifying to witness the first *in vivo* work done with these compounds. Amgen has run some pharmacokinetic studies on both $[\text{Rh}(\text{chrysi})(\text{phen})(\text{PPO})]^{2+}$ and $[\text{Rh}(\text{HDPA})_2(\text{chrysi})]^{3+}$, both of which look very promising. It will be an incredibly rewarding experience if these compounds make it to clinical trials, and we are well on our way there.

Appendix: Crystallographic Data

A.1 [Rh(HDPA)₂(chrysi)]Cl₂

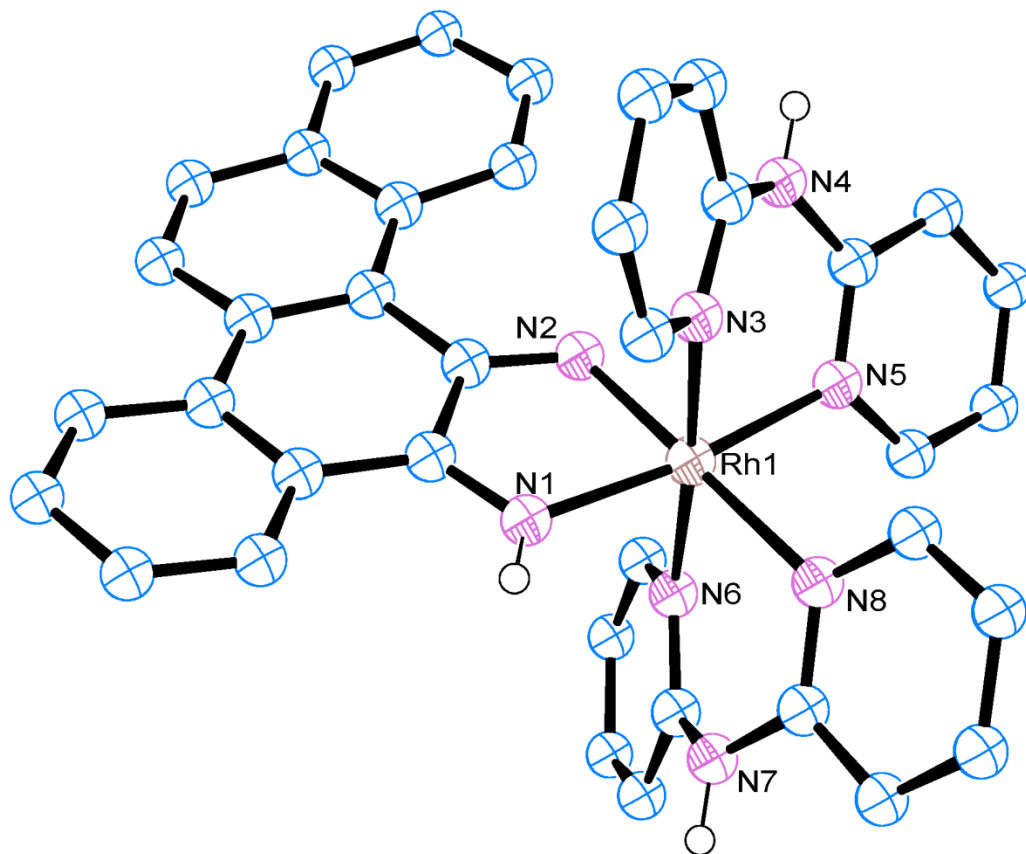


Table A.1 Crystal data and structure refinement for [Rh(HDPA)₂(chrysi)]Cl₂.

Identification code	ack002
Empirical formula	C ₄₂ H ₄₃ Cl ₂ N ₈ O ₃ Rh
Formula weight	881.65
Temperature	100(2) K
Wavelength	0.71073 Å
Crystal system	Monoclinic
Space group	P 21/n

Unit cell dimensions	a = 9.4383(4) Å	$\alpha = 90^\circ$.
	b = 25.4636(10) Å	$\beta = 96.746(2)^\circ$.
	c = 16.6094(6) Å	$\gamma = 90^\circ$.
Volume	3964.1(3) Å ³	
Z	4	
Density (calculated)	1.477 Mg/m ³	
Absorption coefficient	0.617 mm ⁻¹	
F(000)	1816	
Crystal size	0.500 x 0.400 x 0.150 mm ³	
Theta range for data collection	2.315 to 30.547°.	
Index ranges	-13 ≤ h ≤ 13, -35 ≤ k ≤ 36, -23 ≤ l ≤ 23	
Reflections collected	178000	
Independent reflections	12143 [R(int) = 0.0639]	
Completeness to theta = 25.242°	99.9 %	
Absorption correction	Semi-empirical from equivalents	
Max. and min. transmission	0.7461 and 0.6942	
Refinement method	Full-matrix least-squares on F ²	
Data / restraints / parameters	12143 / 13 / 538	
Goodness-of-fit on F ²	1.035	
Final R indices [I > 2σ(I)]	R1 = 0.0284, wR2 = 0.0641	
R indices (all data)	R1 = 0.0371, wR2 = 0.0677	
Largest diff. peak and hole	0.745 and -0.767 e.Å ⁻³	

Table A.2 Atomic coordinates ($\times 10^4$) and equivalent isotropic displacement parameters ($\text{\AA}^2 \times 10^3$) for $[\text{Rh}(\text{HDP A})_2(\text{chrysi})]\text{Cl}_2$. $U(\text{eq})$ is defined as one-third of the trace of the orthogonalized U^{ij} tensor.

	x	y	z	$U(\text{eq})$
Cl(1)	3083(1)	9952(1)	8823(1)	16(1)
Cl(2)	4096(1)	6979(1)	5314(1)	23(1)
Cl(2A)	4496(15)	7220(7)	5078(7)	48(5)
Rh(1)	5622(1)	8722(1)	7938(1)	9(1)
N(1)	5365(1)	9494(1)	7748(1)	11(1)
C(1)	5762(2)	9663(1)	7073(1)	11(1)
C(2)	5582(2)	10197(1)	6763(1)	13(1)
C(3)	4825(2)	10572(1)	7160(1)	16(1)
C(4)	4618(2)	11072(1)	6843(1)	18(1)
C(5)	5158(2)	11197(1)	6123(1)	18(1)
C(6)	5915(2)	10830(1)	5732(1)	17(1)
C(7)	6159(2)	10320(1)	6042(1)	13(1)
C(8)	6939(2)	9921(1)	5612(1)	15(1)
C(9)	7586(2)	10077(1)	4918(1)	22(1)
C(10)	8224(2)	9723(1)	4465(1)	23(1)
C(11)	8229(2)	9181(1)	4653(1)	16(1)
C(12)	8777(2)	8811(1)	4131(1)	20(1)
C(13)	8702(2)	8283(1)	4274(1)	20(1)

C(14)	8093(2)	8108(1)	4959(1)	21(1)
C(15)	7580(2)	8457(1)	5486(1)	18(1)
C(16)	7623(2)	9008(1)	5352(1)	14(1)
C(17)	7017(2)	9394(1)	5852(1)	12(1)
C(18)	6444(2)	9249(1)	6616(1)	11(1)
N(2)	6542(1)	8786(1)	6935(1)	12(1)
N(3)	3767(1)	8591(1)	7202(1)	11(1)
C(21)	2678(2)	8942(1)	7190(1)	13(1)
C(22)	1535(2)	8943(1)	6598(1)	17(1)
C(23)	1505(2)	8571(1)	5973(1)	17(1)
C(24)	2573(2)	8203(1)	5991(1)	15(1)
C(25)	3693(2)	8212(1)	6636(1)	12(1)
N(4)	4704(1)	7825(1)	6657(1)	13(1)
C(26)	5552(2)	7626(1)	7324(1)	12(1)
C(27)	5961(2)	7097(1)	7296(1)	17(1)
C(28)	6778(2)	6880(1)	7954(1)	19(1)
C(29)	7187(2)	7192(1)	8631(1)	17(1)
C(30)	6766(2)	7708(1)	8618(1)	14(1)
N(5)	5979(1)	7929(1)	7969(1)	11(1)
N(6)	7498(1)	8894(1)	8628(1)	11(1)
C(31)	8749(2)	8799(1)	8323(1)	14(1)
C(32)	10030(2)	8987(1)	8676(1)	16(1)
C(33)	10063(2)	9284(1)	9387(1)	16(1)

C(34)	8817(2)	9371(1)	9713(1)	14(1)
C(35)	7532(2)	9164(1)	9323(1)	11(1)
N(7)	6303(1)	9259(1)	9674(1)	15(1)
C(36)	5109(2)	8944(1)	9671(1)	13(1)
C(37)	4382(2)	8946(1)	10363(1)	20(1)
C(38)	3191(2)	8638(1)	10370(1)	21(1)
C(39)	2740(2)	8322(1)	9700(1)	17(1)
C(40)	3511(2)	8335(1)	9049(1)	14(1)
N(8)	4666(1)	8650(1)	9022(1)	11(1)
O(1S)	948(2)	10540(1)	7590(1)	38(1)
C(1S)	-486(2)	10348(1)	7535(1)	32(1)
C(2S)	-1230(2)	10528(1)	8232(1)	28(1)
O(1T)	2272(2)	7456(1)	7645(1)	29(1)
C(1T)	820(2)	7533(1)	7760(2)	36(1)
C(2T)	-190(3)	7445(1)	7002(2)	56(1)
O(1W)	2631(2)	6513(1)	6806(1)	40(1)

Table A.3 Selected bond lengths [\AA] and angles [$^\circ$] for $[\text{Rh}(\text{HDPa})_2(\text{chrysi})]\text{Cl}_2$.

Rh(1)-N(2)	1.9738(12)
Rh(1)-N(1)	2.0019(13)
Rh(1)-N(6)	2.0408(12)
Rh(1)-N(3)	2.0417(12)
Rh(1)-N(5)	2.0450(13)

Rh(1)-N(8)	2.1135(12)
N(2)-Rh(1)-N(1)	80.93(5)
N(2)-Rh(1)-N(6)	90.99(5)
N(1)-Rh(1)-N(6)	87.59(5)
N(2)-Rh(1)-N(3)	86.52(5)
N(1)-Rh(1)-N(3)	89.19(5)
N(6)-Rh(1)-N(3)	176.21(5)
N(2)-Rh(1)-N(5)	90.91(5)
N(1)-Rh(1)-N(5)	171.73(5)
N(6)-Rh(1)-N(5)	93.90(5)
N(3)-Rh(1)-N(5)	89.00(5)
N(2)-Rh(1)-N(8)	179.15(5)
N(1)-Rh(1)-N(8)	99.35(5)
N(6)-Rh(1)-N(8)	88.22(5)
N(3)-Rh(1)-N(8)	94.28(5)
N(5)-Rh(1)-N(8)	88.83(5)

Table A.4 Anisotropic displacement parameters ($\text{\AA}^2 \times 10^3$) for $[\text{Rh}(\text{HDPA})_2(\text{chrysi})]\text{Cl}_2$.

The anisotropic displacement factor exponent takes the form: $-2\pi^2 [h^2 a^{*2} U^{11} + \dots + 2 h k a^* b^* U^{12}]$.

	U11	U22	U33	U23	U13	U12
Cl(1)	15(1)	18(1)	15(1)	-5(1)	4(1)	0(1)

Cl(2)	28(1)	22(1)	15(1)	-8(1)	-5(1)	6(1)
Cl(2A)	44(6)	64(9)	31(5)	-22(6)	-17(4)	37(6)
Rh(1)	9(1)	10(1)	8(1)	-1(1)	2(1)	-1(1)
N(1)	11(1)	12(1)	11(1)	-3(1)	3(1)	0(1)
C(1)	9(1)	12(1)	12(1)	-1(1)	1(1)	-1(1)
C(2)	13(1)	12(1)	14(1)	-1(1)	1(1)	-1(1)
C(3)	16(1)	15(1)	18(1)	-2(1)	4(1)	0(1)
C(4)	17(1)	14(1)	24(1)	-3(1)	2(1)	2(1)
C(5)	18(1)	13(1)	24(1)	2(1)	-1(1)	0(1)
C(6)	18(1)	16(1)	18(1)	3(1)	2(1)	-2(1)
C(7)	12(1)	15(1)	14(1)	0(1)	1(1)	-1(1)
C(8)	15(1)	16(1)	13(1)	1(1)	3(1)	0(1)
C(9)	29(1)	19(1)	19(1)	6(1)	10(1)	1(1)
C(10)	29(1)	26(1)	17(1)	4(1)	12(1)	2(1)
C(11)	16(1)	22(1)	12(1)	0(1)	4(1)	1(1)
C(12)	19(1)	30(1)	12(1)	-2(1)	5(1)	3(1)
C(13)	19(1)	28(1)	14(1)	-8(1)	3(1)	3(1)
C(14)	25(1)	19(1)	19(1)	-6(1)	6(1)	0(1)
C(15)	22(1)	17(1)	15(1)	-3(1)	6(1)	-1(1)
C(16)	13(1)	18(1)	10(1)	-2(1)	2(1)	0(1)
C(17)	12(1)	15(1)	10(1)	0(1)	2(1)	-1(1)
C(18)	11(1)	14(1)	10(1)	-2(1)	2(1)	-2(1)
N(2)	12(1)	14(1)	10(1)	-2(1)	2(1)	-1(1)

N(3)	10(1)	12(1)	10(1)	0(1)	2(1)	-1(1)
C(21)	13(1)	13(1)	15(1)	-1(1)	3(1)	-1(1)
C(22)	14(1)	16(1)	19(1)	1(1)	1(1)	2(1)
C(23)	16(1)	20(1)	15(1)	1(1)	-3(1)	-1(1)
C(24)	18(1)	17(1)	11(1)	-1(1)	-2(1)	-1(1)
C(25)	12(1)	14(1)	10(1)	1(1)	1(1)	-1(1)
N(4)	15(1)	14(1)	10(1)	-4(1)	-1(1)	1(1)
C(26)	11(1)	14(1)	12(1)	-1(1)	2(1)	-1(1)
C(27)	18(1)	15(1)	17(1)	-5(1)	-1(1)	1(1)
C(28)	21(1)	14(1)	22(1)	-1(1)	0(1)	4(1)
C(29)	19(1)	16(1)	15(1)	2(1)	-1(1)	2(1)
C(30)	14(1)	16(1)	11(1)	0(1)	2(1)	-1(1)
N(5)	11(1)	11(1)	10(1)	-1(1)	2(1)	-1(1)
N(6)	10(1)	13(1)	11(1)	-1(1)	2(1)	-1(1)
C(31)	13(1)	16(1)	12(1)	0(1)	3(1)	2(1)
C(32)	12(1)	20(1)	16(1)	1(1)	3(1)	1(1)
C(33)	12(1)	16(1)	19(1)	0(1)	-1(1)	-2(1)
C(34)	14(1)	14(1)	15(1)	-2(1)	0(1)	-2(1)
C(35)	12(1)	11(1)	11(1)	0(1)	2(1)	0(1)
N(7)	12(1)	20(1)	14(1)	-8(1)	4(1)	-3(1)
C(36)	12(1)	15(1)	13(1)	-1(1)	3(1)	1(1)
C(37)	19(1)	26(1)	15(1)	-4(1)	6(1)	-2(1)
C(38)	20(1)	26(1)	19(1)	1(1)	11(1)	1(1)

C(39)	16(1)	17(1)	21(1)	5(1)	6(1)	-1(1)
C(40)	12(1)	13(1)	17(1)	1(1)	2(1)	-1(1)
N(8)	11(1)	13(1)	11(1)	0(1)	3(1)	0(1)
O(1S)	27(1)	55(1)	33(1)	20(1)	3(1)	4(1)
C(1S)	31(1)	41(1)	25(1)	-2(1)	1(1)	3(1)
C(2S)	26(1)	33(1)	24(1)	1(1)	2(1)	0(1)
O(1T)	25(1)	29(1)	31(1)	1(1)	2(1)	-3(1)
C(1T)	30(1)	23(1)	56(1)	-4(1)	10(1)	-3(1)
C(2T)	27(1)	74(2)	66(2)	39(2)	-6(1)	-18(1)
O(1W)	37(1)	39(1)	46(1)	-3(1)	14(1)	-1(1)

Table A.5 Hydrogen coordinates ($\times 10^4$) and isotropic displacement parameters ($\text{\AA}^2 \times 10^3$) for $[\text{Rh}(\text{HDPA})_2(\text{chrysi})]\text{Cl}_2$.

	x	y	z	U(eq)
H(1N)	4920(20)	9708(7)	8041(11)	13
H(3)	4453	10482	7649	19
H(4)	4112	11327	7114	22
H(5)	5005	11538	5897	22
H(6)	6279	10925	5243	21
H(9)	7573	10437	4768	26
H(10)	8673	9841	4015	28
H(12)	9204	8932	3675	24

H(13)	9057	8038	3915	24
H(14)	8036	7742	5059	25
H(15)	7188	8328	5949	21
H(21)	2711	9197	7610	16
H(22)	782	9189	6611	20
H(23)	751	8574	5540	21
H(24)	2559	7946	5576	18
H(4N)	4550(20)	7606(7)	6262(10)	16
H(27)	5676	6890	6828	20
H(28)	7060	6522	7946	23
H(29)	7746	7049	9093	20
H(30)	7036	7919	9083	17
H(31)	8731	8594	7844	16
H(32)	10883	8916	8444	19
H(33)	10937	9424	9639	19
H(34)	8820	9568	10199	17
H(7N)	6440(20)	9477(7)	10082(10)	18
H(37)	4711	9157	10818	23
H(38)	2674	8640	10827	25
H(39)	1923	8104	9696	21
H(40)	3224	8115	8598	17
H(1S)	1470(30)	10344(11)	7944(15)	58
H(1S1)	-474	9959	7522	39

H(1S2)	-1021	10472	7022	39
H(2S1)	-781	10366	8733	42
H(2S2)	-2236	10425	8141	42
H(2S3)	-1162	10911	8278	42
H(1T)	2210(30)	7153(8)	7361(15)	43
H(1T1)	696	7895	7955	43
H(1T2)	570	7288	8185	43
H(2T1)	53	7684	6576	85
H(2T2)	-1169	7514	7114	85
H(2T3)	-112	7081	6821	85
H(1W)	3140(30)	6221(9)	6876(19)	60
H(2W)	2920(30)	6588(12)	6350(13)	60

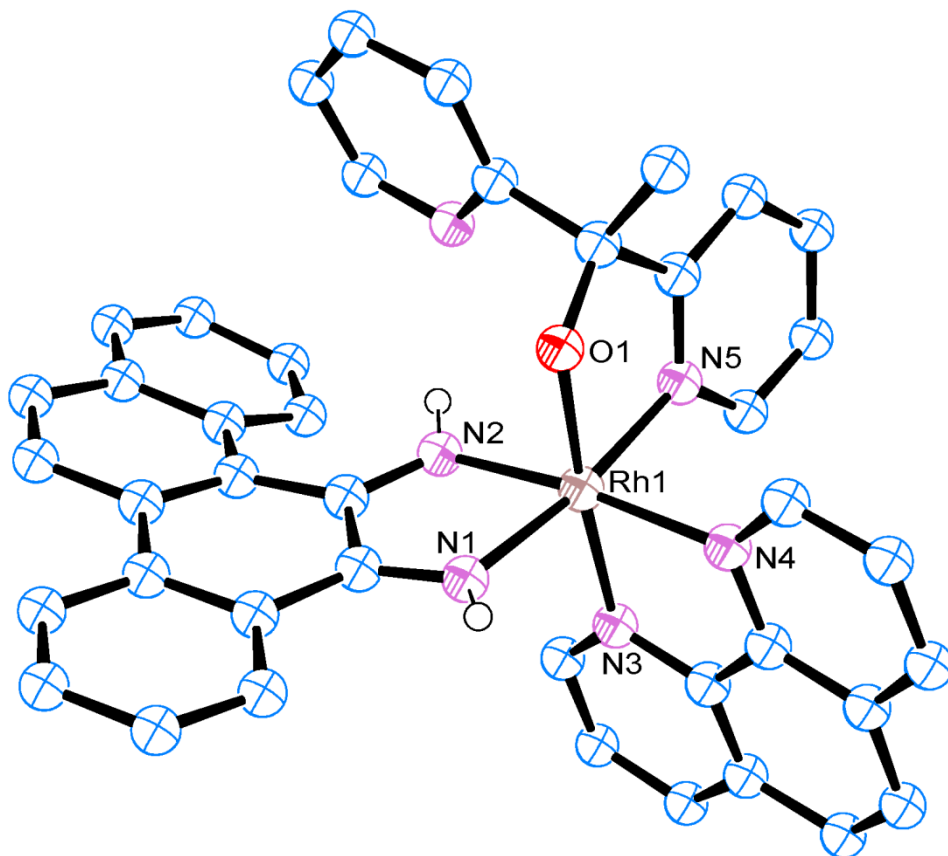
Table A.6 Hydrogen bonds for [Rh(HDPA)₂(chrysi)]Cl₂ [Å and °].

D-H...A	d(D-H)	d(H...A)	d(D...A)	<(DHA)
N(1)-H(1N)...Cl(1)	0.869(14)	2.371(16)	3.1773(13)	154.4(17)
C(21)-H(21)...Cl(1)	0.95	2.78	3.7250(15)	174.5
C(24)-H(24)...Cl(2)	0.95	2.92	3.6648(17)	136.5
C(24)-H(24)...Cl(2A)	0.95	2.79	3.537(8)	135.8
N(4)-H(4N)...Cl(2)	0.861(15)	2.248(15)	3.1068(13)	174.9(19)
N(4)-H(4N)...Cl(2A)	0.861(15)	2.194(17)	3.029(8)	163(2)
C(27)-H(27)...Cl(2)	0.95	2.78	3.5588(16)	139.9

C(29)-H(29)...Cl(2A)#1	0.95	2.87	3.397(11)	116.2
C(30)-H(30)...Cl(2)#1	0.95	2.66	3.4562(16)	141.3
C(30)-H(30)...Cl(2A)#1	0.95	2.71	3.329(8)	123.4
C(34)-H(34)...Cl(1)#2	0.95	2.84	3.6221(16)	140.8
N(7)-H(7N)...Cl(1)#2	0.874(15)	2.329(15)	3.2023(13)	177.3(19)
C(39)-H(39)...Cl(2)#3	0.95	2.98	3.7786(17)	143.0
C(39)-H(39)...Cl(2A)#3	0.95	2.58	3.482(10)	158.0
C(40)-H(40)...O(1T)	0.95	2.41	3.343(2)	168.7
O(1S)-H(1S)...Cl(1)	0.879(17)	2.216(18)	3.0853(15)	170(3)
O(1T)-H(1T)...O(1W)	0.904(16)	1.936(18)	2.816(2)	164(3)
O(1W)-H(1W)...O(1S)#40.884(17)		2.09(2)	2.938(3)	161(3)
O(1W)-H(2W)...Cl(2)	0.855(17)	2.375(19)	3.2044(19)	164(3)

Symmetry transformations used to generate equivalent atoms:

#1 $x+1/2, -y+3/2, z+1/2$ #2 $-x+1, -y+2, -z+2$ #3 $x-1/2, -y+3/2, z+1/2$ #4 $-x+1/2, y-1/2, -z+3/2$.

A.2 [Rh(chrysi)(phen)(DPE)]Cl₂**Table A.7** Crystal data and structure refinement for [Rh(chrysi)(phen)(DPE)]Cl₂.

Identification code	ack007	
Empirical formula	C ₄₆ H ₄₇ Cl ₂ N ₆ O ₅ Rh	
Formula weight	937.70	
Temperature	100(2) K	
Wavelength	0.71073 Å	
Crystal system	Triclinic	
Space group	P -1	
Unit cell dimensions	a = 9.6145(8) Å	α = 64.434(4)°.
	b = 15.7645(13) Å	β = 85.049(4)°.

231

$$c = 16.8583(14) \text{ \AA} \quad \gamma = 73.491(4)^\circ.$$

Volume	2208.0(3) \AA^3
Z	2
Density (calculated)	1.410 Mg/m^3
Absorption coefficient	0.560 mm^{-1}
F(000)	968
Crystal size	0.450 x 0.300 x 0.200 mm^3
Theta range for data collection	2.211 to 30.586°.
Index ranges	-13<=h<=13, -22<=k<=22, -24<=l<=24
Reflections collected	153083
Independent reflections	13536 [R(int) = 0.0310]
Completeness to theta = 25.242°	99.9 %
Absorption correction	Semi-empirical from equivalents
Max. and min. transmission	0.7461 and 0.6678
Refinement method	Full-matrix least-squares on F ²
Data / restraints / parameters	13536 / 299 / 674
Goodness-of-fit on F ²	1.120
Final R indices [I>2sigma(I)]	R1 = 0.0418, wR2 = 0.1050
R indices (all data)	R1 = 0.0468, wR2 = 0.1110
Extinction coefficient	n/a
Largest diff. peak and hole	2.425 and -0.777 e.\AA^{-3}

Table A.8 Atomic coordinates ($\times 10^4$) and equivalent isotropic displacement parameters ($\text{\AA}^2 \times 10^3$) for $[\text{Rh}(\text{chrysi})(\text{phen})(\text{DPE})]\text{Cl}_2$. $U(\text{eq})$ is defined as one-third of the trace of the orthogonalized U^{ij} tensor.

	x	y	z	$U(\text{eq})$
O(1W)	3806(2)	6958(1)	6716(1)	21(1)
O(2W)	1928(2)	6067(1)	7957(1)	26(1)
Cl(1)	4995(1)	6766(1)	4985(1)	21(1)
Cl(2)	3958(1)	3897(1)	8810(1)	36(1)
Rh(1)	1864(1)	3770(1)	2999(1)	12(1)
N(1)	2672(2)	2748(1)	4196(1)	14(1)
C(1)	2487(2)	1890(1)	4438(1)	16(1)
C(2)	3154(2)	1016(2)	5218(1)	20(1)
C(3)	3945(3)	1066(2)	5850(2)	25(1)
C(4)	4699(3)	214(2)	6542(2)	31(1)
C(5)	4655(3)	-683(2)	6603(2)	33(1)
C(6)	3848(3)	-739(2)	5998(2)	29(1)
C(7)	3078(3)	109(2)	5287(2)	22(1)
C(8)	2199(3)	55(2)	4643(2)	22(1)
C(9)	2241(3)	-877(2)	4702(2)	35(1)
C(10)	1470(3)	-959(2)	4110(2)	38(1)
C(11)	497(3)	-139(2)	3473(2)	27(1)

C(12)	-375(3)	-241(2)	2905(2)	36(1)
C(13)	-1376(3)	545(2)	2327(2)	36(1)
C(14)	-1574(3)	1469(2)	2317(2)	36(1)
C(15)	-727(3)	1593(2)	2850(2)	27(1)
C(16)	374(2)	804(2)	3421(2)	21(1)
C(17)	1348(2)	890(2)	3967(1)	18(1)
C(18)	1598(2)	1823(1)	3796(1)	15(1)
N(2)	1244(2)	2636(1)	3081(1)	15(1)
N(3)	38(2)	4327(1)	3530(1)	13(1)
C(21)	-1165(2)	4036(2)	3738(1)	18(1)
C(22)	-2362(2)	4516(2)	4068(2)	22(1)
C(23)	-2307(2)	5306(2)	4200(2)	22(1)
C(24)	-1037(2)	5619(2)	4003(1)	19(1)
C(25)	-839(3)	6413(2)	4138(2)	24(1)
C(26)	423(3)	6668(2)	3948(2)	25(1)
C(27)	1606(2)	6163(2)	3591(1)	19(1)
C(28)	2944(3)	6396(2)	3370(2)	23(1)
C(29)	3961(3)	5895(2)	2990(2)	23(1)
C(30)	3682(2)	5151(2)	2839(1)	18(1)
N(4)	2455(2)	4893(1)	3070(1)	13(1)
C(31)	1420(2)	5396(1)	3437(1)	14(1)
C(32)	109(2)	5110(1)	3663(1)	14(1)
N(5)	1233(2)	4665(1)	1719(1)	13(1)

C(41)	24(2)	5421(1)	1428(1)	17(1)
C(42)	-265(2)	6036(2)	542(1)	19(1)
C(43)	725(2)	5867(2)	-60(1)	20(1)
C(44)	1961(2)	5081(2)	241(1)	18(1)
C(45)	2196(2)	4489(1)	1139(1)	14(1)
C(46)	3549(2)	3637(1)	1521(1)	15(1)
O(1)	3685(2)	3334(1)	2448(1)	14(1)
C(53)	4889(2)	3981(2)	1112(1)	21(1)
C(47)	3442(2)	2778(2)	1345(1)	19(1)
C(48)	4627(3)	2232(2)	1074(2)	32(1)
C(49)	4493(4)	1429(2)	973(2)	45(1)
C(50)	3191(4)	1205(2)	1126(2)	41(1)
C(51)	2058(3)	1790(2)	1375(2)	30(1)
N(6)	2165(2)	2562(1)	1489(1)	22(1)
O(1E)	2690(7)	2953(4)	7910(3)	64(2)
C(11E)	2806(12)	1985(5)	8484(6)	63(2)
C(12E)	2220(13)	1525(6)	8029(7)	77(3)
O(2E)	5257(12)	2014(8)	7005(6)	54(2)
C(21E)	4513(15)	1903(10)	7648(9)	50(3)
C(22E)	3204(14)	2115(10)	7999(8)	46(2)
O(3E)	4777(12)	1536(10)	8491(10)	65(3)
C(31E)	3670(20)	1336(11)	8984(11)	68(3)
C(32E)	2480(14)	2362(11)	8657(10)	46(2)

O(1F)	8115(9)	2310(8)	9372(7)	95(2)
C(11F)	7652(13)	1845(10)	9038(8)	91(2)
C(12F)	8717(14)	1205(10)	8760(8)	91(3)
O(2F)	9572(18)	1499(13)	9924(11)	102(4)
C(21F)	8750(20)	1178(16)	9578(11)	75(3)
C(22F)	7963(15)	552(10)	10165(8)	51(3)
O(3F)	6833(12)	2132(11)	9774(8)	111(5)
C(31F)	8163(19)	2140(20)	9803(13)	96(4)
C(32F)	9128(15)	1970(17)	9142(12)	87(4)

Table A.9 Selected bond lengths [\AA] and angles [$^\circ$] for $[\text{Rh}(\text{chrysi})(\text{phen})(\text{DPE})]\text{Cl}_2$.

Rh(1)-N(2)	1.9870(16)
Rh(1)-O(1)	1.9964(14)
Rh(1)-N(1)	2.0064(17)
Rh(1)-N(5)	2.0315(17)
Rh(1)-N(3)	2.0462(16)
Rh(1)-N(4)	2.0592(16)
N(2)-Rh(1)-O(1)	89.62(6)
N(2)-Rh(1)-N(1)	78.02(7)
O(1)-Rh(1)-N(1)	91.01(6)
N(2)-Rh(1)-N(5)	97.68(7)
O(1)-Rh(1)-N(5)	81.68(6)
N(1)-Rh(1)-N(5)	171.58(7)

N(2)-Rh(1)-N(3)	95.10(7)
O(1)-Rh(1)-N(3)	175.15(6)
N(1)-Rh(1)-N(3)	91.05(7)
N(5)-Rh(1)-N(3)	96.57(7)
N(2)-Rh(1)-N(4)	173.15(7)
O(1)-Rh(1)-N(4)	94.69(6)
N(1)-Rh(1)-N(4)	96.56(6)
N(5)-Rh(1)-N(4)	88.22(6)
N(3)-Rh(1)-N(4)	80.72(6)

Table A.10 Anisotropic displacement parameters ($\text{\AA}^2 \times 10^3$) for

[Rh(chrysi)(phen)(DPE)]Cl₂. The anisotropic displacement factor exponent takes the form: $-2\pi^2 [h^2 a^{*2} U^{11} + \dots + 2 h k a^* b^* U^{12}]$.

	U ¹¹	U ²²	U ³³	U ²³	U ¹³	U ¹²
O(1W)	18(1)	23(1)	24(1)	-13(1)	2(1)	-5(1)
O(2W)	24(1)	29(1)	25(1)	-11(1)	4(1)	-10(1)
Cl(1)	20(1)	23(1)	28(1)	-15(1)	5(1)	-10(1)
Cl(2)	39(1)	36(1)	37(1)	-18(1)	17(1)	-13(1)
Rh(1)	13(1)	11(1)	14(1)	-7(1)	2(1)	-5(1)
N(1)	16(1)	13(1)	14(1)	-6(1)	1(1)	-6(1)
C(1)	18(1)	15(1)	15(1)	-6(1)	4(1)	-7(1)
C(2)	26(1)	16(1)	16(1)	-4(1)	3(1)	-9(1)
C(3)	36(1)	22(1)	17(1)	-4(1)	-1(1)	-14(1)

C(4)	42(1)	29(1)	18(1)	-3(1)	-4(1)	-14(1)
C(5)	42(1)	25(1)	21(1)	1(1)	-2(1)	-11(1)
C(6)	37(1)	18(1)	26(1)	-3(1)	1(1)	-10(1)
C(7)	29(1)	16(1)	21(1)	-5(1)	4(1)	-10(1)
C(8)	26(1)	15(1)	26(1)	-7(1)	3(1)	-10(1)
C(9)	45(2)	15(1)	43(1)	-6(1)	-8(1)	-13(1)
C(10)	46(2)	18(1)	56(2)	-16(1)	-10(1)	-12(1)
C(11)	27(1)	20(1)	42(1)	-17(1)	-1(1)	-10(1)
C(12)	36(1)	26(1)	56(2)	-25(1)	-6(1)	-10(1)
C(13)	29(1)	35(1)	57(2)	-28(1)	-8(1)	-10(1)
C(14)	25(1)	30(1)	60(2)	-25(1)	-11(1)	-3(1)
C(15)	20(1)	22(1)	47(1)	-20(1)	-4(1)	-4(1)
C(16)	18(1)	19(1)	32(1)	-15(1)	4(1)	-9(1)
C(17)	18(1)	15(1)	24(1)	-10(1)	5(1)	-9(1)
C(18)	15(1)	16(1)	19(1)	-9(1)	5(1)	-7(1)
N(2)	16(1)	13(1)	19(1)	-9(1)	1(1)	-6(1)
N(3)	13(1)	14(1)	15(1)	-7(1)	2(1)	-5(1)
C(21)	17(1)	21(1)	20(1)	-10(1)	4(1)	-9(1)
C(22)	16(1)	28(1)	24(1)	-12(1)	6(1)	-9(1)
C(23)	17(1)	26(1)	23(1)	-13(1)	6(1)	-4(1)
C(24)	19(1)	18(1)	19(1)	-9(1)	4(1)	-4(1)
C(25)	28(1)	20(1)	25(1)	-15(1)	8(1)	-5(1)
C(26)	34(1)	18(1)	28(1)	-16(1)	7(1)	-8(1)

C(27)	26(1)	16(1)	21(1)	-10(1)	4(1)	-9(1)
C(28)	31(1)	21(1)	26(1)	-14(1)	6(1)	-16(1)
C(29)	24(1)	22(1)	29(1)	-13(1)	6(1)	-14(1)
C(30)	17(1)	17(1)	20(1)	-9(1)	4(1)	-7(1)
N(4)	14(1)	11(1)	14(1)	-6(1)	2(1)	-5(1)
C(31)	19(1)	13(1)	14(1)	-6(1)	1(1)	-6(1)
C(32)	16(1)	14(1)	15(1)	-7(1)	3(1)	-5(1)
N(5)	13(1)	13(1)	16(1)	-6(1)	1(1)	-5(1)
C(41)	15(1)	16(1)	20(1)	-9(1)	1(1)	-3(1)
C(42)	18(1)	18(1)	20(1)	-8(1)	-2(1)	-2(1)
C(43)	22(1)	21(1)	16(1)	-6(1)	0(1)	-6(1)
C(44)	18(1)	20(1)	17(1)	-9(1)	2(1)	-6(1)
C(45)	14(1)	14(1)	17(1)	-8(1)	1(1)	-4(1)
C(46)	14(1)	17(1)	16(1)	-9(1)	1(1)	-3(1)
O(1)	12(1)	16(1)	14(1)	-7(1)	1(1)	-3(1)
C(53)	15(1)	29(1)	20(1)	-10(1)	4(1)	-7(1)
C(47)	21(1)	16(1)	18(1)	-9(1)	-4(1)	1(1)
C(48)	25(1)	34(1)	43(1)	-28(1)	-6(1)	5(1)
C(49)	42(2)	39(2)	63(2)	-41(2)	-12(1)	11(1)
C(50)	58(2)	24(1)	47(2)	-24(1)	-14(1)	0(1)
C(51)	44(1)	23(1)	29(1)	-14(1)	-1(1)	-13(1)
N(6)	29(1)	19(1)	21(1)	-10(1)	1(1)	-9(1)
O(1E)	97(4)	75(3)	35(2)	-17(2)	-12(2)	-48(3)

C(11E)	94(5)	42(3)	63(4)	-37(2)	-19(4)	-2(3)
C(12E)	107(7)	59(4)	70(5)	-23(4)	-39(5)	-26(5)
O(2E)	74(6)	60(6)	42(4)	-24(4)	14(4)	-39(5)
C(21E)	78(6)	39(5)	48(5)	-29(5)	18(5)	-25(5)
C(22E)	78(5)	46(5)	29(4)	-32(4)	6(4)	-15(5)
O(3E)	53(5)	60(6)	89(7)	-46(5)	-20(4)	2(4)
C(31E)	113(7)	54(5)	51(6)	-33(5)	2(5)	-26(5)
C(32E)	52(5)	64(6)	52(6)	-42(5)	19(5)	-35(4)
O(1F)	53(4)	119(6)	94(5)	-40(5)	-10(4)	2(4)
C(11F)	66(5)	107(6)	68(5)	-5(4)	-5(4)	-29(4)
C(12F)	85(6)	117(8)	71(6)	-32(5)	-24(5)	-31(5)
O(2F)	86(7)	124(8)	81(7)	-18(7)	-16(6)	-42(6)
C(21F)	52(5)	102(6)	55(5)	-18(5)	7(4)	-22(5)
C(22F)	48(7)	60(7)	34(6)	-22(5)	11(5)	3(5)
O(3F)	54(4)	112(8)	73(6)	5(6)	22(4)	36(5)
C(31F)	90(5)	103(7)	62(6)	-15(6)	12(5)	-14(5)
C(32F)	44(5)	118(8)	76(7)	-21(6)	13(5)	-24(6)

Table A.11 Hydrogen coordinates ($\times 10^4$) and isotropic displacement parameters ($\text{\AA}^2 \times 10^3$) for $[\text{Rh}(\text{chrysi})(\text{phen})(\text{DPE})]\text{Cl}_2$.

	x	y	z	U(eq)
H(11W)	4540(30)	6920(30)	6970(20)	32
H(12W)	4060(40)	6890(30)	6257(16)	32

H(21W)	2380(40)	5472(15)	8160(20)	39
H(22W)	2620(30)	6240(30)	7650(20)	39
H(1N)	3270(30)	2800(20)	4528(17)	17
H(3)	3964	1684	5805	30
H(4)	5240	247	6969	37
H(5)	5188	-1267	7068	39
H(6)	3812	-1361	6063	34
H(9)	2813	-1451	5159	42
H(10)	1591	-1586	4128	46
H(12)	-261	-869	2927	43
H(13)	-1935	470	1936	44
H(14)	-2304	2014	1935	43
H(15)	-886	2223	2835	33
H(2N)	920(30)	2630(20)	2619(15)	18
H(21)	-1216	3483	3660	22
H(22)	-3212	4295	4200	26
H(23)	-3115	5636	4422	27
H(25)	-1605	6767	4366	28
H(26)	529	7193	4053	30
H(28)	3136	6893	3484	28
H(29)	4858	6054	2828	27
H(30)	4391	4822	2564	21
H(41)	-647	5535	1843	20

H(42)	-1125	6563	350	23
H(43)	558	6284	-670	24
H(44)	2640	4950	-164	22
H(53A)	4859	4578	1170	32
H(53B)	4894	4115	488	32
H(53C)	5769	3469	1417	32
H(48)	5516	2406	960	39
H(49)	5296	1040	801	55
H(50)	3072	659	1061	50
H(51)	1151	1639	1471	36
H(1E)	3033	3215	8159	96
H(11A)	2253	1952	9015	76
H(11B)	3837	1629	8671	76
H(12A)	2269	847	8436	115
H(12B)	2798	1536	7518	115
H(12C)	1208	1890	7834	115
H(2E)	6028	1556	7143	80
H(21A)	5111	2047	7999	60
H(21B)	4742	1180	7926	60
H(22A)	3294	1742	8640	69
H(22B)	2491	1940	7759	69
H(22C)	2882	2816	7850	69
H(3E)	4987	1999	8530	97

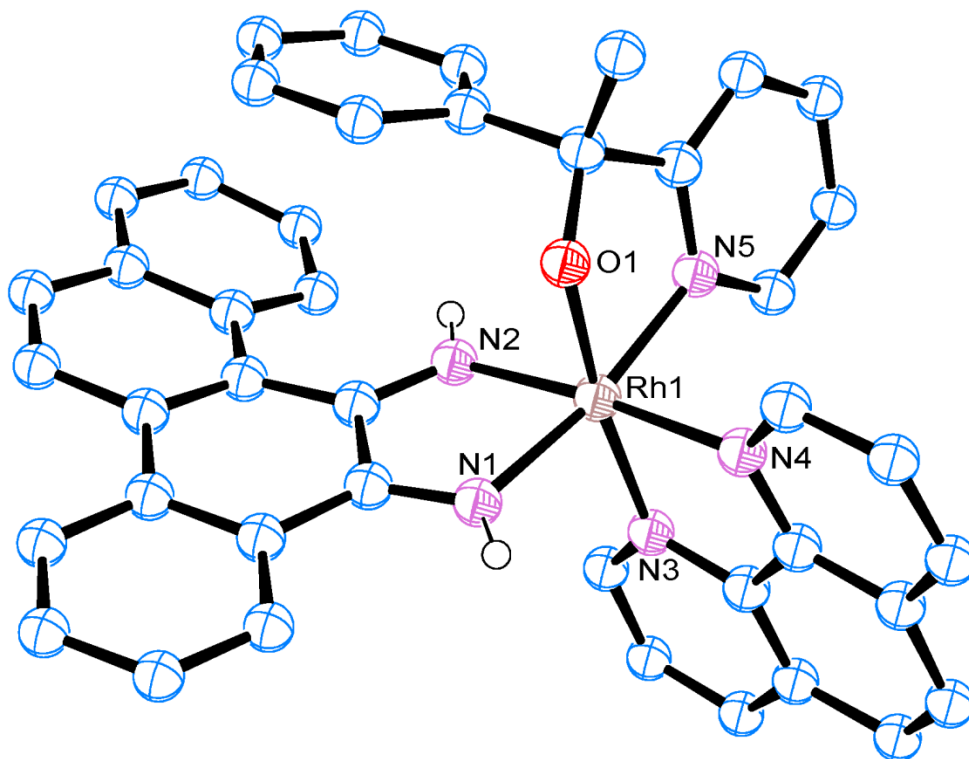
H(31A)	3931	1077	9616	82
H(31B)	3312	854	8888	82
H(32A)	1620	2293	9010	69
H(32B)	2209	2590	8037	69
H(32C)	2878	2836	8723	69
H(1F)	8414	2756	8971	143
H(11C)	6996	2330	8525	109
H(11D)	7062	1457	9479	109
H(12D)	8234	919	8489	137
H(12E)	9325	682	9269	137
H(12F)	9324	1573	8329	137
H(2F)	10366	1493	9673	153
H(21C)	9392	830	9256	90
H(21D)	8056	1754	9140	90
H(22D)	7283	457	9831	77
H(22E)	7422	845	10547	77
H(22F)	8635	-81	10526	77
H(3F)	6805	1593	9799	166
H(31C)	8596	1633	10387	115
H(31D)	8159	2778	9775	115
H(32D)	10127	1892	9303	131
H(32E)	8839	2531	8569	131
H(32F)	9070	1377	9107	131

Table A.12 Hydrogen bonds for [Rh(chrysi)(phen)(DPE)]Cl₂ [Å and °].

D-H...A	d(D-H)	d(H...A)	d(D...A)	<(DHA)
O(1W)-H(11W)...O(1)#10	0.837(18)	1.891(19)	2.723(2)	172(3)
O(1W)-H(12W)...Cl(1)	0.831(18)	2.319(18)	3.1463(17)	174(3)
O(2W)-H(21W)...Cl(2)	0.838(18)	2.34(2)	3.166(2)	170(4)
O(2W)-H(22W)...O(1W)	0.836(18)	1.99(2)	2.804(2)	164(4)
N(1)-H(1N)...Cl(1)#1	0.876(17)	2.305(18)	3.1547(17)	163(3)
N(2)-H(2N)...N(6)	0.870(17)	2.19(3)	2.793(3)	126(2)
C(21)-H(21)...O(2W)#2	0.95	2.60	3.092(3)	112.3
C(21)-H(21)...N(2)	0.95	2.69	3.197(3)	113.7
C(22)-H(22)...Cl(1)#2	0.95	2.62	3.531(2)	160.9
C(29)-H(29)...Cl(2)#1	0.95	2.87	3.433(2)	118.8
C(30)-H(30)...O(1W)#1	0.95	2.65	3.323(3)	128.6
C(41)-H(41)...N(3)	0.95	2.66	3.202(3)	116.6
C(44)-H(44)...Cl(2)#3	0.95	2.87	3.747(2)	153.3
C(53)-H(53A)...Cl(2)#1	0.98	2.95	3.867(2)	156.1
C(48)-H(48)...O(3F)#3	0.95	2.41	2.939(11)	115.2
O(1E)-H(1E)...Cl(2)	0.84	2.21	3.050(5)	179.5
C(32E)-H(32C)...Cl(2)	0.98	2.26	3.240(14)	175.2

Symmetry transformations used to generate equivalent atoms:

#1 -x+1,-y+1,-z+1 #2 -x,-y+1,-z+1 #3 x,y,z-1.

A.3 [Rh(chrysi)(phen)(PPE)]Cl₂**Table A.13** Crystal data and structure refinement for [Rh(chrysi)(phen)(PPE)]Cl₂.

Identification code	ack010	
Empirical formula	C ₄₇ H ₄₈ Cl ₂ N ₅ O ₅ Rh	
Formula weight	936.71	
Temperature	100(2) K	
Wavelength	0.71073 Å	
Crystal system	Triclinic	
Space group	P -1	
Unit cell dimensions	a = 10.7782(6) Å	α = 72.345(3)°.
	b = 12.1739(6) Å	β = 89.877(3)°.

245

$$c = 17.5944(10) \text{ \AA} \quad \gamma = 80.812(3)^\circ.$$

Volume	2169.0(2) \AA^3
Z	2
Density (calculated)	1.434 Mg/m^3
Absorption coefficient	0.570 mm^{-1}
F(000)	968
Crystal size	0.250 x 0.150 x 0.150 mm^3
Theta range for data collection	1.216 to 30.663 $^\circ$.
Index ranges	-15 $\leq h \leq$ 15, -17 $\leq k \leq$ 17, -25 $\leq l \leq$ 25
Reflections collected	115348
Independent reflections	13351 [R(int) = 0.0555]
Completeness to theta = 25.242 $^\circ$	99.9 %
Absorption correction	Semi-empirical from equivalents
Max. and min. transmission	0.7461 and 0.6896
Refinement method	Full-matrix least-squares on F ²
Data / restraints / parameters	13351 / 160 / 625
Goodness-of-fit on F ²	1.055
Final R indices [I > 2sigma(I)]	R1 = 0.0372, wR2 = 0.0859
R indices (all data)	R1 = 0.0499, wR2 = 0.0919
Extinction coefficient	n/a
Largest diff. peak and hole	0.965 and -0.864 e.\AA^{-3}

Table A.14 Atomic coordinates ($\times 10^4$) and equivalent isotropic displacement parameters ($\text{\AA}^2 \times 10^3$) for $[\text{Rh}(\text{chrysi})(\text{phen})(\text{PPE})]\text{Cl}_2$. $U(\text{eq})$ is defined as one-third of the trace of the orthogonalized U^{ij} tensor.

	x	y	z	U(eq)
Rh(1)	2693(1)	3315(1)	2995(1)	16(1)
N(1)	2433(2)	5037(1)	2474(1)	18(1)
C(1)	2575(2)	5401(2)	1716(1)	18(1)
C(2)	2212(2)	6597(2)	1198(1)	21(1)
C(3)	1757(2)	7499(2)	1518(1)	28(1)
C(4)	1358(2)	8622(2)	1013(2)	34(1)
C(5)	1412(2)	8840(2)	196(2)	33(1)
C(6)	1850(2)	7957(2)	-124(1)	30(1)
C(7)	2272(2)	6807(2)	371(1)	23(1)
C(8)	2780(2)	5861(2)	37(1)	22(1)
C(9)	2712(2)	6084(2)	-804(1)	29(1)
C(10)	3143(2)	5243(2)	-1139(1)	32(1)
C(11)	3772(2)	4137(2)	-680(1)	28(1)
C(12)	4262(2)	3278(2)	-1044(2)	35(1)
C(13)	4901(2)	2221(3)	-606(2)	39(1)
C(14)	5140(2)	1998(2)	217(2)	33(1)
C(15)	4686(2)	2814(2)	588(1)	25(1)
C(16)	3930(2)	3886(2)	164(1)	23(1)

C(17)	3326(2)	4746(2)	521(1)	20(1)
C(18)	3126(2)	4461(2)	1372(1)	17(1)
N(2)	3292(2)	3438(1)	1904(1)	19(1)
N(3)	4367(2)	3371(1)	3525(1)	19(1)
C(21)	5499(2)	3385(2)	3225(1)	26(1)
C(22)	6544(2)	3470(2)	3660(2)	31(1)
C(23)	6424(2)	3521(2)	4425(1)	29(1)
C(24)	5241(2)	3499(2)	4762(1)	24(1)
C(25)	5001(2)	3571(2)	5548(1)	29(1)
C(26)	3827(2)	3588(2)	5823(1)	31(1)
C(27)	2786(2)	3532(2)	5344(1)	27(1)
C(28)	1536(2)	3570(2)	5581(1)	35(1)
C(29)	614(2)	3515(2)	5073(1)	36(1)
C(30)	912(2)	3422(2)	4318(1)	28(1)
N(4)	2080(2)	3381(1)	4079(1)	20(1)
C(31)	3002(2)	3442(2)	4578(1)	21(1)
C(32)	4237(2)	3433(2)	4284(1)	19(1)
N(5)	2786(2)	1550(1)	3368(1)	23(1)
C(41)	3670(2)	769(2)	3870(1)	32(1)
C(42)	3624(3)	-413(2)	4113(2)	44(1)
C(43)	2631(3)	-793(2)	3833(2)	45(1)
C(44)	1720(3)	8(2)	3319(2)	37(1)
C(45)	1811(2)	1188(2)	3085(1)	27(1)

C(46)	879(2)	2151(2)	2510(1)	25(1)
O(1)	972(1)	3230(1)	2646(1)	23(1)
C(47)	-475(2)	1933(2)	2678(2)	35(1)
C(51)	1137(2)	2232(2)	1637(1)	25(1)
C(52)	558(2)	3233(2)	1044(1)	29(1)
C(53)	720(2)	3345(2)	242(1)	31(1)
C(54)	1468(2)	2465(2)	20(1)	32(1)
C(55)	2052(2)	1483(2)	600(1)	33(1)
C(56)	1887(2)	1360(2)	1408(1)	30(1)
CI(1)	1877(1)	6439(1)	3680(1)	25(1)
CI(2)	5971(1)	1151(1)	2442(1)	77(1)
O(1M)	-1157(2)	4705(2)	2678(1)	37(1)
C(1M)	-962(2)	5850(2)	2320(2)	37(1)
O(2M)	6712(3)	9455(3)	4209(2)	88(1)
C(2M)	7926(4)	9647(4)	4304(2)	67(1)
C(2MA)	6880(20)	10615(12)	4027(11)	58(4)
O(3M)	4512(3)	9503(2)	1827(2)	60(1)
C(3M)	4789(7)	8480(4)	2460(3)	67(2)
O(3MA)	5573(17)	8317(16)	2301(9)	90(4)
C(3MA)	4330(18)	8100(20)	2399(13)	75(5)
O(4M)	8468(4)	9977(3)	1948(2)	60(1)
C(4M)	8242(8)	8851(6)	2028(6)	78(2)
O(4MA)	9825(9)	8629(7)	2836(6)	56(3)

C(4MA)	8748(13)	8761(15)	2358(9)	48(3)
O(4MB)	7647(15)	9150(16)	1585(7)	65(4)
C(4MB)	7459(13)	8662(12)	2398(7)	24(2)

Table A.15 Selected bond lengths [Å] and angles [°] for [Rh(chrysi)(phen)(PPE)]Cl₂.

Rh(1)-O(1)	1.9827(14)
Rh(1)-N(1)	1.9905(15)
Rh(1)-N(2)	1.9934(16)
Rh(1)-N(5)	2.0339(16)
Rh(1)-N(4)	2.0373(16)
Rh(1)-N(3)	2.0530(17)
O(1)-Rh(1)-N(1)	91.59(6)
O(1)-Rh(1)-N(2)	90.74(6)
N(1)-Rh(1)-N(2)	77.79(6)
O(1)-Rh(1)-N(5)	80.78(7)
N(1)-Rh(1)-N(5)	170.43(7)
N(2)-Rh(1)-N(5)	96.43(7)
O(1)-Rh(1)-N(4)	90.69(6)
N(1)-Rh(1)-N(4)	96.09(6)
N(2)-Rh(1)-N(4)	173.75(6)
N(5)-Rh(1)-N(4)	89.81(6)
O(1)-Rh(1)-N(3)	171.30(6)
N(1)-Rh(1)-N(3)	90.66(6)

N(2)-Rh(1)-N(3)	97.95(7)
N(5)-Rh(1)-N(3)	97.74(7)
N(4)-Rh(1)-N(3)	80.72(7)

Table A.16 Anisotropic displacement parameters ($\text{\AA}^2 \times 10^3$) for

[Rh(chrysi)(phen)(PPE)]Cl₂. The anisotropic displacement factor exponent takes the

form: $-2\pi^2[h^2 a^{*2}U^{11} + \dots + 2 h k a^* b^* U^{12}]$.

	U ¹¹	U ²²	U ³³	U ²³	U ¹³	U ¹²
Rh(1)	18(1)	13(1)	17(1)	-4(1)	4(1)	-3(1)
N(1)	19(1)	15(1)	19(1)	-5(1)	4(1)	-4(1)
C(1)	16(1)	17(1)	20(1)	-5(1)	2(1)	-6(1)
C(2)	20(1)	19(1)	22(1)	-3(1)	2(1)	-6(1)
C(3)	33(1)	19(1)	28(1)	-3(1)	4(1)	-4(1)
C(4)	40(1)	18(1)	40(1)	-3(1)	3(1)	-3(1)
C(5)	30(1)	22(1)	38(1)	6(1)	-2(1)	-5(1)
C(6)	28(1)	30(1)	25(1)	3(1)	-2(1)	-10(1)
C(7)	21(1)	25(1)	21(1)	-1(1)	-1(1)	-8(1)
C(8)	19(1)	30(1)	19(1)	-5(1)	2(1)	-12(1)
C(9)	25(1)	42(1)	19(1)	-4(1)	0(1)	-13(1)
C(10)	26(1)	55(1)	19(1)	-12(1)	4(1)	-19(1)
C(11)	20(1)	47(1)	25(1)	-17(1)	7(1)	-15(1)
C(12)	27(1)	61(2)	28(1)	-27(1)	9(1)	-14(1)
C(13)	30(1)	58(2)	43(1)	-35(1)	13(1)	-12(1)

C(14)	23(1)	43(1)	40(1)	-24(1)	11(1)	-8(1)
C(15)	19(1)	36(1)	26(1)	-15(1)	9(1)	-10(1)
C(16)	17(1)	36(1)	23(1)	-15(1)	7(1)	-12(1)
C(17)	17(1)	28(1)	18(1)	-8(1)	4(1)	-10(1)
C(18)	14(1)	21(1)	19(1)	-7(1)	3(1)	-7(1)
N(2)	20(1)	18(1)	21(1)	-9(1)	5(1)	-5(1)
N(3)	20(1)	17(1)	21(1)	-6(1)	3(1)	-2(1)
C(21)	24(1)	27(1)	27(1)	-10(1)	6(1)	-5(1)
C(22)	22(1)	34(1)	39(1)	-12(1)	5(1)	-5(1)
C(23)	27(1)	24(1)	35(1)	-8(1)	-5(1)	-4(1)
C(24)	30(1)	14(1)	25(1)	-4(1)	-2(1)	-2(1)
C(25)	42(1)	21(1)	23(1)	-5(1)	-5(1)	-4(1)
C(26)	48(1)	27(1)	18(1)	-6(1)	1(1)	-6(1)
C(27)	39(1)	22(1)	18(1)	-3(1)	7(1)	-4(1)
C(28)	44(1)	38(1)	20(1)	-7(1)	14(1)	-3(1)
C(29)	31(1)	43(1)	29(1)	-7(1)	14(1)	-3(1)
C(30)	25(1)	31(1)	26(1)	-4(1)	8(1)	-4(1)
N(4)	22(1)	17(1)	18(1)	-3(1)	6(1)	-3(1)
C(31)	28(1)	14(1)	18(1)	-2(1)	4(1)	-1(1)
C(32)	25(1)	12(1)	19(1)	-3(1)	2(1)	-2(1)
N(5)	32(1)	16(1)	21(1)	-5(1)	3(1)	-5(1)
C(41)	48(1)	18(1)	26(1)	-5(1)	-4(1)	-2(1)
C(42)	78(2)	18(1)	31(1)	-2(1)	-10(1)	0(1)

C(43)	84(2)	18(1)	34(1)	-3(1)	-1(1)	-14(1)
C(44)	60(2)	25(1)	31(1)	-8(1)	5(1)	-22(1)
C(45)	38(1)	21(1)	24(1)	-7(1)	6(1)	-12(1)
C(46)	27(1)	25(1)	26(1)	-6(1)	3(1)	-12(1)
O(1)	21(1)	22(1)	27(1)	-8(1)	2(1)	-5(1)
C(47)	33(1)	44(1)	33(1)	-10(1)	9(1)	-22(1)
C(51)	26(1)	27(1)	25(1)	-8(1)	4(1)	-15(1)
C(52)	24(1)	33(1)	30(1)	-8(1)	2(1)	-11(1)
C(53)	27(1)	38(1)	28(1)	-4(1)	-2(1)	-14(1)
C(54)	30(1)	48(1)	26(1)	-14(1)	5(1)	-22(1)
C(55)	36(1)	36(1)	34(1)	-17(1)	8(1)	-15(1)
C(56)	34(1)	28(1)	30(1)	-9(1)	3(1)	-12(1)
Cl(1)	31(1)	26(1)	24(1)	-13(1)	8(1)	-10(1)
Cl(2)	120(1)	50(1)	48(1)	-22(1)	-22(1)	37(1)
O(1M)	23(1)	40(1)	42(1)	-7(1)	5(1)	-4(1)
C(1M)	35(1)	39(1)	38(1)	-13(1)	2(1)	-4(1)
O(2M)	115(2)	78(2)	61(2)	-2(2)	-14(2)	-21(2)
C(2M)	78(2)	52(2)	48(2)	13(2)	20(2)	1(2)
C(2MA)	75(10)	61(5)	31(8)	-17(7)	-4(7)	14(7)
O(3M)	89(2)	36(1)	44(2)	-6(1)	0(1)	6(1)
C(3M)	128(5)	36(2)	32(2)	-14(1)	11(3)	9(3)
O(3MA)	130(9)	95(8)	54(7)	-17(6)	-9(7)	-52(8)
C(3MA)	115(9)	76(10)	33(7)	-11(8)	6(8)	-24(9)

O(4M)	91(3)	36(2)	59(2)	-14(2)	38(2)	-28(2)
C(4M)	90(6)	47(3)	109(6)	-35(4)	41(4)	-24(4)
O(4MA)	65(6)	27(4)	72(6)	-16(4)	-20(4)	9(4)
C(4MA)	49(6)	51(6)	50(6)	-26(5)	8(4)	-8(5)
O(4MB)	50(7)	83(8)	29(5)	20(6)	4(5)	8(6)
C(4MB)	25(6)	26(6)	26(5)	-11(4)	11(5)	-11(5)

Table A.17 Hydrogen coordinates ($\times 10^4$) and isotropic displacement parameters ($\text{\AA}^2 \times 10^3$) for $[\text{Rh}(\text{chrysi})(\text{phen})(\text{PPE})]\text{Cl}_2$.

	x	y	z	U(eq)
H(1N)	2160(20)	5526(18)	2733(13)	21
H(3)	1722	7341	2080	33
H(4)	1051	9238	1226	41
H(5)	1143	9611	-151	40
H(6A)	1867	8127	-687	36
H(9)	2355	6841	-1138	35
H(10)	3019	5403	-1699	38
H(12)	4140	3445	-1605	42
H(13)	5185	1639	-853	47
H(14)	5622	1274	520	39
H(15)	4884	2654	1141	30
H(2N)	3540(20)	2872(17)	1735(14)	22
H(21)	5601	3336	2699	31

H(22)	7338	3493	3425	37
H(23)	7134	3571	4724	35
H(25)	5676	3607	5882	35
H(26)	3693	3639	6346	37
H(28)	1336	3635	6093	42
H(29)	-230	3539	5231	43
H(30)	260	3388	3968	34
H(41)	4349	1037	4063	38
H(42)	4263	-953	4466	53
H(43)	2576	-1602	3994	54
H(44)	1032	-246	3124	45
H(47A)	-619	1819	3245	53
H(47B)	-600	1232	2545	53
H(47C)	-1068	2607	2353	53
H(52)	49	3842	1190	34
H(53)	318	4027	-156	38
H(54)	1575	2540	-529	39
H(55)	2573	883	451	40
H(56)	2290	675	1804	36
H(10)	-500(20)	4270(30)	2630(20)	55
H(1M1)	-1763	6386	2260	56
H(1M2)	-623	5920	1793	56
H(1M3)	-363	6049	2655	56

H(2M)	6437	9805	3737	133
H(2MA)	6311	9367	3828	133
H(2M1)	7909	10472	4259	101
H(2M2)	8441	9451	3889	101
H(2M3)	8287	9155	4831	101
H(2M4)	6210	11042	4260	86
H(2M5)	6833	10972	3446	86
H(2M6)	7697	10650	4247	86
H(3M)	4920	10002	1895	90
H(3M1)	4985	8669	2945	100
H(3M2)	5516	7975	2340	100
H(3M3)	4062	8073	2543	100
H(3MA)	6060	7687	2343	136
H(3M4)	3978	8365	2840	113
H(3M5)	4325	7263	2519	113
H(3M6)	3821	8529	1906	113
H(4M)	7782	10417	1947	90
H(4M1)	9028	8357	1975	117
H(4M2)	7623	8884	1610	117
H(4M3)	7914	8522	2554	117
H(4MA)	9622	8582	3305	84
H(4M4)	8178	8251	2656	72
H(4M5)	8984	8548	1877	72

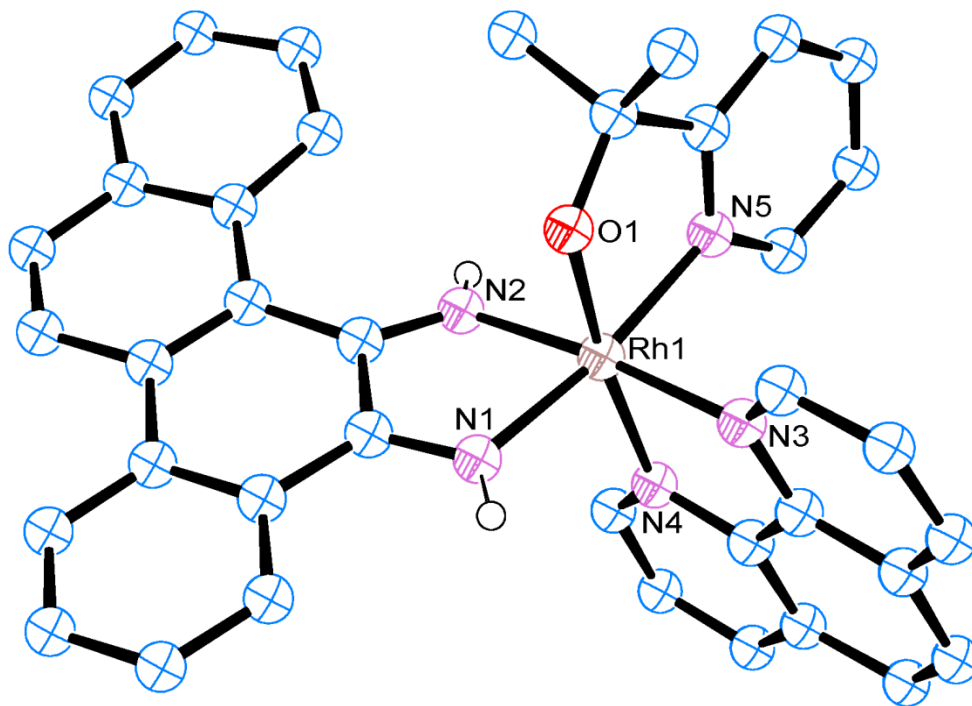
H(4M6)	8324	9576	2205	72
H(4MB)	7877	9801	1509	97
H(4M7)	8266	8259	2679	37
H(4M8)	6877	8102	2463	37
H(4M9)	7104	9283	2621	37

Table A.18 Hydrogen bonds for [Rh(chrysi)(phen)(PPE)]Cl₂ [Å and °].

D-H...A	d(D-H)	d(H...A)	d(D...A)	<(DHA)
N(1)-H(1N)...Cl(1)	0.870(16)	2.263(17)	3.1054(17)	163(2)
C(21)-H(21)...Cl(2)	0.95	2.80	3.374(2)	119.9
C(22)-H(22)...O(1M)#1	0.95	2.47	3.314(3)	147.5
C(29)-H(29)...Cl(1)#2	0.95	2.61	3.468(2)	150.1
C(30)-H(30)...O(1)	0.95	2.50	3.021(3)	114.5
C(44)-H(44)...O(4MA)#3	0.95	2.19	3.111(9)	161.8
C(47)-H(47B)...O(4M)#3	0.98	2.43	3.369(4)	159.9
O(1M)-H(1O)...O(1)	0.834(18)	1.860(18)	2.691(2)	173(3)
O(2M)-H(2M)...Cl(2)#4	0.84	2.37	3.187(3)	165.3
C(2MA)-H(2M5)...Cl(2)#4	0.98	1.93	2.804(19)	146.4
O(3M)-H(3M)...Cl(2)#4	0.84	2.34	3.162(3)	164.8
O(4M)-H(4M)...Cl(2)#4	0.84	2.30	3.091(4)	157.7
C(4MB)-H(4M9)...Cl(2)#4	0.98	2.33	3.217(14)	149.8

Symmetry transformations used to generate equivalent atoms:

#1 $x+1, y, z$ #2 $-x, -y+1, -z+1$ #3 $x-1, y-1, z$ #4 $x, y+1, z$.

A.4 [Rh(chrysi)(phen)(PPO)]Cl₂**Table A.19** Crystal data and structure refinement for [Rh(chrysi)(phen)(PPO)]Cl₂.

Identification code	ack013	
Empirical formula	C ₄₅ H ₄₈ Cl ₂ N ₅ O ₃ Rh	
Formula weight	880.69	
Temperature	100(2) K	
Wavelength	0.71073 Å	
Crystal system	Triclinic	
Space group	P -1	
Unit cell dimensions	a = 9.1633(11) Å	α = 110.881(2)°.
	b = 15.4046(19) Å	β = 94.610(2)°.
	c = 16.791(2) Å	γ = 105.705(2)°.

258

Volume	2090.2(4) Å ³
Z	2
Density (calculated)	1.399 Mg/m ³
Absorption coefficient	0.583 mm ⁻¹
F(000)	912
Crystal size	0.500 x 0.500 x 0.400 mm ³
Theta range for data collection	1.324 to 30.043°.
Index ranges	-12<=h<=12, -21<=k<=21, -23<=l<=22
Reflections collected	61440
Independent reflections	11087 [R(int) = 0.0277]
Completeness to theta = 25.242°	99.9 %
Absorption correction	Semi-empirical from equivalents
Max. and min. transmission	0.7460 and 0.6697
Refinement method	Full-matrix least-squares on F ²
Data / restraints / parameters	11087 / 3 / 521
Goodness-of-fit on F ²	1.112
Final R indices [I>2sigma(I)]	R1 = 0.0308, wR2 = 0.0703
R indices (all data)	R1 = 0.0387, wR2 = 0.0750
Extinction coefficient	n/a
Largest diff. peak and hole	1.020 and -0.486 e.Å ⁻³

Table A.20 Atomic coordinates ($\times 10^4$) and equivalent isotropic displacement parameters ($\text{\AA}^2 \times 10^3$) for $[\text{Rh}(\text{chrysi})(\text{phen})(\text{PPO})]\text{Cl}_2$. $U(\text{eq})$ is defined as one-third of the trace of the orthogonalized U^{ij} tensor.

	x	y	z	$U(\text{eq})$
Cl(1)	1297(1)	4156(1)	7867(1)	19(1)
Cl(2)	2592(1)	2117(1)	5123(1)	21(1)
Rh(1)	3196(1)	6463(1)	2924(1)	10(1)
N(1)	3955(2)	6414(1)	4040(1)	12(1)
C(1)	3105(2)	5737(1)	4242(1)	12(1)
C(2)	3470(2)	5578(1)	5027(1)	14(1)
C(3)	4863(2)	6154(1)	5623(1)	17(1)
C(4)	5158(2)	6015(1)	6384(1)	19(1)
C(5)	4080(2)	5306(2)	6548(1)	20(1)
C(6)	2716(2)	4730(1)	5956(1)	18(1)
C(7)	2369(2)	4846(1)	5178(1)	14(1)
C(8)	924(2)	4221(1)	4531(1)	14(1)
C(9)	-98(2)	3464(1)	4707(1)	19(1)
C(10)	-1470(2)	2876(1)	4163(1)	20(1)
C(11)	-1890(2)	2935(1)	3359(1)	18(1)
C(12)	-3269(2)	2258(1)	2776(1)	23(1)
C(13)	-3648(2)	2259(2)	1972(1)	24(1)
C(14)	-2646(2)	2944(1)	1731(1)	22(1)

C(15)	-1322(2)	3625(1)	2293(1)	19(1)
C(16)	-878(2)	3662(1)	3136(1)	15(1)
C(17)	514(2)	4348(1)	3766(1)	13(1)
C(18)	1569(2)	5169(1)	3636(1)	12(1)
N(2)	1350(2)	5524(1)	3058(1)	11(1)
N(3)	5185(2)	7459(1)	2927(1)	13(1)
C(21)	6442(2)	7286(1)	2670(1)	17(1)
C(22)	7742(2)	8050(2)	2712(1)	21(1)
C(23)	7738(2)	8998(2)	3027(1)	22(1)
C(24)	6421(2)	9202(1)	3326(1)	19(1)
C(25)	6278(2)	10162(1)	3674(1)	25(1)
C(26)	4990(2)	10308(1)	3962(1)	25(1)
C(27)	3707(2)	9503(1)	3933(1)	20(1)
C(28)	2346(2)	9596(1)	4237(1)	24(1)
C(29)	1203(2)	8772(1)	4177(1)	21(1)
C(30)	1395(2)	7848(1)	3808(1)	16(1)
N(4)	2670(2)	7735(1)	3524(1)	13(1)
C(31)	3825(2)	8554(1)	3586(1)	15(1)
C(32)	5174(2)	8405(1)	3272(1)	15(1)
N(5)	2416(2)	6281(1)	1683(1)	13(1)
C(41)	1803(2)	6876(1)	1450(1)	17(1)
C(42)	1410(2)	6728(2)	588(1)	21(1)
C(43)	1617(2)	5929(2)	-49(1)	21(1)

C(44)	2223(2)	5308(1)	192(1)	18(1)
C(45)	2642(2)	5505(1)	1069(1)	14(1)
C(46)	3341(2)	4877(1)	1398(1)	14(1)
C(47)	2102(2)	3886(1)	1193(1)	23(1)
C(48)	4698(2)	4699(2)	961(1)	23(1)
O(1)	3933(1)	5361(1)	2304(1)	14(1)
O(1S)	5474(3)	1234(2)	9592(1)	57(1)
C(1S)	4384(4)	1360(2)	9035(2)	55(1)
C(2S)	3435(6)	1899(3)	9575(3)	95(2)
C(3S)	6343(4)	670(2)	9131(2)	52(1)
C(4S)	7480(5)	583(3)	9769(2)	78(1)
O(1T)	177(2)	1093(1)	3360(1)	32(1)
C(1T)	904(2)	1483(2)	2785(1)	27(1)
C(2T)	-245(3)	1054(2)	1938(2)	48(1)
C(3T)	2393(3)	1257(2)	2671(2)	42(1)

Table A.21 Selected bond lengths [\AA] and angles [$^\circ$] for $[\text{Rh}(\text{chrysi})(\text{phen})(\text{PPO})]\text{Cl}_2$.

Rh(1)-O(1)	1.9725(12)
Rh(1)-N(1)	1.9803(14)
Rh(1)-N(2)	1.9936(14)
Rh(1)-N(3)	2.0385(14)
Rh(1)-N(5)	2.0407(14)
Rh(1)-N(4)	2.0667(15)

O(1)-Rh(1)-N(1)	89.38(5)
O(1)-Rh(1)-N(2)	89.84(6)
N(1)-Rh(1)-N(2)	78.17(6)
O(1)-Rh(1)-N(3)	91.41(6)
N(1)-Rh(1)-N(3)	95.51(6)
N(2)-Rh(1)-N(3)	173.55(6)
O(1)-Rh(1)-N(5)	81.86(5)
N(1)-Rh(1)-N(5)	170.60(6)
N(2)-Rh(1)-N(5)	98.30(6)
N(3)-Rh(1)-N(5)	88.14(6)
O(1)-Rh(1)-N(4)	172.06(6)
N(1)-Rh(1)-N(4)	93.31(6)
N(2)-Rh(1)-N(4)	98.02(6)
N(3)-Rh(1)-N(4)	80.90(6)
N(5)-Rh(1)-N(4)	95.83(6)

Table A.22 Anisotropic displacement parameters ($\text{\AA}^2 \times 10^3$) for

$[\text{Rh}(\text{chrysi})(\text{phen})(\text{PPO})]\text{Cl}_2$. The anisotropic displacement factor exponent takes the

form: $-2\pi^2 [h^2 a^{*2} U^{11} + \dots + 2 h k a^* b^* U^{12}]$.

	U ¹¹	U ²²	U ³³	U ²³	U ¹³	U ¹²
Cl(1)	15(1)	24(1)	20(1)	8(1)	1(1)	10(1)
Cl(2)	21(1)	15(1)	21(1)	6(1)	-2(1)	2(1)

Rh(1)	10(1)	11(1)	12(1)	6(1)	1(1)	3(1)
N(1)	11(1)	12(1)	12(1)	5(1)	1(1)	4(1)
C(1)	14(1)	11(1)	12(1)	4(1)	2(1)	6(1)
C(2)	18(1)	15(1)	13(1)	7(1)	4(1)	9(1)
C(3)	18(1)	18(1)	16(1)	7(1)	2(1)	8(1)
C(4)	22(1)	23(1)	15(1)	7(1)	0(1)	12(1)
C(5)	27(1)	27(1)	15(1)	11(1)	6(1)	18(1)
C(6)	23(1)	22(1)	18(1)	13(1)	9(1)	13(1)
C(7)	18(1)	15(1)	14(1)	7(1)	6(1)	11(1)
C(8)	18(1)	12(1)	16(1)	6(1)	7(1)	8(1)
C(9)	25(1)	17(1)	20(1)	11(1)	8(1)	9(1)
C(10)	23(1)	14(1)	26(1)	11(1)	10(1)	6(1)
C(11)	18(1)	13(1)	23(1)	7(1)	7(1)	6(1)
C(12)	21(1)	17(1)	30(1)	11(1)	6(1)	3(1)
C(13)	19(1)	18(1)	28(1)	7(1)	1(1)	0(1)
C(14)	22(1)	20(1)	20(1)	7(1)	1(1)	2(1)
C(15)	20(1)	17(1)	19(1)	7(1)	4(1)	2(1)
C(16)	16(1)	12(1)	16(1)	5(1)	5(1)	5(1)
C(17)	15(1)	13(1)	14(1)	6(1)	6(1)	6(1)
C(18)	13(1)	12(1)	12(1)	5(1)	4(1)	5(1)
N(2)	10(1)	12(1)	12(1)	6(1)	1(1)	3(1)
N(3)	12(1)	14(1)	15(1)	9(1)	1(1)	3(1)
C(21)	13(1)	19(1)	20(1)	11(1)	1(1)	5(1)

C(22)	12(1)	27(1)	26(1)	15(1)	3(1)	4(1)
C(23)	15(1)	23(1)	27(1)	16(1)	-1(1)	-1(1)
C(24)	18(1)	16(1)	22(1)	11(1)	-3(1)	1(1)
C(25)	25(1)	14(1)	30(1)	11(1)	-4(1)	-2(1)
C(26)	30(1)	13(1)	28(1)	6(1)	-3(1)	4(1)
C(27)	23(1)	14(1)	19(1)	5(1)	-2(1)	6(1)
C(28)	29(1)	18(1)	22(1)	4(1)	0(1)	12(1)
C(29)	22(1)	23(1)	18(1)	6(1)	2(1)	12(1)
C(30)	17(1)	18(1)	14(1)	7(1)	2(1)	6(1)
N(4)	16(1)	13(1)	12(1)	6(1)	1(1)	5(1)
C(31)	16(1)	13(1)	14(1)	7(1)	-2(1)	3(1)
C(32)	16(1)	15(1)	15(1)	9(1)	-2(1)	3(1)
N(5)	10(1)	17(1)	14(1)	10(1)	1(1)	3(1)
C(41)	15(1)	17(1)	19(1)	10(1)	1(1)	4(1)
C(42)	19(1)	24(1)	24(1)	16(1)	-2(1)	4(1)
C(43)	18(1)	30(1)	15(1)	14(1)	0(1)	2(1)
C(44)	14(1)	25(1)	16(1)	8(1)	2(1)	5(1)
C(45)	9(1)	19(1)	16(1)	8(1)	2(1)	3(1)
C(46)	14(1)	17(1)	13(1)	5(1)	2(1)	6(1)
C(47)	22(1)	18(1)	25(1)	7(1)	-1(1)	4(1)
C(48)	19(1)	35(1)	17(1)	6(1)	5(1)	15(1)
O(1)	16(1)	15(1)	11(1)	5(1)	1(1)	8(1)
O(1S)	97(2)	43(1)	31(1)	8(1)	-2(1)	34(1)

C(1S)	74(2)	43(2)	37(1)	14(1)	-8(1)	12(2)
C(2S)	150(4)	80(3)	56(2)	6(2)	-10(2)	77(3)
C(3S)	76(2)	33(1)	38(1)	9(1)	7(1)	14(1)
C(4S)	118(4)	80(3)	59(2)	28(2)	20(2)	63(3)
O(1T)	26(1)	30(1)	30(1)	10(1)	0(1)	-5(1)
C(1T)	24(1)	25(1)	30(1)	10(1)	5(1)	7(1)
C(2T)	43(2)	67(2)	36(1)	16(1)	2(1)	26(1)
C(3T)	30(1)	48(2)	39(1)	5(1)	6(1)	12(1)

Table A.23 Hydrogen coordinates ($\times 10^4$) and isotropic displacement parameters ($\text{\AA}^2 \times 10^3$) for $[\text{Rh}(\text{chrysi})(\text{phen})(\text{PPO})]\text{Cl}_2$.

	x	y	z	U(eq)
H(1N)	4861(19)	6777(14)	4365(13)	14
H(3)	5601	6636	5505	21
H(4)	6096	6405	6793	23
H(5)	4280	5215	7072	24
H(6)	1996	4243	6079	22
H(9)	186	3367	5218	23
H(10)	-2163	2416	4326	24
H(12)	-3941	1797	2946	27
H(13)	-4575	1802	1584	29
H(14)	-2888	2938	1167	27

H(15)	-681	4088	2112	23
H(2N)	461(19)	5372(15)	2753(13)	14
H(21)	6468	6632	2454	20
H(22)	8628	7905	2519	25
H(23)	8608	9513	3045	26
H(25)	7104	10709	3704	30
H(26)	4930	10955	4188	30
H(28)	2220	10224	4482	28
H(29)	285	8829	4384	25
H(30)	586	7283	3760	20
H(41)	1635	7412	1889	20
H(42)	1005	7167	436	26
H(43)	1346	5809	-646	25
H(44)	2351	4750	-240	22
H(47A)	2544	3487	1419	34
H(47B)	1743	3541	562	34
H(47C)	1228	3998	1468	34
H(48A)	5465	5331	1064	35
H(48B)	4321	4325	334	35
H(48C)	5176	4328	1205	35
H(1S1)	3707	713	8605	65
H(1S2)	4924	1739	8716	65
H(2S1)	2915	1523	9893	142

H(2S2)	2660	1982	9196	142
H(2S3)	4110	2545	9989	142
H(3S1)	6898	989	8775	62
H(3S2)	5648	10	8736	62
H(4S1)	8133	1240	10173	117
H(4S2)	8128	222	9456	117
H(4S3)	6921	232	10094	117
H(1TO)	800(30)	1330(20)	3854(14)	49
H(1T)	1139	2211	3038	33
H(2T1)	-506	338	1692	72
H(2T2)	209	1317	1530	72
H(2T3)	-1184	1229	2044	72
H(3T1)	3117	1577	3232	63
H(3T2)	2847	1503	2253	63
H(3T3)	2184	546	2456	63

Table A.24 Hydrogen bonds for [Rh(chrysi)(phen)(PPO)]Cl₂ [Å and °].

D-H...A	d(D-H)	d(H...A)	d(D...A)	<(DHA)
N(1)-H(1N)...Cl(2)#1	0.871(15)	2.360(16)	3.2012(15)	162.6(19)
N(2)-H(2N)...Cl(1)#2	0.852(15)	2.261(17)	3.0219(15)	148.7(19)
C(21)-H(21)...Cl(1)#1	0.95	2.65	3.3762(19)	133.9
C(21)-H(21)...O(1)	0.95	2.53	3.039(2)	114.0
C(29)-H(29)...Cl(2)#2	0.95	2.98	3.819(2)	147.7

		268		
C(30)-H(30)...Cl(1)#2	0.95	2.87	3.4777(19)	123.2
C(41)-H(41)...N(4)	0.95	2.65	3.195(2)	116.8
C(44)-H(44)...Cl(1)#3	0.95	2.97	3.5805(19)	123.1
O(1T)-H(1TO)...Cl(2)	0.861(17)	2.286(18)	3.1420(17)	173(3)

Symmetry transformations used to generate equivalent atoms:

#1 -x+1,-y+1,-z+1 #2 -x,-y+1,-z+1 #3 x,y,z-1.